

DISS. ETH NO. 29861

**BIOMATERIALS FOR CRANIO-MAXILLOFACIAL BONE REPAIR:  
THE NEED FOR A BETTER VALIDATION PROCESS**

A thesis submitted to attain the degree of

DOCTOR OF SCIENCES

(Dr. sc. ETH Zurich)

presented by

*LUAN PHELIPE HATT*

*MSc ETH HST, ETH Zürich*

born on 20.03.1994

accepted on the recommendation of

*Prof. Dr. Marcy Zenobi-Wong*

*Prof. Dr. Martin Stoddart*

*Prof. Dr. Fergal O'Brien*

2024



## Abstract

Large bone defects in the cranio-maxillofacial (CMF) region resulting from tumour resection, infection or trauma pose significant challenges as they cannot regenerate naturally and require complex clinical interventions. Current treatments include the implantation of autologous bone grafting (ABG) or a collagen sponge combined with recombinant human bone morphogenic protein 2 (rhBMP-2). However, ABG is associated with donor site morbidities, limited availability, and inadequate restoration of aesthetic facial geometries. Furthermore, the use of rhBMP-2 has been shown to cause ectopic bone formation and increase the risk of cancer. Consequently, patients continue to suffer due to these drawbacks, highlighting the urgent need for alternative options. Bone tissue engineering (BTE) has emerged as a promising strategy to develop alternative bone graft substitutes (BGSs). Their easy fabrication process provides precise architecture and geometry, and allows for the incorporation of regenerative cells and factors. Properties including mechanical stability, biodegradability, biocompatibility, and osteogenic properties are necessary to successfully achieve the repair of large bone defects in the CMF region. Once a BGS prototype is developed, it is crucial to validate its safety and efficacy before clinical translation can be considered. In this thesis, several BGSs were developed and assessed through established evaluation methods including *in vitro* osteogenic differentiation of human bone marrow-derived mesenchymal stromal cells (hBM-MSCs) or *in vivo* subcutaneous implantation in mice and calvarial implantation in rabbits. However, the limitations of the validation protocols highlighted in this thesis calls for a better validation process that can offer a more robust insight into the osteogenic potency of the BGS.

## Zusammenfassung

Grosse Knochendefekte im Bereich der Schädel-Gesichts-Region, die durch Tumorresektionen, Infektionen oder Traumata entstehen, stellen erhebliche Herausforderungen für die Chirurgie dar, da sie oft komplexe chirurgische Eingriffe erfordern. Aktuelle Behandlungen umfassen die Transplantation von autologem Knochenmaterial oder Kollagenschwämmen kombiniert mit rekombinantem humanem knochenmorphogenetischem Protein 2 (rhBMP-2). Die Transplantation von autologem Knochenmaterial ist jedoch mit Morbiditäten an der Entnahmestelle, begrenzter Verfügbarkeit und unzureichender Wiederherstellung ästhetischer Gesichtsgeometrien assoziiert. Zudem zeigte sich ein erhöhtes Krebsrisiko bei der Verwendung von rhBMP-2 und es kann zu einer Bildung von Knochen an unerwünschten Stellen führen. Die Entwicklung von alternativen Optionen ist daher eine Notwendigkeit. Die Knochengewebezüchtung hat sich als vielversprechende Strategie zur Herstellung alternativer Knochenimplantate herausgestellt. Ihr einfacher Produktionsprozess von Biomaterialien ermöglicht eine präzise Architektur und Geometrie und erlaubt die Einbeziehung von regenerativen Zellen und Faktoren. Eigenschaften wie mechanische Stabilität, Biokompatibilität, Bio-Abbaubarkeit und osteogene Eigenschaften sind notwendig, um die erfolgreiche Regeneration grosser Knochendefekte zu erreichen. Sobald ein Knochenimplantat-Prototyp entwickelt ist, ist es entscheidend, seine Sicherheit und Wirksamkeit zu validieren, bevor eine klinische Anwendung in Betracht gezogen werden kann. In dieser Arbeit wurden mehrere Biomaterialien für Knochenimplantate entwickelt und mittels etablierte Beurteilungsmethoden wie *in-vitro* osteogene Differenzierung von mesenchymalen Stromazellen des menschlichen Knochenmarks, *in-vivo* subkutane Implantation bei Mäusen und Schädelimplantation bei Kaninchen getestet und evaluiert. Eine Verbesserung der aufgezeigten Limitationen der Validierungsprotokolle ist notwendig, um eine präzisere Prognose über das osteogene Potenzial eines Knochenimplantates zu treffen.



## Abbreviations

3D	Three-dimensional
ALP	Alkaline phosphatase
ABG	Autologous bone grafting
CaP	Calcium phosphate
CMF	Cranio-maxillofacial
BGP	$\beta$ -glycerophosphate
BGS	Bone graft substitute
BM	Basal medium
BTE	Bone tissue engineering
$\beta$ -TCP	$\beta$ -tricalcium phosphate
CaP	Calcium phosphate
CCP	Cell-culture plastic
CTB	CellTiter-Blue®
DCM	Dichloromethane
Dexa	Dexamethasone
EC	Ethylene carbonate
EDX	Energy-dispersive X-ray spectroscopy
FBS	Foetal bovine serum
FDM	Fused deposition modelling
FGF	Fibroblast growth factor
GelMA	Gelatin methacryloyl
HA	Hyaluronic acid
HAp	Hydroxyapatite

## Abbreviations

---

hBM-MSCs	Human bone marrow-derived mesenchymal stromal cells
MA	Methacrylic anhydride
MeHA	Methacrylated hyaluronic acid
NMR	Nuclear magnetic resonance
PBS	Phosphate buffered saline
PCL	Polycaprolactone
PDGF	Platelet-derived growth factor
PEN/STREP	Penicillin/ Streptomycin
PLGA	poly(lactic-co-glycolic acid)
RGD	Arginine–glycine–aspartate
rhBMP-2	Recombinant human bone morphogenic protein-2
RT-qPCR	Reverse transcription-quantitative polymerase chain reaction
SOC	Standard of care
TGFb	Transforming growth factor b
TPU	Thermoplastic polyurethane
μCT	Micro-computed tomography
VEGF	Vascular endothelial growth factor

# Table of Contents

<b>Abstract</b> .....	<b>i</b>
<b>Zusammenfassung</b> .....	<b>ii</b>
<b>Abbreviations</b> .....	<b>iii</b>
<b>1 Introduction</b> .....	<b>1</b>
1.1 Cranio-maxillofacial Bone Anatomy, Physiology and Pathology .....	1
1.2 Bone Tissue Engineering .....	2
1.2.1 Biomaterials for Bone Graft Substitute Development .....	3
1.2.2 Fabrication Processes .....	4
1.2.3 Regenerative Cells and Bioactive Factors .....	6
1.3 Validation of Bone Graft Substitutes .....	7
1.3.1 <i>In vitro</i> Validation .....	7
1.3.2 <i>In vivo</i> Validation .....	9
1.4 Scope of the Thesis .....	11
<b>2 Micro-porous PLGA/<math>\beta</math>-TCP/TPU Scaffolds Prepared by Solvent-based 3D Printing for Bone Tissue Engineering Purposes</b> .....	<b>13</b>
Abstract .....	15
2.1 Introduction .....	17
2.2 Material and Methods .....	19
2.3 Results .....	30
2.4 Discussion .....	43
2.5 Conclusions .....	48
2.6 Conflicts of Interest .....	48
2.7 Funding .....	49
2.8 Supplementary Materials .....	49

## Table of Contents

---

<b>3 <math>\beta</math>-TCP from 3D-printed Scaffold can act as an Effective Phosphate Source during the Osteogenic Differentiation of Human Mesenchymal Stromal Cells .....</b>	<b>50</b>
Abstract.....	52
3.1 Introduction.....	53
3.2 Material and Methods .....	55
3.3 Results.....	62
3.4 Discussion .....	75
3.5 Conclusions .....	81
3.6 Conflicts of Interest.....	82
3.7 Funding.....	82
3.8 Supplementary Materials .....	83
<b>4 Osteogenic Differentiation of hBM-MSCs Seeded on Collagen Membranes Embedded within LEGO®-inspired 3D-Printed PCL Construct for Mandibular Bone Repair .....</b>	<b>85</b>
Abstract.....	87
4.1 Introduction.....	88
4.2 Material and Methods .....	89
4.3 Results.....	95
4.4 Discussion .....	100
4.5 Conclusions .....	104
4.6 Funding.....	105
<b>5 Clinically Relevant Preclinical Animal Models for Testing novel Cranio-maxillofacial Bone 3D-printed Biomaterials.....</b>	<b>106</b>
Abstract.....	107
5.1 Introduction.....	109
5.2 CMF Bone Structure and Healing .....	110
5.3 Standard Care and Clinically Available Solutions .....	113

## Table of Contents

---

5.4 Tissue Engineering as a Promising Alternative.....	114
5.5 From a Promising Tissue Engineering Concept to a Clinically Justified Product.....	117
5.6 Preclinical Studies Targeting the Regeneration of CMF Bone Defects	118
5.7 Towards Clinically Driven Animal Models .....	123
5.8 Conclusions .....	135
<b>6 Standard <i>in vitro</i> Evaluations of Engineered Bone Substitutes are not Sufficient to Predict <i>in vivo</i> Preclinical Model Outcomes.....</b>	<b>147</b>
Abstract.....	149
6.1 Introduction .....	151
6.2 Material and Methods .....	154
6.3 Results.....	166
6.4 Discussion .....	179
6.5 Funding.....	184
6.6 Acknowledgements.....	184
6.7 Supplementary Materials .....	184
<b>7 Concluding Remarks .....</b>	<b>194</b>
<b>References .....</b>	<b>199</b>
<b>Acknowledgements.....</b>	<b>241</b>
<b>Curriculum Vitae.....</b>	<b>243</b>
<b>List of Publications .....</b>	<b>244</b>
<b>List of Conference Attendances .....</b>	<b>246</b>

# 1 Introduction

## 1.1 Cranio-maxillofacial Bone Anatomy, Physiology and Pathology

The cranio-maxillofacial (CMF) region encompasses various bones, including cranial bones (temporal, occipital, ethmoid, frontal parietal, and sphenoid) and facial bones (nasal, nasal conchae, vomer, lacrimal, zygomatic, palatine, maxilla, and mandible) (**Figure 1.1**). These bones can be categorised as flat bones such as the occipital, frontal and vomer, or irregular bones such as the mandible and maxilla. The cranial bones provide protection for the brain and fixes the position of the eyes and ears. Facial bones protect soft tissues and contribute to breathing, eating and facial expression.

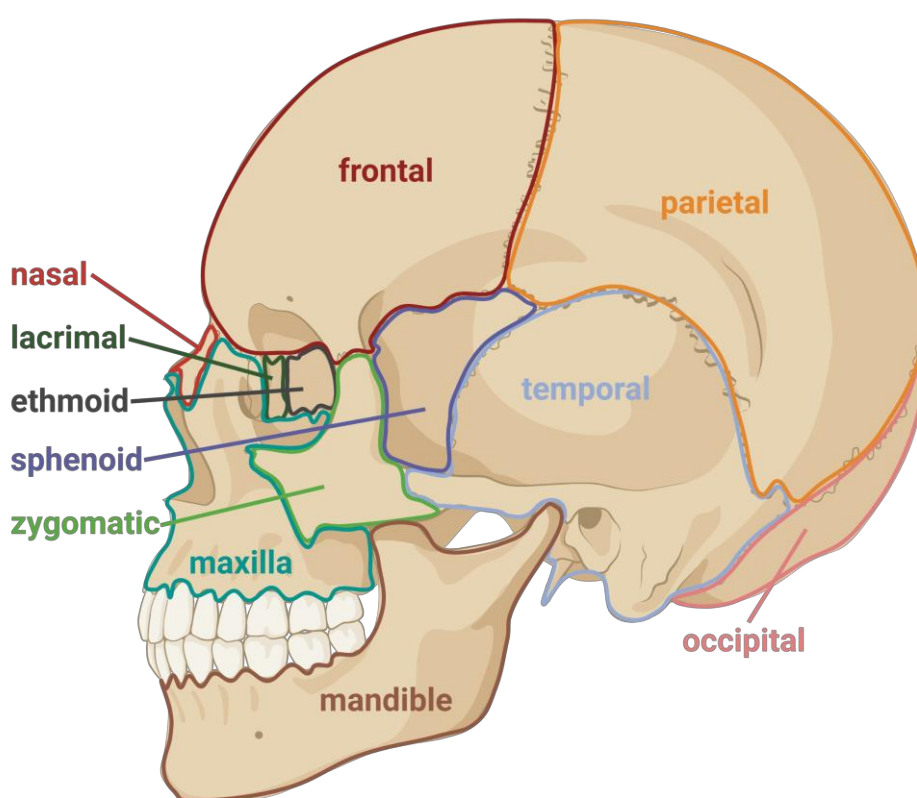


**Figure 1.1: Anatomy cranio-maxillofacial (CMF) bones.** Created with BioRender.

Large bone defects in the CMF region can arise from different causes such as tumour resection, congenital deformity, trauma, and infection.<sup>1</sup> Under a

mechanically stable environment CMF bones undergo healing through the intramembranous route, in which the mesenchyme directly converts into bone without a cartilage template, unlike the endochondral ossification process manifested in long bones in the presence of micromotion.<sup>2</sup> Successful fracture healing occurs without scarring. However, when the defect size surpasses the natural healing capacity, called large or critical-sized bone defect, clinical intervention becomes necessary.<sup>3</sup> The size of a large bone defect depends on the type of bone, severity of the surrounding soft tissue damage and the patient's own healing capacity.

Current treatments for CMF bone defects involve surgical implantation of various materials including autografts, allografts, demineralised bone matrix, hydroxyapatite (HAp), calcium phosphate (CaP), bone marrow aspirate concentrate or growth factors, such as bone morphogenic protein 2 (BMP-2) and BMP-7, often delivered through collagen sponges.<sup>4</sup> Despite the availability of numerous options autologous bone grafting (ABG) remains to be the standard of care (SOC). The drawbacks such as ectopic bone formation, osteoclast-mediated bone resorption, postoperative inflammation, and increased cancer risk<sup>4</sup> of these treatment options still require the search for novel solutions. The face is an integral part of a patient's identity and therefore needs a repair as anatomically perfect as possible. Hence, 3D printing offers an advantages solution to create patient-specific implants through bone tissue engineering (BTE).

## 1.2 Bone Tissue Engineering

A novel solution may be found within the field of BTE, aimed at creating a bone graft substitute (BGS). This highly interdisciplinary field combines principles from biology, materials science, and engineering to develop practical approaches capable of addressing the repair of large bone defects.<sup>5</sup> The BTE approach integrates the use of biocompatible and biodegradable biomaterials, regenerative progenitor cells possessing osteogenic differentiation capabilities and growth factors or bioactive factor to facilitate bone regeneration.<sup>6</sup> The BTE approach has

the potential to innovate the development of BGSs with the goal to effectively replace the current SOC and transform CMF surgery.

### **1.2.1 Biomaterials for Bone Graft Substitute Development**

Biomaterials such as natural and synthetic polymers or CaP-based ceramics are commonly used for the development of a BGS, due to their biocompatibility, availability, biodegradability, and easy fabrication.<sup>7-9</sup> Natural polymers such as fibrin, laminin, fibronectin, collagen, gelatin, hyaluronic acid (HA), alginate, chitosan or dextran<sup>10</sup>, are known for their rapid biodegradability and excellent biological activity. They promote cell adhesion and migration through the presence of arginine–glycine–aspartate (RGD) peptide sites.<sup>10</sup> They are typically used as hydrogels, which are three-dimensional (3D) networks of hydrophilic polymers capable of swelling in water.<sup>11</sup> Despite poor mechanical stability, hydrogels remain relevant for bone tissue engineering approaches due to their cell compatibility and ability to deliver bioactive factors to the defect site.<sup>10</sup>

Synthetic polymers such as polycaprolactone (PCL), poly(vinyl alcohol), polylactic acid (PLA), poly(glycolic acid) or poly(lactic-co-glycolic acid) (PLGA), polyurethane (PU)<sup>8</sup> are widely used in BTE. They are easy to fabricate, process, and possess mechanical stability, particularly useful in load-bearing bone defects. However, synthetic polymers can lead to acidic degradation and lack biological activity due the absence of necessary binding sites for cell adhesion.<sup>8</sup>

The inorganic part of bone tissue consists mainly of CaP. Therefore, utilizing ceramic materials such as CaP (tricalcium phosphate (TCP), HAp, bioglass or nanosilicates (e.g. Laponite) is a logical choice. They allow for bone growth (osteoconductivity) while resembling the inorganic component of bone. However, their brittle nature poses a limitation in terms of mechanical stability.

Due to the inherent strengths and weakness of each individual biomaterial, BGSs are often combined with multiple components to create a composite that possesses the desirable properties of different biomaterials.<sup>12</sup> The creation of



such mechanically stable, porous, biodegradable and osteoconductive composites from the raw materials requires a fabrication process.

### 1.2.2 Fabrication Processes

A fabrication process is employed to create biomaterials with specific geometry, architecture, and surface topography, all of which important properties for successful integration between the material and bone. The geometric shape of the BGS is crucial for achieving desirable aesthetic outcomes. The architecture of the BGS determines the macro porosity, which plays a pivotal role in optimal tissue and blood vessel infiltration into the BGS upon *in vivo* implantation. The goal is to mimic Haversian and Volkmann's canals, which are tubes in the cortical bone to allow blood vessels and nerves to travel through. To allow endothelial cells to infiltrate and form tubular structures, to provide exchange of metabolic components, a minimum macro pore size of 30 – 40  $\mu\text{m}$  is recommended.<sup>13</sup> However, larger pore sizes up to 400  $\mu\text{m}$  are preferred for optimal vessel infiltration upon implantation.<sup>14</sup> The surface porosity of the BGS influences the adsorption of proteins on a micro level, consequently altering cell adhesion.<sup>15</sup> The BGS initially serves as a temporary template for native bone tissue infiltration and provision of osteogenic cues to ignite the healing process. Therefore, graduate biodegradation of the BGS is essential once the healing process is underway without producing any toxic by-products.<sup>16</sup>

Various fabrication options are available for biomaterials, including emulsion freeze drying, solvent casting, electrospinning, and 3D printing (**Figure 1.2**).<sup>17</sup> Emulsion freeze drying is effective in creating highly porous scaffolds but lacks control over shape and architecture. Solvent casting is a straightforward, rapid and cost effective process for shaping a biomaterial.<sup>18</sup> However, it often requires the use of toxic solvents<sup>17</sup> and presents challenges in controlling the architecture. Electrospinning allows for the generation of fine nano-sized fibres by applying electrostatic forces to a polymer solution, resulting in a mesh with a high surface to volume ratio suitable for drug loading and cell adhesion.<sup>19</sup> However, the random nature of this process leads to reproducibility issues, as well as lack over

precise architecture. Furthermore, low cell infiltration capabilities due to the small pores of the mesh is a concern.<sup>20</sup>

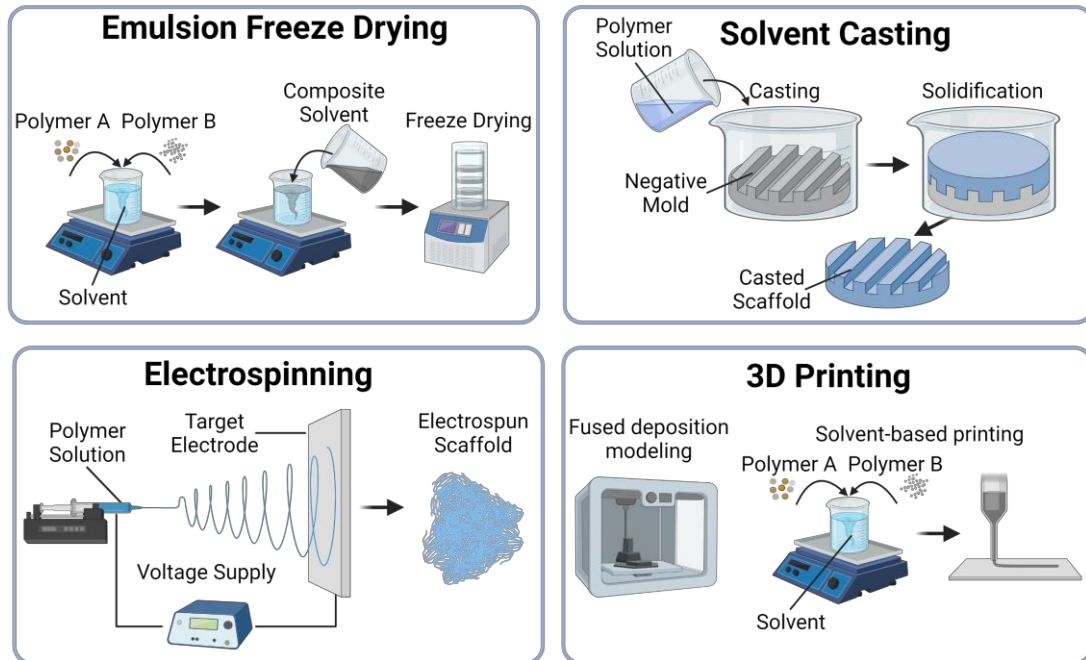


**Figure 1.2: Schematic overview of different fabrication processes.** Created with BioRender.

3D printing has emerged as a versatile fabrication technique and is a widely used process in the field of BTE. Based on additive manufacturing principles, 3D printing involves extruding consecutive filaments layer by layer to create a construct with precise architecture, controllable pore size and shape. It has gained widespread use thanks to its ability to create patient-specific constructs that fit the defect site, resulting in improved aesthetics, particularly important for CMF defects. Fused deposition modelling (FDM) is the most commonly used 3D printing technique due to its low cost, fast processing and capacity to provide complex and controllable architecture.<sup>21</sup> However, FDM is limited to thermoplastic polymers which inherently do not possess bioactive properties<sup>22,23</sup> and can often result in the formation of an undesired smooth surface on the extruded filament. To address the FDM-associated disadvantages, solvent-based 3D-printing can be employed to create porous scaffolds that facilitate protein adsorption and cell adhesion. Furthermore, solvent-based printing allows for easy combination of

polymers with additional biomaterials such as CaPs to create a composite. Each component can be dissolved in a solvent and homogeneously mixed to obtain a viscous printable ink. After the printing process, solvent removal leads to the spontaneous formation of surface porosity on the scaffold. By utilizing advanced fabrication techniques like 3D printing, biomaterials can be created to obtain composites with control over important material properties such as architecture, pore size and shape that have an influence on mechanical and biological outcomes. However, 3D-printed composites are not considered a powerful inducer of bone formation and therefore the combination with regenerative cells and bioactive factors is necessary to create a BGS with osteoinductive properties.

### **1.2.3 Regenerative Cells and Bioactive Factors**

Mesenchymal stromal cells (MSCs) are the most commonly used progenitor cell type for bone tissue repair due to their ease of harvesting, and regenerative capabilities.<sup>24</sup> Furthermore, they are considered to have low immunogenicity<sup>25</sup>, an important property when these cells are used as part of an allogenic implant. They can be isolated from various sources including adipose tissue, bone marrow, umbilical cord, umbilical cord blood, placenta, and amniotic fluid.<sup>26</sup> MSCs possess a trilineage differentiation potential allowing them to differentiate into either adipocytes, chondrocytes or osteoblasts.<sup>27</sup> They play a crucial role during bone fracture healing through extensive interaction with immune – and angiogenic cells using paracrine signalling to promote bone regeneration and inhibit undesired immune responses.<sup>28</sup>

Recombinant proteins, particularly BMP-2, have been extensively studied as therapy options for promoting bone tissue repair.<sup>29,30</sup> However, these factors have significant disadvantages such as high costs, protein instability, contamination issues, and unwanted immunogenic responses from the host.<sup>31</sup> In the case of BMP-2, it has been clinically associated with ectopic bone formation and tumorigenesis.<sup>32</sup> Therefore, alternative osteogenic stimulators that are not growth factors have gained attention in the research field by providing osteogenic induction without the side effects associated with growth factors. Bioactive factors

such as dexamethasone (dexa) microparticles<sup>33,34</sup> and inorganic polyphosphate (polyP)<sup>35-37</sup> nanoparticles have shown to be potential options to be combined with biomaterials. Dexa is an anti-inflammatory glucocorticoid with versatile medical use and known to activate and enhance osteogenic differentiation of BM-MSCs.<sup>38,39</sup> Due to its pro-osteogenic capabilities, dexa is part of the osteogenic cocktail and the main driver that activates the osteogenesis process of MSCs *in vitro*.<sup>38</sup> Furthermore, dexa-laden HAp particles with sizes between 500 nm and 5  $\mu\text{m}$  have shown to enhance bone regeneration in a rat calvaria defect model.<sup>40</sup> PolyP is a high-energy containing polymer, present in osteoblasts and shown to promote osteogenesis.<sup>41</sup> Amorphous calcium polyP nanoparticles with a size of  $280 \pm 120$  nm have shown to promote *in vitro* osteogenesis of rat BM-MSCs.<sup>42</sup> Furthermore, the composite consisting of strontium polyP nanoparticles embedded within PLGA microspheres has resulted in increased bone healing outcomes in a rat calvaria defect model.<sup>43</sup>

By incorporating MSCs and exploring alternative osteogenic stimulators, regenerative capabilities of BGSs could improve bone tissue repair outcomes by increasing osteoinductive properties. Once a promising BGS prototype is developed its potential future clinical use is decided through a validation process.

### 1.3 Validation of Bone Graft Substitutes

#### 1.3.1 *In vitro* Validation

Before a BGS can be tested clinically, it must undergo a rigorous validation *in vitro* process that includes the evaluation of its cytocompatibility and osteogenic potential. Biocompatibility can indirectly be assessed through *in vitro* cytotoxicity tests following ISO guidelines 10993-5: "Tests for Cytotoxicity—In Vitro Methods". These tests evaluate the metabolic activity of cells exposed to the conditioned media of the BGS. Direct cytotoxicity can be assessed by seeding cells directly on the BGS and measuring cell metabolic activity and performing LIVE/DEAD staining.

*In vitro* osteogenic differentiation experiments with seeded MSCs have been the predominant validation process to evaluate the osteogenic potential of a BGS. Traditionally, osteogenesis is induced by supplementing the basal medium (low glucose DMEM, foetal bovine serum (FBS), penicillin and streptomycin) with an osteogenic cocktail. This cocktail typically contains, dexamethasone (dexa), which activates Runx2 through the WNT/ $\beta$ -catenin and mitogen-activated protein kinase phosphatase pathway, ascorbic acid to facilitate collagen fibrillation and  $\beta$ -glycerophosphate (BGP) to provide the necessary phosphate source for the cells to mineralise.<sup>38</sup>

The assessment of mineralisation is one of the primary and most important indicators of osteogenic differentiation and can be performed through staining with dyes such as Alizarin Red for calcium deposition, von Kossa for phosphate deposition and fluorescence staining OsteoImage®, which is claimed to stain positive to HAp. A major limitation of these dyes is that they also stain any calcium-phosphate-based material making it very challenging to investigate the mineral output secreted from the cells. Additionally, the measurement of enzymatic activity or staining of alkaline phosphatase (ALP) is also one of the most used assays to show osteogenesis. The concentration of calcium or phosphate content in the matrix can be measured by applying an acidic solution to break the ionic bonds and reading the concentrations using a plate reader to show mineral deposition only indirectly. Gene expression analysis of matrix related genes such as *COL1A1*, type 1 collagen encoding gene, *ALPL*, ALP encoding gene and *IBSP*, bone sialoprotein encoding gene, or transcription factors such as *SP7*, osterix encoding gene and *RUNX2* are also commonly used to assess the osteogenic potential of a BGS. Staining of matrix proteins, such as osteocalcin or osteopontin or quantification of protein concentrations within the conditioned medium (e.g. osteoprotegerin) can also indicate osteogenic differentiation.

Together, these comprehensive evaluations provide insights into the cytocompatibility and osteogenic capabilities of the BGS (**Figure 1.3**) and are believed to help pre-select for further necessary *in vivo* validation before its

suitability for clinical translation can be determined. However, *in vitro* evaluations do not consistently align with the subsequent *in vivo* results, casting doubt in their ability to reliably predict a causal connection.<sup>44,45</sup>

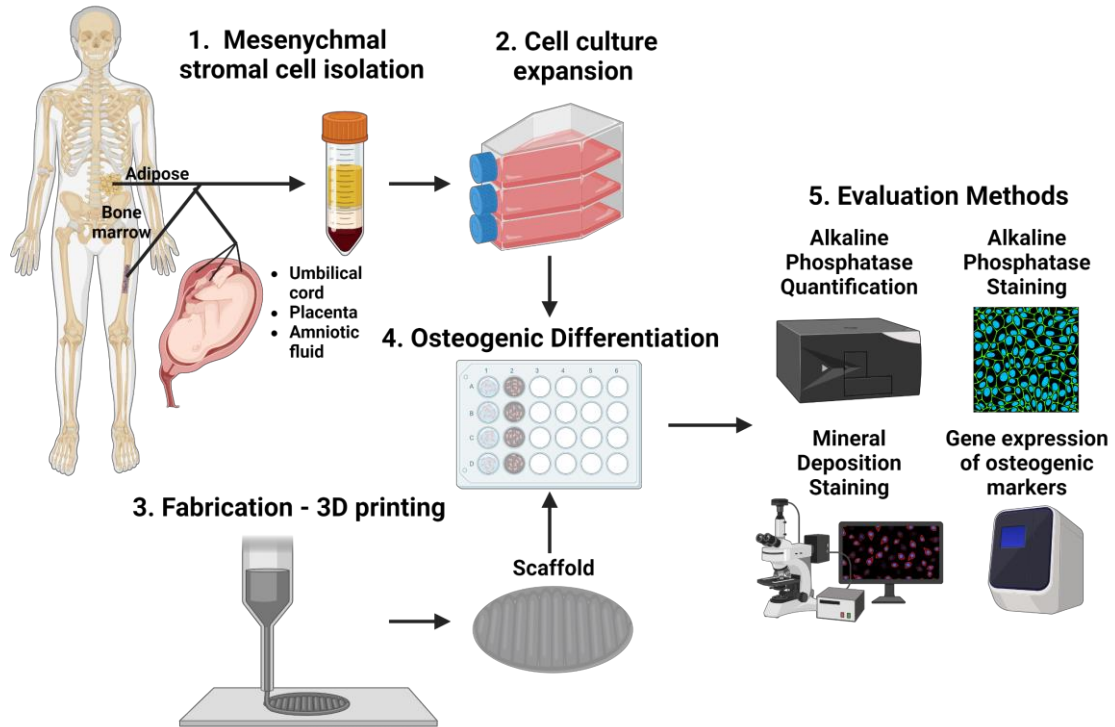


**Figure 1.3: Schematic overview of *in vitro* validation of fabricated scaffolds.** Created with BioRender.

### 1.3.2 *In vivo* Validation

There is a significant discrepancy between *in vitro* studies and the clinical scenario<sup>46</sup>, necessitating the testing of a BGS for safety and efficacy using *in vivo* animal models before considering translation to the clinic.<sup>47</sup> Unfortunately, no *ex vivo* bone model has been developed that adequately validates a BGS due to limited complexity. Consequently, the use of animal models remains essential.<sup>46</sup>

The selection of an appropriate animal model is crucial to closely resemble the human scenario. Ideally, the animal model should involve a large animal species with a large bone defect that reflects the intended research question. For initial screening and larger sample size, small animal models such as rodents (mice

and rats) are commonly used due to their cost-effectiveness, ease of housing and limited social concerns.<sup>48</sup> For large animals models pigs, sheep and dogs are often employed to evaluate the osteogenic potential of a BGS.<sup>49</sup>

The biocompatibility and osteogenic characterisation of a BGS are typically evaluated in heterotopic models as a first step, which include subcutaneous, intramuscular, intraperitoneal, or mesentery locations (**Figure 1.4**), with subcutaneous implantation on the back being the most common approach.<sup>48</sup> The mineralisation observed in an environment where no native bone exists indicates osteoinductive properties of the BGS. However, to assess the osteogenic potential of a BGS more accurately, orthotopic bone models are more suitable (**Figure 1.4**). Calvarial defects or mandibular defects are particularly used in the field of CMF repair.

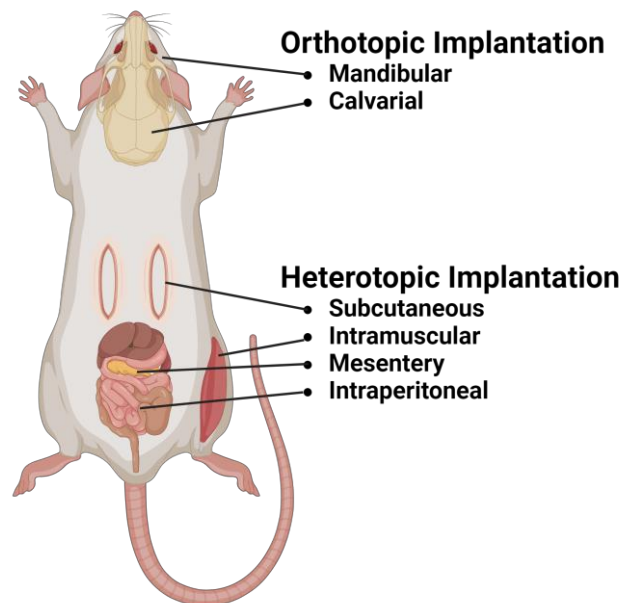


**Figure 1.4: Schematic overview of *in vivo* orthotopic and heterotopic implantation options.** Created with BioRender.

Animal studies provide valuable insights into the safety, efficacy, and osteogenic potential of a BGS and are an important step before considering clinical translation. These models evaluate the performance of the BGS in a manner that better represents the clinical scenario compared to *in vitro* models by closer

representation of the *in vivo* environment. Discrepancies between animal and human bone biology exist, but *in vivo* models are still the superior option available but should always be used with ethical consideration under the 3Rs (Replacement, Reduction and Refinement) principles.

### 1.4 Scope of the Thesis

Although the development of BGSs has gained significant focus, clinical translation has been limited. The overall aim of this thesis is to address this limitation. Multiple strategies to construct BGSs based on different biomaterials and fabrication techniques are used and both *in vitro* cell cultures and *in vivo* animal models are employed and critically discussed.

In the second chapter of this thesis, the development of a solvent-based 3D printing approach is described with the aim to create porous scaffolds composed of PLGA/ $\beta$ -TCP with and without thermoplastic polyurethane (TPU). Material characterisation is conducted, and the evaluation of the biocompatibility and osteogenic potential of these scaffolds is assessed by performing an *in vitro* osteogenic differentiation experiment using hBM-MSCs. In chapter 3, BGP associated side effects during *in vitro* osteogenic differentiation of hBM-MSCs are addressed by investigating if  $\beta$ -TCP embedded within the 3D-printed PLGA/ $\beta$ -TCP scaffold can act as a sufficient alternative phosphate source. In chapter 4, the development of a layer-by-layer multicomponent construct that is inspired by LEGO®-blocks is presented. The construct consists of 3D-printed PCL scaffolds, embedded with hBM-MSC-laden collagen membranes to demonstrate easy and spatial distribution of biological elements within the construct. The 5<sup>th</sup> chapter provides an overview of the use of animal models for validating tissue engineered 3D-printed scaffolds for CMF bone repair in the format of a review. The limitations of the studies presented are discussed and challenges faced in translating these findings to clinical applications are highlighted. Finally, in chapter 6, the development of drug-carrying hydrogels including fibrin, hyaluronic acid methacrylate (MeHA) and gelatin methacrylate (GelMA) combined with bioactive



factors such as dexamethasone (dexa) microparticles and/or polyphosphazene (polyP) nanoparticles is accomplished. Their osteogenic capacities are assessed by evaluating the *in vitro* osteogenic differentiation of embedded human bone marrow-derived mesenchymal stem cells (hBM-MSCs) and the *in vivo* response upon implanting these drug-loaded hydrogels in a subcutaneous mouse model and a calvarial rabbit model.

## **2 Micro-porous PLGA/ $\beta$ -TCP/TPU Scaffolds Prepared by Solvent-based 3D Printing for Bone Tissue Engineering Purposes**

### **Statement of Significance:**

The functional and aesthetical restoration of lost bone in the cranio-maxillofacial area represents a major surgical challenge. The commonly used 3D printing technique known as fused deposition modelling can create bone graft substitutes with the desired patient-specific geometry, but often lacks the necessary micro-porous surface required for protein and cell adhesion. Within this study we investigated the creation of micro-porous and patient-specific scaffolds by applying the solvent-based printing approach and characterised materials properties and biological potential.

Note: This chapter was published in *Regenerative Biomaterials* as **Micro-porous PLGA/ $\beta$ -TCP/TPU Scaffolds Prepared by Solvent-based 3D Printing for Bone Tissue Engineering Purposes**, Luan P. Hatt, Sylvie Wirth, Aapo Ristaniemi, Daniel J. Ciric, Keith Thompson, David Eglin, Martin J. Stoddart and Angela R. Armiento

Reprinted with permission<sup>50</sup>. Copyright 2023, Oxford Academics

### Author Contributions:

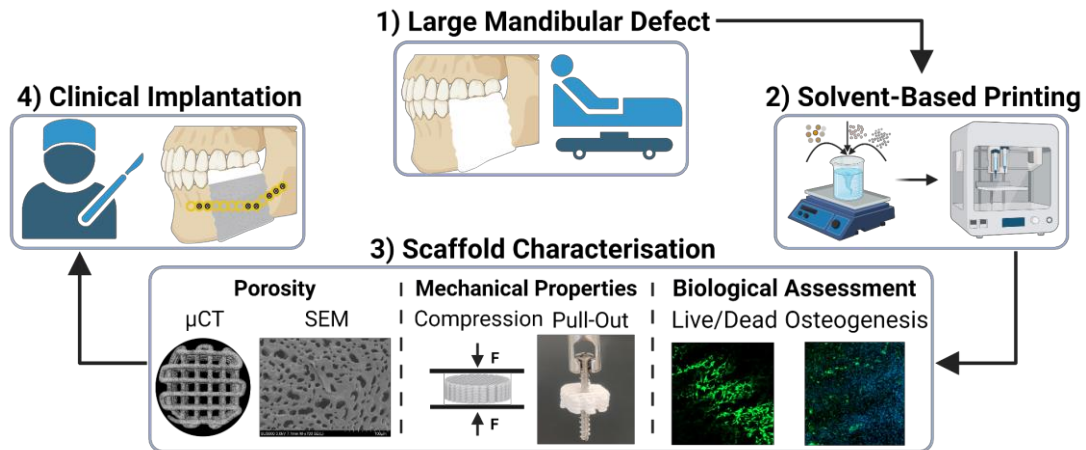
LPH performed the investigation, methodology, validation, data curation and formal analysis of all the experiments, hence generated all the data in this paper. LPH also wrote the original draft, visualised the data, and created all the figures. SH contributed to the paper in terms of assistance in the methodology, investigation, validation during the ink development and editing and reviewing of the writing. AR contributed to the paper in terms assistance in methodology and

software for mechanical testing, as well as editing and reviewing of the writing. DJC contributed to the paper in terms methodology for  $\mu$ CT scanning and porosity analysis. KT contributed to the paper in terms editing and reviewing of the writing. DE contributed to the paper in terms conceptualisation of the project and editing and reviewing of the writing. MJS contributed to the paper in terms conceptualisation of the project, co-supervision, provision of the resources, acquisition of the funding and editing and reviewing of the writing. ARA contributed to the paper in terms conceptualisation of the experiments and the project, supervision, assistance in validation, leading of the project administration, and editing and reviewing of the writing. All authors read and approved the final manuscript.

## **Abstract**

The 3D printing process of fused deposition modelling (FDM) is an attractive fabrication approach to create tissue engineered bone substitutes to regenerate large mandibular bone defects, but often lacks desired surface porosity for enhanced protein adsorption and cell adhesion. Solvent-based printing leads to the spontaneous formation of micropores on the scaffold's surface upon solvent removal, without the need for further post processing. Our aim is to create and characterise porous scaffolds using a new formulation composed of mechanically stable poly(lactic-co-glycol acid) (PLGA) and osteoconductive  $\beta$ -tricalcium phosphate ( $\beta$ -TCP) with and without the addition of elastic thermoplastic polyurethane (TPU) prepared by solvent-based 3D-printing technique. Large scale regenerative scaffolds can be 3D-printed with adequate fidelity and show porosity at multiple levels analysed via micro-computer tomography, scanning electron microscopy and  $N_2$  sorption. Superior mechanical properties compared to a commercially available CaP ink are demonstrated in compression and screw pull out tests. Biological assessments including cell activity assay and live-dead staining prove the scaffold's cytocompatibility. Osteoconductive properties are demonstrated by performing an osteogenic differentiation assay with primary human bone marrow mesenchymal stromal cells. We propose a versatile fabrication process to create porous 3D-printed scaffolds with adequate mechanical stability and osteoconductivity, both important characteristics for segmental mandibular bone reconstruction.

## Micro-porous PLGA/ $\beta$ -TCP/TPU Scaffolds Prepared by Solvent-based 3D Printing for Bone Tissue Engineering Purposes



**Graphical Abstract: Process of 3D-printing and characterising a micro-porous scaffold.**

Created with BioRender.com.

**Keywords:** Solvent-based Printing, Porosity, Regenerative Scaffold, Osteogenesis, Mesenchymal Stromal Cells

## **2.1 Introduction**

Trauma, tumour, infection, and congenital malformation are among the main causes of large segmental mandibular defects, which require a complex surgical procedure for successful functional and aesthetic reconstruction.<sup>4</sup> The current standard of care (SOC) is autologous bone grafting from either the iliac crest or the fibula<sup>51</sup>, which is associated with several drawbacks such as limited tissue availability, donor site morbidity, lack of patient-specific graft geometry and excessive resorption. To improve patient care, an effective alternative is required ideally overcoming the aforementioned disadvantages. The replacement of the current SOC should be a product that not only possesses mechanical stability enabling fixation with a plate-screw system and biological properties such as biocompatibility, biodegradability and osteoconductivity, but it should also provide practical advantages such as simple, cost-effective, and versatile biofabrication process.

3D printing is a powerful fabrication tool enabling the creation of patient-specific and mechanically stable scaffolds in a cost- and time-effective manner. A very common printing approach is fused deposition modelling (FDM) that involves heat-melting and deposition of thermoplastic polymers, such as polycaprolactone (PCL) or polylactic acid (PLA).<sup>52</sup> However they degrade at temperatures higher than 200°C<sup>53</sup> and have been shown to undergo a 48% reduction of PLA average molecular weight after printing at 186°C.<sup>54</sup> This degradation is detrimental for the performance of the 3D-printed scaffold.<sup>55,56</sup> Additionally, FDM printing requires the use of a filament, which makes the combination of osteoconductive calcium phosphate (CaP) material or other compounds tedious and requires a pre-processing step involving melt-blending extruding to create a filament composed of the desired mixed composition.<sup>57-61</sup> Finally, FDM printing of PLA is associated with the formation of an undesirable smooth surface topography.<sup>62,63</sup> Surface

microroughness and porosity are both important features for protein adsorption, cell adhesion and tissue infiltration for enhanced osteogenesis.<sup>64-66</sup>

A variety of postprocessing surface modification strategies can be applied to improve these features such as plasma treatment, coating, or protein grafting.<sup>67-69</sup> An elegant printing alternative to FDM is low temperature solvent-based printing. Ink components are easily mixed, avoiding extreme temperatures and consequent degradation, to create a 3D printable blend. The post-printing removal of the solvent spontaneously leads to the creation of micropores on the surface of the scaffold, beneficial for cell-adhesion and osteogenesis<sup>65</sup> without the need of further chemical surface modifications.<sup>70,71</sup>

Our aim is to fabricate a micro-porous scaffold prepared by a newly developed solvent-based 3D-printing technique for bone tissue engineering purposes. To replace commonly used toxic organic solvents, we used water-soluble and non-toxic ethylene carbonate (EC). To demonstrate the versatility of the method, we modulated material properties by creating a composite made of poly(lactic-co-glycolic acid) PLGA, for printability and mechanical strength,  $\beta$ -tricalcium phosphate ( $\beta$ -TCP) for osteoconductivity, with and without the addition of thermoplastic polyurethane (TPU), which is known to be biodegradable<sup>72,73</sup> and elastic<sup>74</sup>, and subsequently characterised the material properties. Increasing the elastic properties of biomaterials can be beneficial for the mandibular bone repair regarding the mandible's chewing function. As a control, the newly developed inks were compared with a commercially available 3D printable CaP ceramic, OsteoInk®. In this study, we report an advanced low-temperature solvent-based printing approach to develop a versatile, medically relevant manufacturing process that allows fabrication of patient-specific regenerative bone substitutes for bone defect repair.

## 2.2 Material and Methods

Human bone marrow aspirates are obtained with informed consent of all donors and with full approval from the Ethics Committee of the University of Freiburg Medical Centre (EK-Freiburg: 135/14, 25 March 2014) and the ethical commission of Zürich (KEK-ZHNR: 2016-00141). All reagents are purchased from Sigma-Aldrich unless otherwise stated. An overview of the methods is reported in **Figure 2.1**.

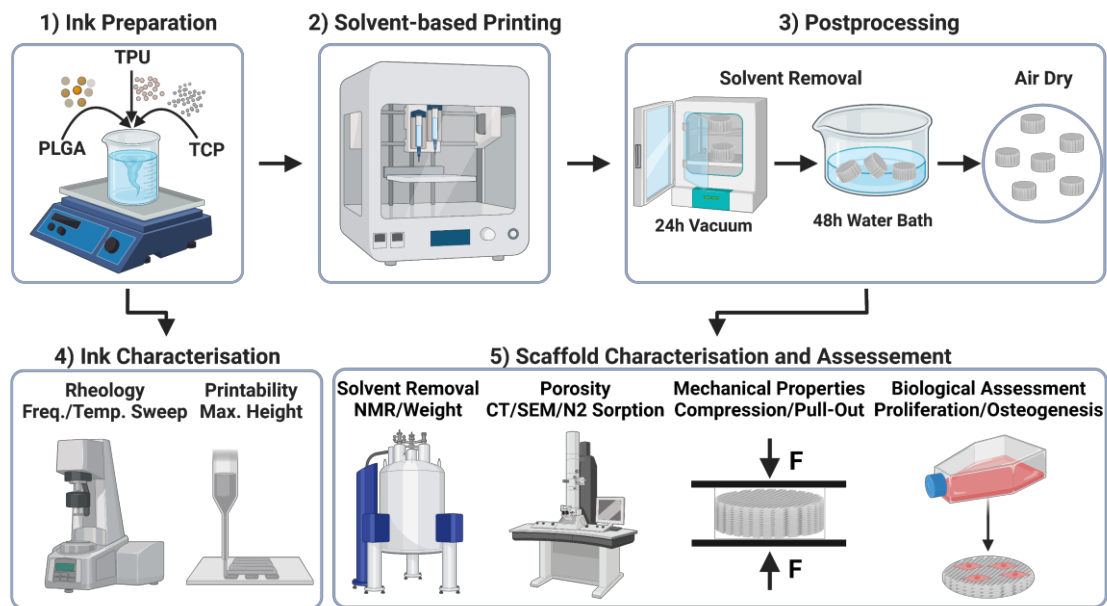


**Figure 2.1: Overview of the methods:** 1) Ink Preparation, 2) Solvent-based Printing, 3) Scaffold Postprocessing, 4) Ink Characterisation and 5) Scaffold Characterisation and Assessment. Created with BioRender.com.

### **Preparation of PLGA/ $\beta$ -TCP $\pm$ TPU Ink**

TPU (ROLASERIT®, AM Polymers GmbH) powder is dissolved in ethylene carbonate (EC) at 120°C using a hot plate stirrer and a rotor mixing system. After cooling the hot plate stirrer to 90°C, PLGA (PURASORB® PLG 8531, 85/15 L-lactic/Glycolide, Corbion, Amsterdam, Netherlands) powder is added and mixed until dissolution. Subsequently, the system is cooled to 80°C,  $\beta$ -TCP powder



(BABI-TCP-N100, Berkeley Advanced Biomaterials) is added, and the blend stirred overnight using a Hei-TORQUE Expert 200 (Heidolph Instruments) set to 30 rpm to obtain a viscous, homogenous ink. The ink is transferred to 3 cc syringe barrels (Nordson EFD) and kept at -20°C until printing. Two ink formulations, PLGA/ $\beta$ -TCP -TPU (without TPU) denoted as group 1 (G1) and PLGA/ $\beta$ -TCP +TPU (addition of TPU) denoted as group 2 (G2), are prepared and the ratio between individual components is presented in **Table 2.1**.

**Table 2.1. Ink Formulations**

Group	PLGA (w/V)	$\beta$ -TCP (w/V)	TPU (w/V)
1	40%	20%	-
2	40%	20%	10%


### ***Rheological Characterisation of the Inks***

Viscoelastic properties of the inks are investigated using an Anton Paar MCR-302 rheometer (Anton Paar). Oscillatory and rotational tests are performed using a flat-plate geometry with the gap set at 0.5 mm. An amplitude sweep test is carried out with strain ranging between 0.01% and 100% at constant angular velocity of 10 rad/s and a temperature of 80°C. Viscosity is evaluated using a frequency sweep test (N=3) between 0.1 and 100 Hz, with a constant strain of 1% based on the amplitude test and a temperature of 80°C. A temperature sweep test (N=3) is performed with the temperature ranging from 80°C to 40°C to investigate the rheological properties of the thermo-responsive ink with constant strain of 0.1% and frequency of 1 Hz. Storage modulus (G') and loss modulus (G'') values are acquired for all tests.

### ***Design of 3D-Printed Scaffolds***

Two different scaffold structures are used in this study and designed using BioCAD software (RegenHU). Design 1 is round and has a porous grid structure. Design 2 is a round dense disc with only two layers and can be press-fit into 24 well-plates, especially practical for cell seeding. Using the discs (Design 2) for cell experiments allows for higher standardisation of cell seeding and attachment on top of the biomaterial compared to the Design 1, which can lead to uneven cell-attachment starting point between groups. Scaffold dimensions and corresponding measurement are summarised in **Table 2.2**.

**Table 2.2. Characteristics of 3D-printed scaffold structures and physico-chemical characterisations performed**

Design	Schematic	Dimensions (mm)	Measurement/Characterisation
1		D = 5 H = 4 LS = 0.4	NMR
			Weight solvent extraction test (N=3)
			Degradation/swelling (N=6)
			$\mu$ CT scanning (N=3)
			SEM images
			N <sub>2</sub> sorption
			Mechanical compression test (N=13/14)
			Screw pull-out test (N=12)
			Indirect cytotoxicity test (N=4)
			2
Live/Dead staining			
Alizarin Red staining (N=3)			
Osteogenesis (N=2)			

D = Diameter, H = Height, LS = Line Spacing, D1 = Diameter for 96 well-plate, D2 = Diameter for 48 well-plate, OS = Offset, NMR = Nuclear magnetic resonance,  $\mu$ CT = Micro-computed tomography, SEM = Scanning electron microscope, N2 = Nitrogen

## ***Solvent-Based 3D Printing and Postprocessing of PLGA/ $\beta$ -TCP $\pm$ TPU and Osteoink®***

### *Scaffold Fabrication*

Low-temperature solvent-based 3D printing is performed using 3D Discovery® bioprinter (RegenHU). Ink-laden cartridges are equipped with a stainless steel needle with a 0.5 mm inner diameter and a piston. During printing the cartridge heater is set at 80°C and a pressure between 0.5 and 1.8 bars is applied for the different groups. The velocity of the print head is 4 mm/s, and the layer height is set at 0.4 mm. The ink is extruded onto a dry glass slide which is mounted onto an aluminium cool plate with the temperature kept between 3 and 10°C. The printing of the commercially available Osteoink® (RegenHu) is performed at room temperature onto a glass slide using the same needle size, pressure, print head velocity and layer height.

### *Postprocessing*

To remove the solvent, the 3D-printed PLGA/ $\beta$ -TCP  $\pm$  (TPU) scaffolds are placed first in a vacuum oven at room temperature for 24 hours and then in a water bath at 37°C for 48 hours (4x Milli-Q® water changes). Scaffolds are then air dried and stored at room temperature until further use. 3D-printed discs (Design 2) are size-fitted for a 96 well plate and 48 well plate using a hollow punch with a dimension of 7 mm and 11 mm in diameter, respectively. The discs are sterilised using a cold ethylene oxide gas protocol, degassed under vacuum for at least 5 days, and press-fit into the cell-culture wells under sterile conditions prior to use. 3D-printed Osteoink® scaffolds are hardened post-printing using a steam autoclave (Belimed Infection Control, Belimed Sauter AG) as previously described <sup>75</sup>.

### *Post-Printing Solvent Removal Confirmation*

To verify complete removal of the solvent, the 3D-printed scaffolds (Design 1) are dried and weighed during the extraction process after 0, 24 and 48 hours (N=3). <sup>1</sup>H nuclear magnetic resonance (NMR) is carried out to further confirm complete solvent removal using Bruker Avance AV-500 18 MHz NMR spectrometer. Prior to measurement, (10-30 mg/ml) of scaffolds are dissolved in trichloromethane/chloroform (Carl Roth GmbH) for 3 hours on a spinning wheel, centrifuged and the supernatants transferred into NMR tubes. The presence of EC is defined by the peak at 4.541 ppm of the four hydrogen protons.

### ***Degradation/Swelling Test***

To investigate degradation and swelling, Design 1 3D-printed scaffolds (N=6) are placed individually in a well of a 6 well-plate and incubated in 5 mL phosphate-buffered saline (PBS) for 28 days at 37°C under constant shaking. Beforehand, the weight of the scaffolds is measured in dry state, which is used as the normaliser. Wet scaffolds are measured at day 1, 7, 14 and 28. After the incubation period the scaffolds are air dried for 2 days and the weight is measured in dry state. The pH of the PBS is measured at 1, 7, 14 and 28 to identify possible reduction caused by scaffold degradation.

### ***Micro-Computed Tomography***

Visualisation of 3D-printed scaffolds is performed via micro-computed tomography ( $\mu$ CT) using vivaCT 40 (SCANCO Medical AG) with 45 kVp voltage, 177  $\mu$ A current and 10.5  $\mu$ m isotropic voxel size. Printing porosity of 3D-printed scaffolds is calculated using the Amira image processing software (V. 6.4.0; Thermo Fisher Scientific) (N=3). A standardised image processing protocol is used. Firstly, the scaffold is segmented and using a filling algorithm, the inside of the segmentation is defined, leaving the total volume of the scaffold and the inside segmented. The scaffold is segmented again and combined with the total volume

mask. With the combined mask, the scaffold's porosity is calculated as a percentage of the total volume divided by the volume of the scaffold mask.

### ***Scanning Electron Microscopy***

Surface topography of 3D-printed scaffolds (Design 1) is visualised using a scanning electron microscope (SEM) (Hitachi SU 5000). Upon solvent extraction, scaffolds are mounted onto stubs using carbon conductive cement Leit-C, dried overnight and subsequently sputter coated with a layer of platinum/palladium using CCU-010 Metal Sputter Coater (Safematic). SEM images are taken at 3 kV voltage, 10 mA beam current and a working distance of 5 and 50 mm for surface images and overview images, respectively. Quantification of surface porosity is based on the close-up surface images and obtained using ImageJ software (N=7).

### ***N<sub>2</sub> Sorption***

Mesoporous properties (2 – 50 nm) 24 of 3D-printed scaffolds (Design 1) are determined via Nitrogen (N<sub>2</sub>) sorption using Micromeritics ASAP 2020 (Instrument Corp.) under liquid N<sub>2</sub> (–195.8°C). Scaffolds (ca. 0.5 g) are degassed at room temperature under vacuum for 48 hours prior to measurement. Specific surface area (SSA) and desorption average pore width (4V/A) values are determined by applying the Brunauer–Emmett–Teller theory (BET).

### ***Compression Test***

Mechanical compression tests (Design 1, G1 and G2: N=14, Osteoink: N=13 of pre-wetted 3D-printed scaffolds are performed using Instron 5866 (Instron) equipped with a 1 kN load cell. The compression test is divided into two parts: 1) 4 loading-unloading cycles at the rate of 1 %/s to 15 or 8% compressive strain, are applied to the PLGA/ $\beta$ -TCP  $\pm$  TPU and the Osteoink® scaffolds respectively, and the slope from the linear region of the stress-strain curve of the fourth cycle

is taken to calculate the Young's modulus; 2) subsequent ultimate test using a speed of 0.1 %/s until a strain of 50% to break the scaffold and measure yield strain, yield stress and toughness at yield.

### ***Screw Pull-Out Test***

Screw Pull out tests of 3D-printed scaffolds (Design 1) are performed using Instron 5866 equipped with a 50 N load cell (N=12). Prewetted scaffolds are divided into 2 groups: 1) no pre-drilling is applied; 2) scaffolds are pre-drilled using 1.8 mm drill head (DePuy Synthes). An 18 mm "MatrixMANDIBLE" screw (DePuy Synthes) with diameter of 2 mm is screwed into the scaffolds. The screw is installed in a custom-made screw holder that is connected to the load cell, placed into a chamber with a slot and pulled out with a velocity of 0.25 mm/s and the maximum force during testing is recorded.

### ***Cell Culture of L929 Fibroblasts***

L929 fibroblasts (85011425, mouse C3H/An connective tissue, Sigma) are cryopreserved according to the company's instructions in liquid nitrogen. Upon thawing,  $1 \times 10^6$  cells are seeded in a T300 flask (cell density  $3.33 \times 10^3$  cells/cm<sup>2</sup>) for culture expansion. The expansion medium (EM) consists of low glucose (1g/L) – DMEM (LG-DMEM) (Gibco, Carlsbad) supplemented with 10% (v/v) foetal bovine serum (Corning) and 100 U/mL Penicillin, 100  $\mu$ g/mL Streptomycin (PEN/STREP) (Gibco). Cells are cultured under standard cell culture conditions of 37°C with 5% CO<sub>2</sub> and 90% humidity with 3 media changes per week.

### ***Cell Isolation and Culture of Human Bone Marrow-derived Mesenchymal Stromal Cells***

Isolation and cryopreservation of human bone marrow mesenchymal stromal cells (hBM-MSCs) from bone marrow aspirates is performed as previously described <sup>76</sup>, as well as cell culture expansion as previously described <sup>77</sup>. hBM-

MSC donor details are as follows: Donor A, 52-year old female, spine vertebral body aspirate, Donor B, 51-year old female, spine vertebral body aspirate; Donor C, 48-year old female, spine vertebral body aspirate; Donor D, 74-year old female spine vertebral body aspirate; Donor E, 44-year old male, iliac crest cancellous bone.

### ***Indirect Cytotoxicity Test via CellTiter-Blue®***

The indirect toxicity test of 3D-printed scaffolds (Design 1) is carried out according to the ISO 10993 guideline using the L929 fibroblasts (N=4). Cells are harvested using 0.05% Trypsin-EDTA (Gibco) and seeded on 96-well plates at a density of  $1 \times 10^4$  cells/well in 6 replicates. For the first 24 h, cells are cultured in EM. In the meantime, 3D-printed scaffolds are incubated in EM in triplicates for 24 hours to obtain conditioned media (CM1-3). At this point (Day 0), cells are switched into their corresponding culture media: 1) Positive control: EM supplemented with 0.1% Triton X-100; 2) Negative control: EM; 3) CM1-3. CellTiter-Blue® (CTB) is performed at day 1 and day 3. Media are removed and EM supplemented with 16.6% (v/v) CTB reagent is added. After 4 hours of incubation at 37°C with 5% CO<sub>2</sub> and 90% humidity the supernatant is transferred into a 96 clear bottom well plate (Corning, New York, USA) and fluorescence is read at 560/590 nm using Infinite® 200 PRO plate reader (Tecan Trading AG).

### ***DNA Quantification and Live/Dead Staining on 3D-printed Discs***

hBM-MSCs are harvested using 0.05% Trypsin-EDTA and seeded at a density of  $8.75 \times 10^3$  cells/well ( $10 \times 10^3$  cells/cm<sup>2</sup>) in duplicates on either tissue culture plastic as control or onto 3D-printed discs (Design 2) and cultured in EM. At day 1 and day 7 DNA quantification is performed using the CyQuant™ Cell Proliferation Assay (Invitrogen) according to the manufacturer's instructions (N=3). In short, cells are lysed with 0.1% Triton X-100 in 10 mM TrisHCl for 2 hours at 4°C, cell lysate is transferred into a 96 clear bottom well plate, working

solution containing dye is added and fluorescence is read at 490/530 nm using Infinite® 200 PRO plate reader.

At day 1 and day 7 cells are washed with PBS, stained with staining solution that contains 1  $\mu$ M Calcein, AM (Invitrogen) and 1  $\mu$ M Ethidium Homodimer-1 (Invitrogen) in serum-free LG-DMEM and incubated at 37°C for 1 h. The staining solution is rinsed with PBS and the cells are subsequently imaged using a confocal microscope (LSM800, Leica Microsystems).

### ***Alizarin Red Staining and Quantification of 3D-printed Discs***

3D-printed discs (Design 2) are stained with Alizarin Red (ScienCell Research Laboratories) according to the manufacturer's instructions (N=3). In short, the discs are incubated with 40 mM Alizarin red solution for 1 hour at room temperature under gentle movement. The discs are washed with Milli-Q® water until no discolouration is visible. The stained discs are imaged and incubated with 10% (v/v) acetic acid for 30 minutes at room temperature on an orbital shaker to extract the dye. The solution is transferred into Eppendorf tubes (Eppendorf, Hamburg, Germany), incubated for 10 minutes at 85°C, cooled on ice for 5 minutes and centrifuged at 20,000 x g for 15 minutes at room temperature. 10% (v/v) ammonium hydroxide is used to adjust the pH to 4.1-4.5 of the transferred supernatant. The absorbance at 405 nm is measured using Infinite® 200 PRO plate reader.

### ***Osteogenic Assessment of hBM-MSCs Cultured on G1 (-TPU) Osteogenic Differentiation***

hBM-MSCs are harvested using 0.05% Trypsin-EDTA and seeded at a density of  $28.5 \times 10^3$  cells/well ( $15 \times 10^3$  cells/cm<sup>2</sup>) in duplicates onto either coverslips (SARSTEDT AG) cultured in osteocontrol medium (EM) or 3D-printed discs of G1 (-TPU) (Design 2) and cultured either in osteocontrol – or osteogenic medium (EM supplemented with 10 nM dexamethasone, 5 mM  $\beta$ -glycerophosphate and



50  $\mu\text{g}/\text{mL}$  L-ascorbic acid-2-phosphate) for 28 days under normal culture conditions (N=2).

### ***Quantification of Alkaline Phosphatase (ALP) Activity and DNA Content***

At day 14, alkaline phosphatase (ALP) activity is measured as previously described.<sup>77</sup> In short, after cell lysis with 0.1% Triton X-100 in 10 mM TrisHCl, the enzymatic reaction is started by adding alkaline buffer solution, substrate solution (25 mg/mL phosphate substrate in 1 mM diethanolamine) and Milli-Q® water and stopped by adding 0.1 M NaOH solution after 15 minutes at 37°C. The absorbance is read at 405 nm using the Infinite® 200 PRO plate reader. ALP activity is normalised to the DNA content, which is performed as described in section (DNA Quantification and Live/Dead Staining on 3D-printed Discs).

### ***Staining of Mineral Deposition***

At day 28, cells are fixed with 10% neutral buffered formalin for 30 minutes, permeabilised with 0.25% Triton X-100 in PBS for 20 minutes and stained with 2  $\mu\text{g}/\text{mL}$  4',6-Diamidino-2-phenylindole solution for 10 minutes with a PBS wash before each step. Mineral deposition is stained with OsteoImage™ Mineralization Assay (Lonza) according to the manufacturer's instructions and imaging is performed using a confocal microscope (LSM800, Leica Microsystems).

### ***RNA Isolation and RT-qPCR***

Cells are harvested for gene expression analysis, RNA isolation at day 28 and real-time quantitative PCR is performed using the QuantStudio™ Flex Real-Time PCR System as previously described [28]. Reverse transcription is performed using the Superscript Vilo cDNA Synthesis Kit (Thermo Fisher Scientific) according to the company's instructions. Gene expressions of osteo-relevant markers: *ALPL* (encodes for ALP), *IBSP* (encodes for bone sialoprotein), *SP7* (encodes Osterix) and *SPP1* (encodes Osteopontin) are investigated. Primer

sequences used are listed in **Table 2.3**. The  $\Delta\Delta$ Ct method is applied for data analysis using RPLP0 as an endogenous normaliser and day 0 samples as a calibrator.

**Table 2.3. Primers/probes used for qPCR**

Gene		Assay on Demand <sup>1</sup>	
<i>ALPL</i>		<i>Hs00758162_m1</i>	
<i>IBSP</i>		<i>Hs00173720_m1</i>	
<i>SP7</i>		<i>Hs00541729_m1</i>	
<i>SPP1</i>		<i>Hs00959010_m1</i>	
Gene	Forward	Reverse	Probe
<i>RPLP0</i>	5'-TGG GCA AGA ACA CCA TGA TG-3'	5'-CGG ATA TGA GGC AGC AGT TTC-3'	5'-AGG GCA CCT GGA AAA CAA CCC AGC-3'

*ALPL*: Alkaline phosphatase, biomineralisation associated; *IBSP*: integrin binding sialoprotein; *SP7*: Sp7 transcription factor; *RPLP0*: ribosomal protein lateral stalk subunit P0; *SPP1*: osteopontin, organic component of bone matrix. <sup>1</sup>TaqMan® Gene Expression Assay (Applied Biosystems®).

### **3D Printing of a Patient-specific Mandible Defect-sized PLGA/ $\beta$ -TCP Scaffold**

The self-created defect in the mandible SYNBONE® is  $\mu$ CT-scanned using the vivaCT 40. The defect geometry is exported as a STL. file using the Amira image processing software and converted into the g-code using the MM Converter software (RegenHu). Solvent-based printing is applied to the PLGA/ $\beta$ -TCP (G1 (-TPU)) ink to create a patient-specific mandible defect-sized scaffold to demonstrate the precise printability of relevant defect sizes.

### **Statistics**

Statistical analyse is performed using GraphPad Prism software version 9.3.1 (GraphPad

Software). An unpaired parametric test based on the Welch's test, which assumes different standard deviation is applied to the data of the printing porosity,

surface porosity, gene expression and Alizarin red quantification. A One-Way ANOVA is applied to the data of the Young's modulus, yield stress - and strain. A Two-Way ANOVA is applied to the data of the peak displacement, screw pull-out test, DNA quantification and ALP activity. P-values higher than 0.05 are not significant and marked as ns.

## **2.3 Results**

### ***Both PLGA/ $\beta$ -TCP $\pm$ TPU Inks Demonstrate Adequate Rheological Properties for 3D Printing and Superior Printability Compared to OsteoInk®***

In the frequency sweep test, both inks remain viscous ( $G' < G''$ ) with increasing frequency when the temperature and the amplitude is kept constant at 80°C and 1%, respectively (**Figure 2.2A**).  $G'$  values start at  $5 \pm 1.1$  Pa and  $12 \pm 6$  Pa and increase up to  $9433 \pm 887$  Pa and  $1480 \pm 10^4$  Pa for G1(-TPU) and G2(+TPU), respectively. The addition of TPU decreases both the storage and loss modulus at frequencies higher than 0.25 Hz. Temperature-dependent viscosity changes are measured using a temperature sweep test (Figure 2B). Viscous behaviour ( $G' < G''$ ) dominates for G1(-TPU) ink with decreasing temperature, while for G2(+TPU) ink solid-like behaviour already starts to occur at 42°C.  $G'$  values start at  $198 \pm 1.1$  Pa and  $63 \pm 6.4$  Pa and increase up to ca.  $1736 \pm 10^2$  Pa and  $2511 \pm 252$  Pa for G1(-TPU) and G2(+TPU), respectively.

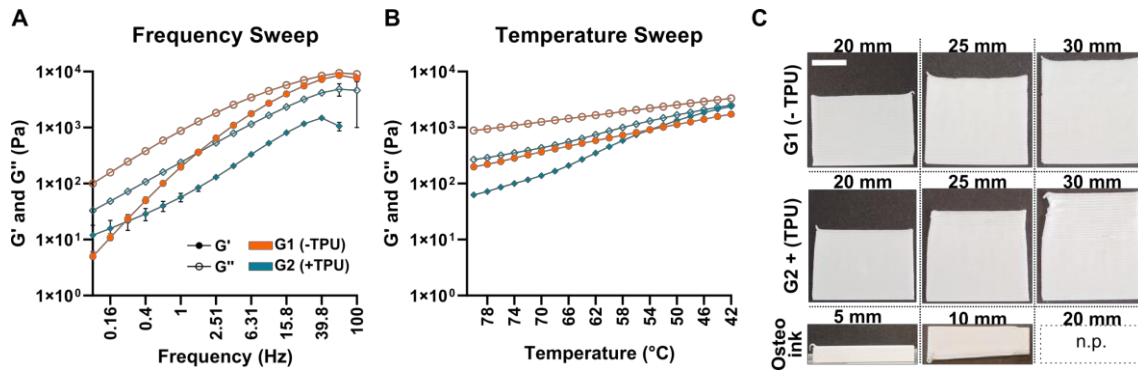


**Figure 2.2: Ink Rheology and Maximum Printability:** Representative Sweep Curves (N=3) of A) Frequency and B) Temperature; C) Three different inks (G1, G2 and OsteoInk®) are printed to the maximal height until artifacts or failure (Collapsed structure for OsteoInk at 10 mm, top view); scale bar: 1 cm, n.p.=not possible.

The addition of TPU accelerates solidification of the ink with decreasing temperatures (**Figure 2.2B**). Rheologic characteristics of both inks display viscous behaviour at printing temperatures, which is important for successful printing.

Printability is measured by investigating the maximum printing height until failure or artifact (**Figure 2.2C**). Single line printing of G1(-TPU) ink can be achieved up to 30 mm without visual artifacts, while with G2(+TPU) ink artifacts appear after a height of 25 mm. OsteoInk® shows a successful single line printing up to 5 mm, but construct collapse occurs when a 10 mm height is attempted. Printing the OsteoInk® up to 20 mm is therefore not possible. Both G1 and G2 inks show artifact-free printing for constructs larger than 25 mm, while the OsteoInk® collapses after 5 mm of printing.

### ***Total Solvent Removal is confirmed and does not Jeopardise Filament Shape***

The weight of the 3D-printed scaffold is measured during the two-step solvent removal process, which starts with a 24-hour step under vacuum and ends at 48-

hour following an additional 24-hour step in a water bath (**Figure 2.3A**). The vacuum step causes a reduction of ca. 10% of the scaffold weight, while the water step accounts for additional ca. 55% weight lost in both groups, which corresponds to the ca. 65% weight ratio of the solvent within the scaffold before removal. Total solvent removal is indirectly confirmed by  $^1\text{H}$  NMR after the water step at 48-hour. No EC peak is present at 4.54 ppm in both spectra of G1(-TPU) (**Figure 2.3B**) and G2(+TPU) (**Figure 2.3C**).

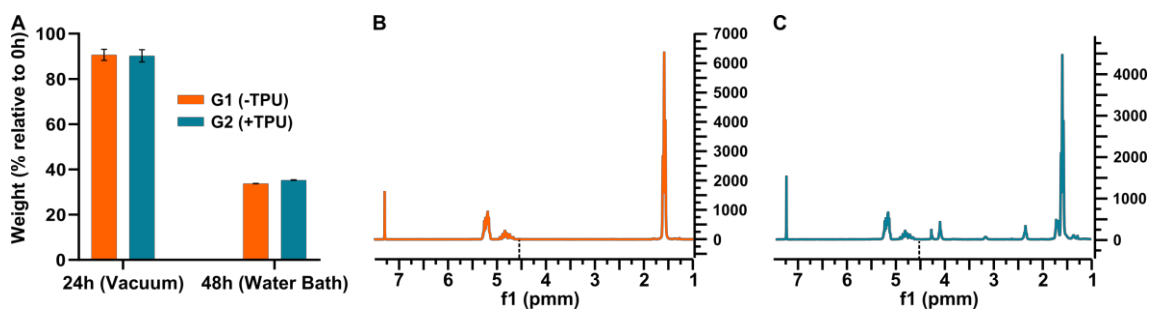


**Figure 2.3: Solvent Removal:** A) Scaffold Weight relative to 0h after incubation under vacuum at 24 hours and water bath at 48 hours (N=3); B) Representative nuclear magnetic resonance (NMR) Spectrum of G1 (- TPU) and C) Representative NMR Spectrum of G2 (+ TPU). The NMR peak of ethylene carbonate (EC) is marked with a black dotted line in both spectra at 4.45 pmm.

Representative photo - and SEM images of 3D-printed scaffolds (Design 1) (**Figure 2.4**) after solvent removal illustrates the shape of the overall scaffold, the filament, and the surface, as well as the side view of both groups. Filament shape remains intact after solvent removal. Increased surface roughness is visible in G2(+TPU) compared to G1(-TPU) as noticeable from  $\mu\text{CT}$  images (**Figure 2.5A**). The side view of cut filaments in the SEM images show slightly elliptic shape in both groups.

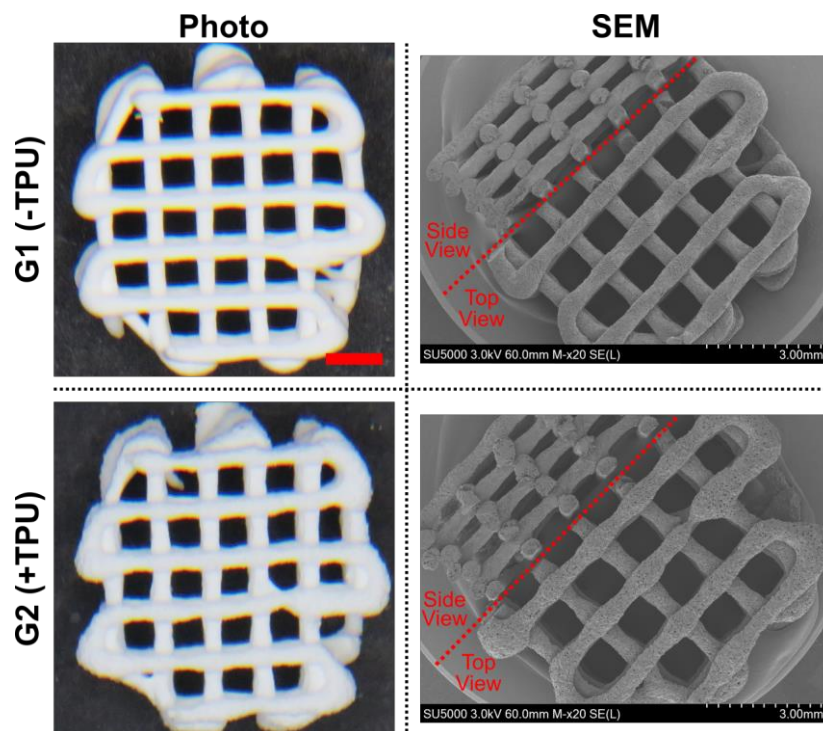
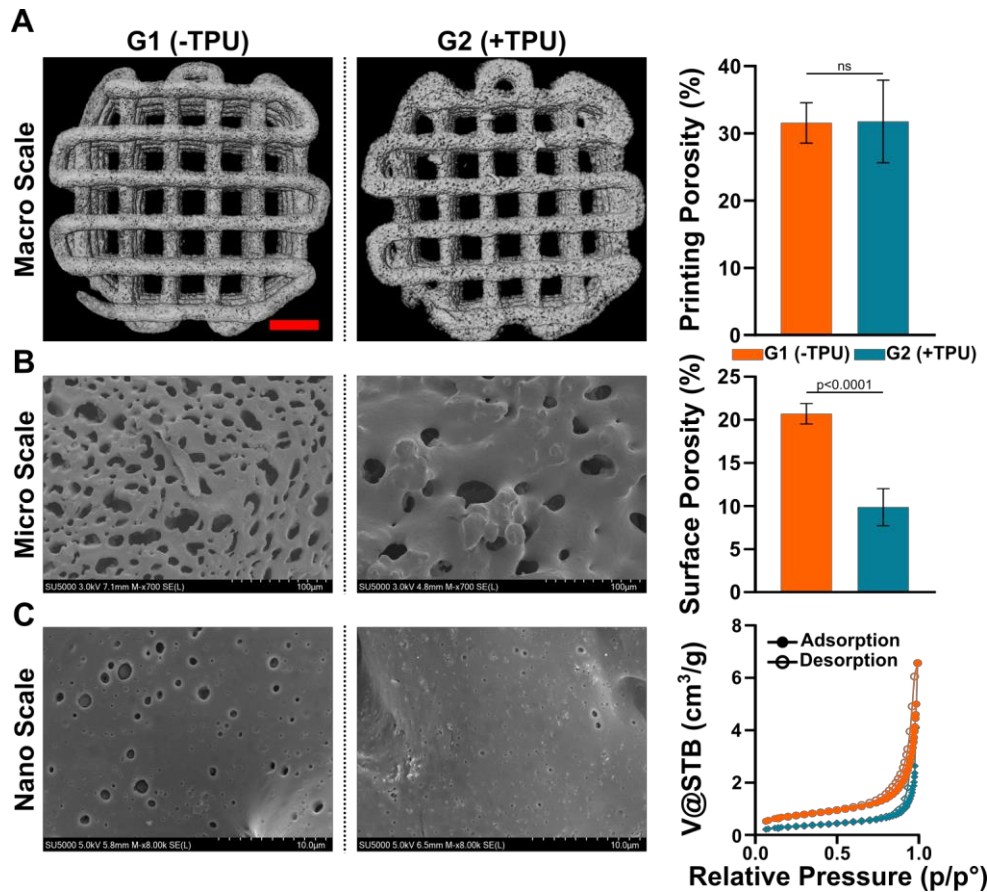


Figure 2.4: Representative Images of 3D-printed Scaffold (Design 1): Photo Scanning Electron Microscopy (SEM); scale bar = 1.5 mm.



**Figure 2.5: 3-Level Porosity Measurement from macro to nano through micro scale:** A) Printing Porosity (100 $\mu$ m – 1mm) based on  $\mu$ CT (N=3), scale bar = 1.5 mm; B) Surface Porosity (2 $\mu$ m – 50 $\mu$ m) (N=7) based on SEM and C) Nano- and Mesoporosity based on nitrogen sorption isotherms (2nm – 100nm) of 3D-printed scaffolds. ns = not significant.

### ***Porosity is Present at Three Levels from Macro to Micro to Nano Scale***

The macro-scale printing porosity, representing the negative space within the 3D-printed scaffold in-between the struts, is calculated to be  $31.5 \pm 3.0\%$  for G1(-TPU) and  $32 \pm 6.1\%$  for G2(+TPU) (**Figure 2.5A**). No statistical differences are observed between the two groups indicating indistinguishable shape fidelity. Micro-scale SEM images of G1(-TPU) show smaller, but a higher number of pores compared to G2(+TPU) (**Figure 2.5B**). The SEM images confirms increased topography roughness of the second group, which was already visible

on  $\mu$ CT images. G1(-TPU) has a surface porosity of  $21 \pm 1.2\%$ , a significantly increased number compared to  $10 \pm 2.2\%$  of G2(+TPU). Nano-scale porosity is visible in the SEM images for both groups (**Figure 5C**). The adsorption and desorption isotherm profiles of both groups are considered type 3 isotherms and show H3 type hysteresis loops according to the IUPAC classification.<sup>78</sup> The addition of TPU decreases mesoporosity, the specific surface area (SSA), while the desorption average pore width value is increased (**Table 2.4**). Solvent-based printing allows for a 3-level macro, micro and nano scale porosity, the microscale decreases when TPU is added, while the macro and nanoscale remain unchanged.

**Table 2.4. Specific surface area (SSA) and desorption average pore width values (4V/A by BET) of 3D-printed scaffolds after solvent removal**

Value	G1(-TPU)	G2(+TPU)
SSA (m <sup>2</sup> /g)	$2.5 \pm 0.05$	$1.2 \pm 0.02$
Desorption Average Pore Width (nm)	15	19

SSA = Specific Surface Area

### ***3D-printed Scaffolds Swell without Acidic Change in pH***

3D-printed scaffolds (Design 1) swell upon incubation in PBS at 37°C up to  $164.4\% \pm 5.5$  in G1(-TPU) and  $156.1\% \pm 9.8$  in G2(+TPU) relative to day 0 (dry) until 21 days, after which the weight of the scaffolds slightly decreases at day 28 (**Figure 2.6A**). The majority of the swelling occurs in the first 7 days. The addition of TPU reduces the swelling effect. The weights of the dry scaffolds after 28 days of incubation is measured at  $100.4\% \pm 0.1$  in G1 and  $100.7\% \pm 2.6$  in G2 indicating that the scaffolds did not degrade in PBS under *in vitro* conditions. The pH of the PBS slightly decreases over the incubation period but remains close to neutral between ca. 7.4 and 7 in both groups confirming no acidic change of the milieu (**Figure 2.6B**).



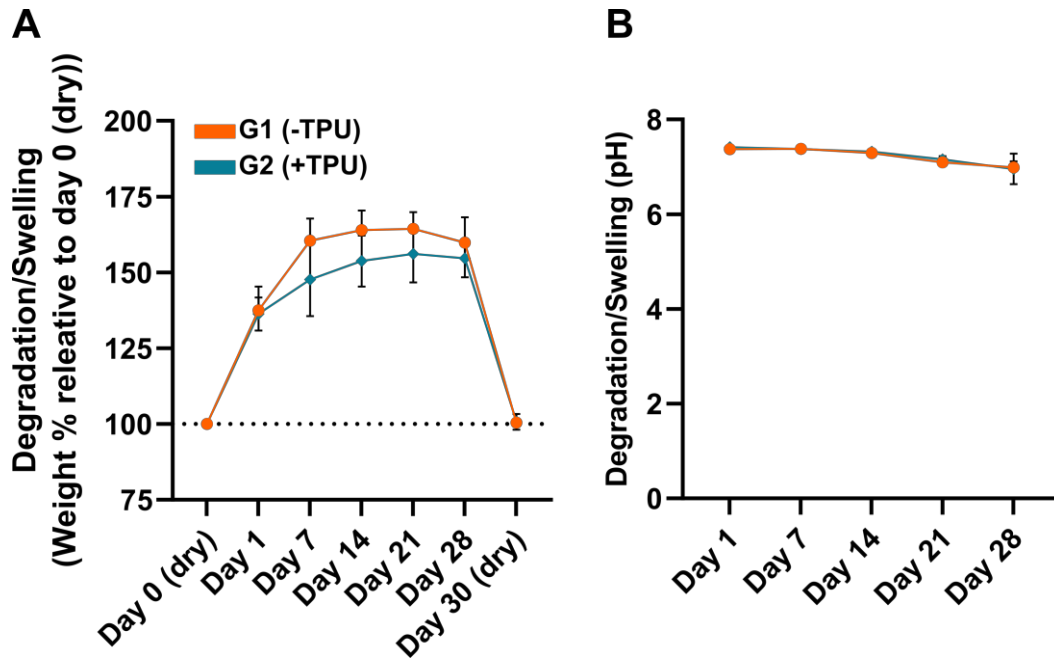


**Figure 2.6: Degradation/Swelling of 3D-printed scaffolds (Design 1) incubated in PBS at 37°C measured at day 1, 7, 14, 21 and 28 (N=6): A) Weight percentage relative to day 0 (dry) and B) pH of PBS.**

### ***The Addition of TPU Leads to a Decreased Compressive Stiffness***

The addition of TPU significantly decreases the Young's Modulus (**Figure 2.7A**) of 3D-printed scaffolds from  $43 \pm 4.2$  MPa in G1(-TPU) to  $33 \pm 4.8$  MPa in G2(+TPU) (Design 1) under cyclic mechanical compression, while no difference is measured for the yield stress (**Figure 2.7B**) (G1(-TPU):  $1.5 \pm 0.16$  MPa and G2(+TPU):  $1.5 \pm 0.26$  MPa) and yield strain (**Figure 2.7C**) (G1(-TPU):  $0.06 \pm 0.005$  and G2(+TPU):  $0.06 \pm 0.004$ ). Both groups show significantly increased Young's modulus and yield stress compared to the OsteoInk® ( $13 \pm 2.8$  MPa and  $0.5 \pm 0.1$  MPa, respectively), but not for the yield strain ( $0.07 \pm 0.02$ ).

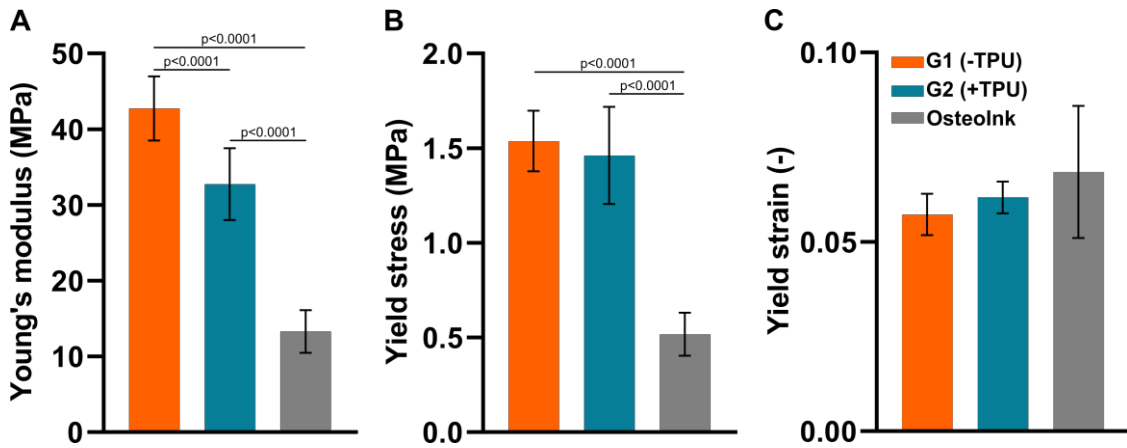


**Figure 2.7: Mechanical Properties of 3D-printed scaffolds (Design 1):** (G1 and G2: N=14, OsteoInk: N=13) A) Young's Modulus, B) Yield stress and C) Yield strain.

### ***Scaffolds of Both Groups Resist Drilling and Screwing***

Drilling using a 1.8 mm drill head and screwing using 2 mm medical grade screw does not break or impair the 3D-printed scaffolds (Design 1) (**Figure 8A**) but does break the OsteoInk® scaffold (Supplementary Video), which therefore cannot be used for the screw pull-out test. To pull out the screw from pre-drilled scaffolds of G1(-TPU) a maximal force of  $10 \text{ N} \pm 2.4$  is required, while a significantly increased force of  $14 \text{ N} \pm 4.5$  is required for G2/+TPU (**Figure 2.8B**). The force is significantly decreased compared to the scaffolds in which no pre-drilling was performed for both groups (**Figure 2.8B**). The addition of TPU leads to an increased trend of maximal force, but no statistical significance was calculated with G1(-TPU) being at  $16 \pm 2.1 \text{ N}$  and G2(+TPU) being at  $19 \pm 4.1 \text{ N}$ .

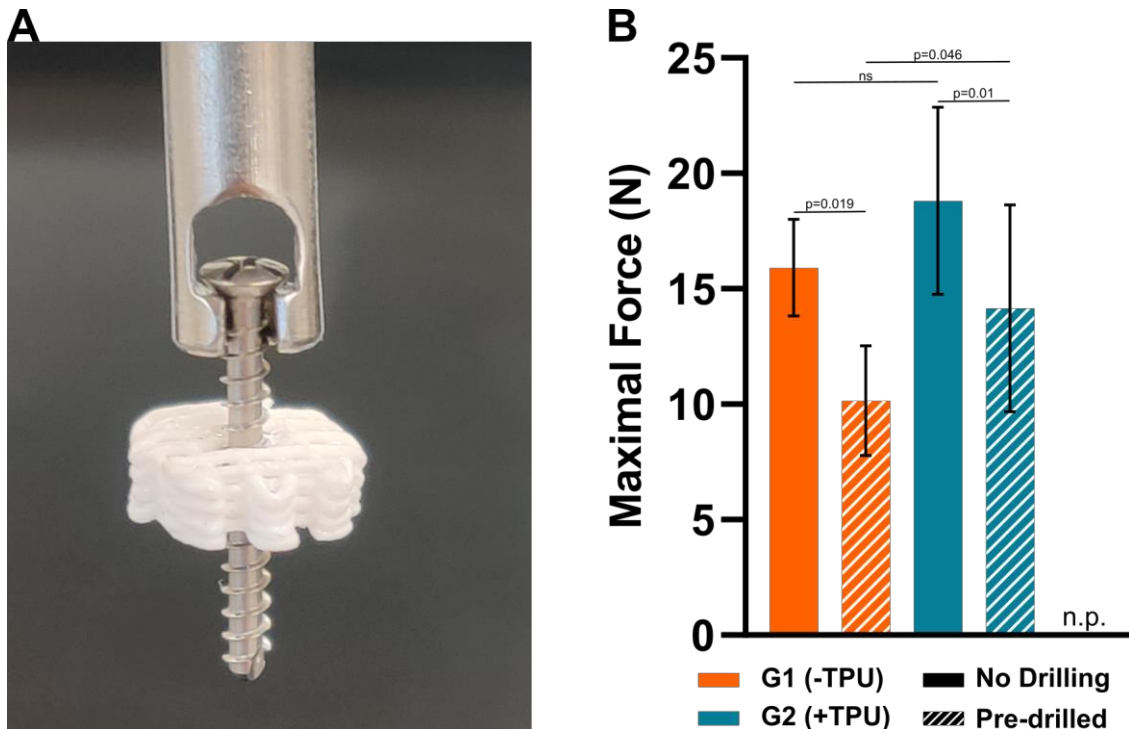


**Figure 2.8: Screw Pull-Out Test:** A) Representative image of the screw within the 3D-printed scaffold, screw length: 18 mm; B) Maximal Force with and without pre-drilling (N=12); n.p. = not possible to perform test on OsteoInk, due to scaffold breakage upon drilling or screwing, ns = not significant.

### ***The Addition of TPU Decreases Proliferation of Seeded hBM-MSCs after 7 Days of Culture***

Biocompatibility of 3D-printed scaffolds (Design 1) is investigated via an indirect cytotoxicity test using the L929 fibroblast cell line. Cells are cultured with conditioned media from both scaffold groups and showed metabolic activity greater than 100% when normalised to cells in control medium (**Figure 2.9A**).

DNA quantification of hBM-MSCs from 3 independent donors directly seeded on 3D-printed discs (Design 2) shows proliferation from day 1 to day 7 for both groups. While no difference is measured between the two groups at day 1, a statistically significant difference is observed between G1(-TPU) and G2(+TPU) at day 7 (**Figure 2.9B**). The proliferation is confirmed by live/dead images (**Figure**

**2.9C)** in which more live cells are visible on G1(-TPU) compared to G2(+TPU) at day 7. Both groups show no cytotoxicity, while G1(-TPU) favours cell proliferation compared to G2(+TPU).

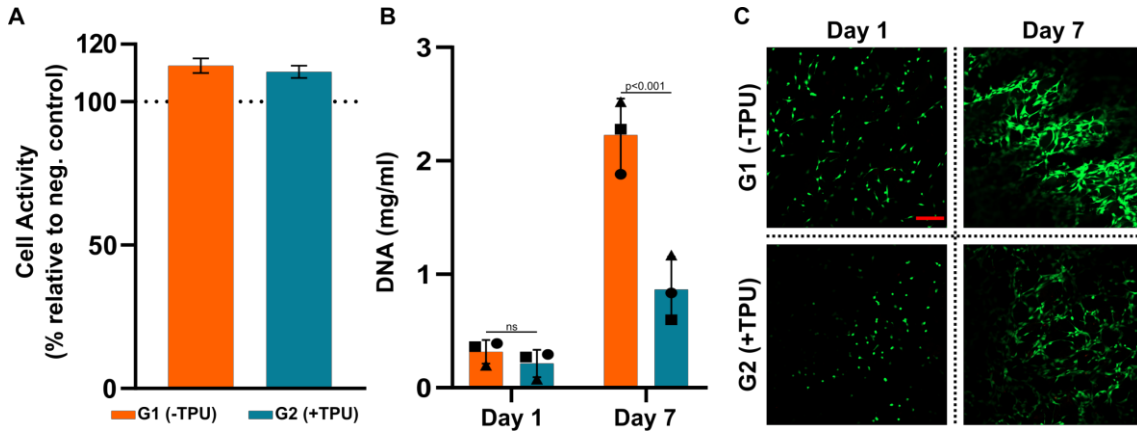


**Figure 2.9: Biological Assessment:** A) Indirect Cytotoxicity of L929 mouse fibroblasts activity relative to neg. control on plastic based on Cell Titer Blue® (N=4); B) DNA quantification at day 1 and 7 of three independent donors (N=3: donor A (●), donor B (■) and donor C (▲) of mesenchymal stromal cells (MSCs) seeded directly on 3D-printed discs; C) Live/Dead staining of donor B at day 1 and 7, Scale bar: 200  $\mu$ m, ns = not significant.

### ***$\beta$ -TCP Particles are Homogeneously Distributed on 3D-printed Discs of Both Groups***

To understand the  $\beta$ -TCP exposure on the scaffolds, 3D-printed discs (Design 2) are stained with Alizarin red.  $\beta$ -TCP particles are homogeneously distributed on the discs for both groups and the addition of TPU leads to a decrease of  $\beta$ -TCP exposure, visible with less red stained surface on G2(+TPU) (**Figure 2.10A**). The measured concentration of Alizarin red confirms the images with a trend of higher dye concentration in G1(-TPU) compared to G2(+TPU), but with no statistically significant difference (**Figure 2.10B**). These findings are in accordance with the increased ratio of  $\beta$ -TCP within the scaffold in G1(-TPU) compared to G2(+TPU) as a consequence of the TPU addition.

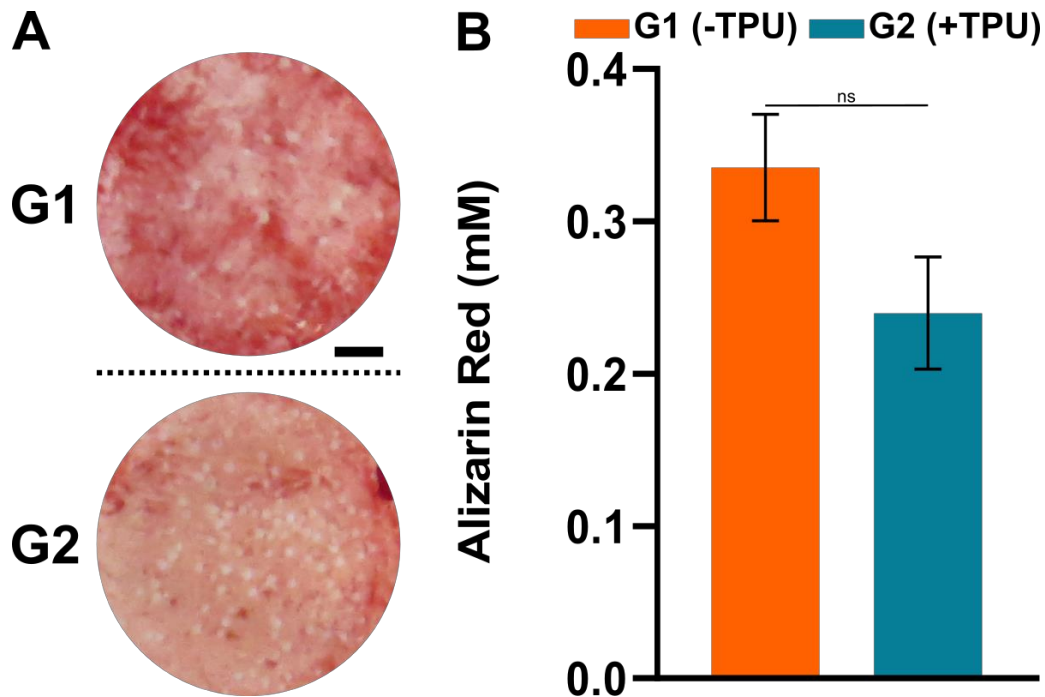


**Figure 2.10: Surface Calcium Staining of 3D-printed discs with Alizarin Red:** A) Representative Images; B) Alizarin Red Quantification (N=3), scale bar = 2 mm, ns = not significant.

### ***hBM-MSCs Undergo Osteogenesis when Seeded on 3D-printed Discs G1 (-TPU)***

In light of the enhanced proliferation profile of G1 (-TPU) (**Figure 2.9B/C**), this group was selected to carry out the osteogenic assay using hBM-MSCs of three independent donors. Cells are seeded and cultured on either coverslip under osteocontrol condition or on 3D-printed discs (Design 2) under osteocontrol and osteogenic condition for 28 days. ALP activity at day 14, normalised to the DNA content is upregulated in both disc groups compared to the coverslip osteocontrol group, and in the disc osteogenic group compared to the disc osteocontrol group (**Figure 2.11A**). Confocal images of the fluorescent-stained mineral deposition at day 28 show visibly increased mineralisation in the disc osteogenic group compared to the disc osteocontrol group, while no mineralisation is detected in the coverslip osteocontrol group (**Figure 2.11B**). Gene expression of hBM-MSCs

on 3D-printed discs show an upregulation of *ALPL*, *IBSP*, *SP7* and *SPP1*, all relevant makers for osteogenesis, when cultured under osteogenic conditions compared to control conditions without statistical significance (**Figure 2.11C**).

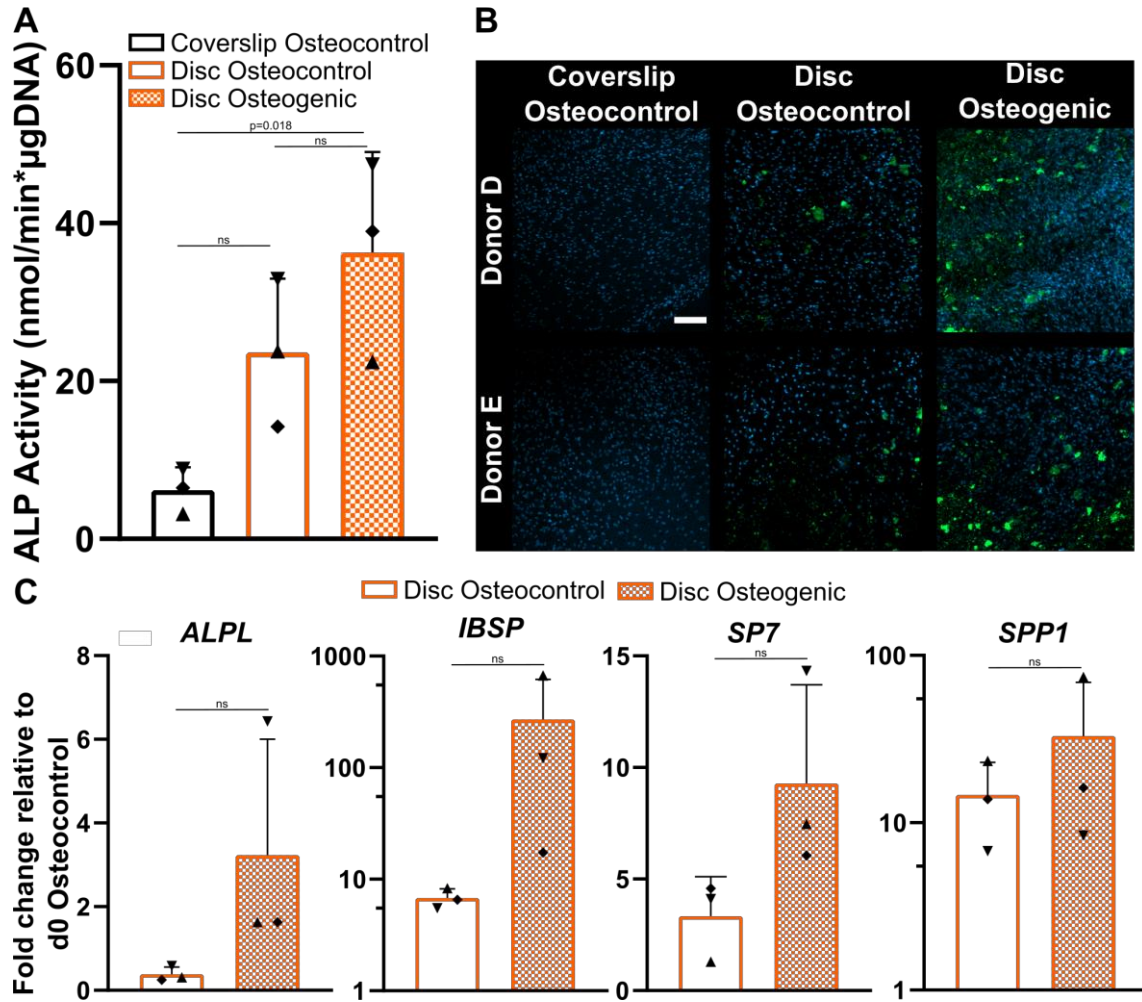


**Figure 2.11: Osteogenic Assessment** of hBM-MSCs cultured on G1 (-TPU) of three independent donors (N=3): A) ALP activity normalised to DNA content at day 14; B) Staining of mineral deposition (green) and nucleus (blue) at day 28 of two representative donors, scale bar: 200  $\mu$ m; C) Gene expression of osteogenic markers (*ALPL*, *IBSP*, *SP7* and *SPP1*). Each data



point represents each individual donor: donor C ( $\blacktriangle$ ), donor D ( $\blacklozenge$ ) and donor E ( $\blacktriangledown$ ), ns = not significant.

ALP activity and mineral deposition indicates osteogenic differentiation of hBM-MSCs when cultured on G1 (-TPU) discs, with enhanced effects under osteogenic culture conditions, especially visible looking at the gene expression of osteo-relevant markers.

### ***Solvent-based Printing can Create Precise Large-scalecaffolds***

To further demonstrate the clinical compatibility of this biofabrication tool, a precise and patient-specific mandible defect-sized scaffold based on PLGA/ $\beta$ -TCP is printed using the solvent-based printing approach (**Figure 2.12**). The macro-porous 3D-printed scaffold shows precise defect fitting upon implantation in the defect site, a highly desired characteristic for patient's aesthetics.

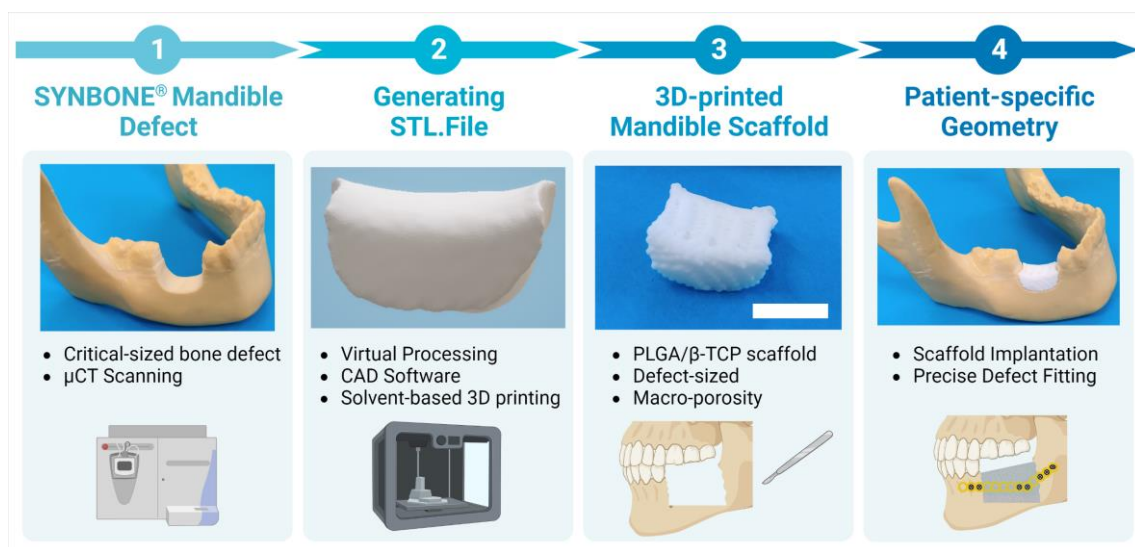


**Figure 2.12: Workflow of the creation of a patient-specific 3D-printed scaffold** via 1)  $\mu$ Ct scanning of a critical-sized defect, 2) generating and virtual processing the STL. file, 3) solvent-based printing of a defect-sized scaffold based on PLGA/ $\beta$ -TCP (G1 (-TPU)) and 4) precise defect implantation of the scaffold, scale bar = 1 cm. Created with BioRender.com.

## 2.4 Discussion

The purpose of this study was to develop a 3D-printing fabrication technique to create porous scaffolds for bone tissue engineering. To increase the availability of different bone substitutes and maximise the possibility to eventually replace the current SOC of ABG for the repair of bone defects an easy, cheap, and versatile biofabrication process is advantageous. By applying a low-temperature solvent-based printing approach, we successfully fabricated a bone substitute with a 3-level macro-, micro- and nano-porosity based on a new formulation PLGA/ $\beta$ -TCP  $\pm$  TPU with adequate fidelity, cytocompatibility and osteogenic potential. To 3D print PLGA/CaP-based materials for the creation of bone substitutes, the heat-melt printing approach has been generally used, which involves the extrusion of blended granules upon pressure<sup>79-87</sup> and has been applied to variety of PLGA combinations with either HAp<sup>88-91</sup> or TCP<sup>92</sup>, but it is associated with FDM disadvantages. As an alternative for 3D printing of PLA-based materials the solvent based printing approach can not only create porous surfaces upon solvent removal of 3D-printed scaffolds but also allows for easy loading and mixing of bioactive factors without the need for post-process chemical modification as previously shown.<sup>70</sup> The presented fabrication method demonstrates the modulation of final material properties such as surface roughness and porosity, both highly connected to osteogenesis outcomes<sup>64,65</sup> via the addition of TPU to the PLGA/ $\beta$ -TCP composite, which has not been reported previously. To avoid the use of toxic organic solvents such as chloroform<sup>70,93</sup>, dichloromethane<sup>88,94</sup> or dimethyl sulfoxide<sup>95</sup>, commonly used for dissolving the polymeric component, we use EC. It has no toxicity, and it is water-soluble. EC solidifies at temperatures lower than 37°C, which allows solidification at lower temperatures and for easy removal in a warm water bath without modification of the fabricated water insoluble polymeric scaffold.



Both inks show viscous like behaviour confirmed by rheological characterisation and adequate printability for constructs in the size range relevant to large bone defects of ~3 cm in height, which is according to the human critical-sized defects of 2.5 cm.<sup>96</sup> Furthermore, the comparison to the commercially available OsteoInk® demonstrates the superior printability of both inks.

3D-printed PLGA/ $\beta$ -TCP  $\pm$  TPU scaffolds retain fidelity after total EC removal confirmed by NMR analysis and take up ca. 55 – 65% of aqueous liquid compared to their original weights. Biodegradation plays a pivotal role in facilitating optimal bone healing *in vivo*. For scaffolds to be used as bone graft substitutes (BGS), their primary function should be to initiate the bone healing process by serving as initial templates. The scaffolds should gradually degrade as new bone forms, without causing toxic side effects such as releasing acidic products.<sup>16</sup> However, determining the ideal degradation rate of an implanted scaffold is challenging and remains to be unclear. PLGA,  $\beta$ -TCP and TPU are known to be biodegradable.<sup>72,97,98</sup> However, observations from the degradation measurements showed no indication of degradation in 3D-printed scaffolds over a 28-day *in vitro* incubation period in PBS. To gain insight into the degradation rate, long-term *in vivo* degradation experiments would be necessary to, a limitation of this study. The biodegradation of polymers such as PLGA has shown to cause acidic alterations in the surrounding environment.<sup>99</sup> This phenomenon was not observed in the case of the scaffolds presented.

The porosity of the scaffold is an important material property for the adhesion of cells through enhanced adsorption of proteins, due to larger surface area<sup>66</sup> and the potential vessel and bone tissue infiltration into the scaffold *in vivo*.<sup>64,65</sup> We report the presence of the porosity on the scaffolds in 3 different levels: the macro porosity determined by the printing design, the micro – and nano porosity created from the EC removal. The macro pore size of the scaffold is strongly related to neovascularisation with larger pore sizes being beneficial for desired ingrowth of

blood vessels.<sup>100</sup> *In vivo* fibrous tissue ingrowth is decreasing with increasing pore sizes, with 400  $\mu\text{m}$  being the minimum pore size for optimal blood vessel growth<sup>100</sup>, which is in accordance with an average macro pore size of 1 mm of the scaffolds of both groups. Furthermore, interconnected macropores promote body fluid circulation and cell migration to the core of the implant.<sup>101</sup> Previous studies report macro porosities of scaffolds created from solvent-based printing between 70 and 80%<sup>70,102</sup>, much higher than obtained in this study at ca. 32%. Increasing the macro porosity can benefit tissue ingrowth, but decreases mechanical properties.<sup>103,104</sup> It is therefore important to find the balance of an optimal macro pore size without sacrificing mechanical strength of the scaffold. The presence of surface porosity in the micro<sup>65</sup> and nano<sup>105</sup> range is known to be advantageous for cell -adhesion and osteogenesis, but the optimal pore size is still unclear. The average surface pore size of G1 (-TPU) is measured to be 60  $\mu\text{m}$ , while the addition of TPU increases the average pore size to 130  $\mu\text{m}$ . The decreased surface porosity upon addition of TPU is credited to the decreased number of pores in G2 (+TPU) compared to G1 (-TPU). Nano mesoporosity reported from literature regarding the SSA is 6  $\text{m}^2/\text{g}$  and an average pore size of 22 nm of PCL/HAp/CNT based on  $\text{N}_2$  sorption higher<sup>94</sup> compared to the reported SSA of 1 - 2.5  $\text{m}^2/\text{g}$  and average pore size of 15 -19 nm in this study. Controlling the macro porosity of a 3D-printed scaffold is simple thanks to the nature of 3D printing but challenging for the micro and nano-range. The differences in the micro and nano range can be related to processing and the choice of material. Process related changes such as the choice of the solvent can have an effect: porosities can be created via the evaporation of a volatile solvent or water mediated dissolution such as in this study. Adding an additional material has also shown to change the micro porosity when CNT were added to the PCL/HAp scaffold<sup>94</sup> or TPU to PLGA/ $\beta$ -TCP in this study. The presence of porosity in the 3 level ranges is a relevant factor for enhanced osteogenic potential of a scaffold and therefore should preferably be available when a new bone substitute is created.

The addition of TPU was hypothesised to increase elasticity, but the presented mechanical properties suggest otherwise. The addition caused a significant decrease in Young's modulus from 43 MPa in G1(-TPU) to 33 MPa G2(+TPU), which are similar values of PLGA/TCP at 46 MPa from literature.<sup>92</sup> To assess the potential clinical translation mechanical properties of the PLGA/ $\beta$ -TCP  $\pm$  TPU scaffolds are compared to the commercially available OsteoInk®, which shows significantly decreased Young's modulus and yield stress. Natural bone on the other hand has a much higher stiffness compared to the presented scaffolds: trabecular: 10 GPa and cortical: 19 GPa when tested mechanically.<sup>106</sup> The advantage of adding TPU, known for its high ductility properties<sup>107</sup>, is shown by increased resilience against pulling out screws to potentially decrease the possibility for mechanical implant failure. The brittle nature of OsteoInk® is demonstrated when the screw-pull out test were not possible to perform, due to the breakage of the scaffolds beforehand, while the PLGA/ $\beta$ -TCP  $\pm$  TPU scaffolds remain structurally intact. Mechanical resilience of the scaffold is credited to the inclusion of the mechanical stable polymer PLGA and is an important aspect because the breakage of a bone substitute *in vivo* in a load-bearing environment such as the mandible or femur can have detrimental consequences to the patient's healing outcome. The lack for precise reproducibility of the printing process and resulting high variances might be explained by the mixing mechanism of the components itself or unstable room conditions due to varying room temperatures and humidities.

The PLGA/ $\beta$ -TCP  $\pm$  TPU scaffolds show cytocompatibility when tested with two different cellular types: a L929 mouse fibroblast cell line and primary hBM-MSCs. Additionally, hBM-MSCs showed good adhesion and viability over 7 days of culture. The decreased proliferation rate of hBM-MSCs after 7 days of culture on G2(+ TPU) can be explained by lower surface porosity values and decreased  $\beta$ -TCP exposure on the surface or due to the polyurethane's natural anti fouling properties<sup>108</sup>, but not by the surface hydrophilicity, measured by water contact

angle experiment (**Supplementary Figure 2.1**). OsteoInk® has shown cytocompatibility with MSCs<sup>109</sup> and allows for micro channel formation of vascular endothelial cells.<sup>110</sup> An Osteoink® like calcium phosphate cement paste produced from INNOTERE GmbH showed promising osteogenic *in vitro* and *in vivo* results.<sup>111,112</sup> The used polymers have shown to be advantages for printability and mechanical stability, but are not bioactive, nor are known to have osteoconductive properties, a disadvantage when included in bone substitutes. The scaffold's functional osteogenic assessment revealed that hBM-MSCs are capable to differentiate toward an osteoblastic phenotype when seeded on the G1 (-TPU) disc during a long-term culture of 28 days. Different methodical assays indicate the same trend of hBM-MSC's osteogenic response to the osteogenic culture condition, shown by the increased ALP protein expression profile, the stained area of hydroxyapatite, as well as the upregulated gene expression of important osteogenic markers such as *ALPL*, *IBSP*, *SP7* and *SPP1*. ALP, encoded by the *ALPL* gene, a well-known maker for bone formation and calcification<sup>113</sup>, provides a high phosphate concentration for osteoblasts during bone mineralisation.<sup>114</sup> *IBSP* encodes for bone sialoprotein, a late stage osteoblast differentiation marker.<sup>115</sup> *SP7* encodes for the transcription marker Osterix, which activates the osteogenic differentiation of preosteoblasts into mature osteoblasts.<sup>116</sup> *SPP1* encodes for Osteopontin, a late marker for osteogenic differentiation and important player in bone metabolism and homeostasis.<sup>117</sup> Statistical analysis does not show significant differences of osteogenically differentiated hBM-MSCs compared to cells cultured under control conditions, due to a limited donor number and high donor variability, a common consequence when primary hBM-MSCs are tested.<sup>118,119</sup> However, all donors behaved similarly, the only difference being the magnitude of the response. The PLGA/ $\beta$ -TCP scaffold shows osteoconductive results and can be a promising candidate for further *in vivo* studies but requires additional in-depth *in vitro* investigation using more donors and timepoints to elucidate the mechanism behind the osteogenesis of hBM-MSCs seeded on these 3D-printed scaffolds.

A pre-clinical *in vivo* study to investigate the osteogenic potential of this composite will be required before clinical translation can be undertaken. Future work also aims to upgrade the presented scaffold towards a vascularised bone substitute capable of supplying essential nutrients, cells, and oxygen, as well as facilitating nutrient exchange, to promote vascularisation and innervation upon implantation into a bone defect, both crucial aspects for successful bone repair.<sup>120</sup>

## **2.5 Conclusions**

Low temperature solvent-based 3D printing is a suitable and versatile fabrication technique to create porous and precise scaffolds composed of a new formulation of PLGA/ $\beta$ -TCP  $\pm$  TPU scaffolds for bone tissue engineering. The presented 3D-printed scaffolds not only show superior mechanical properties compared to a commercially available CaP ink, but also show adequate cytocompatibility and osteoconductive properties. The addition of TPU to PLGA/ $\beta$ -TCP changes material properties such as porosity and roughness, which influences the osteogenic outcome. The fabrication tool also shows printing scaffolds with a patient-specific geometry and relevant size, that fits precisely into the defect site, which drives towards personalised oral and cranio-maxillofacial orthopaedics. The future incorporation of vascularised components is of great necessity for the success of such scaffolds. The constant development and continuous increase in the availability of regenerative bone substitutes maximises the possibility to eventually replace the current SOC of ABG. With regards to clinical application, safety and efficacy need to be further tested in a preclinical bone model.

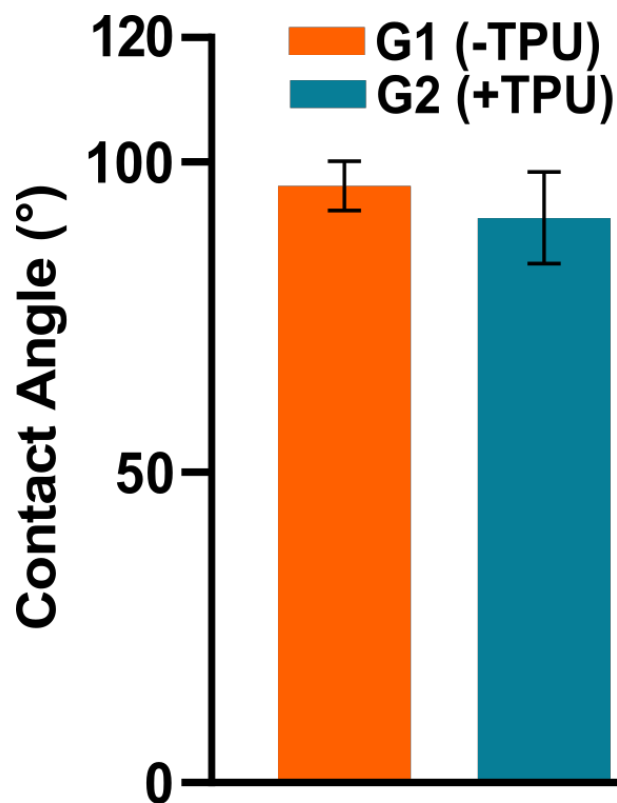
## **2.6 Conflicts of Interest**

There are no conflicts to declare.

## 2.7 Funding

This work was supported by AO CMF and AO Foundation.

## 2.8 Supplementary Materials



Supplementary Figure 2.1: Contact Angle Hydrophilicity Measurement (N=3).

### **3 $\beta$ -TCP from 3D-printed Scaffold can act as an Effective Phosphate Source during the Osteogenic Differentiation of Human Mesenchymal Stromal Cells**

#### **Statement of Significance:**

Phosphate is generally supplemented to osteogenic cultures in the form of exogenous  $\beta$ -glycerophosphate. When calcium-phosphate based materials are used as scaffolds the amount of phosphate can negatively affect mesenchymal stromal cell performance. Consequently, osteogenic differentiation of these cells can be impaired. Within this study, we removed the  $\beta$ -glycerophosphate as part of the osteogenic cocktail and investigated if  $\beta$ -TCP from 3D-printed scaffold alone can act as an effective phosphate source for the osteogenesis of these cells.

Note: This chapter was published in *Frontiers in Cell and Development Biology* as  **$\beta$ -TCP from 3D-printed Scaffold can act as an Effective Phosphate Source during the Osteogenic Differentiation of Human Mesenchymal Stromal Cells**, Luan P. Hatt, Daphne van der Heide, Angela R. Armiento and Martin J. Stoddart

Reprinted with permission<sup>121</sup>. Copyright 2023, Frontiers.

#### Author Contributions:

LPH performed the investigation, methodology, validation, data curation and formal analysis of all the experiments, hence generated all the data in this paper. LPH also wrote the original draft, visualised the data, and created all the figures. DvdH contributed to the paper in terms of assistance in the methodology and editing and reviewing of the writing. ARA contributed to the paper in terms of conceptualisation of the project, co-supervision, validation of the experiments and editing and reviewing of the writing. MJS contributed to the paper in terms of

conceptualisation of the project, supervision, provision of resources, acquisition of, editing and reviewing of the writing and leading project administration. All authors read and approved the final manuscript.



## **Abstract**

Human bone marrow-derived mesenchymal stromal cells (hBM-MSCs) are often combined with calcium phosphate (CaP) - based 3D-printed scaffolds with the goal of creating a bone substitute that can repair segmental bone defects. *In vitro*, the induction of osteogenic differentiation traditionally requires, among other supplements, the addition of  $\beta$ -glycerophosphate (BGP), which acts as a phosphate source. The aim of this study is to investigate whether phosphate contained within the 3D-printed scaffolds can effectively be used as a phosphate source during hBM-MSC *in vitro* osteogenesis. hBM-MSCs are cultured on 3D-printed discs composed of poly(lactic-co-glycolic acid) (PLGA) and  $\beta$ -tricalcium phosphate ( $\beta$ -TCP) for 28 days under osteogenic conditions, with and without the supplementation of BGP. The effects of BGP removal on various cellular parameters, including cell metabolic activity, alkaline phosphatase (ALP) presence and activity, proliferation, osteogenic gene expression, levels of free phosphate in the media and mineralisation, are assessed. The removal of exogenous BGP increases cell metabolic activity, ALP activity, proliferation, and gene expression of matrix-related (*COL1A1*, *IBSP*, *SPP1*), transcriptional (*SP7*, *RUNX2/SOX9*, *PPAR $\gamma$* ) and phosphate-related (*ALPL*, *ENPP1*, *ANKH*, *PHOSPHO1*) markers in a donor dependent manner. BGP removal leads to decreased free phosphate concentration in the media and maintained mineral deposition staining. Our findings demonstrate the detrimental impact of exogenous BGP on hBM-MSCs cultured on a phosphate-based material and propose  $\beta$ -TCP embedded within 3D-printed scaffold as a sufficient phosphate source for hBM-MSCs during osteogenesis. The presented study provides novel insights into the interaction of hBM-MSCs with 3D-printed CaP based materials, an essential aspect for the advancement of bone tissue engineering (BTE) strategies aimed at repairing segmental defects.

### **3.1 Introduction**

Reconstructing large segmental mandibular bone defects using autologous bone grafting (ABG) is met with several disadvantages such as limited availability or donor site morbidities.<sup>122</sup> Tissue engineered bone substitutes have emerged as a promising alternative with the aim to replace ABG as the standard of care (SOC).<sup>4</sup> Human bone marrow-derived mesenchymal stromal cells (hBM-MSCs) are multipotent cells that possess the ability to differentiate into bone forming osteoblasts, making them a promising candidate for the treatment of bone-related conditions.<sup>123</sup> Consequently, osteogenically driven hMSCs are often used in combination with calcium-phosphate (CaP)-based 3D-printed scaffolds to create a bone substitute, offering a solution for bone defect repair.<sup>124-127</sup> The introduction of 3D printing of bone substitutes provided numerous advantages for bone tissue engineering (BTE) such as creating patient-specific scaffolds, tailored design patterns for improved tissue guidance and tuneable porosity to facilitate cell and tissue infiltration. Among the various biomaterials used for scaffold fabrication, composites have attracted significant attention, due to the possibility to combine diverse properties from different materials such as CaP and polymers.<sup>12</sup>  $\beta$ -tricalcium phosphate ( $\beta$ -TCP) is a CaP-based ceramic, that provides osteoconductivity and biodegradability, resembling the mineral phase of natural bone tissue.<sup>128</sup> However, it lacks optimal mechanical stability<sup>129,130</sup>, which can be overcome by incorporating a polymer such as poly(lactic-co-glycolic acid) (PLGA).<sup>131,132</sup>

Before clinical translation of a bone substitute can occur, it is crucial to assess and validate its osteogenic capacity. *In vitro* osteogenesis of MSCs serves as initial step in this validation process.<sup>133</sup> The traditional *in vitro* induction of osteogenesis requires medium supplementation with a differentiation cocktail that includes dexamethasone (dexa), ascorbic acid and organic  $\beta$ -glycerophosphate (BGP)<sup>44</sup>. This osteogenic cocktail induces cell morphology changes, increases

alkaline phosphatase (ALP) activity, the expression of osteogenic gene markers and secretion of matrix minerals.<sup>38,134</sup> BGP acts as a phosphate source to be cleaved by MSCs resulting in the release of phosphate ions needed for the cells to produce and secrete HAp.<sup>134-137</sup> However, high phosphate levels are known to have toxic effects in several cell types including embryonic kidney (HEK) 293<sup>138</sup>, epithelial HeLa<sup>138</sup> and EA hy926 endothelial cells<sup>139</sup>. Hyperphosphatemia causes vascular calcification of vascular smooth muscle cells, which is associated with cardiovascular diseases<sup>140</sup>, as well as metabolic bone diseases.<sup>141,142</sup> MSCs are sensitive to exogenous phosphate ions and optimal phosphate levels are known to be important for osteoblast differentiation.<sup>143,144</sup> BM-MSc proliferation and differentiation is decreased with greater or lower concentration of inorganic phosphate supplementation, with greater concentrations leading to cell apoptosis.<sup>144</sup> The cellular and molecular mechanism, by which elevated phosphate alters cell behavior, remains unclear.<sup>145</sup> Therefore, caution must be taken when using exogenous BGP in medium supplementation.

Replacing BGP with inorganic phosphate as an alternative phosphate source has been shown to stabilise free phosphate levels in the culture medium, to improve the quality of HAp secreted by MSCs<sup>146</sup> and to enhance the mineral deposition outcome.<sup>77</sup> Osteogenic differentiation of MSCs cultured on a 3D-printed phosphate-based scaffold using BGP as the phosphate source has been investigated in several studies: adipose-derived MSCs cultured on 3D-printed PLGA/TCP<sup>127</sup> scaffold, polycaprolactone/hydroxyapatite (PCL/HAp) scaffold<sup>147-149</sup> or PCL/TCP<sup>149</sup> scaffold, as well as BM-MSCs cultured on 3D-printed PLGA/CaP cement scaffold<sup>150</sup>,  $\beta$ -TCP scaffold<sup>151,152</sup> or polylactic acid/HAp scaffold<sup>57</sup>. However, the ability of MSCs to use inorganic phosphate contained within the 3D-printed scaffolds during *in vitro* osteogenesis is poorly understood. Hence, this study aims to investigate the potential of  $\beta$ -TCP embedded within 3D-printed PLGA/ $\beta$ -TCP scaffolds to serve as an effective phosphate source during the osteogenic differentiation of hBM-MSCs. Through systematic osteogenic *in*

*in vitro* experiments, we evaluate the proliferation and osteogenic differentiation by examining key osteogenic markers of hBM-MSCs cultured on 3D-printed PLGA/ $\beta$ -TCP discs. Understanding the underlying interactions between bone substitutes and MSC behaviour is essential for the advancement of BTE strategies aimed at repairing bone defects.

## **3.2 Material and Methods**

Human bone marrow aspirates are obtained with informed consent of all donors and with full approval from the Ethics Committee of the University of Freiburg Medical Centre (EK-Freiburg: 135/14, 25 March 2014) and the ethical commission of Zürich (KEK-ZH-NR: 2016-00141). All reagents are purchased from Sigma-Aldrich unless otherwise stated. An overview of the methods is reported in **Figure 3.1**.

## $\beta$ -TCP from 3D-printed Scaffold can act as an Effective Phosphate Source during the Osteogenic Differentiation of Human Mesenchymal Stromal Cells

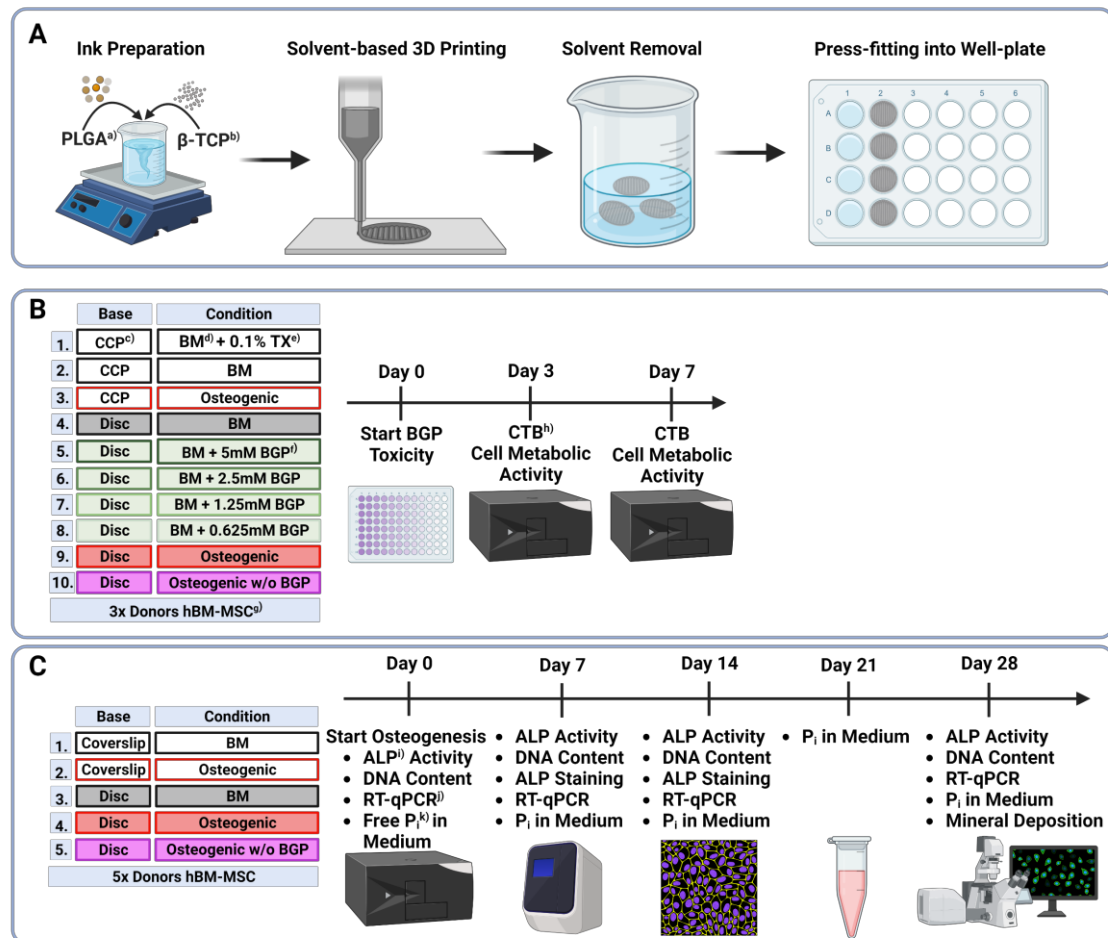


**Figure 3.1: Methodical Overview of** A) Preparation, solvent-based 3D printing and postprocessing of PLGA/ $\beta$ -TCP discs, B) Groups and timeline of  $\beta$ -glycerophosphate (BGP) cytotoxicity assessment of hBM-MSCs cultured on either culture-plate plastic or 3D-printed PLGA/ $\beta$ -TCP discs for 7 days under different condition measured using the CellTiter-Blue® Cell Viability Assay and C) Groups and timeline of osteogenic differentiation assessment of hBM-MSCs cultured on either coverslips or 3D-printed discs for 28 days under different conditions measuring ALP Activity, DNA content, ALP staining, gene expression via RT-qPCR, free phosphate concentration in the medium and mineral deposition via OsteoImage® staining. <sup>a)</sup>PLGA = as poly(lactic-co-glycolic acid), <sup>b)</sup> $\beta$ -TCP =  $\beta$ -tricalcium phosphate, <sup>c)</sup>CCP = cell-culture plastic, <sup>d)</sup>BM = basal medium, <sup>e)</sup>TX = Triton X-100, <sup>f)</sup>BGP =  $\beta$ -glycerophosphate, <sup>g)</sup>hBM-MSCs = human bone marrow-derived mesenchymal stromal cells, <sup>h)</sup>CTB = CellTiter-Blue®, <sup>i)</sup>ALP = alkaline phosphatase, <sup>j)</sup>RT-qPCR = reverse transcription-quantitative polymerase chain reaction, <sup>k)</sup>P<sub>i</sub> = phosphate. Created with BioRender.com.

### ***Preparation, Solvent-based Printing and Postprocessing of PLGA/ $\beta$ -TCP Discs***

PLGA (PURASORB® PLG 8531, 85/15 L-lactic/Glycolide, Corbion) powder is dissolved in EC at 90°C using a hot plate stirrer and a Hei-TORQUE Expert 200 (Heidolph Instruments) mixing system set to 30 rpm. Subsequently, the system is cooled to 80°C,  $\beta$ -TCP powder (BABI-TCP-N100, Berkeley Advanced Biomaterials) is added, and the blend stirred overnight. The ink is transferred to 3 cc syringe barrels (Nordson EFD) and kept at -20°C until printing. Low-temperature solvent-based 3D printing is applied to the ink-laden cartridges equipped with a 0.5 mm stainless steel needle using a 3D Discovery® bioprinter (RegenHU). The ink is extruded onto a dry glass slide which is mounted onto an aluminium cool plate according to printing parameters shown in **Table 3.1**. Dense 3D-printed discs with a total height of 0.8 mm (2 layers) and a diameter of 19 mm are printed. Subsequently, discs are placed in a vacuum oven at room temperature for 24 hours and then in a water bath at 37°C for 48 hours (4x Milli-Q® water changes) to extract the solvent. Total solvent extraction is confirmed via 1H nuclear magnetic resonance. Upon air drying at room temperature, discs are sterilised using a cold ethylene oxide gas protocol, degassed under vacuum, and cut using a 13 mm or 7.5 mm diameter puncher to be press-fit into a 24 cell-culture plate or a 96 well-plate, respectively. All steps are presented in **Figure 3.1A**.

**Table 3.1. Solvent-based printing parameters**

Cartridge Heater	Pressure	Velocity	Layer Height	Cool Plate
80°C	3.5 – 4 bar	4 mm/s	0.4 mm	3 -10°C

### ***Cell Isolation and Culture of hBM-MSCs***

Isolation and cryopreservation of hBM-MSCs from bone marrow aspirates are conducted following published protocols.<sup>153</sup> Cell culture expansion was performed following the protocols as previously described.<sup>77</sup> In short, upon

thawing,  $0.9 \times 10^6$  cells are seeded in a T300 flask (cell density  $3 \times 10^3$  cells/cm<sup>2</sup>) for culture expansion. The expansion medium consists of  $\alpha$ -MEM (Gibco) supplemented with 10% (v/v) foetal bovine serum (FBS) (Corning) and 100 U/mL Penicillin, 100  $\mu$ g/mL Streptomycin (PEN/STREP) (Gibco). Cells are cultured under standard cell culture conditions of 37°C with 5% CO<sub>2</sub> and 90% humidity with 3 media changes per week before they are used for the BGP cytotoxicity assessment (**Figure 3.1B**) or osteogenic differentiation experiment (**Figure 3.1C**). hBM-MSCs donor details are as follows: Donor A, 24-year old male, iliac crest, Donor B, 73-year old female, spine vertebral body; Donor C, 54-year old male, hip cancellous bone; Donor D, 48-year old female, spine vertebral body, Donor E, 61-year old female, hip cancellous bone; Donor F, 51-year old female, spine vertebral body; Donor G, 74-year old female spine vertebral body; Donor H, 71-year old female, spine vertebral body.

#### ***Cytotoxicity of BGP on hBM-MSCs via CellTiter-Blue® Assessment***

Cytotoxicity of BGP on hBM-MSCs when seeded on either cell-culture plastic (CCP) or 3D-printed PLGA/ $\beta$ -TCP discs that are press fitted into well plates is carried out using the CellTiter-Blue® (CTB) Cell Viability Assay (Promega) performed according to the company's instructions (**Figure 3.1B**). Cells are harvested using 0.05% Trypsin-EDTA (Gibco) and seeded in 96-well plates at a density of  $1 \times 10^4$  cells/well in 4 replicates. For the first 24 h, cells are cultured in basal medium (BM) (LG-DMEM (Gibco) supplemented with 10% (v/v) FBS and 1% (v/v) PEN/STREP. At this point (Day 0), cells are switched into their corresponding culture media: cells cultured on CCP 1) Positive control: BM supplemented with 0.1% Triton X-100; 2) Negative control: BM; 3) Osteogenic: BM supplemented with 10 nM dexamethasone (dexa), 5 mM BGP and 50  $\mu$ g/mL L-ascorbic acid-2-phosphate; cells cultured on discs: 4) BM; 5) BM supplemented with 5 mM BGP; 6) 2.5 mM BGP; 7) 1.25 mM BGP; 8) 0.625 mM BGP; 9) Osteogenic and 10) Osteogenic w/o BGP: BM supplemented with 10 nM dexa

and 50  $\mu$ g/mL L-ascorbic acid-2-phosphate. Cell metabolic activity measurement is performed at day 3 and day 7. Media are removed and BM supplemented with 16.6% (v/v) CTB reagent is added. After 4 hours of incubation at 37°C with 5% CO<sub>2</sub> and 90% humidity the supernatant is transferred into a 96 clear bottom well-plate (Corning) and fluorescence is read at 560/590 nm using Infinite® 200 PRO plate reader (Tecan Trading AG).

### ***Osteogenic Differentiation of hBM-MSCs***

hBM-MSCs are harvested using 0.05% Trypsin-EDTA and seeded at a density of  $28.5 \times 10^3$  cells/well ( $15 \times 10^3$  cells/cm<sup>2</sup>) in duplicates onto either coverslips (SARSTEDT AG) or PLGA/ $\beta$ -TCP 3D-printed discs that are press fitted into a 24-well plate (**Figure 3.1C**). Media compositions are presented in **Table 3.2**. For the first 24 hours, cells are cultured in BM and subsequently switched into their corresponding media. The experiment is performed under 5 different conditions: 1) coverslip BM; 2) coverslip osteogenic; 3) disc BM; 4) disc osteogenic and 5) disc osteogenic without BGP for 28 days under standard culture conditions.

**Table 3.2. Media composition**

	Basal Medium	Osteogenic	Osteogenic w/o BGP
LG-DMEM	+	+	+
PEN/STREP	+	+	+
FBS	+	+	+
Dexa	-	+	+
AA2P	-	+	+
BGP	-	+	-

LG-DMEM: low glucose (1 g/L) DMEM, PEN/STREP: Penicillin/Streptomycin, FBS: fetal bovine serum, Dexa: dexamethasone, AA2P: L-ascorbic acid 2-phosphate sesquimagnesium salt hydrate, BGP:  $\beta$ -Glycerophosphate disodium salt hydrate

### ***Quantification of ALP Activity and DNA Content***

At day 0, 7, 14 and 28, ALP activity and DNA content are measured as previously described<sup>77</sup> (**Figure 3.1C**). In short, after cell lysis with 0.1% Triton X-100 in 10



mM TrisHCl, the enzymatic reaction is started by adding alkaline buffer solution, substrate solution (25 mg/mL phosphate substrate in 1 mM diethanolamine) and Milli-Q® water and stopped by adding 0.1 M NaOH solution after 15 minutes at 37°C. The absorbance is read at 405 nm using the Infinite® 200 PRO plate reader. ALP activity is normalised to the DNA content. DNA concentration is quantified at day 0, 7, 14 and 28 using the CyQuant™ Cell Proliferation Assay (Invitrogen) according to the manufacturer's instructions. Cell lysate is transferred into a 96 clear bottom well plate, working solution containing dye is added, incubated for 5 minutes and fluorescence is read at 490/530 nm using Infinite® 200 PRO plate reader.

### ***ALP Staining***

At day 7 and 14 ALP is stained using the alkaline phosphatase staining kit (Procedure No. 85) according to the company's instructions (**Figure 3.1C**). In short, cells are washed 3x with phosphate buffered saline (PBS), fixed with 10% neutral buffered formalin for 30 minutes and, after 3x Milli-Q® water rinses, stained with the alkaline dye solution for 30 minutes at room temperature. 50 mL alkaline dye solution is composed of one Fast Blue RR Salt capsule and 2 mL Naphthol AS-MX Phosphate Alkaline solution. Upon water rinsing the samples are imaged.

### ***RNA Isolation and Reverse Transcription-quantitative Polymerase Chain Reaction (RT-qPCR)***

Cells are harvested for gene expression analysis at day 0, 7, 14 and 28. RNA isolation and RT-qPCR is performed using the QuantStudio™ Flex Real-Time PCR System as previously described<sup>77</sup> (**Figure 3.1C**). Reverse transcription is performed using the Superscript Vilo cDNA Synthesis Kit (Thermo Fisher Scientific) according to the company's instructions. *ALPL* (encodes for ALP), *ANKH* (encodes for progressive ankylosis protein homolog), *COL1A1* (encodes

## **$\beta$ -TCP from 3D-printed Scaffold can act as an Effective Phosphate Source during the Osteogenic Differentiation of Human Mesenchymal Stromal Cells**

for alpha-1 type 1 collagen), *ENPP1* (encodes for ectonucleotide pyrophosphatase/phosphodiesterase family member 1), *IBSP* (encodes for bone sialoprotein), *PHOSPHO1* (encodes for phosphoethanolamine/phosphocholine phosphatase 1), *PPAR $\gamma$*  (encodes for peroxisome proliferator- activated receptor gamma), *RUNX2* (encodes for runt-related transcription factor 2), *SP7* (encodes osterix), *SPP1* (encodes osteopontin) and *SOX9* (encodes for SRY-box transcription factor 9) gene expressions are investigated. Primer sequences used are listed in **Table 3.3**. The  $2^{-\Delta\Delta C_t}$  method is applied for data analysis using *RPLP0* as an endogenous normaliser and day 0 samples as a calibrator.

**Table 3.3. Primers/probes used for RT-qPCR**

Gene	Assay on Demand <sup>1</sup>		
<i>ALPL</i>	<i>Hs00758162_m1</i>		
<i>ANKH</i>	<i>Hs01064613_m1</i>		
<i>ENPP1</i>	<i>Hs01054040_m1</i>		
<i>IBSP</i>	<i>Hs00173720_m1</i>		
<i>PHOSPHO1</i>	<i>Hs01370290_m1</i>		
<i>PPAR<math>\gamma</math></i>	<i>Hs00234592_m1</i>		
<i>SP7</i>	<i>Hs00541729_m1</i>		
<i>SPP1</i>	<i>Hs00959010_m1</i>		
<i>SOX9</i>	<i>Hs00165814_m1</i>		
Gene	Forward	Reverse	Probe
<i>COL1A1</i>	5'-CCC TGG AAA GAA TGG AGA TGA T-3'	5'-ACT GAA ACC TCT GTG TCC CTT CA-3'	5'-CGG GCA ATC CTC GAG CAC CCT-3'
<i>RPLP0</i>	5'-TGG GCA AGA ACA CCA TGA TG-3'	5'-CGG ATA TGA GGC AGC AGT TTC-3'	5'-AGG GCA CCT GGA AAA CAA CCC AGC-3'
<i>RUNX2</i>	5'-AGC AAG GTT CAA CGA TCT GAG AT-3'	5'-TTT GTG AAG ACG GTT ATG GTC AA-3'	5'-TGA AAC TCT TGC CTC GTC CAC TCC G-3'

*ALPL*: Alkaline phosphatase, biomineralisation associated; *IBSP*: integrin binding sialoprotein; *SP7*: Sp7 transcription factor; *RPLP0*: ribosomal protein lateral stalk subunit P0; *SPP1*: osteopontin, organic component of bone matrix. <sup>1</sup>TaqMan® Gene Expression Assay (Applied Biosystems®).

### **Free Phosphate Quantification**

Levels of free phosphate are assessed in conditioned media once per week (**Figure 3.1C**) using the Qumaticrome Phosphate Assay Kit (DPI-500, BioAssay Systems) according to the company's instructions. Conditioned media are collected at day 0, 7, 14, 21 and 28 and stored at  $-20^{\circ}\text{C}$  prior to analysis.

### ***Staining of Mineral Deposition***

At day 28, cells are washed 3x with PBS, fixed with 10% neutral buffered formalin for 30 minutes, rinsed 3x with Milli-Q® water, permeabilised with 0.25% Triton X-100 in Milli-Q® water for 20 minutes and stained with 2  $\mu\text{g}/\text{mL}$  4',6-Diamidino-2-phenylindole solution for 10 minutes with a Milli-Q® water wash in between each step (**Figure 3.1C**). Mineral deposition is stained with OsteoImage™ Mineralization Assay (Lonza) according to the manufacturer's instructions and imaging is performed using a confocal microscope (LSM800, Leica Microsystems).

### ***Statistics***

Statistical analyse is performed using GraphPad Prism software version 9.3.1 (GraphPad Software). A One-Way ANOVA is applied to the data of the cell metabolic activity. A Two-Way ANOVA is applied to the data of the ALP activity, DNA quantification, gene expression and free phosphate quantification. P-values lower than 0.05 are considered significant and thus marked.

## **3.3 Results**

### ***Exogenous BGP decreases Cell Metabolic Activity of hBM-MSCs Cultured on 3D-printed PLGA/ $\beta$ -TCP Discs in a Dose-responsive Manner***

hBM-MSCs of three independent donors cultured on either culture-plate plastic or 3D-printed PLGA/ $\beta$ -TCP discs for 7 days under either BM, BM with different concentrations of BGP or osteogenic medium with and without the standard

concentration of 5 mM BGP (Figure 3.2). Cell metabolic activity measurements reveal a decrease of approximately 13% and 25% on day 3 and 7, respectively, in BM supplemented with 5mM BGP compared to the corresponding BM set to 100%. A trend of dose-responsive increase of cell activity is measured when BGP concentrations are decreased from 5 mM to 0.625 mM. Cell metabolic activity of cells cultured under osteogenic condition without BGP supplementation is significantly increased compared to all BM groups supplemented with BGP at day 3 and 7 and insignificantly increased compared to the osteogenic group.

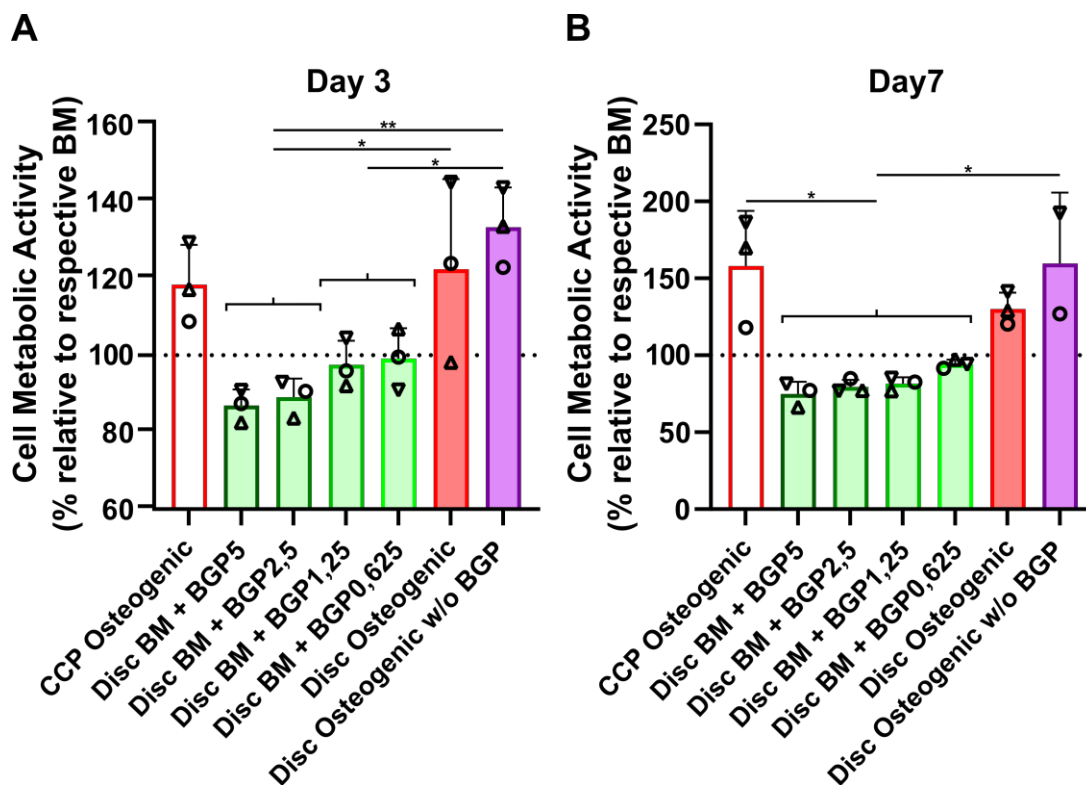


**Figure 3.2: Cytotoxicity of  $\beta$ -glycerophosphate (BGP) on hBM-MSC cultured either on cell-culture plastic (CCP) or 3D-printed PLGA/ $\beta$ -TCP discs of three independent donors (N=3). Individual data points shown are the mean of three technical replicates for each individual donor: donor A ( $\circ$ ), donor B ( $\Delta$ ), donor C ( $\nabla$ ). Cells are cultured in basal medium (BM), BM supplemented with 5 mM, 2,5 mM, 1,25 mM or 0,625 mM of BGP, osteogenic medium or osteogenic medium without BGP for 7 days. Cell metabolic activity is measured at A) day 3 and B) day 7 using the CellTiter-Blue® Cell Activity Assay with the corresponding BM as normaliser. One-way ANOVA is performed: \* $p < 0.5$ , \*\* $p < 0.01$ .**

BM supplementation with exogenous BGP decreases cell activity of hBM-MSCs when cultured on 3D-printed PLGA/ $\beta$ -TCP discs in a dose-responsive manner and results in cytotoxic-like consequences.

***Absence of Exogenous BGP Increases Presence and Activity of ALP and Proliferation of hBM-MSCs Cultured on 3D-printed PLGA/ $\beta$ -TCP Discs under Osteogenic Conditions***

The ALP activity measurement normalised to DNA content, shows a trend of mean upregulation of osteogenically driven cells cultured on the 3D-printed discs at day 14 and no difference at day 7 and 28 (**Figure 3.3A**). The removal of BGP from the osteogenic medium slightly increases the trend of mean ALP activity at day 7 and more profoundly at day 14 and 28 compared to the osteogenic group. ALP activity seems to be delayed of osteogenically driven cells cultured on the disc to day 28, while cells cultured on coverslips peak at day 14. ALP staining confirms the protein expression at day 7 and 14 shown by two representative donors (donor D and H). Cells cultured on 3D-printed discs visibly show increased stained area of ALP at day 7 and 14 in the osteogenic group compared to the BM group (**Figure 3.3B**). The removal of BGP even further enhances ALP staining at day 7 and 14 in donor H and maintains the stained area for donor D compared to the osteogenic group. The degree of ALP staining is in accordance with the protein expression for each donor from the ALP activity profile. Osteogenic treatment increases the trend of mean proliferation of the cells at all time points when cultured on coverslips or 3D-printed discs (**Figure 3.3C**). The subtraction of BGP further increases the proliferation compared to the osteogenic group.

The absence of exogenous BGP leads to an overall increase in ALP activity and staining, as well as enhanced proliferation of hBM-MSCs cultured on 3D-printed PLGA/ $\beta$ -TCP discs.

## $\beta$ -TCP from 3D-printed Scaffold can act as an Effective Phosphate Source during the Osteogenic Differentiation of Human Mesenchymal Stromal Cells

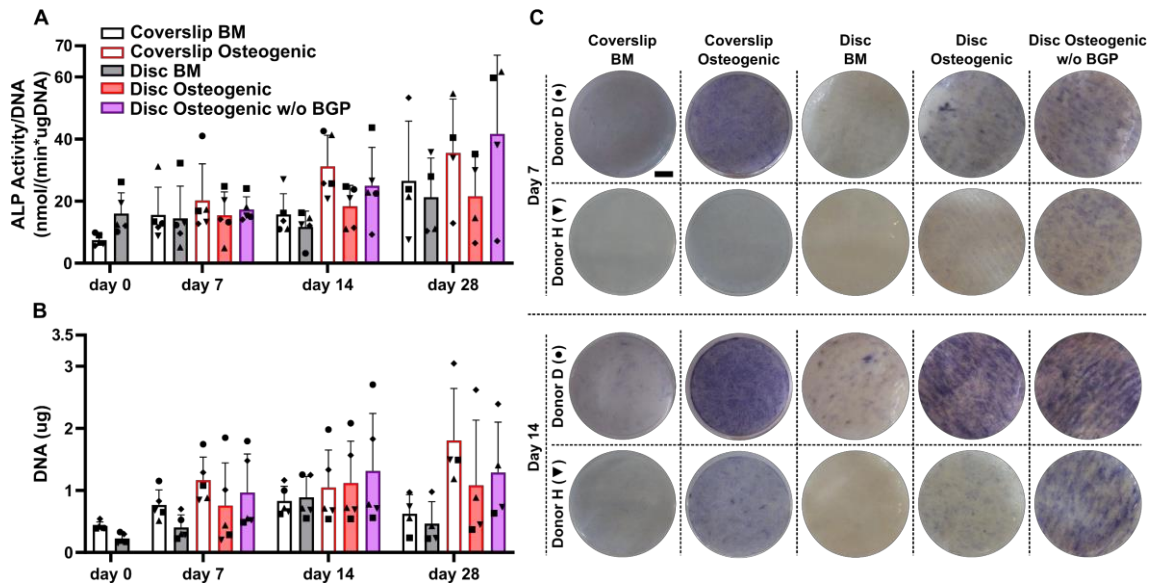


**Figure 3.3: Alkaline phosphatase (ALP) and proliferation assessment** of hBM-MSC cultured either on coverslips or 3D-printed PLGA/ $\beta$ -TCP discs of five independent donors (N=5). Individual data points shown are the mean of two technical replicates for each individual donor: donor D (●), donor E (▲), donor F (◆), donor G (■) and donor H (▼). Cells are cultured in basal medium (BM), osteogenic medium or osteogenic medium without  $\beta$ -glycerophosphate (BGP) for 28 days. A) ALP activity normalised to DNA content at day 0, 7, 14 and 28; B) Images of ALP staining of two representative donors: donor D (●) and donor H (▼) at day 7 and 14, scale bar 2,5 mm; C) DNA content at day 0, 7, 14 and 28.

### ***Absence of Exogenous BGP Upregulates or Maintains Gene Expression of Osteogenic Markers Involved in Matrix Production of hBM-MSCs Cultured on 3D-printed PLGA/ $\beta$ -TCP Discs under Osteogenic Conditions***

*COL1A1*, which encodes for alpha-1 type 1 collagen, an organic protein necessary for the formation bone tissue, is an important early osteogenic marker for matrix production of osteogenically driven hBM-MSCs. The fold change gene expression, relative to the corresponding day 0 BM of five independent donors cultured on 3D-printed discs under standard osteogenic conditions, is downregulated compared to the BM groups for all time points (**Figure 3.4A**). The subtraction of BGP causes the expression of *COL1A1* to rise compared to the osteogenic medium with statistical significance at day 14 from  $0.6 \pm 0.46$  to 1.56

$\pm 0.53$  ( $p = 0.39$ ) and without statistical significance at day 7 and 28. Applying the standard osteogenic cocktail to the cells slightly decreases the trend of mean fold change of *IBSP* gene expression, the bone sialoprotein encoding gene, a late stage osteoblast differentiation marker for matrix production at day 7, but increases at day 14 and 28 (**Figure 3.4B**). The removal of BGP upregulates the mean fold change gene expression of *IBSP* at day 7 and maintains it at day 14 and 18 and compared to the osteogenic group. The fold change of *SPP1*, the osteopontin encoding gene, a late osteogenic marker involved in matrix regulation, is significantly downregulated in the osteogenic group at day 7 compared to the BM from  $1.16 \pm 0.53$  to  $0.21 \pm 0.11$  ( $p = 0.0311$ ), which recovers over time and the trend increases at day 28 (**Figure 3.4C**). The subtraction of BGP increases the *SPP1* fold change expression trend at day 7, 14 and 28 compared to the osteogenic medium.

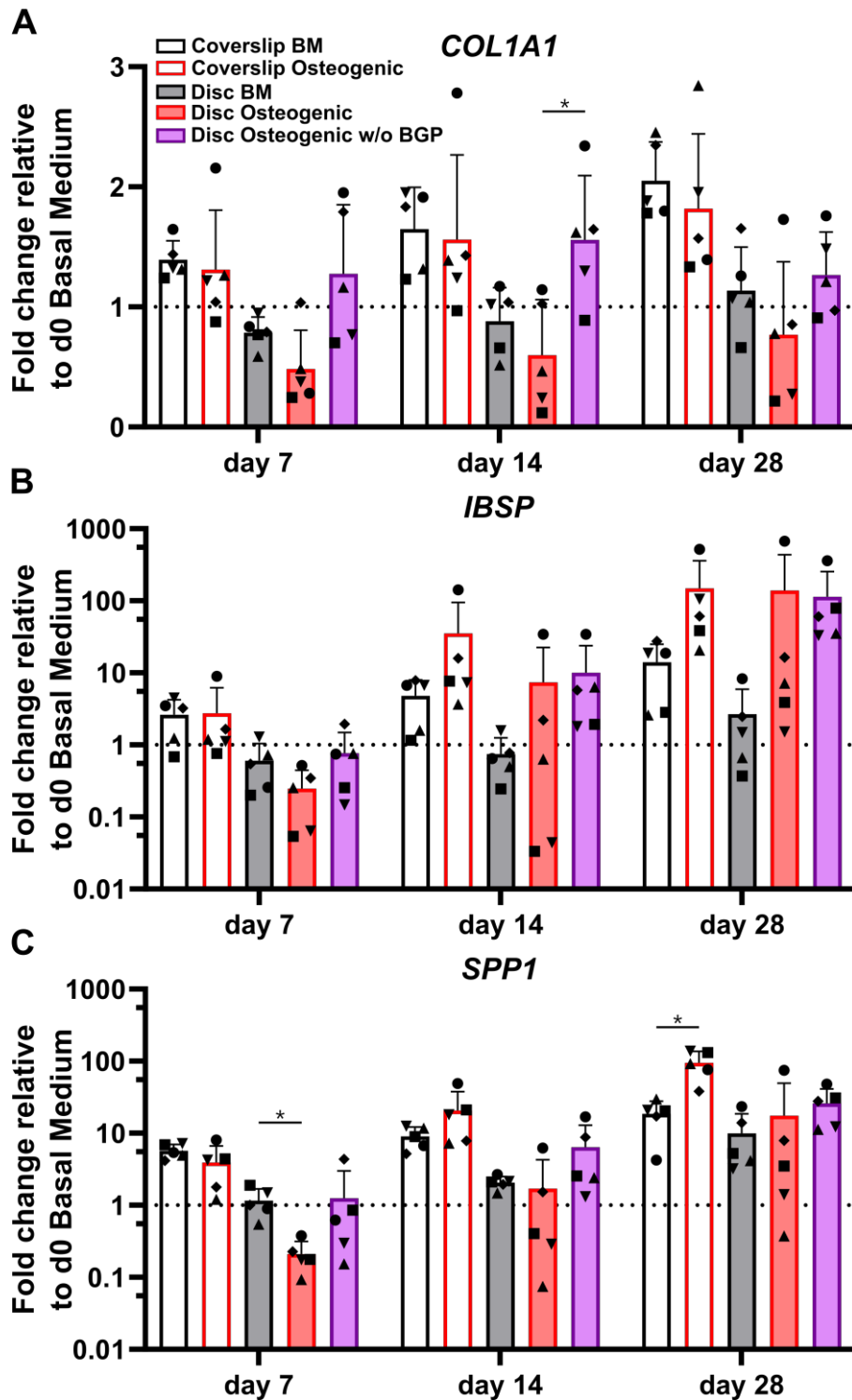


Figure 3.4: Gene expression of osteogenic markers involved in matrix production of hBM-MSC cultured either on coverslips or 3D-printed PLGA/ $\beta$ -TCP discs of five independent donors



(N=5). Individual data points shown are the mean of two technical replicates for each individual donor: donor D (●), donor E (▲), donor F (◆), donor G (■) and donor H (▼). Cells are cultured in basal medium (BM), osteogenic medium or osteogenic medium without  $\beta$ -glycerophosphate (BGP) for 28 days. Fold changes in A) *Col1A1*, B) *IBSP* and C) *SPP1* expression at day 7, 14 and 28 are calculated according to the  $2^{-\Delta\Delta Ct}$  method using *RPLP0* as the endogenous calibrator and the corresponding day 0 BM the normaliser. Two-way ANOVA is performed: \*p < 0.05.

The absence of exogenous BGP leads to an overall trend of upregulated gene expression levels relevant to matrix production of hBM-MSCs cultured on 3D-printed PLGA/ $\beta$ -TCP discs.

***Absence of Exogenous BGP Upregulates or Maintains Gene Expression of Transcription Factors Involved in the Differentiation of hBM-MSCs Cultured on 3D-printed PLGA/ $\beta$ -TCP Discs under Osteogenic Conditions***

*SP7*, the osterix encoding gene, is an important transcription factor and driver of MSCs differentiation into osteoblasts and therefore used as an osteogenic marker for hBM-MSC osteogenesis. The *SP7* fold change gene expression trend of cells cultured on 3D-printed discs show a positive response under osteogenic treatment compared to BM (**Figure 3.5A**). The removal of BGP further enhances the *SP7* fold change expression trend at day 7, 14 and 28 compared to the osteogenic medium. The ratio between *RUNX2* and *SOX9* transcription factors is relevant for MSC osteogenesis and chondrogenesis, respectively and therefore also used as an osteogenic predictor for the differentiation of hBM-MSCs. Osteogenically driven cells show an increased trend of fold change ratio compared to BM, which is maintained when the BGP is subtracted from the osteogenic medium (**Figure 3.5B**). *PPAR $\gamma$*  is a transcription factor that drives MSC adipogenesis, the third possible lineage of MSCs differentiation.<sup>154</sup> Cells cultured under osteogenic conditions with or without the supplementation of BGP show a significant upregulation of the fold change expression of *PPAR $\gamma$*  compared to BM from  $0.91 \pm 0.089$  to  $3 \pm 0.65$  or  $4.41 \pm 1.23$ , respectively (p = 0.004, p = 0.0068, respectively) at day 7 and from  $0.96 \pm 0.27$  to  $3.96 \pm 1.1$  or

$3.77 \pm 1.52$ , respectively ( $p = 0.0114$ ,  $p = 0.0292$ , respectively) at day 14, while the change at day 28 is only significant for the osteogenic group without BGP from  $0.86 \pm 0.2$  to  $3.68 \pm 1.46$  ( $p = 0.0262$ ) (**Figure 3.5C**). The removal of BGP leads to increased trend of expression levels of *PPAR $\gamma$*  compared to the osteogenic group at day 7, maintained at day 14 and decreased at day 28.

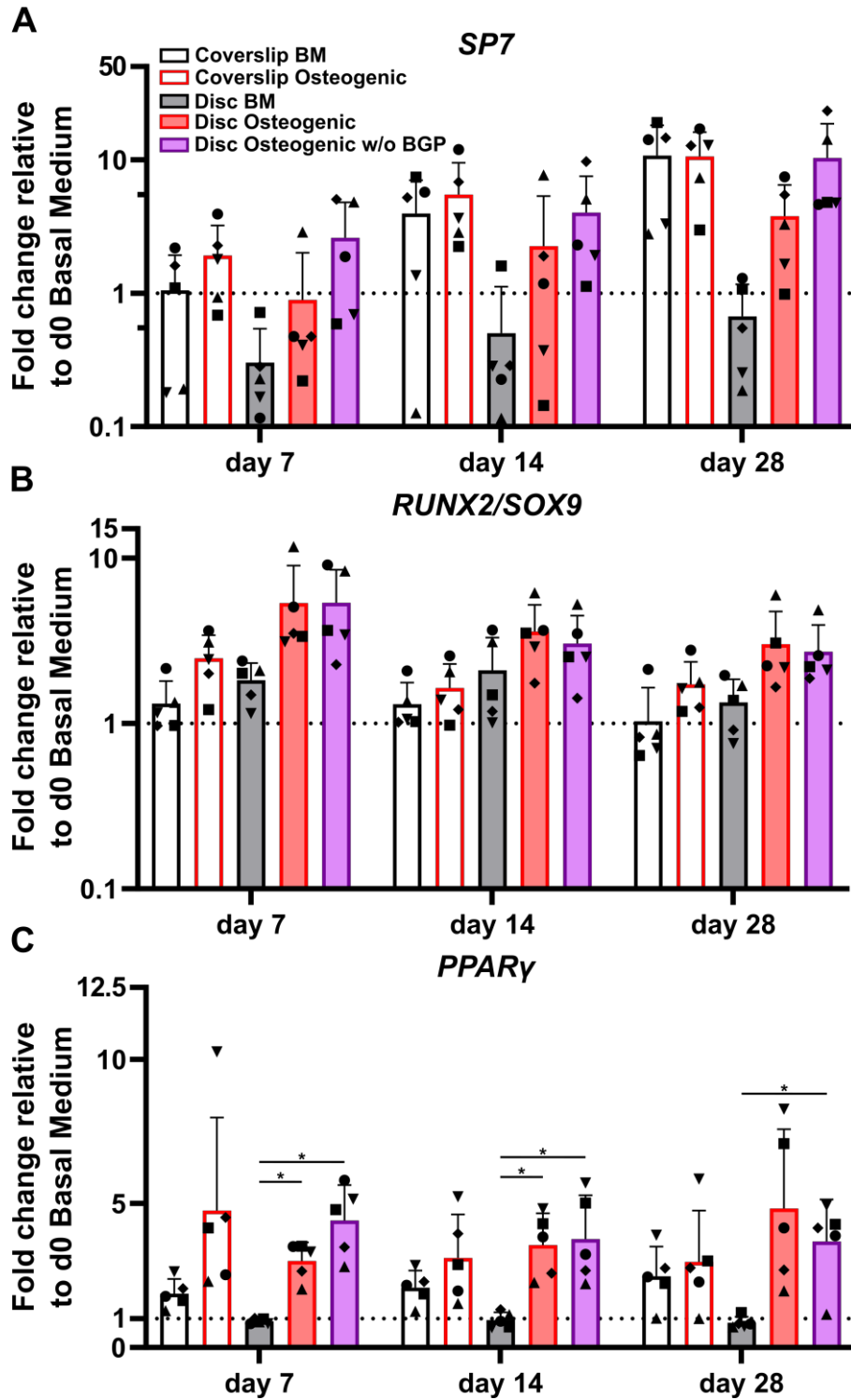


Figure 3.5: Gene expression of transcription factors involved in MSC differentiation fate of hBM-MSC cultured either on coverslips or 3D-printed PLGA/ $\beta$ -TCP discs of five independent

donors (N=5). Individual data points shown are the mean of two technical replicates for each individual donor: donor D (●), donor E (▲), donor F (◆), donor G (■) and donor H (▼). Cells are cultured in basal medium (BM), osteogenic medium or osteogenic medium without  $\beta$ -glycerophosphate (BGP) for 28 days. Fold changes in A) *SP7*, B) *RUNX2/SOX9* ratio and C) *PPAR $\gamma$*  expression at day 7, 14 and 28 are calculated according to the  $2^{-\Delta\Delta C_t}$  method using *RPLP0* as the endogenous calibrator and the corresponding day 0 BM the normaliser. Two-way ANOVA is performed: \*p < 0.5, \*\* p < 0.01.

The absence of exogenous BGP leads to an overall maintenance or upregulation of genes involved in the differentiation pathways of hBM-MSCs cultured on 3D-printed PLGA/ $\beta$ -TCP discs.

***Absence of Exogenous BGP Upregulates and Recovers Gene Expression of Phosphate Relevant Markers of hBM-MSCs Cultured on 3D-printed PLGA/ $\beta$ -TCP Discs under Osteogenic Conditions***

The *ALPL*, *ENPP1*, *ANKH* and *PHOSPHO1* genes are related to phosphate cleavage and regulation during mineralisation of the extracellular matrix. The *ALPL* fold change expression cultured on 3D-printed discs under standard osteogenic condition shows a significant increase compared to BM from 0.26 to 1.34 at day 7 (p = 0.0313), from 0.14 to 1.98 at day 14 (p = 0.0195) and from 0.3 to 2.01 at day 28 (p = 0.0073) (**Figure 3.6A**). The subtraction of BGP leads to a slight trend of upregulation at day 7 and 28 and maintenance at day 14 compared to the osteogenic group. The fold change expression trend of *ENPP1* is downregulated in osteogenically driven cells for all time points compared to BM (**Figure 3.6B**). The subtraction of BGP recovers the downregulated trend of the osteogenic group to similar levels as the BM for all time points. The *ANKH* and *PHOSPHO1* genes share the same expression profile pattern, which is also similar to the *ENPP1* gene expression profile. Osteogenically driven cells show a downregulated trend for all time points compared to BM (**Figure 3.6C/D**). The subtraction of BGP recovers the downregulation of the osteogenic group to

similar levels as the BM only at day 28 and remains downregulated at day 7 and 14.

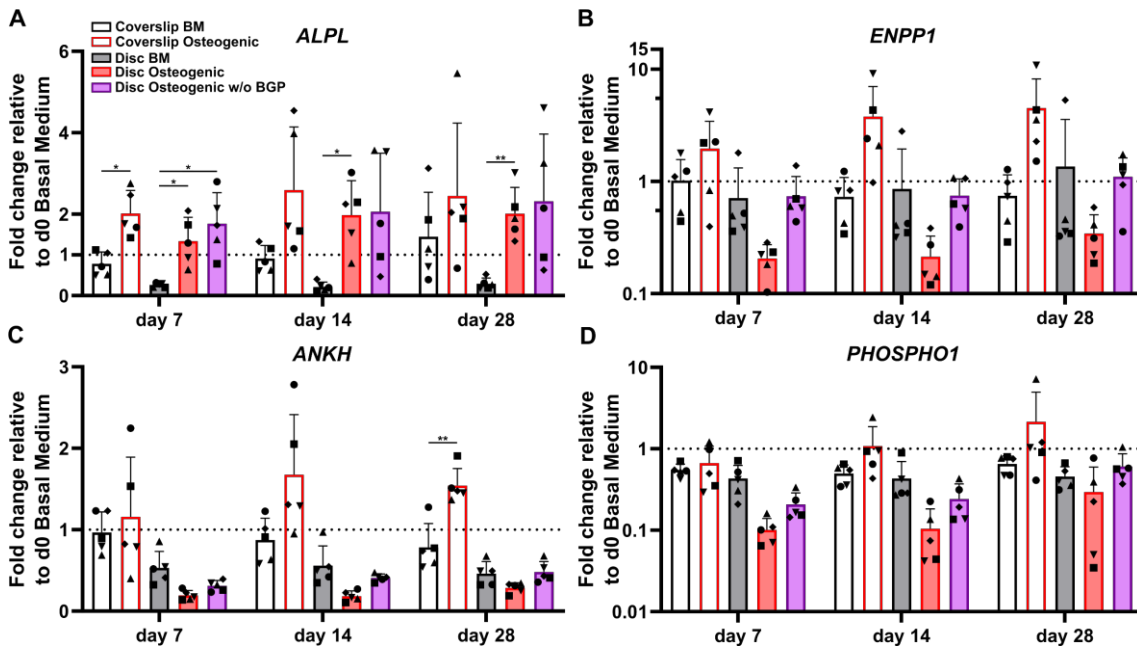


**Figure 3.6: Gene expression of phosphate-related markers** of hBM-MSC cultured either on coverslips or 3D-printed PLGA/ $\beta$ -TCP discs of five independent donors (N=5). Individual data points shown are the mean of two technical replicates for each individual donor: donor D ( $\bullet$ ), donor E ( $\blacktriangle$ ), donor F ( $\blacklozenge$ ), donor G ( $\blacksquare$ ) and donor H ( $\blacktriangledown$ ). Cells are cultured in basal medium (BM), osteogenic medium or osteogenic medium without  $\beta$ -glycerophosphate (BGP) for 28 days. Fold changes in A) *ALPL*, B) *ENPP1* C) *ANKH* and D) *PHOSHO1* expression at day 7, 14 and 28 are calculated according to the  $2^{-\Delta\Delta C_t}$  method using *RPLP0* as the endogenous calibrator and the corresponding day 0 BM the normaliser. Two-way ANOVA is performed: \*p < 0.5, \*\* p < 0.01.

The absence of exogenous BGP leads to an overall trend of upregulation of *ALPL*, *ENPP1*, *ANKH* and *PHOSHO1* compared to the osteogenic group levels of hBM-MSCs cultured on 3D-printed PLGA/ $\beta$ -TCP discs and gene expression recovery close to BM levels in *ENPP1*, *ANKH* and *PHOSHO1* gene expression.

***Absence of Exogenous BGP Decreases Free Phosphate Concentration in the Conditioned Media of hBM-MSCs Cultured on 3D-printed PLGA/ $\beta$ -TCP Discs under Osteogenic Conditions***

The measurement of free phosphate concentration in the conditioned media of hBM-MSCs of five independent donors cultured on 3D-printed discs reveals a strong increased trend in osteogenic medium with an average of  $1.64 \pm 0.15$  mg/dl compared to BM with an average of  $1.07 \pm 0.17$  or osteogenic medium without BGP (average of  $1.24 \pm 0.2$  mg/dl) for all measured timepoints (**Figure 3.7**). The unconditioned BM is measured at 1.57 mg/dl, osteogenic medium at 1.68 mg/dl and osteogenic medium without BGP at 1.54 mg/dl. The osteogenic group remains stable, while the BM group and osteogenic medium without BGP group are decreased compared to their corresponding unconditioned media.

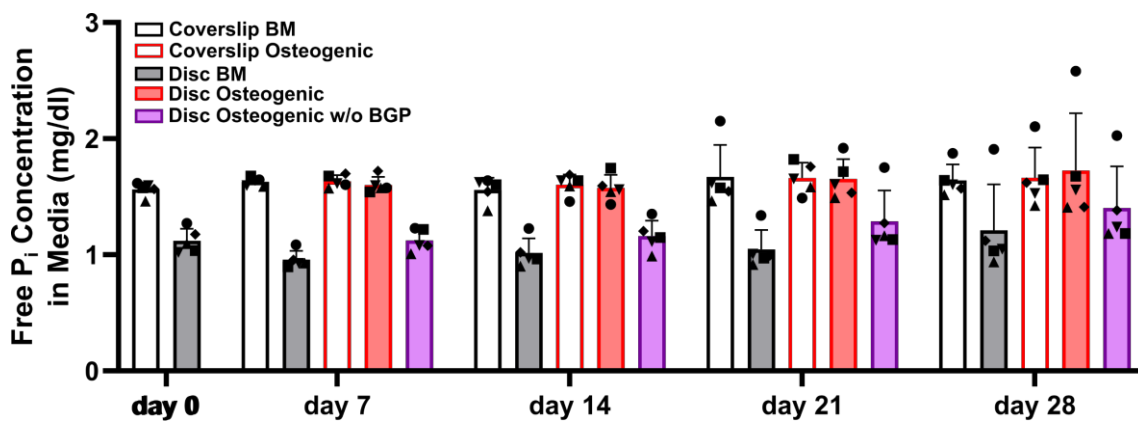


**Figure 3.7: Free phosphate concentration in the media** of hBM-MSC cultured either on coverslips or 3D-printed PLGA/ $\beta$ -TCP discs of five independent donors (N=5). Individual data points shown are the mean of two technical replicates for each individual donor: donor D (●), donor E (▲), donor F (◆), donor G (■) and donor H (▼). Cells are cultured in basal medium (BM), osteogenic medium or osteogenic medium without  $\beta$ -glycerophosphate (BGP) for 28 days. Conditioned media samples are collected at day 0, 7, 14, 21 and 28.

The absence of exogenous BGP decreases the free phosphate levels in the conditioned media compared to the osteogenic group of hBM-MSCs cultured on 3D-printed PLGA/ $\beta$ -TCP discs and keeps them reduced over the period of the experiment.

***Absence of Exogenous BGP Leads to Similar Stained Area of Mineral Deposition of hBM-MSCs Cultured on 3D-printed PLGA/ $\beta$ -TCP Discs under Osteogenic Conditions***

Mineral deposition of hBM-MSCs of five independent donors cultured on 3D-printed discs for 28 days is stained using the OsteoImage™ Mineralisation Assay. The three representative donors (donor D, G and H) show visible stained area of mineralisation in all images under the three culture conditions when cells are cultured on 3D-printed discs (**Figure 3.8**). No differences in staining can be detected between these groups. The number of nuclei is visibly increased, which is in accordance with the increased DNA content of **Figure 3C**.  $\beta$ -TCP from the 3D-printed disc and HAp secreted by the differentiated cells are not distinguishable from each other.

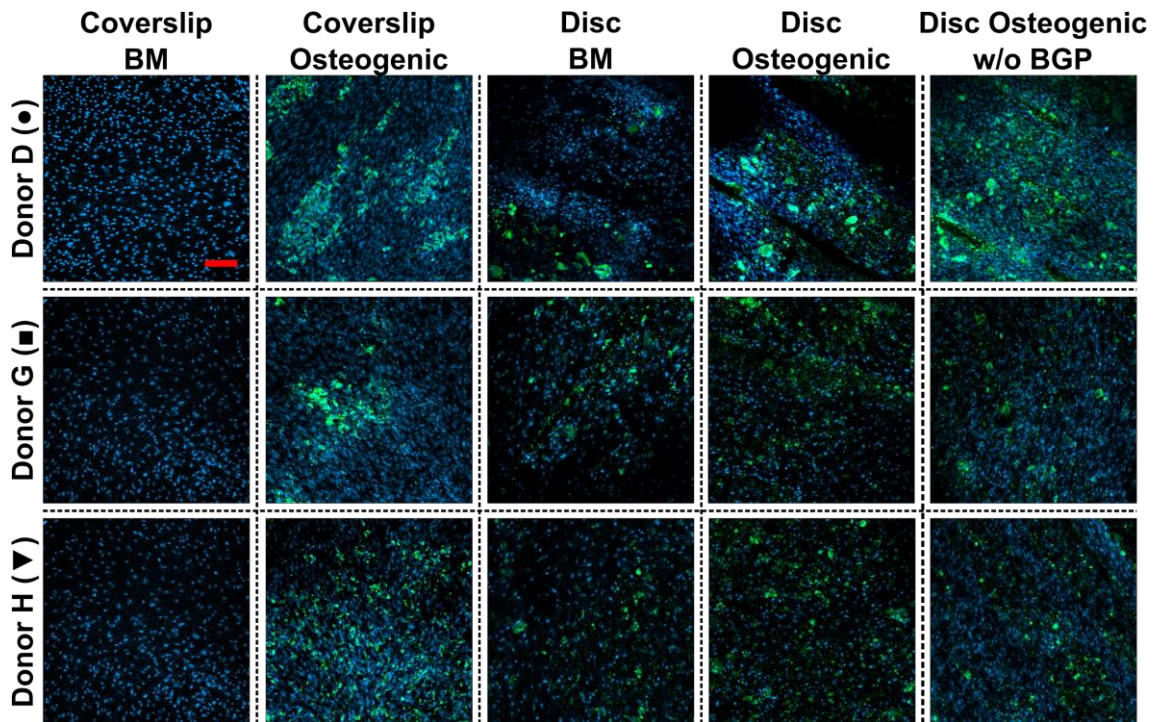


**Figure 3.8: Images of bone cell mineralisation** of hBM-MSC cultured either on coverslips or 3D-printed PLGA/ $\beta$ -TCP discs of three representative donors: donor D (●), donor G (■) and donor H (▼) stained OsteoImage™ (green) and DAPI (blue). Cells are cultured in basal medium (BM),

osteogenic medium or osteogenic medium without  $\beta$ -glycerophosphate (BGP) for 28 days. Fluorescent confocal images are taken at day 28, scale bar: 200  $\mu$ m.

The absence of exogenous BGP leads to a visibly similar stained area of mineral deposition and number of nuclei of hBM-MSCs cultured on 3D-printed PLGA/ $\beta$ -TCP discs compared to BM and osteogenic medium. Applying the osteogenic cocktail to cells cultured on coverslips leads to higher secretion of mineral deposition.

### **3.4 Discussion**

The purpose of this study was to investigate whether  $\beta$ -TCP embedded within 3D-printed PLGA/ $\beta$ -TCP scaffolds can serve as an effective phosphate source during the osteogenic differentiation of hBM-MSCs and replace organic BGP as part of the osteogenic cocktail. The results of the cytotoxicity and thorough osteogenic *in vitro* experiments by examining cell activity, proliferation, and key osteogenic markers of hBM-MSCs cultured on 3D-printed discs show that BGP supplementation can have detrimental effects in a donor dependent manner. The results clearly indicate that cells can undergo osteogenesis with and without the supplementation of BGP when the scaffold contains  $\beta$ -TCP. Consequently, the use of exogenous BGP is redundant when cells are cultured on a phosphate-based material.

Despite the dose dependent decline in cell metabolic activity upon supplementation of BGP, the activity remains above 70% and therefore considered non-cytotoxic according to the ISO 10993-5 guidelines.<sup>155</sup> However, the data suggests that while viable, cells may be stressed in the presence of exogenous BGP. The negative outcome of cells exposed to BGP when cultured on a phosphate-based material might be attributed to their exposure to high phosphate concentrations, which previously has been shown to have detrimental effects for BM-MSCs.<sup>144,146</sup> Previous studies have already demonstrated the



advantages of replacing exogenous BGP with alternative phosphate sources such as inorganic  $\text{Na}_x\text{H}_{3-x}\text{PO}_4$  and polyP nanoparticles.<sup>77,146</sup> 10 mM BGP supplementation has been shown to cause non-physiological fluctuations of extracellular phosphate levels. Replacing BGP with inorganic  $\text{Na}_x\text{H}_{3-x}\text{PO}_4$  resulted in improved quality of mineralised matrix closer to HAp, demonstrated by the ratio between calcium and phosphate.<sup>146</sup> The hypothesis that excessive quantities of phosphate results in the disruption of hBM-MSc homeostasis and consequent reduction in cellular activity appears to be donor dependent. Different donors exhibited varying responses in terms of ALP activity and proliferation under osteogenic conditions with and without BGP. These donors can be loosely classified into two groups: 1) those less affected and 2) those detrimentally affected by BGP supplementation. To demonstrate donor responses of the two groups, we divided the presented data into two Figures (**Supplementary Figure 3.1/2**) only containing the two osteogenic groups for comparison. ALP activity normalised to the DNA content of Donor D and F seems to be less disrupted by the supplementation with the traditional osteogenic cocktail (group 1), while donor E, G and H seem to be much more affected (group 2). Donor variability is also evident in the varying levels of ALP staining intensity observed among representative donors. Donors from group 1 were 48 and 51 years old at the time of the bone marrow donation and the donors from group 2 were 61, 74 and 71 years old. Donors from group 1 might have been in their premenopausal phase, which could arguably have an influence on the condition of the isolated MSCs<sup>156,157</sup>, although further investigation with more donors is needed to draw a definitive conclusion. Replacing BGP with polyP nanoparticles has been shown to provide stable means for inducing osteogenic responses and reduce inter-donor variability in osteogenesis assays of hBM-MSCs.<sup>77</sup> Donor variability is commonly associated with the use of primary MSCs and can limit the statistical significance of findings, an important limitation in this study.

The removal of BGP has a positive effect on genes involved in matrix production such as *COL1A1*, *IBSP* and *SPP1* and supports the assumption that BGP supplementation might negatively influence the osteogenic differentiation of hBM-MSCs when cultured on a phosphate-based material. The early osteogenic marker, *COL1A1*, an important driver for collagen 1 production, is highly expressed in differentiated osteoblasts.<sup>158,159</sup> BGP removal leads to a substantial upregulation and recovery of *COL1A1*, particularly in donors belonging to group 2. The average expression of late osteogenic markers *IBSP* (bone sialoprotein encoding gene) and *SPP1* (osteopontin encoding gene), which are involved in matrix production, do not appear to be strongly influenced by the removal of BGP. However, each donor exhibits largely different gene expression patterns for *IBSP* and *SPP1* under standard osteogenic conditions, which leads to a substantial inter-donor variance. The variance can be diminished when BGP is removed, partially evident in donors from group 2.

The expression of the transcription factor *SP7*, which plays a crucial role in the maturation of preosteoblasts and their differentiation into osteoblast<sup>160,161</sup>, not only shows an increase in the group without BGP supplementation, but also displays a reduced variance similar to the gene expression profiles of *IBSP* and *SPP1*. *RUNX2*, a transcription factor essential for osteoblast differentiation<sup>162</sup>, has been shown to display minimal differences in osteogenesis of hBM-MSCs.<sup>77,163</sup> However, the downregulation of the chondrogenic marker *SOX9* makes it an indirect marker for osteogenesis, therefore the *RUNX2/SOX9* ratio can be used as an osteogenic marker.<sup>163</sup> The subtraction of BGP does not influence the *RUNX2/SOX9* ratio. The gene expression of *PPAR $\gamma$*  indicates off-target differentiation of hBM-MSCs into adipocyte-like cells under osteogenic conditions. This phenomenon is a common characteristic of hBM-MSCs and is induced by the presence of dexamethasone, which activates the glucocorticoid receptor.<sup>154</sup> The continuous increase of *PPAR $\gamma$*  expression observed under standard

osteogenic treatment could potentially be attributed by the presence of glycerol that is cleaved from the BGP.

To deepen our understanding of the impact of removing BGP from the osteogenic cocktail and highlight its redundancy, we investigated the gene expression of phosphate-related genes such as *ALPL*, *ENPP1*, *ANKH* and *PHOSPHO1*, genes involved in phosphate cleavage and regulation. *ALPL* is responsible for encoding the membrane-bound ALP. ALP is a commonly used osteogenic marker to show osteogenic differentiation of MSCs<sup>113,164</sup> and plays a crucial role in releasing phosphate by cleaving the phosphate ester bond.<sup>165</sup> Cells cultured on a phosphate-based material seem to show a delay in *ALPL* peak expression. Ectonucleotide pyrophosphatase/phosphodiesterase family member 1 (E-NPP1), encoded by the *ENPP1* gene, plays an important role in maintaining the balance of bone mineralisation.<sup>166</sup> Its expression is vital for osteogenic differentiation of preosteoblastic cells.<sup>167</sup> E-NPP1 is known to increase the levels of extracellular pyrophosphate<sup>167</sup>, a well-established inhibitor for HAp formation<sup>168</sup>. However, the use of exogenous pyrophosphate has been shown to stimulate the expression of osteogenic genes in osteoblastic MC3T3 cells.<sup>169</sup> *ENPP1* gene expression has been reported to play a key role in the process of osteoinduction by CaP ceramics on hBM-MSCs.<sup>170</sup> However, the fundamental role of E-NPP1 in MSCs is not extensively studied. Progressive ankylosis protein homolog (ANK), encoded by the *ANKH* gene, is highly expressed in osteoblasts.<sup>171</sup> It is involved in the osteogenic fate decision of adult mesenchymal precursor cells and its absence has been shown to favour adipogenesis.<sup>172</sup> *ANKH* is used as a osteogenic marker of BM-MSCs due to its association with ALP<sup>173</sup>. Phosphoethanolamine/phosphocholine phosphatase, encoded by the *PHOSPHO1* gene, is a matrix vesicle phosphatase that is involved in skeletal mineralisation.<sup>174,175</sup> It generates inorganic phosphate<sup>176</sup>, essential for the mineralisation process. The downregulation of *ENPP1*, *ANKH* and *PHOSPHO1* gene expression observed when cells are cultured on a phosphate-based

material upon osteogenic treatment in contrary to the coverslip suggest an active role of the material itself on the expression of these genes. However, the mechanism by which  $\beta$ -TCP from 3D-printed scaffolds can be cleaved remains to be investigated. These results support the theory that hBM-MSCs are sensitive to high concentrations of phosphate and suggest that the supplementation of BGP may overwhelm the cells when they are already exposed to a phosphate-based material. The delicate sensitivity of osteoblastic cells to exogenous phosphate has been shown in previous studies, in which high levels of inorganic phosphate induced cell apoptosis.<sup>144,177</sup> Our findings suggest that the regulation of matrix and phosphate-related genes are influenced by the presence of BGP, and together with the cell metabolic activity measurements, caution should be exercised when using BGP supplementation.

Interestingly, the decrease in gene expression profile of phosphate-related genes upon osteogenic treatment shows the opposite trend compared to the increased concentration of free phosphate in the media. The inactivity of these genes under osteogenic treatment indicates that the cells control the excessive amounts free phosphates in the media by their downregulation. hBM-MSCs undergoing osteogenic differentiation cleave the BGP nearby their membrane, releasing free phosphate to the surrounding medium, thereby maintaining a high concentration of free phosphate. In contrast, cells cultured without the supplementation of BGP have an increased expression of these phosphate-related genes but result in the decline of free phosphate in the medium. This phenomenon suggests that the cells that are cultured on the CaP material without BGP supplementation uptake the cleaved free phosphate from the 3D-printed PLGA/ $\beta$ -TCP disc locally, without secreting free phosphate into the surrounding medium. Consequently, high concentration of free phosphate in the medium is prevented. In summary, ALP activity and proliferation results, along with the gene expression profile of matrix-related, – transcriptional – and phosphate-related genes, supports the

assumption that BGP supplementation has a detrimental impact on osteogenic differentiation of hBM-MSCs when cultured on a phosphate-based material.

Additional limitations encountered in this study is the difficulty of measuring mineralised deposition of the cells. Common staining protocols such as Alizarin Red or Von Kossa, which are used to visualise and quantify cell-secreted HAp, are strongly positive to any CaP containing materials. This circumstance increases the challenge in distinguishing mineralisation of the underlying material from the matrix secreted by the cells. Therefore, the application of these histological methods cannot be used for such experiments. Chemical analysis of the material at the element level using techniques like energy-dispersive X-ray spectroscopy (EDX) or Fourier transform infrared spectroscopy can indirectly confirm the presence of HAp by measuring the CaP ratio.<sup>38,146</sup> However, these methods present their own technical difficulties. Uneven densities in the PLGA/ $\beta$ -TCP blend does not allow for accurate measurement using the EDX method. Quantification calcium concentration has been employed as a method to indicate mineralisation.<sup>147,148</sup> However, the chemical interaction between free phosphate and the material and consequential precipitation of CaP can give false positive results. *In vitro* fluorescence imaging using the OsteoImage™ Mineralization Assay is specifically designed to stain the HAp portion of bone-like nodules deposited by cells. Unexpectedly, we discovered positive staining of the OsteoImage™ dye on cell-free 3D-printed  $\beta$ -TCP discs (images not shown). This occurrence weakens the interpretation of the presented confocal images. The investigation of mineral output has always been a crucial marker for osteogenesis. However, due to the nature of the CaP-based material, accurately quantifying cell-secreted mineral deposition remains a limitation in this study. Necessary controls must be included, and caution must be taken when testing biomaterials as artifacts can alter data interpretations. Further research and alternative methods may be necessary to overcome this limitation and provide a more comprehensive analysis of mineralisation in this context.

The use of the osteogenic cocktail has been specifically defined for 2D cell culture systems and cannot be easily translated into complex 3D matrices systems. The findings presented in this study emphasise the importance of investigating the optimal osteogenic culture medium to differentiate MSCs when combined with phosphate-based materials for BTE. The removal of BGP from the medium enhances the resemblance of a cell-laden bone substitute to the *in vivo* situation, thereby improving the validation of biomaterials for their osteogenic potential. The osteogenic cocktail is a potent osteogenic inducer that pushes MSCs to differentiate into osteoblasts even in an unnatural environment such as CCP or coverslips, that would not be expected to osseointegrate *in vivo*. In this experimental *in vitro* set-up, bioinert plastics exhibit osteoconductive properties. Therefore, conducting an osteogenic differentiation experiment using MSCs cultured on plastic or coverslips should primarily serve as negative a control. An important aspect in BTE is to assess whether a biomaterial is suitable to be used as a bone substitute *in vivo*. By minimizing the enormous difference between *in vitro* and *in vivo* studies, the translational potential of tissue engineered bone substitutes can be enhanced. Optimizing the osteogenic culture medium to create a scenario closer to the natural environment can contribute to reducing this disparity. We therefore propose that researchers consider removing BGP from their osteogenic medium when testing phosphate-based bone substitutes using MSCs. By addressing these considerations and refining the experimental conditions to better mimic the *in vivo* environment, researchers can improve the relevance and applicability of their findings in the field of BTE.

### **3.5 Conclusions**

The presented results provide evidence for osteogenic differentiation of hBM-MSCs cultured on 3D-printed PLGA/ $\beta$ -TCP discs with and without the supplementation of BGP in the osteogenic medium. Our findings suggest that hBM-MSCs can use the  $\beta$ -TCP embedded within a 3D-printed scaffold as a

phosphate source, eliminating the need for exogenous BGP. Nevertheless, the mechanisms by which the phosphate is cleaved remains to be investigated. Furthermore, we demonstrated the donor dependent negative impact of BGP on various aspects including cell metabolic activity, ALP activity, proliferation, and gene expression of osteo- and phosphate-relevant markers when cells are cultured on a phosphate-based material. Understanding the interaction between cells and 3D-printed scaffolds can help tailor the design and composition of the scaffold. Thus, leading to a pro-osteogenic environment that supports cell differentiation and infiltration with the aim of improving successful translation of such bone substitutes to *in vivo* bone defect repair.

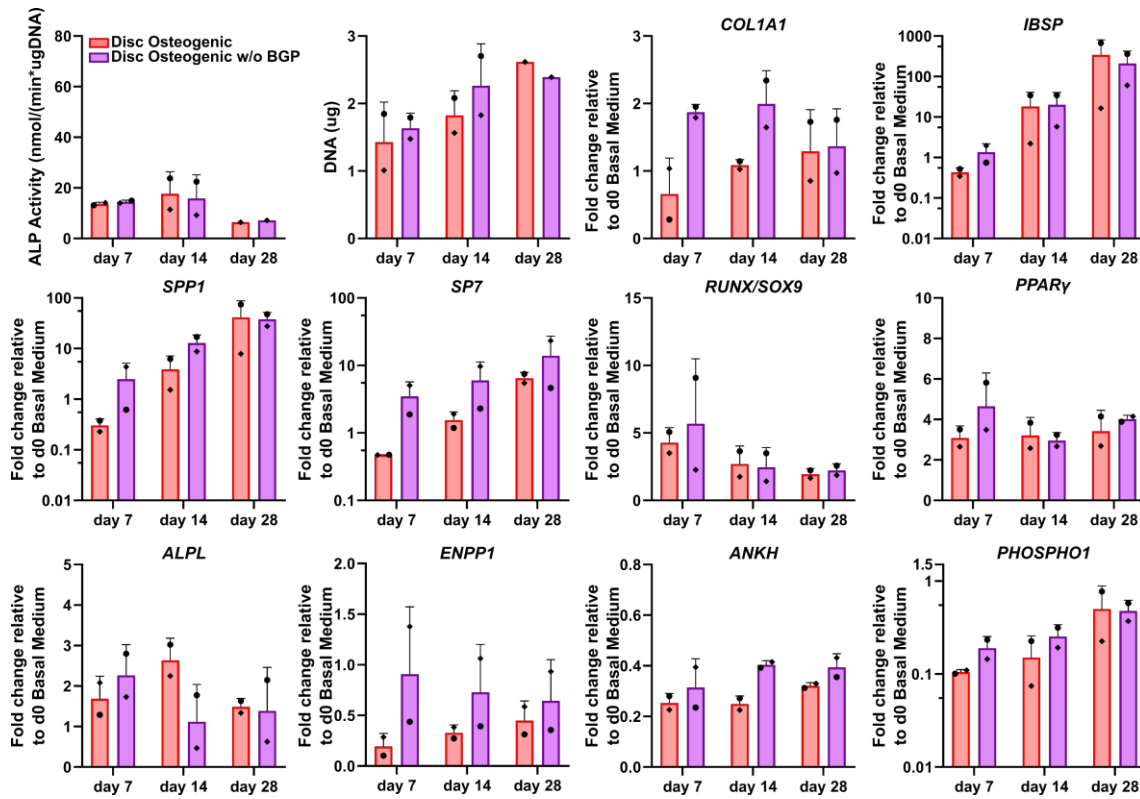
### **3.6 Conflicts of Interest**

There are no conflicts to declare.

### **3.7 Funding**

This work was supported by AO CMF and AO Foundation.

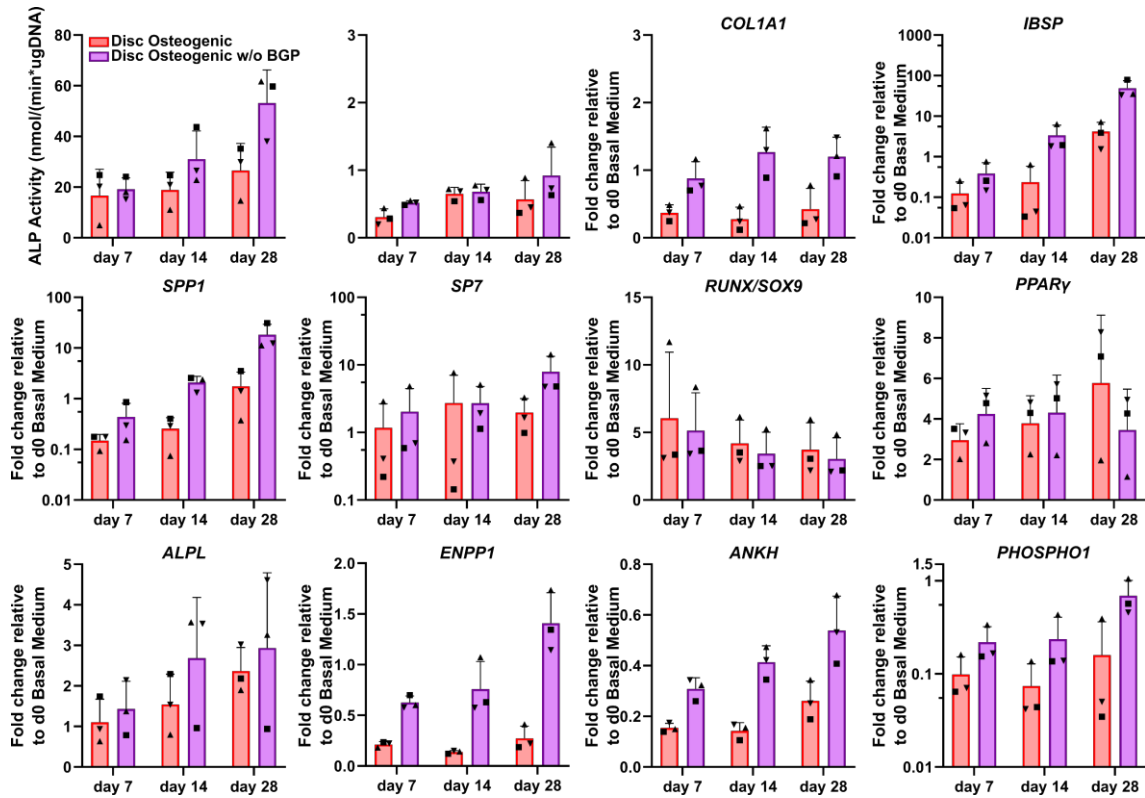
### 3.8 Supplementary Materials



**Supplementary Figure 3.1: Data comparison group 1** (less affected by the supplementation with  $\beta$ -glycerophosphate (BGP)) of hBM-MSC cultured either on 3D-printed PLGA/ $\beta$ -TCP discs of two independent donors (N=2). Individual data points shown are the mean of two technical replicates for each individual donor: donor D ( $\bullet$ ) and donor F ( $\blacklozenge$ ). Cells are cultured in osteogenic medium or osteogenic medium without BGP for 28 days. ALP activity normalised to DNA content, DNA content, fold changes in *COL1A1*, *IBSP*, *SPP1*, *SP7*, *RUNX2/SOX9*, *PPAR $\gamma$* , *ALPL*, *ENPP1*, *ANKH* and *PHOSHO1* expression at day 7, 14 and 28 are calculated according to the  $2^{-\Delta\Delta Ct}$  method using *RPLP0* as the endogenous calibrator and the corresponding day 0 basal medium (BM) the normaliser.



**$\beta$ -TCP from 3D-printed Scaffold can act as an Effective Phosphate Source during the Osteogenic Differentiation of Human Mesenchymal Stromal Cells**



**Supplementary Figure 3.2: Data comparison group 2** (detrimentally affected by the supplementation with  $\beta$ -glycerophosphate (BGP)) of hBM-MSC cultured either on 3D-printed PLGA/ $\beta$ -TCP discs of three independent donors (N=3). Individual data points shown are the mean of two technical replicates for each individual donor: donor E ( $\blacktriangle$ ), donor G ( $\blacksquare$ ) and donor H ( $\blacktriangledown$ ). Cells are cultured in osteogenic medium or osteogenic medium without BGP for 28 days. ALP activity normalised to DNA content, DNA content, fold changes in *COL1A1*, *IBSP*, *SPP1*, *SP7*, *RUNX2/SOX9*, *PPAR $\gamma$* , *ALPL*, *ENPP1*, *ANKH* and *PHOSHO1* expression at day 7, 14 and 28 are calculated according to the  $2^{-\Delta\Delta C_t}$  method using *RPLP0* as the endogenous calibrator and the corresponding day 0 basal medium (BM) the normaliser.

## **4 Osteogenic Differentiation of hBM-MSCs Seeded on Collagen Membranes Embedded within LEGO®-inspired 3D-Printed PCL Construct for Mandibular Bone Repair**

### **Statement of Significance:**

The *in vivo* implementation of traditional bulk materials often results in the formation of a necrotic core due to limited provision of oxygen and nutrients. A multicomponent layered scaffold facilitates the pre-distribution of biologics within the scaffold to improve tissue infiltration. Within this study, we investigated the osteogenic differentiation of mesenchymal stromal cells seeded on collagen membranes that are embedded within a layered interlocking scaffold to demonstrate its applicability *in vitro*.

Note: This chapter entitled **Osteogenic Differentiation of hBM-MSCs Seeded on Collagen Membranes Embedded within LEGO®-inspired 3D-Printed PCL Construct for Mandibular Bone Repair**, Luan P. Hatt, Daphne van der Heide, Sylvie Wirth, Maria E. Pirera, Angela R. Armiento and Martin J. Stoddart is in preparation and planned to be submitted to the journal *Biofabrication*.

### **Author Contributions:**

LPH performed the investigation, methodology, validation, data curation and formal analysis of all the osteogenic *in vitro* experiments and hence generated all the data for this paper. LPH also wrote the original draft, visualised the data, and created all the figures. DvdH contributed to the chapter in terms of assistance in the methodology of the osteogenic *in vitro* experiments and reviewing and editing of the writing. SW contributed to the chapter in terms of development of the interlocking system, methodology and data curation of pre-liminary experiments and creation of the schematics for Figure 4.6. MEP contributed to the chapter in terms 3D-printing of the layered constructs for the *in vitro* study. ARA contributed to the chapter in terms of conceptualisation of the project, co-supervision, validation of the experiment and

**Osteogenic Differentiation of hBM-MSCs Seeded on Collagen Membranes Embedded within LEGO®-inspired 3D-Printed PCL Construct for Mandibular Bone Repair**

---

reviewing and editing of the writing. MJS contributed to the chapter in terms of conceptualisation of the project, supervision, provision of resources, acquisition of funding, reviewing, and editing of the writing, and leading project administration.

## **Abstract**

The field of bone tissue engineering (BTE) aims to develop an effective and aesthetical bone graft substitute (BGS) capable of repairing large mandibular defects. However, graft failure resulting from necrosis and insufficient integration with native tissue remains a concern. To overcome these drawbacks, this study aims to establish a process to develop a 3D-printed layered construct with a LEGO®-inspired interlocking mechanism enabling spatial distribution of biological components within the construct. To highlight its osteogenic potential, human bone marrow-derived mesenchymal stromal (hBM-MSCs) are cultured onto Bio-Gide® Compressed collagen membranes, which are embedded within the layered construct under osteogenic conditions for 28 days. The osteogenic response is assessed through the measurement of relevant markers for osteogenesis including alkaline phosphatase (ALP) presence and activity, proliferation, and expression of transcriptional genes (*SP7*, *RUNX2/SOX9*, *PPAR $\gamma$* ), as well matrix-related genes (*COL1A1*, *ALPL*, *IBSP*, *SPP1*). We have successfully 3D-printed a LEGO®-inspired layered construct composed of polycaprolactone (PCL) that can accommodate cell-laden collagen membranes for *in vitro* investigations. Results show increased levels of these osteogenic markers, indicating the layered construct's potential to promote osteogenic differentiation of hBM-MSCs. The presented study provides the establishment of a novel workflow to develop layered constructs to spatially deliver biological elements. These layered constructs have the potential to be employed as a BTE strategy, with particular focus on the repair large mandibular defects.

## **4.1 Introduction**

The treatment of large mandibular bone defects resulting from trauma, tumour removal, congenital deformities, osteoradionecrosis, or infections requires intricate surgical procedures involving autologous bone grafting (ABG).<sup>51,178</sup> However, ABG is associated with major drawbacks including donor side morbidities, prolonged operation time, limited availability, and inability to form patient-specific geometries.<sup>179,180</sup> Alternative approaches such as using recombinant human bone morphogenic protein-2 (rhBMP-2) delivered through a collagen sponge are not exempt from their own drawbacks. The side effects of rhBMP-2 include postoperative inflammation, ectopic bone formation, osteoclast-mediated bone resorption, inappropriate adipogenesis, and elevated risk of cancer.<sup>32</sup>

To address these concerns, bone tissue engineering (BTE) emerged as a focal point of research, aiming to develop a bone graft substitute (BGS) that can overcome these limitations, while achieving both functional and aesthetical outcomes.<sup>6</sup> However, one of the primary causes of construct failure are the formation of necrotic cores and inadequate integration with native tissue, often resulting in non-union scenarios for the patients.<sup>181</sup> A solution to this issue is to divide the scaffold in layers, which allows for the spatial integration of biological elements within the scaffold's core. The ignition of the osteogenic process and attraction of vessels from the surrounding native environment can be provided from within the construct. To achieve the creation of a layered construct the implementation of an interlocking system is a promising approach, inspired by the concept of the LEGO® bricks.

3D printing PCL offers an easy and precise fabrication mechanism, mechanical strength, and biodegradability.<sup>182</sup> All of which are favourable properties to create a BGS suitable for repairing for load-bearing mandibular defects. However, PCL's intrinsic lack of biological cues makes it an inadequate candidate to deliver biological agents.<sup>183</sup> Collagen membranes emerge as the ideal transporter to convey biological substances such as regenerative progenitor cells or biological factors. They provide

molecular cues for cell migration and promotion of osteogenesis.<sup>184-186</sup> Furthermore, they have a thin structure, which makes them well-suited to be placed within a layered construct, where they can assist in keeping the implanted cells within each layer.

In this study, we chose to incorporate the clinically available Bio-Gide® collagen membranes within the layered system, due to its established use in clinical practice and capacity for guiding bone regeneration.<sup>187,188</sup> The aim of this study is to establish a systematic process for creating a patient-specific 3D-printed layered construct featuring an interlocking system capable accommodating collagen membranes. As a demonstration of this system's osteogenic potential, we performed an *in vitro* osteogenic differentiation experiment using human bone marrow-derived mesenchymal stromal cells (hBM-MSCs) seeded onto Bio-Gide® collagen membranes embedded within the layered construct.

## **4.2 Material and Methods**

Human bone marrow aspirates are obtained with informed consent of all donors and with full approval from the Ethics Committee of the University of Freiburg Medical Centre (EK-Freiburg: 135/14, 25 March 2014) and the ethical commission of Zürich (KEK-ZH-NR: 2016-00141). All reagents are purchased from Sigma-Aldrich unless otherwise stated. An overview of the methods is reported in **Figure 4.1**.

## Osteogenic Differentiation of hBM-MSCs Seeded on Collagen Membranes Embedded within LEGO®-inspired 3D-Printed PCL Construct for Mandibular Bone Repair

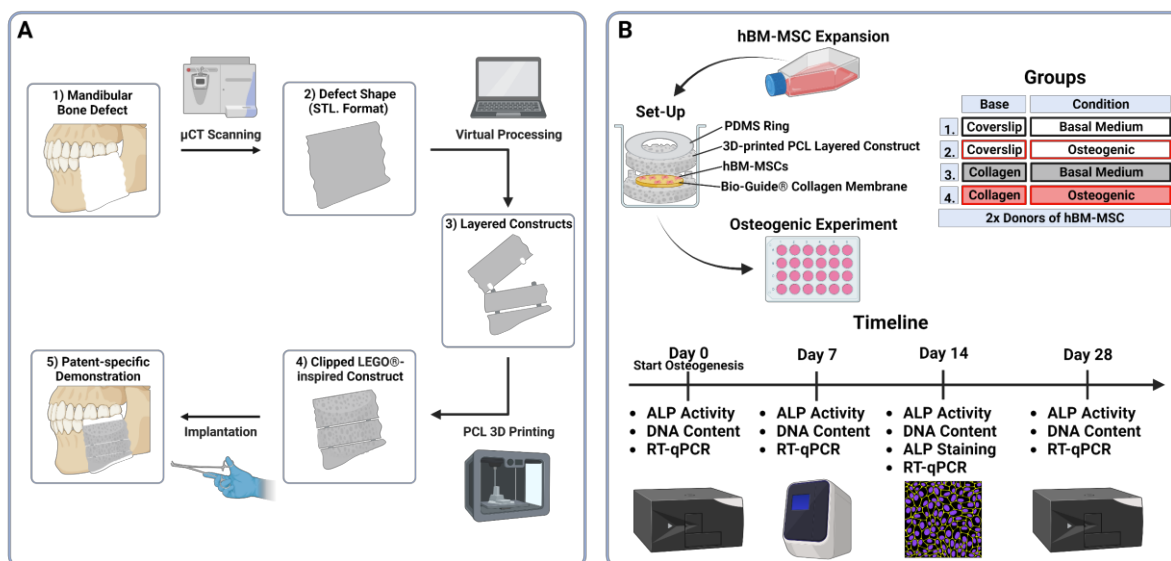


**Figure 4.1: Methodical overview of** A) Schematical workflow from mandibular bone defect to implantation of a patient-specific 3D-printed LEGO®-inspired construct and B) Groups, timeline and experimental set-up of osteogenic differentiation of human bone marrow-derived mesenchymal stromal cells (hBM-MSCs) cultured on either coverslips or Bio-Guide® collagen membranes embedded in a 3D-printed layered polycaprolactone (PCL) construct secured using a polydimethylsiloxane (PDMS) ring for 28 days under either basal or osteogenic conditions measuring alkaline phosphate (ALP) activity and staining, DNA content and gene expression via reverse transcription-quantitative polymerase chain reaction (RT-qPCR). Created with BioRender.com.

### ***Design and 3D Printing of a Patient-specific Layered Construct***

To demonstrate the creation of a patient-specific layered construct inspired by the LEGO® brick system a workflow is developed (**Figure 4.1A**). A SYNBONE® mandibular defect with random shape is created and  $\mu$ CT-scanned using the vivaCT 40. The object based on the geometries of the defect is rendered using the Amira image processing software and exported as STL file. The object file is virtually sliced in 4 layered parts with male and female features placed within the individual parts using the Autodesk Fusion 360 software. The STL files of the 4 layered parts are converted into the g-code using the MM Converter software (RegenHu) and 3D-printed using a 3D Discovery® bioprinter (RegenHU). PCL pellets (average MW: 45000 g/mol) are placed into the heated reservoir chamber of the printer, where they are melted at 75°C.

The PCL is pressed to the extruding chamber with a temperature of 70 °C through a rotor system set at 21 revs/min. Equipped with a 0.33 mm stain-less steel needle the PCL is extruded onto a glass slide heated to 37°C using a heating table to 3D print the 4 individual layered parts with a infill density of 40%. Upon 3D printing the 4 parts can be clipped together to form a patient-specific layered construct.

### ***Design and 3D Printing of Two-part Layered PCL Construct for Biological Assessment***

The 3D-printed layered construct used for the osteogenic experiment is composed of two parts, female and male, with an interlocking mechanism with a tight fit upon clipping (**Figure 4.2A**). It has a round shape with a diameter of 15.3 mm to fit into a 24-tissue culture plate to demonstrate the *in vitro* osteogenesis of hBM-MSCs cultured on collagen membranes embedded within the layered construct. The male part has a height of 1 mm without the bricks and the female part has a height of 1.8 mm. The two bricks on the male part of the construct (1x5x1.3mm) are placed 1.8 mm apart from the edge and 9.8 mm apart from each other leaving space for the collagen membrane. The holes of the female part (1.2x5.2x1.3 mm) are precisely placed over the position of the bricks as the counterpart. The collagen membrane can be placed in between the interlocking two parts (**Figure 4.2B**). The two components of the layered construct are printed as described in section 4.1 with differences being the use of the PCL (average MW: 36000~45000 g/mol, iChemical), the reservoir chamber set at 125°C, the extruding chamber set at 120 °C and the infill density set to 40% to obtain a macro-porous construct. Subsequently, layered parts are sterilised using a cold ethylene oxide gas protocol, degassed under vacuum, before being used for the osteogenic experiments.



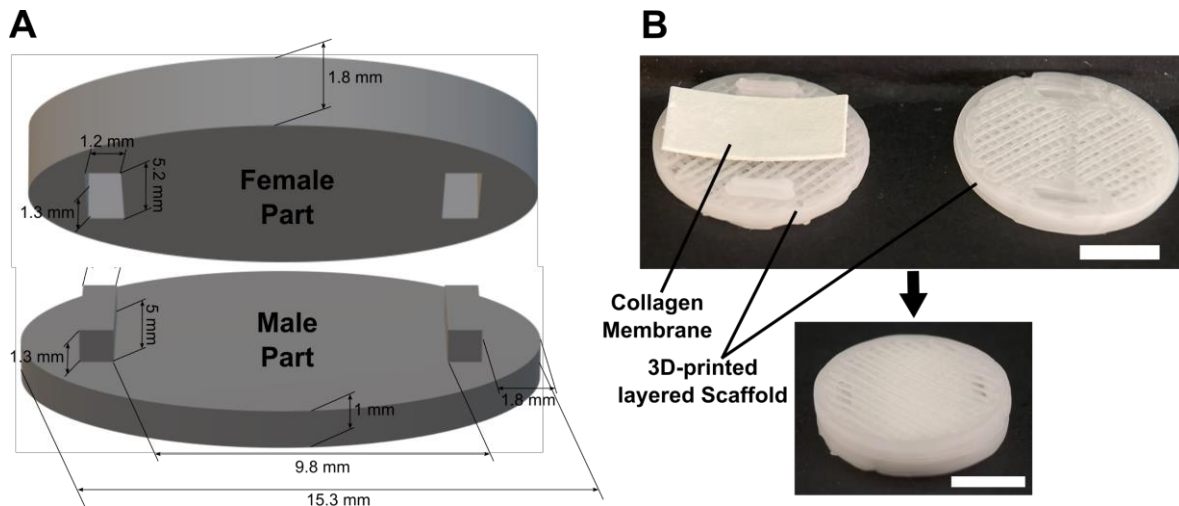


**Figure 4.2: Interlocking layered construct inspired by the LEGO® system:** A) virtual schematic (STL format including dimensions) used for osteogenic experiment and B) images of the collagen membrane embedding within the 3D-printed layered polycaprolactone (PCL) two-part construct with, both scale bars: 0.5 cm.

### ***Cell Isolation and Culture of hBM-MSCs***

Isolation, cryopreservation, and culture expansion of hBM-MSCs are conducted followed by published protocols.<sup>77,153</sup> In short, cells are expanded in T300 flasks (cell density  $3 \times 10^3$  cells/cm<sup>2</sup>) and cultured under standard cell culture conditions of 37°C with 5% CO<sub>2</sub> and 90% humidity with 3 media changes per week. The expansion medium consists of  $\alpha$ -MEM (Gibco) supplemented with 10% (v/v) foetal bovine serum (FBS) (Corning) and 100 U/mL Penicillin, 100  $\mu$ g/mL Streptomycin (PEN/STREP) (Gibco). hBM-MSCs donor details are as follows: donor A, 48-year old female, spine vertebral body and donor B, 51-year old female, spine vertebral body.

### ***Osteogenic Differentiation of hBM-MSCs***

hBM-MSCs are harvested using 0.05% Trypsin-EDTA and seeded at a density of  $15 \times 10^3$  cells/cm<sup>2</sup> in duplicates onto either coverslips (SARSTEDT AG) or Bio-Gide® Compressed bilayer collagen membranes (Geistlich) based on porcine collagen 1 and 3 embedded within 3D-printed layered PCL constructs (**Figure 4.1B**). Cell-laden constructs are placed within a Costar® 24-well Clear Flat Bottom Ultra-Low Attachment

Multiple Well Plates (Corning) and secured using a polydimethylsiloxane (PDMS) (SYLGARD™184 Silicone Elastomer, Dow) ring, which is press-fitted into each well. For the first 24 hours, cells are cultured in basal medium, which consists of low glucose (1g/L) – DMEM (LG-DMEM) (Gibco) supplemented with 10% (v/v) FBS and 100 U/mL PEN/STREP. Subsequently, the media is either maintained with basal medium or switched to osteogenic medium, which consists of basal medium supplemented with 10 nM dexamethasone (dexa), 5 mM  $\beta$ -glycerophosphate (BGP) and 50  $\mu$ g/mL L-ascorbic acid-2-phosphate). In summary, the experiment is performed under 4 different conditions: 1) coverslip basal medium; 2) coverslip osteogenic medium; 3) collagen basal medium and 4) collagen osteogenic medium for 28 days under standard culture conditions.

### ***Quantification of ALP Activity and DNA Content***

At day 0, 7, 14 and 28, ALP activity and DNA content are measured as previously described<sup>77</sup> (**Figure 4.1B**). In short, collagen membranes are taken out of the layered construct and cells are lysed with 0.1% Triton X-100 in 10 mM TrisHCl. Subsequently, the enzymatic reaction is started by adding alkaline buffer solution, substrate solution (25 mg/mL phosphate substrate in 1 mM diethanolamine) and Milli-Q® water and stopped by adding 0.1 M NaOH solution after 15 minutes of incubation at 37°C. The absorbance is read at 405 nm using the Infinite® 200 PRO plate reader (Tecan). ALP activity is normalised to the DNA content. DNA concentration is quantified at day 0, 7, 14 and 28 using the CyQuant™ Cell Proliferation Assay (Invitrogen) according to the manufacturer's instructions. Cell lysate is transferred into a 96 clear bottom well plate, working solution containing dye is added, incubated for 5 minutes and fluorescence is read at 490/530 nm using Infinite® 200 PRO plate reader. The DNA content is normalised to the corresponding culture area.

### ***ALP Staining***

At day 14, collagen membranes are taken out of the layered construct and ALP is stained using the alkaline phosphatase staining kit (Procedure No. 85) according to

the company's instructions (**Figure 4.1B**). In short, cells are washed 3x with phosphate buffered saline (PBS), fixed with 10% neutral buffered formalin for 30 minutes and, after 3x Milli-Q® water rinses, stained with the alkaline dye solution for 30 minutes at room temperature. 50 mL alkaline dye solution is composed of one Fast Blue RR Salt capsule and 2 mL Naphthol AS-MX Phosphate Alkaline solution. Upon water rinsing the samples are imaged.

### **RNA Isolation and Reverse Transcription-quantitative Polymerase Chain Reaction (RT-qPCR)**

Cells are harvested for gene expression analysis at day 0, 7, 14 and 28. Collagen membranes are taken out of the layered construct and RNA isolation and RT-qPCR is performed using the QuantStudio™ Flex Real-Time PCR System as previously described<sup>77</sup> (**Figure 4.1B**). Reverse transcription is performed using the Superscript Vilo cDNA Synthesis Kit (Thermo Fisher Scientific) according to the company's instructions. *ALPL* (encodes for ALP), *COL1A1* (encodes for alpha-1 type 1 collagen), *IBSP* (encodes for bone sialoprotein), *PPAR $\gamma$*  (encodes for peroxisome proliferator-activated receptor gamma), *RUNX2* (encodes for runt-related transcription factor 2), *SP7* (encodes osterix), *SOX9* (encodes for SRY-box transcription factor 9), *SPP1* (encodes for osteopontin) gene expressions are investigated. Primer sequences used are listed in **Table 4.1**. The  $2^{-\Delta\Delta C_t}$  method is applied for data analysis using *RPLP0* as an endogenous normaliser and day 0 samples as a calibrator.

**Table 4.1. Primers/probes used for RT-qPCR**

Gene	Assay on Demand <sup>1</sup>		
<i>ALPL</i>	<i>Hs00758162_m1</i>		
<i>IBSP</i>	<i>Hs00173720_m1</i>		
<i>PPAR<math>\gamma</math></i>	<i>Hs00234592_m1</i>		
<i>SP7</i>	<i>Hs00541729_m1</i>		
<i>SOX9</i>	<i>Hs00165814_m1</i>		
<i>SPP1</i>	<i>Hs00959010_m1</i>		
Gene	Forward	Reverse	Probe
<i>COL1A1</i>	5'-CCC TGG AAA GAA TGG AGA TGA T-3'	5'-ACT GAA ACC TCT GTG TCC CTT CA-3'	5'-CGG GCA ATC CTC GAG CAC CCT-3'

## Osteogenic Differentiation of hBM-MSCs Seeded on Collagen Membranes Embedded within LEGO®-inspired 3D-Printed PCL Construct for Mandibular Bone Repair

---

<i>RPLP0</i>	5'-TGG GCA AGA ACA CCA TGA TG-3'	5'-CGG ATA TGA GGC AGC AGT TTC-3'	5'-AGG GCA CCT GGA AAA CAA CCC AGC-3'
<i>RUNX2</i>	5'-AGC AAG GTT CAA CGA TCT GAG AT-3'	5'-TTT GTG AAG ACG GTT ATG GTC AA-3'	5'-TGA AAC TCT TGC CTC GTC CAC TCC G-3'

---

<sup>1</sup>TaqMan® Gene Expression Assay (Applied Biosystems®).

### Statistics

Statistical analyse is performed using GraphPad Prism software version 9.3.1 (GraphPad Software). A Two-Way ANOVA is applied to the data of the ALP activity, DNA quantification and gene expression data. P-values lower than 0.05 are considered significant and thus marked.

## 4.3 Results

### ***3D-printed LEGO®-inspired Layered Construct can fit a Large-scale Mandibular Defect in a Patient specific Manner***

To demonstrate the clinical compatibility, a patient-specific mandible defect-sized scaffold is printed as 4 parts and clipped together to form a layered construct (**Figure 4.3**). The male and female features of the parts have a tight fit to contain the structure of the construct. The macro-porous 3D-printed layered construct shows precise defect fitting upon implantation in the defect site, a highly desired characteristic for patient's aesthetics. The layered construct allows for the delivery and long-term osteogenic culture of hBM-MSC-laden collagen membranes, which is demonstrated by printing round two-part layered constructs (**Figure 4.2B**).

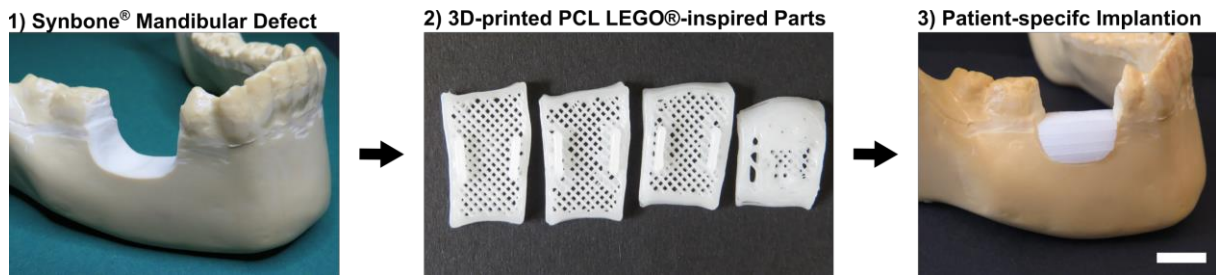


**Figure 4.3: Workflow of the creation of a patient-specific layered interlocking construct:** Image of a SYNBONE® mandibular empty defect (left image), 3D-printed layered PCL parts (middle image) and implantation of patient-specific construct into the mandibular defect (right image), scale bar = 1 cm

***hBM-MSCs Produce Increased ALP under Osteogenic Condition when Seeded on Collagen Membranes Embedded within 3D-printed Layered PCL Construct***

The ALP activity measurement normalised to DNA content, shows a trend of mean upregulation of osteogenically driven cells cultured on collagen membranes embedded in 3D-printed layered PCL constructs compared to cells cultured under basal medium conditions at day 7, 14 and 28 (**Figure 4.4A**). ALP staining confirms the increased protein expression of osteogenically treated cells with increased stained area at day 14 shown by 2 technical replicates of each donor (**Figure 4.4B**). The proliferation profile normalised to the area of cells cultured on the collagen membranes under osteogenic condition compared to the basal medium group shows a maintained DNA content at day 7, decreased trend at day 14 and a decreased trend for donor A and an increased trend for donor B at day 28. (**Figure 4.4C**). ALP, a key protein marker for osteogenic differentiation of hBM-MSCs, is increased upon osteogenic treatment, shown by enzymatic reaction and protein staining (**Figure 4.4A/B**).

## Osteogenic Differentiation of hBM-MSCs Seeded on Collagen Membranes Embedded within LEGO®-inspired 3D-Printed PCL Construct for Mandibular Bone Repair

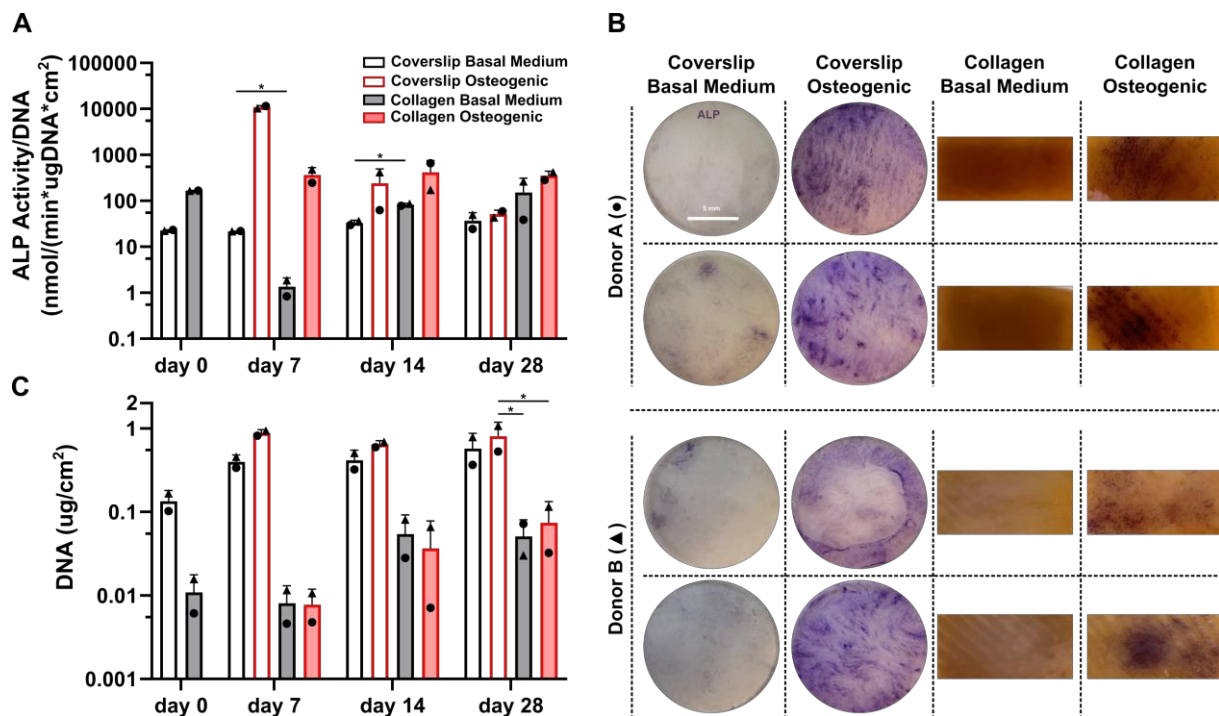


**Figure 4.4: Alkaline phosphatase (ALP) and proliferation assessment** of hBM-MSC cultured either on coverslips or Geistlich Bio-Gide® Compressed collagen membranes embedded within 3D-printed polycaprolactone (PCL) layered constructs of two independent donors. Individual data points shown are the mean of two technical replicates for each individual donor: donor A (●) and donor B (▲). Cells are cultured in basal medium or osteogenic medium for 28 days. A) ALP activity normalised to DNA content at day 0, 7, 14 and 28; B) Images of ALP staining at day 14, scale bar 5 mm; C) DNA content normalised to the area at day 0, 7, 14 and 28. Two-way ANOVA is performed: \*p < 0.05.

### ***hBM-MSC Expression of Osteogenesis Transcription Factor Genes is Upregulated when Cells are Cultured on Collagen Membranes Embedded within 3D-printed Layered Constructs***

*SP7*, the osterix encoding gene, is an important osteogenic transcription factor.<sup>189</sup> The *SP7* fold change gene expression trend of osteogenically driven cells is upregulated at day 7 and day 28 and slightly downregulated at day 14 in donor A compared to basal conditions (**Figure 4.5A**). The ratio of transcription factor expression between *RUNX2* and *SOX9*, an indicator for osteogenesis,<sup>163</sup> shows an upregulation of cells upon osteogenic treatment at day 7 and 14 and a downregulation at day 28 compared to basal conditions (**Figure 4.5B**). Relative to the day 0 basal control the *RUNX2/SOX9*

ratio is downregulated in both groups. *PPAR $\gamma$*  is the main transcription factor that drives MSC adipogenesis,<sup>190</sup> a third possible passage for MSC differentiation. Osteogenically driven cells are upregulated at day 7, 14 and 28 compared to basal conditions (**Figure 4.5C**). The gene expression of transcription factors important for MSC trilineage differentiation reveals an overall upregulated for osteogenic markers (*SP7* and *RUNX2/SOX9*) and adipogenic marker (*PPAR $\gamma$* ) upon osteogenic treatment.

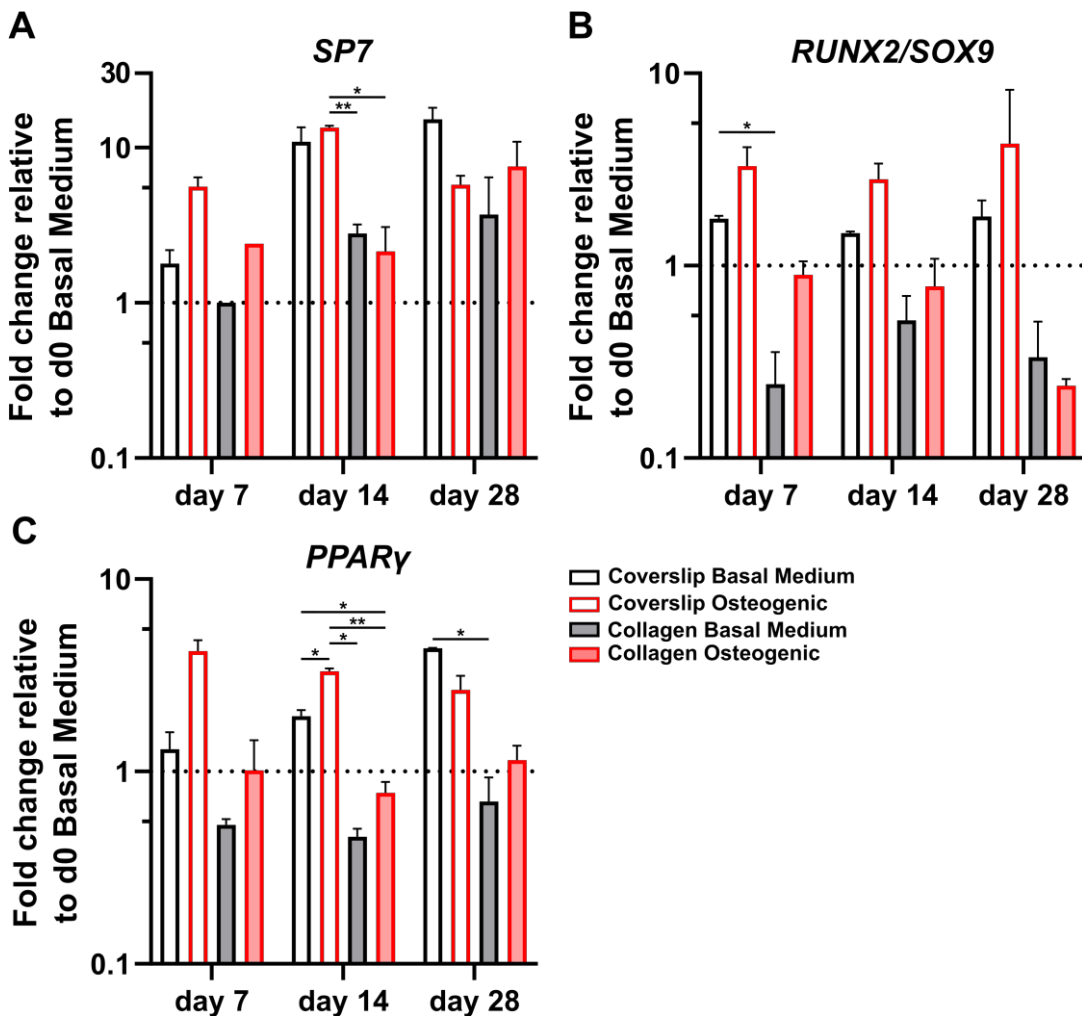


**Figure 4.5: Gene expression of transcription factors involved in MSC differentiation fate of hBM-MSC cultured either on coverslips or Geistlich Bio-Gide® Compressed collagen membranes embedded within 3D-printed polycaprolactone (PCL) layered constructs of donor A (●).** Data are shown as the mean of two technical replicates. Cells are cultured in either basal medium or osteogenic medium for

28 days. Fold changes in A) *SP7*, B) *RUNX2/SOX9* ratio and C) *PPAR $\gamma$*  expressions at day 7, 14 and 28 are calculated according to the  $\Delta\Delta C_t$  method using *RPLP0* as the endogenous calibrator and the corresponding day 0 BM control the normaliser. Two-way ANOVA is performed: \* $p < 0.05$ , \*\*  $p < 0.01$ .

### ***hBM-MSC Expression of Genes Involved in Matrix Production and Regulation is Maintained when Cells are Cultured on Collagen Membranes Embedded within 3D-printed Layered Constructs***

*COL1A1*, alpha-1 type 1 collagen encoding gene, is an important early osteogenic marker for matrix production of osteogenically differentiated hBM-MSCs. The fold change *COL1A1* expression, relative to the corresponding day 0 basal control of donor A is upregulated in the basal and osteogenic groups. The trend of osteogenically driven cells is slightly upregulated at day 7, maintained at day 14 and slightly downregulated at day 28 compared to the cells cultured under basal condition (**Figure 4.6A**). *ALPL*, ALP encoding gene, is an intermediate osteogenic marker and responsible for cleaving phosphates, important for the mineralisation of the extracellular matrix. Cells under osteogenic conditions show a strong trend of *ALPL* upregulation compared to cells cultured under basal condition at day 7, 14 and 28 (**Figure 4.6B**). *IBSP*, bone sialoprotein encoding gene, is a late-stage osteoblast differentiation marker for matrix production of osteogenically differentiated hBM-MSCs. The fold change *IBSP* expression, relative to the corresponding day 0 basal control is downregulated in the basal and osteogenic groups at day 7 and 14 and closely maintained at day 28 (**Figure 4.6C**). The trend of osteogenically driven cells is slightly downregulated at day 7, 14 and 28. *SPP1*, osteopontin encoding gene, is a late-stage osteogenic marker for matrix production. The *SPP1* fold change expression is downregulated in the osteogenic group compared to the basal medium group at day 14 and 28 and maintained at day 7 (**Figure 4.6D**). The gene expression of important osteogenic markers<sup>191</sup> is increased in the early (*COL1A1*) and intermediate (*ALPL*) markers with an enhanced response upon osteogenic treatment, while the late-stage osteogenic markers *IBSP* and *SPP1* are decreased.



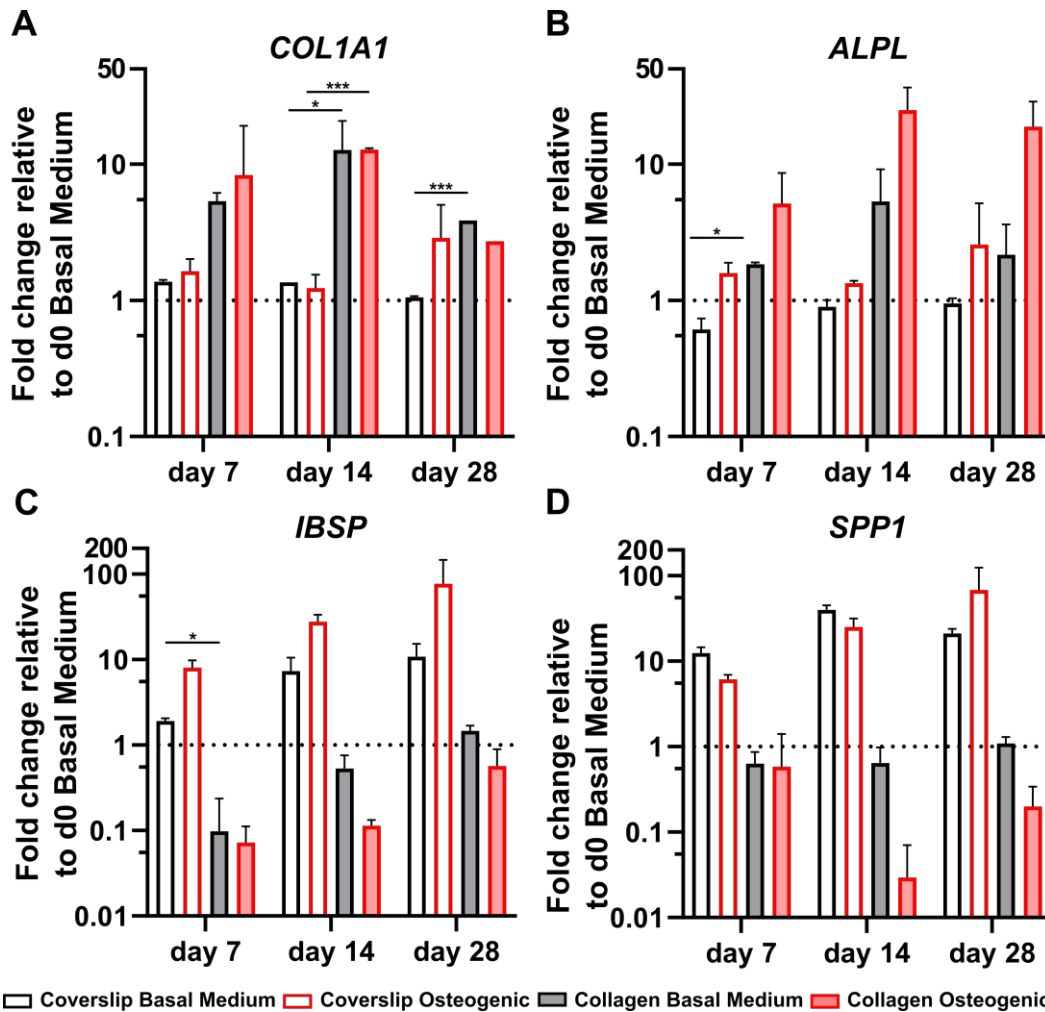


**Figure 4.6: Gene expression of osteogenic markers involved in matrix production and regulation** of hBM-MSC cultured either on coverslips or Geistlich Bio-Gide® Compressed collagen membranes embedded within 3D-printed polycaprolactone (PCL) layered constructs of donor A (●). Data are shown as the mean of two technical replicates. Cells are cultured in either basal medium or osteogenic medium for 28 days. Fold changes in A) *Col1A1*, B) *ALPL* C) *IBSP* and D) *SPP1* expressions at day 7, 14 and 28 are calculated according to the  $\Delta\Delta C_t$  method using *RPLP0* as the endogenous calibrator and the corresponding day 0 Basal Medium control the normaliser. Two-way ANOVA is performed: \*p < 0.05, \*\* p < 0.001.

## 4.4 Discussion

In this study, our objective was to develop a patient-specific 3D-printed PCL construct with multiple layers clipped into each other using an interlocking mechanism inspired

by the LEGO® system. We successfully established a systematic workflow for generating patient-specific 3D-printed layered constructs, simulating the size of a mandibular defect.

Furthermore, the aim was to demonstrate an application of this layered construct through an *in vitro* experiment involving the osteogenic differentiation of hBM-MSCs. These cells are seeded onto commercially available Bio-Gide® collagen membranes, commonly used in clinical settings, which were integrated in-between the layered constructs. The assessment of the osteogenic *in vitro* experiments by examining key osteogenic markers and proliferation indicates a commitment of hBM-MSCs to the osteogenic differentiation lineage. The Bio-Gide® collagen membrane remained stable and structurally intact after 28 days of *in vitro* culture. Easy handling, retained structural stability, thin shape and osteoconductivity makes this collagen membrane an excellent candidate for delivering osteogenically primed cells into the layered construct, opening avenues for potential *in vivo* investigation.

The concept of employing a layered configuration to facilitate the spatial distribution of biologic substances within the construct has been demonstrated in previous research. A layered construct composed alternating electro-spun PLLA/gelatin nanofibers and MSC meshes has been created with the aim to enhance bone repair.<sup>192</sup> Additionally, recent research shows the development of PCL or titanium constructs employing the LEGO®-inspired block arrangements to be used to repair or augment bony defects.<sup>193,194</sup> The assembly of these constructs are based on small blocks, while our approach revolves around a more user friendly layer-by-layer system. This system allows for the development of a variety of customizable multicomponent constructs (**Figure 4.7**). Through this layer-based approach different materials can be easily combined as demonstrated by creating a layered osteochondral construct.<sup>195</sup> By modulating the porosity of each layer, an outer frame with lower porosity to mimic cortical bone and an inner bulk with higher porosity emulating trabecular bone can be created. Furthermore, this approach allows for spatial delivery options of biological material including different cell types with potential co-culture systems, bioactive

factors, or membranes to create a multicomponent construct. The layer-based approach accommodates the real-time intraoperative integration of autologous substances such as stromal vascular fraction or bone marrow aspirate concentrate into the bone graft substitute (BGS) prior to implantation. The addition of the collagen membrane offers an additional advantage the cells are retained within the layer where they were seeded, rather than falling through the large macropores to the lower layer (data not shown).

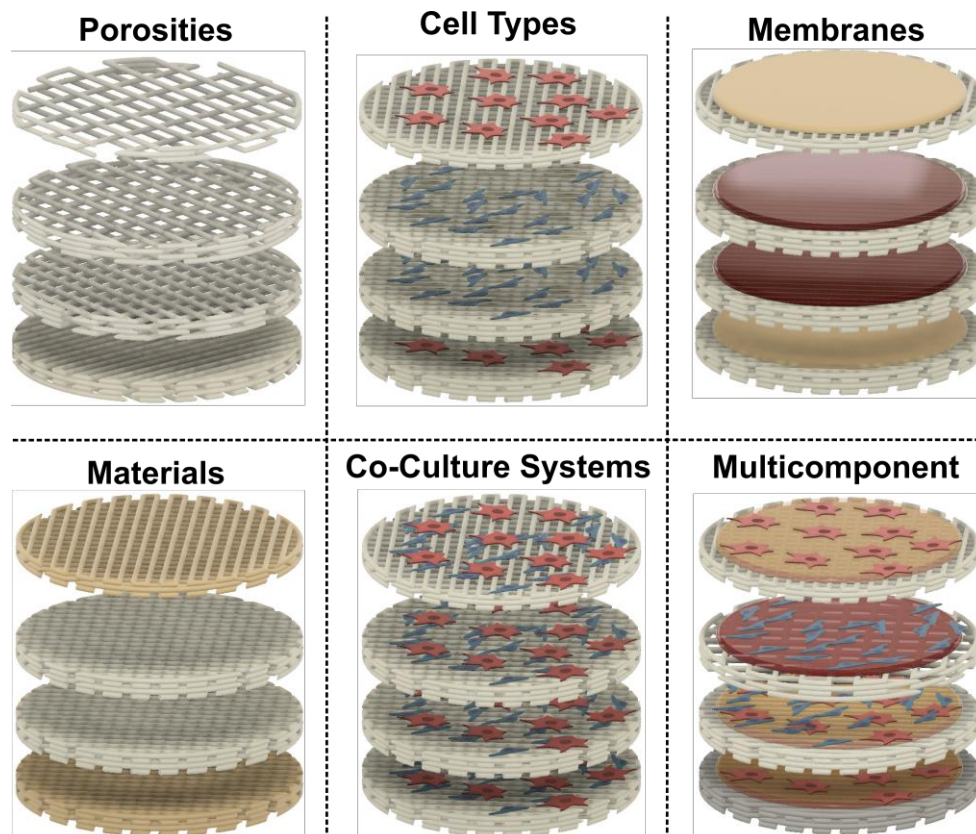


**Figure 4.7: Schematical illustrations** of the different variety of customizing the layer-by-layer multicomponent system.

To demonstrate the osteogenic capabilities of this system, we chose to employ a collagen membrane. Collagen has proven its efficacy in promoting osteogenesis through various applications including hydrogels, membranes, or sponges.<sup>196</sup> Extensive research has been focused on collagen sponges which have been clinically used in conjunction with bone morphogenic protein-2 (BMP-2) for repairing bony

defects.<sup>197</sup> Also, collagen membranes have been utilised in clinical settings to support bone guided regeneration in medicine and dentistry.<sup>198</sup>

Within the scope of this study, we demonstrate that Bio-Gide® collagen membranes allow for hBM-MSCs to differentiate into osteoblasts upon osteogenic treatment, while being incorporated in layered constructs. Other collagen-based membranes including Lyostypt® (BBraun) and collagen cell carrier® (Viscofan Bioengineering) were also tested. However, due to limitations such swelling and structural breaking, respectively (data not shown), these collagen membranes were excluded from this study.

An increased activity and staining of ALP, the main osteogenic marker on the protein level, of the cells is shown under osteogenic condition. Moreover, expression levels of important transcription factors for MSC differentiation options (*SP7*, *RUNX2*, *SOX9* and *PPAR $\gamma$* ) and genes responsible for matrix production and regulation (*COL1A1* and *ALPL*) are increased in response to osteogenic conditions. However, osteogenic markers that are important for late-stage matrix production (*IBSP* and *SPP1*) show an overall unexpected downregulation under osteogenic conditions. The reason of this downregulation is unclear.

One of the primary indicators of osteogenic differentiation lies in the assessment of mineral deposition. This assessment is commonly conducted through staining techniques such as Alizarin Red or OsteoImage® to visualise mineralisation. However, a significant challenge arises due to the fact that collagen membranes, similarly to many biomaterials, stain positive when using these methods. Consequently, distinguishing mineralisation either originating from cells or artifacts present a difficulty. The absence of conclusive mineral deposition results stands as a limitation of this study.

PCL is selected as the foundational material for each layer due to its favourable properties including ease of 3D printability, biodegradability, and robust mechanical strength. Given the load-bearing nature of a large segmental mandibular defect the structural integrity of the implanted scaffold becomes important to withstand the fixation

of a screw-plate system. We acknowledge that layered construct might exhibit reduced mechanical properties compared to the bulk, nevertheless the layered construct should possess sufficient mechanical strength to withstand forces associated with screw fixation, and clinically, load would be distributed over an implanted metal plate. However, the potential decline of mechanical properties of the layered construct remains to be a limitation. Furthermore, the 3D structure of the collagen membrane must be considered in the design of the layered system to prevent the unclipping of the interlocking parts.

A major drawback of the *in vivo* implantation of traditional 3D-printed scaffold in the bulk form is the potential formation of a necrotic core due to limited oxygen diffusion and nutrient supply. To prevent this limitation, the layered construct presents the possibility to create a pre-cellularised/ pre-vascularised system containing endothelial cells within its layers, capable of anastomosing with native vessels post implantation, a future perspective of this study. Furthermore, to enhance successful bone repair, the incorporation of innervation alongside vascularisation can be applied to the system. The combined elements would increase the functional approach to create a BGS. Ultimately, to fully evaluate the osteogenic potential of the layered construct, the final assessments involve an *in vivo* animal study. Such an investigation would serve as a pivotal step before clinical translation can be considered and remains a limitation of this study.

## **4.5 Conclusions**

In this study, we successfully established the development of a patient-specific 3D-printed layered construct composed of PCL. The presented results provide evidence for the osteogenic differentiation of hBM-MSCs cultured on the Bio-Guide® collagen membrane, which are integrated within the layered construct. Herein, we demonstrate the osteogenic potential of a layer-based construct inspired by the LEGO® block arrangements. The adaptability of this system allows for the generation of customizable multicompetent constructs and facilitates the distribution of biological

material within the construct. The versatility of the fabrication system has the potential to bridge the gap in creating a functional BGS that is tailored for the task of repairing large mandibular defects.

## **4.6 Funding**

This work was supported by AO CMF and AO Foundation.

## **5 Clinically Relevant Preclinical Animal Models for Testing novel Cranio-maxillofacial Bone 3D-printed Biomaterials**

### **Statement of Significance:**

Despite intensive research into 3D-printed graft substitutes for repair of cranio-maxillofacial bone defects, their clinical translation has been limited. In this review, we discussed 3D-printed biomaterials tested using preclinical models and highlighted their limitations. Furthermore, we proposed a clinically driven path for the development of new tissue engineered bone graft substitutes for cranio-maxillofacial reconstruction.

Note: This chapter was published in *Clinical and Translational Medicine* as **Clinically Relevant Preclinical Animal Models for Testing novel Cranio-maxillofacial Bone 3D-printed Biomaterials**, Luan P. Hatt, Keith Thompson, Jill A. Helms, Martin J. Stoddart, Angela R. Armiento

Reprinted with permission<sup>4</sup>. Copyright 2022, Wiley

### Author Contributions:

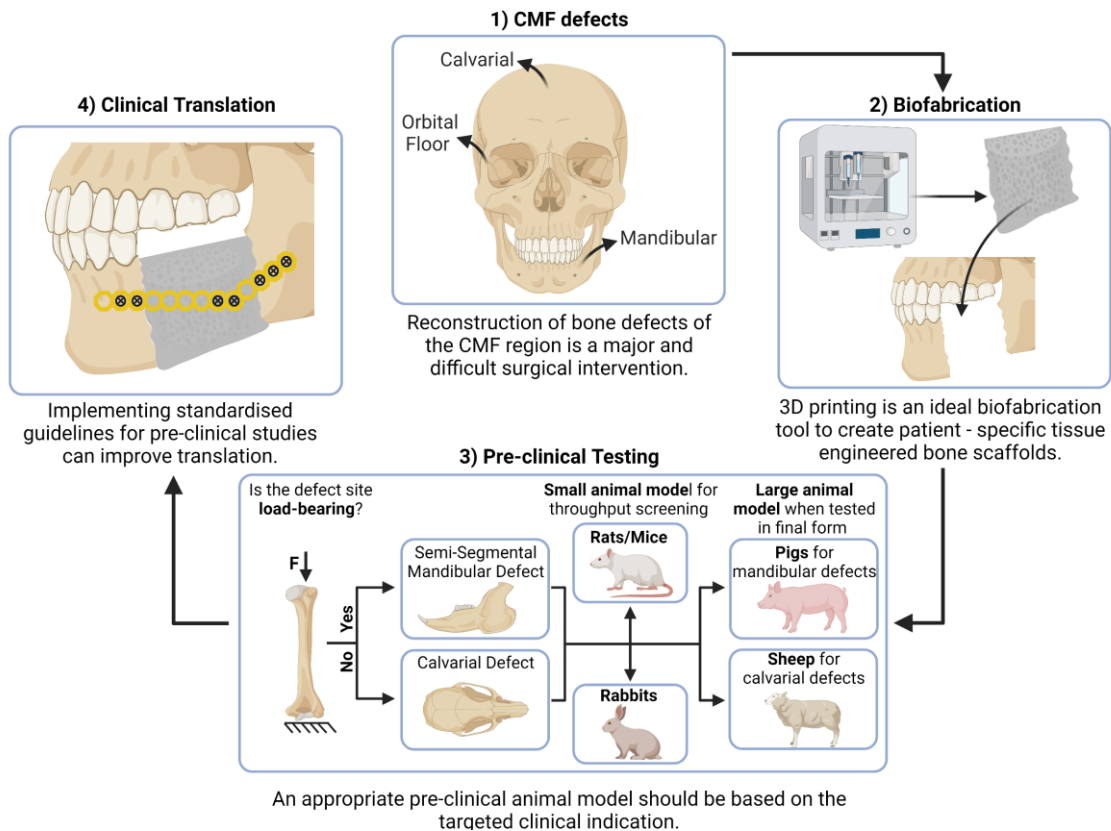
LPH contributed to the paper in terms of conducting and reviewing database searches, extraction and analysis of the data and writing of the original draft. KT contributed to paper in terms of consultation and assistance to the concept development and reviewing and editing of the writing. JAH and MJS contributed to the paper in terms of reviewing and editing of the writing. ARA contributed to the paper in terms of development of the concept, assistance in data analysis, and reviewing and editing of the writing. All authors read and approved the final manuscript.

## **Abstract**

Bone tissue engineering (BTE) is a rapidly developing field with potential for the regeneration of cranio-maxillofacial (CMF) bones, with 3D printing being a suitable fabrication tool for patient-specific implants. The CMF region includes a variety of different bones with distinct functions. The clinical implementation of tissue engineering concepts is currently poor, likely due to multiple reasons including the complexity of the CMF anatomy and biology, and the limited relevance of the currently used preclinical models. The "recapitulation of a human disease" is a core requisite of preclinical animal models, but this aspect is often neglected, with a vast majority of studies failing to identify the specific clinical indication they are targeting and/or the rationale for choosing one animal model over another. Currently, there are no suitable guidelines that propose the most appropriate animal model to address a specific CMF pathology and no standards are established to test the efficacy of biomaterials or tissue engineered constructs in the CMF field. This review reports the current clinical scenario of CMF reconstruction, then discusses the numerous limitations of currently used preclinical animal models employed for validating 3D printed tissue engineered constructs and the need to reduce animal work that does not address a specific clinical question. We will highlight critical research aspects to consider, to pave a clinically driven path for the development of new tissue engineered materials for CMF reconstruction.



## Clinically Relevant Preclinical Animal Models for Testing novel Cranio-maxillofacial Bone 3D-printed Biomaterials



**Graphical Abstract:** Reconstruction of bone defects of the CMF region is a major and difficult surgical intervention. 3D printing is an ideal biofabrication tool to create patient specific tissue engineered bone scaffolds. An appropriate pre-clinical animal model should be based on the targeted clinical indication. Implementing standardised guidelines for preclinical studies can improve translation. Created with BioRender.com.

## 5.1 Introduction

Reconstruction of bone defects of the cranio-maxillofacial (CMF) region, such as large segmental mandibular defects resulting from trauma, tumour excision, infections, or congenital deformities, is a major surgical intervention. To date, transplantation of an autologous bone graft (ABG) is the standard of care (SOC) to restore both the functional and aesthetic aspects of such defects.<sup>51</sup> However, ABG is associated with a number of important drawbacks including limited availability, donor site morbidity<sup>122</sup>, a loss of osteogenic potential as the patient ages and, perhaps most importantly, the fact that autografts tend to undergo significant resorption over time. Together, these drawbacks highlight an urgent clinical need for alternative effective approaches to optimally restore bone tissue in the CMF arena.

To replace autologous bone grafts as the SOC, the replacement should demonstrate equivalent or improved functional and aesthetic outcomes, with minimal drawbacks. The bone graft substitute (BGS) should be osteoconductive, as well as osteoinductive, unlimited in supply, and mouldable to adapt to the irregular geometries frequently encountered in CMF reconstructions. Lastly, the material should be long lasting, i.e., withstand resorption, and should integrate seamlessly into the existing bone tissue at a rate equivalent to that of an autologous bone graft. To date, no BGS has fulfilled all these functions. Although promising tissue engineering concepts have passed both *in vitro* and *in vivo* safety assessments<sup>199</sup> the BGS must also demonstrate superior performance, to effectively replace the current SOC and ensure wide-scale clinical deployment. This requires robust preclinical models that closely recapitulate the features of the corresponding human clinical disease. In reality, the “recapitulation” aspect has often been neglected, with many research groups failing to describe the clinical indication they are targeting, and/or the particular rationale for choosing a specific animal model.<sup>200</sup> Without suitable guidelines that indicate the specific pathology being addressed, and a rigorous analysis of the most appropriate animal model, it should come as no surprise that most BGS fail to achieve the effects observed in preclinical studies when deployed in the clinical setting.

Although many technologies and fabrication innovations have been applied to produce such a BGS, the focus of this review concerns the use of the 3D printing approach, which is a particularly interesting tool for the CMF area since it allows for recapitulation of complex architecture and patient-specific geometry. Given this focus, we discuss only 3D printed strategies used in preclinical studies as representative examples, to narrow the otherwise very large pool of publications in the field of bone tissue engineering (BTE).

This review reports the current clinical scenario of CMF reconstruction, to first discuss the limitations of current preclinical models, followed by the ethical need to reduce animal work that does not address a specific clinical question and highlight critical research and clinical aspects. Factors to consider in choosing a preclinical model – including the anatomical location and type/size of the defect, as well as the incorporation of critical variables that affect patient outcomes, such as age and other co-morbidities that potentially impact bone healing, are also discussed. To conclude, we propose a clinically driven path for the development of new tissue engineered BGS for CMF reconstruction.

## **5.2 CMF Bone Structure and Healing**

CMF bones (**Figure 5.1A**) not only differ in their healing process<sup>201</sup>, but also differ in their structural framework and function. The macrostructure of CMF bone exists in the form of compact bone, which is permeated by interconnected canals called the haversian system, and cancellous bone, which has a porous structure that gives a honeycomb appearance. The interconnected haversian canals allow for a highly vascularised and innervated bone tissue. In the CMF complex, the bone supporting the teeth has a cancellous microstructure until teeth are lost then, concomitant with the edentulous state, cancellous bone is replaced by compact bone.<sup>202</sup>

Bone is a highly dynamic tissue that maintains its homeostasis through the process of bone remodelling. During this process, the activity of osteoblasts, osteocytes and osteoclasts is orchestrated by a multitude of tightly regulated molecular signalling

## Clinically Relevant Preclinical Animal Models for Testing novel Cranio-maxillofacial Bone 3D-printed Biomaterials

pathways including canonical Wnt/ $\beta$ -catenin and receptor activator of nuclear factor- $\kappa$ B (RANK)/RANK ligand pathways. In the context of the CMF skeleton, osteoblasts have a dual origin, arising from either mesoderm (parietal and occipital bones) or the neural crest (frontal, ethmoid, sphenoid and facial bones)<sup>203,204</sup>, with neural crest derived osteoblasts possessing a reported greater osteogenic potential.<sup>205</sup>

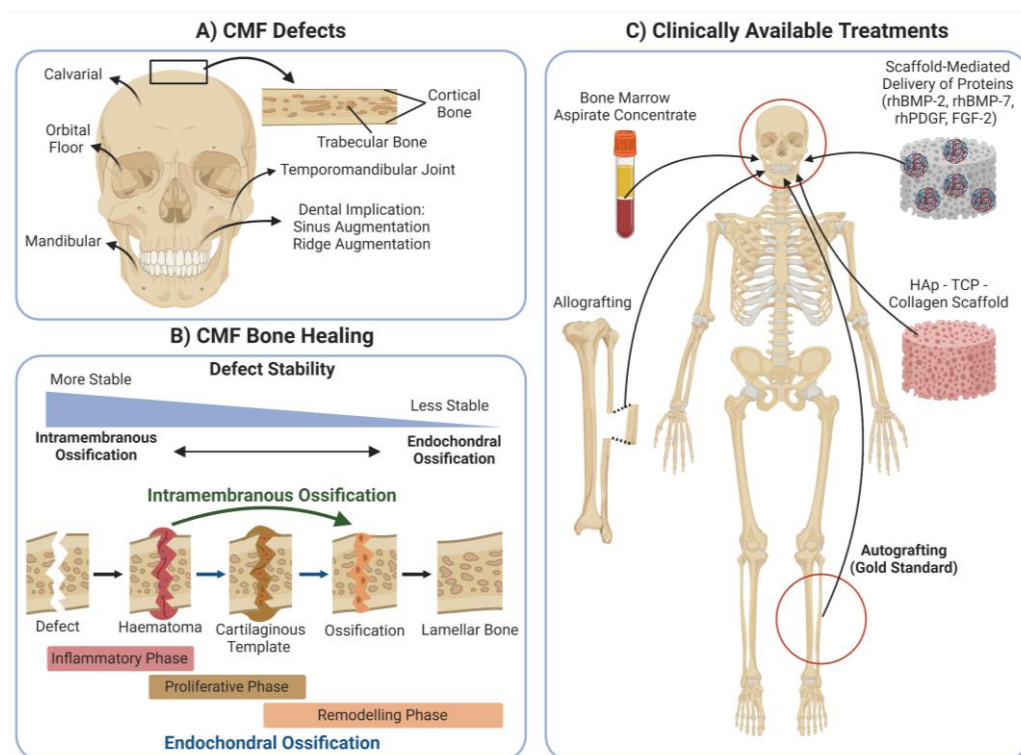


**Figure 5.1: Schematic overview of A) Cranio-maxillofacial (CMF) defects, B) CMF bone healing through either intramembranous or endochondral ossification and C) Clinically available treatments.** rhBMP: recombinant human bone morphogenic protein; rhPDGF: recombinant human platelet-derived growth factor; FGF-2: fibroblast growth factor 2; HAp: hydroxyapatite; TCP: tricalcium phosphate. Created with BioRender.com.

The regenerative capacity of CMF bone healing is often diminished (**Figure 5.1B**), perhaps in part due to limiting factors such as the relatively thin nature of the periosteum and the comparative lack of marrow space. A temporal and spatial coordinated response of numerous cell types is also required during bone healing.<sup>206</sup>

During the initial acute inflammation of bone healing, inflammatory cells including lymphocytes, macrophages, eosinophils and neutrophils are recruited to the haematoma of the fracture site.<sup>207</sup> Important pro-inflammatory cytokines in this process include TNF $\alpha$ , the interleukins IL-1 and IL-6, as well as growth factors such as fibroblast growth factor (FGF), platelet-derived growth factor (PDGF) and transforming growth factor  $\beta$  (TGF $\beta$ ), which initiate and coordinate the repair process.<sup>208,209</sup> The repair also involves vasculogenic and angiogenic responses driven by vascular endothelial growth factor (VEGF), and the recruitment of reparative progenitor cells including mesenchymal stromal cells (MSCs).<sup>207</sup> These MSCs may then differentiate to either osteoblasts or chondrocytes, depending on the nature of the injury and the local mechanical environment, leading to the initiation of bone formation<sup>210</sup>.

Bone healing occurs via two distinct processes, termed endochondral or intramembranous ossification, which is critically dependent on the stability of the injured bone and the degree of interfragmentary strain generated during the reparative process.<sup>211,212</sup> The endochondral route of bone healing predominantly occurs in response to instability of the bone fragments, and is the major route of healing in long bones and vertebrae<sup>213</sup>, as well as flat and irregular CMF bones without rigid stabilisation<sup>214</sup>, as demonstrated by the presence of a cartilaginous tissue during the healing of a mandibular defect in a rabbit model<sup>215</sup> and in a mouse mandibular fracture model.<sup>216</sup>

Intramembranous ossification is characterised by the direct differentiation of osteoprogenitor cells into osteoblasts<sup>206</sup> and is the primary route for the formation of the flat bones in the cranium and some irregular bones such as the mandibles. To achieve direct ossification during bone healing, a correct anatomical reduction and a rigid fixation is required to limit movement of the bone fragments.<sup>217</sup> Both bone healing mechanisms are tightly connected to angiogenesis and rely on the establishment of a functional vascularisation.<sup>213,218</sup>

### 5.3 Standard Care and Clinically Available Solutions

Clinically available treatments for the reconstruction of bone defects are numerous and include autologous bone graft, allograft, demineralised bone matrix, hydroxyapatite (HAp), calcium phosphate (Cap), bone morphogenetic proteins (BMPs; e.g. BMP-2 and BMP-7), collagen scaffolds, and bone marrow aspirate concentrate (**Figure 5.1C**).<sup>219</sup>

Autologous bone graft is the current SOC for bone reconstruction, with a 90% success rate, for which the free vascularised fibular flap was concluded to be a reliable source for the reconstruction of mandibular defects with positive aesthetic and functional outcomes including mastication, radiodensity of the bone and bone resorption rate, as well as minimum failure rate.<sup>51</sup> Advantages of using an autologous bone graft are the availability of osteoprogenitor cells and the presence of a mineralised matrix scaffold that include desirable osteo-inductive/conductive properties, thereby allowing the graft to integrate at the site of transplantation<sup>220</sup>, and improved regeneration due to anastomosis of the vital tissue. However, numerous drawbacks of autologous bone graft use have been highlighted, including: donor site morbidity issues (e.g. pain or infection)<sup>221</sup>; limited availability from the host<sup>222</sup>; diminished osteogenic potential in older patients<sup>223</sup>; significant loss in volume of the autologous bone graft over time due to resorption<sup>224,225</sup>; potential for increased blood loss due to extended surgical duration; and lack of geometric accuracy for the defect site compared to its original shape.

Due to their increased availability, cadaveric donor allografts are also used clinically as an alternative to autologous bone grafts.<sup>226,227</sup> However, allografts are devoid of osteoprogenitors and pro-osteogenic proteins<sup>228,229</sup> and have a rapid resorption rate<sup>230</sup>, which diminishes their clinical efficacy<sup>231</sup>.

A tissue engineering alternative to autologous bone grafts is the scaffold-mediated delivery of proteins such as rhBMP-2<sup>32</sup>, rhBMP-7<sup>232</sup>, recombinant human PDGF-BB<sup>233,234</sup>, or FGF-2.<sup>235</sup> Administration of rhBMP7 in combination with bovine collagen (OP-1<sup>®</sup>), or rhBMP-2 via a resorbable collagen sponge or HAp/ $\beta$ -tricalcium phosphate

( $\beta$ -TCP) (INFUSE® Bone Graft and MASTERGRAFT™ Granules, respectively) are FDA-approved options. INFUSE® Bone Graft is approved for lumbar spine fusion, open tibial fractures and CMF reconstruction, and is often used off-label for large segmental defects.<sup>236</sup> However, the use of rhBMP has been associated with major side-effects including ectopic bone formation<sup>237</sup>, osteoclast-mediated bone resorption<sup>238</sup>, postoperative inflammation and inappropriate adipogenesis<sup>239</sup>, as well as increased cancer risk for off-label<sup>240</sup> or high dosage rhBMP-2 administration<sup>241</sup>. Given these major safety issues, an FDA black box warning on high-dose BMP-2 was issued in 2008.<sup>32</sup> Although BMP-2 use has been associated with potential carcinogenic effects, this remains a contentious issue in clinical practice due to a limited number of high-quality clinical studies on the subject.<sup>242</sup> However, since CMF bone reconstruction is frequently required following tumour resection, further high-quality and independent clinical studies involving the safe use of BMP-2 are clearly warranted.

Thus, although autologous bone grafting (ABG) remains the SOC in the clinic today due to the inherent limitations associated with its availability there is an urgent and, as yet unmet clinical need for safe and viable alternatives.

## **5.4 Tissue Engineering as a Promising Alternative**

Tissue engineering is a rapidly developing field that has been applied in multiple research disciplines, including the musculoskeletal realm. Tissue engineered constructs for bone applications are typically composed of a biocompatible, resorbable material with specific architecture, often combined with progenitor or differentiated cells and/or osteogenic/angiogenic growth factors to provide the biomolecular cues that mimic the complexity of bone tissue. While biological factors are crucial for the initial host cell invasion of the tissue engineered construct, it is evident that mechanical stability and porosity of the material play also an important functional role. A tissue engineered product targeting the restoration of a large bone defect must act as a place holder, promote the ingrowth of native tissue, and degrade over a suitable timeframe to allow regeneration of the defect area.

Modern tissue engineering increasingly relies on biofabrication technologies to design and manufacture complex biomimetic materials. Of particular interest for the regeneration of CMF defects is the process of additive manufacturing, also known as 3D printing, which allows the creation of complex patient-specific solutions. 3D printing now refers to more than merely thermal-based extrusion of polymers. The choice of material ranges from materials such as CaP pastes or metals to hydrogels, and may also include cells, referred to as bioprinting. The use of 3D printing for CMF bone repair is summarised in a recent systematic review, which includes human and animal studies, with a focus on the scaffold's fabrication process and properties, as well as its combination with growth factors and cells.<sup>243</sup> Different types of 3D printing technologies are also described, which encompasses inkjet printing, laser assisted printing and extrusion-based printing.<sup>243</sup> In further developments of 3D printing, novel 4D printing materials can be produced, which can change shape through the application of an external stimulus post-printing.<sup>244</sup>

Commonly used materials in BTE can be divided into CaP-based materials, such as  $\beta$ -TCP, HAp or CaP cement<sup>245</sup>, and polymer-based materials, such as polylactic acid, poly(lactic-co-glycolic acid: PLGA) and polycaprolactone (PCL)<sup>246</sup>, which are often combined to obtain an osteo-conductive and/or -inductive engineered material. Several advanced approaches have been undertaken to improve material properties such as: implementing piezoelectric materials, e.g. poly(vinylidene fluoridetrifluoroethylene) tested in the rat calvarial defect model<sup>247</sup>; incorporating magnetic components, e.g. magnetite nanoparticles into a nano-HAp/chitosan/collagen mixture, tested in a rat calvarial defect model<sup>248</sup>; or exploiting further advanced strategies like biomimetic 4D printing<sup>249</sup> or shape memory polymers, evaluated in a mouse femoral defect model,<sup>250</sup> to name but a few examples. Additional advanced and smart biomaterials, and strategies to improve bone healing, have been covered in detail in numerous reviews.<sup>199,251</sup>

Encapsulation of MSCs (derived from bone marrow, adipose tissue, or perivascular MSCs<sup>252</sup>) within the scaffold is another approach to improve the osteo-conductive and



-inductive properties of the construct by exploiting the secretome of the embedded MSCs, which has been shown to successfully heal a mouse calvarial defect when osteogenically pre-differentiated MSCs were implanted in combination with a chitosan collagen microtissue<sup>253</sup>, as well a rat calvarial defect with a dental pulp stem cell-laden collagen gel scaffold.<sup>254</sup> Incorporation of endothelial cells in co-cultures with MSCs have also been used to create pre-vascularised constructs to improve nutrient delivery, as shown by incorporating peripheral blood-derived MSCs in combination with endothelial colony-forming cells into a PLGA/fibrin construct.<sup>255</sup> Further strategies have been developed to create such a vascularised implant, for example, by perfusing HUVECs through a channelled biomaterial to create functional vessels<sup>256</sup>, or via applying a flow bioreactor to a HUVEC-laden biomaterial.<sup>257</sup> Osteogenic factors can be chemically bound to the scaffold (biofunctionalisation), or the scaffold may be used as a carrier to deliver osteogenic and/or angiogenic factors, as demonstrated by creating a HAp complexed with BMP-2 and VEGF peptides, tested in a diabetic rat femoral model.<sup>258</sup> Increased delivery of these factors can be achieved by genetically engineering cells via gene delivery, as reported for hBM-MSCs transfected with hBMP-2 using a lentiviral vector system implanted into a intramuscular mouse model<sup>259</sup>, and the implementation of hBM-MSCs co-transfected with hBMP-2 and FGF-2 via a polyethylenimine complex into a rabbit radial defect model<sup>260</sup>.

It is increasingly realised that the immune system plays a crucial role in the efficacy of tissue regenerative approaches. As such, the material of choice should prevent undesirable inflammatory responses and preferably promote favourable reparative immunological responses, such as the induction of reparative macrophage populations capable of secreting cytokines TGF $\beta$  and interleukin 10, which have been shown to enhance bone formation.<sup>261</sup> Furthermore, a specific population of periosteum-resident macrophages (osteomacs) have been shown to play critical roles in bone homeostasis and the healing response following fracture.<sup>262</sup> Thus, it is likely that successful bone reparative responses will require consideration of effects on such cell populations.

In addition, extracellular stimuli such as the stiffness, roughness, and porosity of the material can also affect cell proliferation, migration, and differentiation. Increased surface roughness of the material results in enhanced protein adsorption, thus improving cell attachment<sup>263</sup> and osteogenic differentiation of MSCs.<sup>264</sup> Effective invasion of cells is also dependent on the pore size of the material, as demonstrated in calcium-based ceramic materials within which bone and blood vessel ingrowth requires a minimum pore size of 150  $\mu\text{m}$ , with 400  $\mu\text{m}$  being the upper limit for vascularisation.<sup>14</sup> Material stiffness also affects cell morphology and differentiation. Fibroblasts acquire a round morphology on soft materials (180 Pa) while they flatten on stiffer ones (16 kPa)<sup>265</sup>, with similar effects observed with MSCs.<sup>266</sup> Materials with a stiffer elastic modulus (25-40 kPa) also induce osteogenic differentiation of MSCs when compared to softer materials.<sup>267</sup> Optimal biomaterial design strategies have been discussed by Dewey and Harley with specific insights on the importance of immune responses, as well as the interaction of multiple cell types for CMF bone healing.<sup>268</sup>

## **5.5 From a Promising Tissue Engineering Concept to a Clinically Justified Product**

*In vitro* studies have identified a variety of promising materials of differing degrees of complexity and yet, with the exception of a scaffold-based delivery of factors previously mentioned, most of the tissue engineered products identified to date have failed to demonstrate equivalent efficacy when compared to autologous bone grafts.

It is therefore important to consider the typical routine behind the development of a new material and discuss the reasons why the multitude of promising materials fail to translate into the clinical setting. Currently, the most widely used model for assessing material efficacy is the calvarial defect model in rodents. However, the specific features of the calvaria raises the question as to the wider applicability of findings from efficacy testing for other sites in not only the CMF region but also other parts of the skeleton, with their specific anatomical and mechanical loading environments. Thus, it is important to tailor a specific animal model according to the bone tissue of interest, to

more faithfully recapitulate the appropriate clinical scenario in which the material will ultimately be deployed.

## **5.6 Preclinical Studies Targeting the Regeneration of CMF Bone Defects**

In this section we provide a series of recently reported applications of preclinical animal models to test the safety and efficacy of materials claimed to target CMF bone reconstruction. For clarity, the examples will be divided into calvarial, mandibular and orbital floor models. The presented studies are representatives from a large pool of preclinical studies using these models. Since 3D printing is a crucial technology for patient-specificity, an inevitable direction for future CMF bone repair strategies, only studies that use a scaffold-based tissue engineered approach fabricated using additive manufacturing printing have been included, with the aim to regenerate critical-sized bone defects and using a CMF bone model. We did not focus on all biomaterials as these have been well described and discussed in other recent reviews.<sup>268-270</sup> Further inclusion criteria are that the studies are being recent, being published between 2015 and 2021, and need to contain an animal study in which the 3D printed tissue engineered construct has been evaluated. Studies that involve 3D printing indirectly as a support system have also been excluded. 48 out of 75 papers were identified using PubMed for the calvarial defect model with the keywords "calvarial defect 3D printing", 17 out of 123 for the mandibular defect model with the keywords "mandibular defect 3D printing", and 1 out of 1 for the orbital floor defect model with the key words: "orbital floor defect additive manufacturing". The search was conducted on the 8<sup>th</sup> of October 2021. Multiple implant strategies (surface modification, drug and cell delivery) specifically aimed for bone tissue restoration, were taken into consideration.

### ***Calvarial defect model***

Preclinical models involving calvarial bone defects are one of the most widely employed approaches to assess safety and efficacy of biomaterials due to their relative simplicity and reproducible nature. A sagittal incision is made to expose the calvarium

and circular defects are created using a trephine burr.<sup>271</sup> The anatomical location allows for easy surgical access and intraoperative handling without the need for internal or external fixation of the material.<sup>48</sup> Reproducibility of the created defect and bone formation<sup>272</sup> can be easily assessed radiologically and histologically<sup>48</sup> but, due to the unloaded nature of the calvaria, the impact of mechanical stimulation cannot be routinely assessed in this model.<sup>48</sup> Studies using the calvarial model to validate tissue engineered constructs are presented in **Table 5.1**. Common strategies include the delivery of drugs, biofunctionalisation of the construct, incorporation of MSCs, and the use of endothelial cells to create a prevascularised construct. Rats, followed by rabbits, are the most used preclinical animal models for this CMF region. The defects are generally created using a trephine burr and have a diameter ranging from 2.7-4 mm in mice, 4-9 mm in rats, 8-15 mm in rabbits, and 11 mm in sheep, which are considered critical-sized (and are therefore unable to heal naturally without intervention). The duration of the study typically ranges from 4 weeks up to 72 weeks, with time points typically starting after 2-4 weeks. Histological analysis (48 out of 48) is the prevailing method used to assess bone healing, together with CT scanning (35 out of 48) and immunohistochemistry (13 out of 48). Although the technique is relatively standardised and reproducible, care must be taken to avoid injuring the dura mater that leads to reduced healing.<sup>273</sup> As previously mentioned, the periosteum is a critical tissue for bone repair, being a valuable source for regenerative cells, blood vessels for nutrient supply<sup>274</sup>, but also contains sensory neurons. As a source of the neuropeptides substance P and calcitonin gene-related peptide, sensory neurons appear to play important roles in the bone healing process<sup>275</sup>, and fracture repair in long bones has recently been shown to require nerve growth factor expression in periosteal cells and tropomyosin receptor kinase A signalling in skeletal sensory nerve fibres<sup>276</sup>. Therefore, damage to the periosteum may limit bone healing by interfering with these reparative processes and/or cell populations and should therefore be avoided where at all possible.

### ***Mandibular defect model***

Mandibular defects can be distinguished in continuity and non-continuity defects. Non-continuity defects have a circular or rectangular geometry without the loss of the mandibular unity so that an additional mechanical fixation is not required. These defects are more often used in small animal models that can provide information on both biocompatibility and efficacy of tested constructs, but often fail to adequately mimic the clinical setting such as load-bearing and size, as previously described for calvarial defects.<sup>277</sup> A clinical example for using non-continuity defects in a preclinical model is bone healing following tooth extraction. Continuity defects are typically segmental resections with loss of mandibular continuity, such as those seen clinically following tumour resection, and therefore require internal fixation to provide adequate mechanical stability, illustrated in **Figure 5.2A**. Due to the complexity of the procedure, this type of defect is more often used in large animal models, with which the clinical condition is more accurately resembled<sup>277</sup> and the load-bearing capacities of BGSs can be adequately assessed.<sup>48</sup>

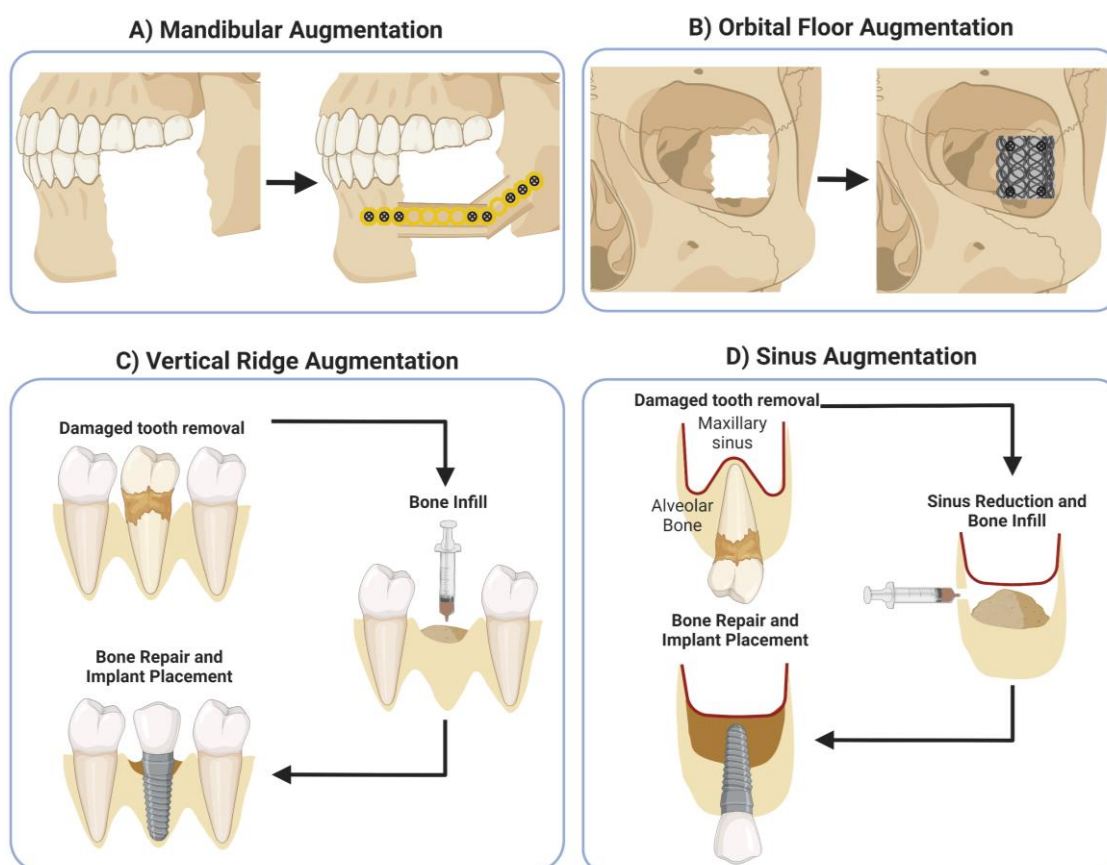


**Figure 5.2: CMF augmentation techniques.** Created with BioRender.com.

Preclinical studies using the mandibular defect model are shown in **Table 5.2**. In addition to small animal models, such as rats and rabbits, large animal models such as minipigs, beagle dogs and sheep are also used. Most of the created defects are semi- or completely segmental and are therefore created using a saw instead of a burr. Semi- or completely segmental defects have a high range of sizes used across different species, with  $30 \text{ mm}^3$  in rats, 240 to  $750 \text{ mm}^3$  in rabbits, 105 to  $2000 \text{ mm}^3$  in beagle dogs and 2800 to  $12000 \text{ mm}^3$  in pigs. Typically, cylindrical defects are created using a burr and have a diameter of 4-5 mm in rats and 8 mm in rabbits. As described for the calvarial defect, histological-based assessment (17 out of 17) is the main method to assess healing, and most studies also include CT scanning (15 out of 17) and some include immunohistochemistry (3 out of 17) or mechanical testing (2 out of 17) as additional approaches. Study duration is typically 8 or 12 weeks, with longer

studies up to 24 and 32 weeks. Complications associated with mandibular defects include microbial infections when using intra-oral approaches<sup>278</sup>, and also plate failure in continuity defects.<sup>279</sup> In addition, the choice of suitable animal species for mandibular defects is complicated due to confounding effects of the long, continuously erupting incisors present in small animal models (e.g. mice, rats, rabbits). Such mandibular defects typically cut into the tooth in such species, with resulting injury to the tooth, periodontal ligament, cementum, dentine and pulp. As such, these mandibular defects in small animals are markedly different to equivalent defects in large animal models and patients.

### ***Orbital floor model***

Common materials utilised to clinically reconstruct the orbital floor following injury include metal alloy, titanium, polylactic acid and HAp composites. These reconstruction strategies target the replacement rather than regeneration of bone, illustrated in **Figure 5.2B**. Only one preclinical study with the aim to regenerate the lost bone in the orbital floor was chosen according to the criteria and is presented in **Table 5.3**. The described sheep study involved an irregular shaped defect created using a retractor and pean forceps, being 6x 9 mm<sup>2</sup> in size.<sup>280</sup> Histological analysis is, again, the main evaluation method used, in addition to CT scanning. Specific for this model, the restoration of the normal position of the eyeball within the socket is often assessed. The duration of the animal study is 12 weeks. Complications arising from the surgical approach in this model have not been reported.

### ***Vertical ridge augmentation and sinus augmentation***

Additional CMF-relevant issues include dental reconstructive approaches such as vertical ridge augmentation and sinus augmentation in combination with dental implant placement. Main reasons for tooth loss are periodontal disease and dental caries, and the osseointegrated dental implant is one of the most used biomaterials to replace missing teeth with long term outcome success.<sup>281</sup> The lack of supporting bone due to atrophy, trauma, failure to develop, or surgical resection prevents implant placement

and can be repaired via vertical ridge augmentation, illustrated in **Figure 5.2C**.<sup>282</sup> ABG used as the BGS is considered the SOC for bone augmentation in this context.<sup>282</sup> Dental implant placement in the posterior region of the maxilla is prone to implant failure caused by trauma, atrophy in the alveolar process or sinus pneumatization, the development of air-filled cavities, which can be minimised by applying a sinus augmentation prior to implant placement.<sup>283</sup> Sinus augmentation, illustrated in **Figure 5.2D**, enables the reduction of the sinus cavity and the filling of bone material, mostly in the form of autologous bone graft, to maximise bone area for improved implant stability.<sup>284</sup>

## **5.7 Towards Clinically Driven Animal Models**

The previous section has demonstrated that numerous studies investigating regeneration of CMF bone defects use a variety of different materials, fabrication technologies and animal models. Only 18 out of 48 studies employing a calvarial model clearly state the CMF application to be targeted with the developed material (**Table 5.1**). Conversely, 15 out of 17 studies using a mandibular model define a CMF application as their clinical target (**Table 5.2**). Only 7 out of 66 of the presented preclinical studies justify the use of a specific animal model (**Table 5.3**). Two examples of preclinical studies from Guillaume *et al.*<sup>280</sup> and Konopnicki *et al.*<sup>285</sup> can be highlighted in which both studies not only target a specific CMF application including employment of the appropriate defect site, but also use a large animal model with justification of its usage (**Figure 5.3**). While there are some obvious similarities in the approaches used, there remain important differences in the size/geometry of the defects, the surgical procedures, study durations and outcome assessments, which makes conclusive judgements regarding efficacy challenging, and also raises questions on the relevance of multiple animal models targeting the same CMF application. In addition, there are a number of further highly relevant clinical CMF indications that lack appropriate model systems. As an example, temporomandibular joint (TMJ) reconstruction is a particular clinical challenge, which, given the complex mechanical environment of the TMJ, poses additional concerns about how to faithfully recapitulate such an environment in



## Clinically Relevant Preclinical Animal Models for Testing novel Cranio-maxillofacial Bone 3D-printed Biomaterials

a preclinical model to investigate the efficacy of regenerative approaches. Established solutions and key developments for targeting the reconstruction of TMJ has been presented in a review by Imola and Liddell.<sup>286</sup> and the use of preclinical models for TMJ tissue engineering has been reviewed by Almarza et al.<sup>287</sup>

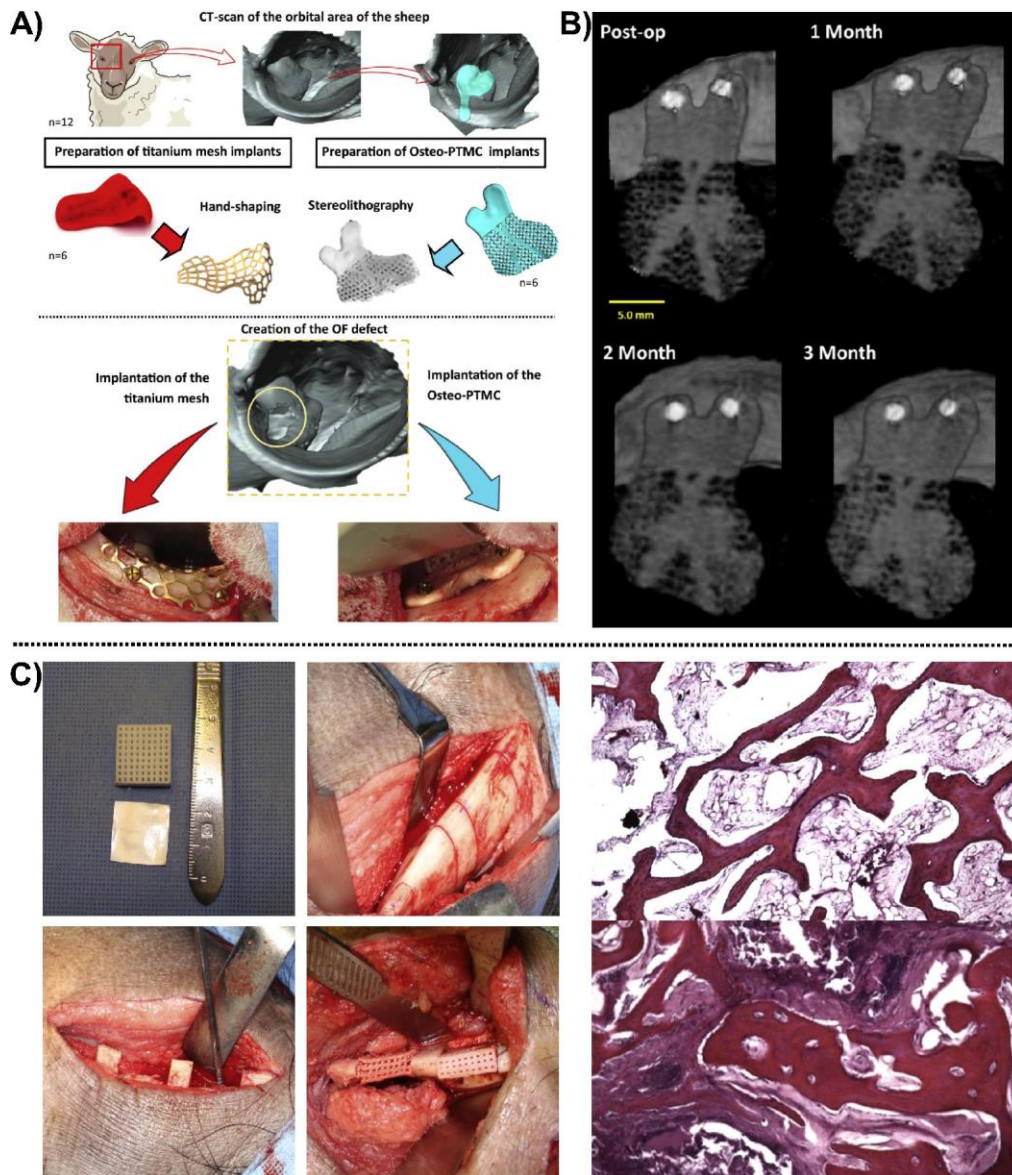


**Figure 5.3: The use of large animal models for CMF application:** A) General workflow and study involving pre-operative phase and surgery phase using an orbital floor sheep model, B) Results of time-lapse CT scans of the implanted 3D-printed scaffold show increased mineralisation over time. Reproduced from Guillaume et al. with permission<sup>280</sup>. C) Left column: Intraoperative images of a pig

mandibular reconstruction surgery using a 3D-printed porous scaffold. Right column: Results of histology images (stained with hematoxylin and eosin) show increased bone formation in the experimental group (lower image) compared to the empty defect (upper image). Reproduced from Konopnick et al. with permission<sup>285</sup>.

Preclinical safety and efficacy testing of bone implants is initially performed *in vitro* prior to *in vivo* assessment.<sup>288</sup> Regulatory agencies demand the validation of a preclinical animal model prior to clinical investigation, but selecting the appropriate model can be challenging.<sup>289</sup> Stating the selection criteria or justification of the relevance of the chosen animal to humans is rarely included.<sup>290</sup> Current ISO requirements (ISO 7405:2018) dictate that medical and dental implants should be tested in their final human form and, consequently, large animals must be employed for such pivotal preclinical efficacy testing. Thus, the choice of an appropriate experimental animal model is essential to obtain clinically justifiable preclinical data on which to base subsequent trials in humans. An animal model should guarantee minimal morbidity and maximal reproducibility, but, most importantly, should faithfully reproduce the clinical condition for which the material will be employed.<sup>200,291</sup> From a regenerative point of view, critical size defects of CMF bones such as segmental mandibular defects pose the biggest challenge<sup>292</sup>, because of their poor intrinsic healing capacity<sup>293</sup> and the additional complications posed by the use of internal plate fixation in animals that may frequently fail during the time course of the study. In addition, the definition of what constitutes a critical-sized defect in different species remains an important consideration in order to standardise preclinical models.<sup>96</sup> This is further compounded by the additional variability also arising from the choice of specific animal species/strain, the location, size and type of defect, the choice of appropriate control groups, the time points assessed, and the experimental outcome evaluation.

### ***Size animal/species/strain***

Small animals remain the preferred choice for most research laboratories due to the lower costs associated with animal purchase and housing, and the surgery skills are widely available.<sup>294</sup> However, there are potential species-specific differences in bone

remodelling, composition and healing responses that require careful consideration to assess material efficacy between species. This is especially challenging for the CMF bone, due to the limited knowledge about the reproduction of the human condition using particular models<sup>290</sup> and the lack of evidence that appendicular bone can appropriately represent CMF bone.<sup>288</sup> A review on differences in large animal appendicular bone remodelling suggested human, pig, dog, sheep and goat were moderately similar, while the rabbit was least comparable.<sup>295</sup> Aerssens et al. in 1998 compared the composition, density and mechanical competences of appendicular bone in human, dog, pig, cow, chicken, rat and sheep and showed distinct interspecies differences, with the dog and rat being the most and least comparable, respectively, to human bone properties.<sup>296</sup> Specifically, femoral bone samples from seven species were compared and reported that rat bones differed from human bones in terms of their ash, collagen and IGF1 contents.<sup>296</sup> However, studies using more modern analysis methods have challenged the relevance of these differences. A 2011 study utilising CT analysis concluded that smaller animals are a useful tool, depending on the specific research question being asked.<sup>297</sup> Furthermore, other researchers provide evidence that rodent remodelling is similar to humans, thereby suggesting that rodent models are justified since the relevant cellular and molecular cues for remodelling are consistent with humans<sup>298</sup>, and regulation of the process via growth factors, chemokines and cytokines is also comparable.<sup>299</sup> In a 2020 study specifically investigating alveolar bone morphology, Pilawski et al did not find evidence to conclude the superiority of pig models over rodent models in an interspecies comparison study using histology, immunohistochemistry and vital dye labels.<sup>288</sup> One known biological discrepancy between rodents and humans is the reduced efficacy of rhBMP-2 in human orofacial bone regeneration, including tooth extraction socket healing, sinus augmentation or reconstruction of alveolar clefts.<sup>300</sup> Thus, this is a particularly contentious area and the limited number of in-depth, comparative interspecies analyses, particularly in relevance to alveolar bone and CMF applications, make conclusive statements difficult. Given the fact that none of the animal models under evaluation perfectly resembles the human situation, aspects such as quantifiable

differences in bone mechanical strength, size of the test material and the potential biological mechanism of action should all be considered when choosing the correct animal model.

A further issue arises concerning the predominant use of young, healthy animals in preclinical models, which does not typically reflect the increased age and potential comorbidities, such as impaired vascular function and reduced angiogenic responses<sup>218</sup>, present in human patients. For example, young rabbits are often used for preclinical studies but, due to their high rate of cortical bone remodelling compared to humans, they can be a poor representative of such a process.<sup>301</sup> Furthermore, aging is increasingly realised as influencing numerous cellular processes including immune responses, potentially impacting on fracture healing outcome.<sup>302</sup> Until more representative preclinical models, such as those involving aged or diabetic models<sup>218</sup>, the predictive nature of such studies will continue to frustrate researchers regarding clinical translation.

Studies involving the implantation of human cells use immunocompromised small animal models, thereby creating an additional issue for subsequent extrapolation to human physiology, leads to a major challenge: what is a suitable animal model to study the bone healing potential of a cell-based therapy? It is established that immunocompetent mice have differences in bone regenerative potential compared to immunodeficient mice within the same strain.<sup>303</sup> Even within species, different mice strains are known to have differences in bone mechanical properties<sup>304</sup>, immune responses<sup>305</sup>, rates of fracture healing<sup>306</sup> and healing capacities overall.<sup>307</sup> Thus, it is important to consider different strain types and include strain information in each study.<sup>307</sup> Even in large animal models, immunological differences are evident, with different breeds of sheep shown to have altered disease susceptibilities<sup>308</sup>, highlighting the need for this information to be routinely provided.

***Location/size/type of defect***

"The rat calvarial defect is generally used to evaluate bone regeneration in an orthotopic model and to screen biomaterials or tissue engineering constructs before moving to larger animals for potential translation to human applications".<sup>271</sup> This is a typical statement to justify the use of a calvarial defect model after some preliminary *in vitro* tests. We would argue that the validation of a biomaterial/construct when tested in a single unloaded site as the calvaria does not justify efficacy in the vast field of bone regeneration, or to all CMF clinical implications. The calvarial model is a relevant model indeed, but mainly to target a cranial bone defect. Of note, the location within the cranium can also potentially alter the healing capacity, as demonstrated by the superior healing of the frontal bone compared to the parietal/temporal bones in a human calvarial study.<sup>309</sup> Due to intrinsic differences between location sites (e.g. the loadbearing status of a segmental defect compared to a non-loadbearing calvarial defect), the applicability of the results obtained with a calvarial model to any CMF site is diminished. It is known that the reconstruction of a loadbearing bone is dependent on the magnitude and frequency of loading<sup>310</sup>, making a segmental loadbearing defect in an animal model clinically more relevant. So far, the clinical indication for CMF reconstruction has not been appropriately addressed, and most of the preclinical studies use predominately cylindrical defects with a 2.7-15 mm diameter in small animal models. Cylindrical defects mimic the non-continuity mandibular defects, but a segmental defect should be used to reproduce a continuity defect. The orbital floor requires a separate investigation, even though it is not a loadbearing site, since it varies in shape, size and geometry compared to other CMF bones.<sup>280</sup> Only limited studies have reported implanting tissue engineered constructs into the orbital floor.

The CMF defect models discussed in this review are the calvarial, mandibular, and orbital floor defect models. In most cases a trephine<sup>83,89,124,125,311-340</sup> is used to create cylindrical defects in the calvaria and the mandible. Other bone cutting devices for cylindrical defects include a circular knife<sup>341</sup>, a biopsy punch<sup>342</sup>, a drill<sup>89,343-347</sup> and rongeurs.<sup>88</sup> The most used cutting device for creating segmental defects in the mandibular is the reciprocating bone saw, which is mainly used for large animals.<sup>285,348</sup> The spherical burr<sup>349</sup>, diamond burr<sup>350</sup> and surgical drill<sup>351</sup> are also used for segmental

defects in small animals. However, it is crucial that care must be taken to limit additional soft tissue damage during the procedure (e.g. the dura mater in the calvarial model), to allow effective comparisons of efficacy between groups. Hence, the bone cutting device should always be reported, as well as the surgical procedure applied to all the animals included in the study.

As previously stated, it is an important consideration that the chosen animal model adequately reflects the clinical problem, particularly in the CMF realm, and we encourage the use of segmental defects for the mandibular site, since they are known to be a significant issue in the CMF field. In addition, the surgical procedure should ideally be performed by the same person following extensive practice, and excluded animals should be included in the study, along with the relative reasons. To ease the comparison across studies, a standardisation of the cutting device for each animal model should also be encouraged. Detailed reporting of *in vivo* findings, as stipulated in the ARRIVE guidelines 2.0, should now be considered mandatory in modern publishing, to further improve reproducibility of preclinical studies.<sup>352</sup>

### **Control groups**

In most of the reported studies mentioned here, an empty defect is used as a negative control, but only very rarely (3 out of 66 studies)<sup>89,330,353</sup> is a positive control, such as an autologous bone graft, used as a comparator to assess ultimate efficacy of the tested material. This creates a knowledge gap in the current literature: how does the bone-mimetic material perform in a preclinical model against the SOC? And what are the underlying biological mechanisms making bone autologous bone grafts the SOC?

To decrease costs and more importantly the number of animals used, it is common practise to create multiple defects within the same animal and, in some cases, to have control defects in close proximity to tested materials/constructs. The potential confounding effects, both local and systemic, of such an approach is difficult to assess but should be carefully considered depending on the experimental context. Indeed, the risk of systemic inflammatory responses increases during surgeries with injuries of the

dura mater<sup>273</sup>, or during microbial infections from intra-oral surgical sites.<sup>278</sup> Furthermore, the potential systemic effect of drug-loaded scaffolds and the possible influence on the other defect sites should be first carefully evaluated in a pilot study.

We encourage scientists in this field to consider the effect of local and systemic inflammatory responses to the experimental outcome but, more importantly, to implement a positive control such as the autologous bone graft, in addition to empty defect controls, in future studies.

### ***Study duration including time points and analysis strategy***

In the presented studies, the endpoint and time points appear to follow an overall trend, with typical endpoints ranging from 8-12 weeks, which resembles the typical bone healing process of 6-8 weeks (and in some cases, 12 weeks) in humans and also to make use of appropriate endpoints to validate the outcome. The size of the animal model has an impact on the additional intermediate time points as demonstrated by the fact that 1 to 4 additional time points are included for small animal models while for large animal models typically only include 1 or 2 time points, likely due to the increased costs associated with large animal studies.

Unlike histology and immunohistochemistry analyses, which require euthanasia of the animal, radiographical imaging such as 3D image acquisition (CT,  $\mu$ CT) or 2D radiographs can be used to longitudinally assess bone healing in the same animal over time, which is an attractive means to reduce animal usage. Nevertheless, histology remains the main analysis method, and it is used in all presented studies. Histology is a powerful tool to assess the infiltration of native tissue within the construct, which makes it one of the most important outcome assessments. This is closely followed by CT/ $\mu$ CT (55 out of 66 studies), immunohistochemistry (16 out of 66 studies), and 2D radiography (3 out of 66 studies). Mechanical testing of regenerated areas is also used as an evaluation strategy (6 out of 66). To quantify the amount of repaired bone from histological and/or immunohistochemical analysis, either image analysis software is used (mostly ImageJ<sup>91,125,285,316,317,330,331,338,348,354,355</sup>, Image-Pro Plus<sup>311,313,345,356-358</sup> or

i-solution<sup>83,321,324</sup>), or a scoring system<sup>359</sup> is applied. Approximately 50% of studies do not show quantification of the histological and immunohistochemical images leading to potential biased and subjective analyses. New bone regeneration quantified from radiographical imaging is mostly expressed in the form of "bone volume/total volume (BV/TV)", bone mineral density, new bone formation or Hounsfield Units. A variety of software are used to quantify radiographical images including Nrecon<sup>324,327,328,336,338,339,355,360</sup>, Amira<sup>280,330,340</sup>, Skyscan<sup>314,325,351</sup>, AsanJ-Morphometry software<sup>326</sup>, InVesalius 3<sup>353</sup> and many more.

To improve consistency across studies, we would strongly encourage that the study endpoint, time points, and analytical methods be standardised based on individual species. We strongly suggest to at least include histology to assess the native tissue infiltration capacity, as well as CT scanning to measure the newly formed bone volume (BV/TV) in any pre-clinical study. The parameter outcome of BV/TV measurements based on CT scanning is the most important outcome evaluation, because the clinical evaluation of newly formed bone is also based on CT scanning, and it is therefore highly recommended to be included in the preclinical study. Additional assessments such as immunohistochemistry or mechanical testing are welcome additions. The minimum recommended number of timepoints are two, the first time point being after 4 weeks, to assess the performance of bone repair during the earlier stage of the healing process, and the second time point after 8 weeks when the healing process is typically viewed as sufficient to adequately withstand mechanical loading etc. (with the caveat that additional longer-term studies would be required to assess the remodelling process and ultimate integration of the construct, where this is applicable). More timepoints are encouraged only if necessary, to prevent unnecessary use of experimental animals. Summarised suggested guidelines to improve the use of clinically driven animal models is shown as a schematic overview in **Figure 5.4**.



## Clinically Relevant Preclinical Animal Models for Testing novel Cranio-maxillofacial Bone 3D-printed Biomaterials

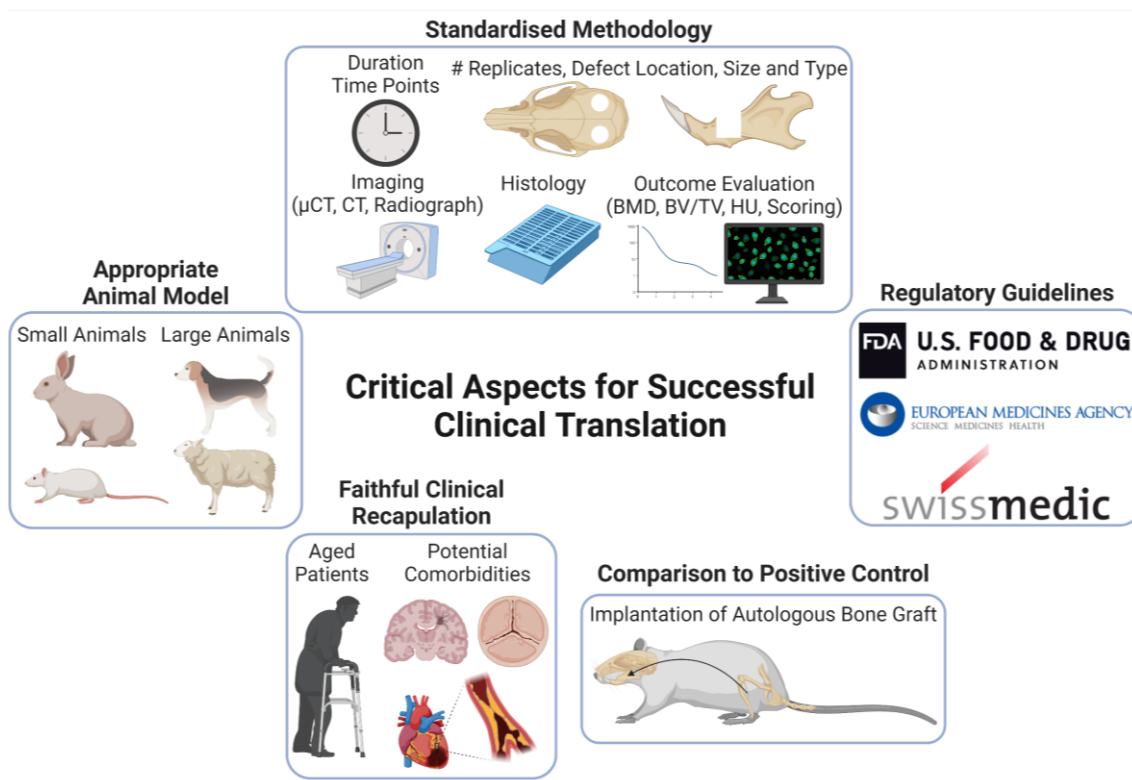


**Figure 5.4: Towards clinically driven animal models:** suggested guidelines. uCT: micro-computed tomography, BMD: bone mineral density, BV/TV: bone volume/total volume; HU: hounsfield units. Created with BioRender.com.

### ***Selection of the material***

There is a large selection of possible materials and combinations to choose from that ranges from: natural polymers such as collagen, gelatin, silk or alginate; synthetic polymers such as PLGA, poly(propylene fumarate) and PCL; bioceramics such as HAp, TCP and bioactive glass; biodegradable metals such as magnesium and its alloys; and carbon-based nanomaterials such as carbon nanotubes and graphene.<sup>361</sup> To name a few novel combinations: PCL functionalised with deferoxamine<sup>362</sup>, magnesium incorporated into a PLGA/TCP scaffold<sup>92</sup>, mesoporous bioactive glass for the delivery of growth factors<sup>363</sup> and chemically synthesised phosphate graphene<sup>364</sup>. However, these materials require further evaluation for efficacy in CMF-specific contexts. A cyclic pathway on how to design a material for BTE, specifically in terms of strategy, optimisation cycle and evaluation is proposed in a review by Koons et al.,

which also presents recent advances and development strategies in this field.<sup>361</sup> Advances in tissue-engineered bone technology and future aspects are also discussed in a review by Tang et al.<sup>365</sup>

The choice of the material must be based on the application. In this review the focus lays in 3D-printed scaffolds for CMF application. Due to non-loadbearing nature of the calvarial defect, a suitable material does not require to have high stiffness and resilience. Conversely, these properties might be essential for materials used to regenerate loadbearing segmental mandibular defects. We have previously highlighted the importance of material properties and vascularisation for a successful initial interaction with the host tissue. The implanted construct should lead to an early invasion of immune cells, bone cells, progenitor cells and vascular cells. To test the native ability of a material for integration with the host tissue, it should be additionally assessed in the absence of cell encapsulation.

We propose a clinically driven guideline path for the development of a new TE material for CMF repair purposes, as well as guidelines for selecting the suitable CMF animal defect model (**Figure 5.5**).

## Clinically Relevant Preclinical Animal Models for Testing novel Cranio-maxillofacial Bone 3D-printed Biomaterials

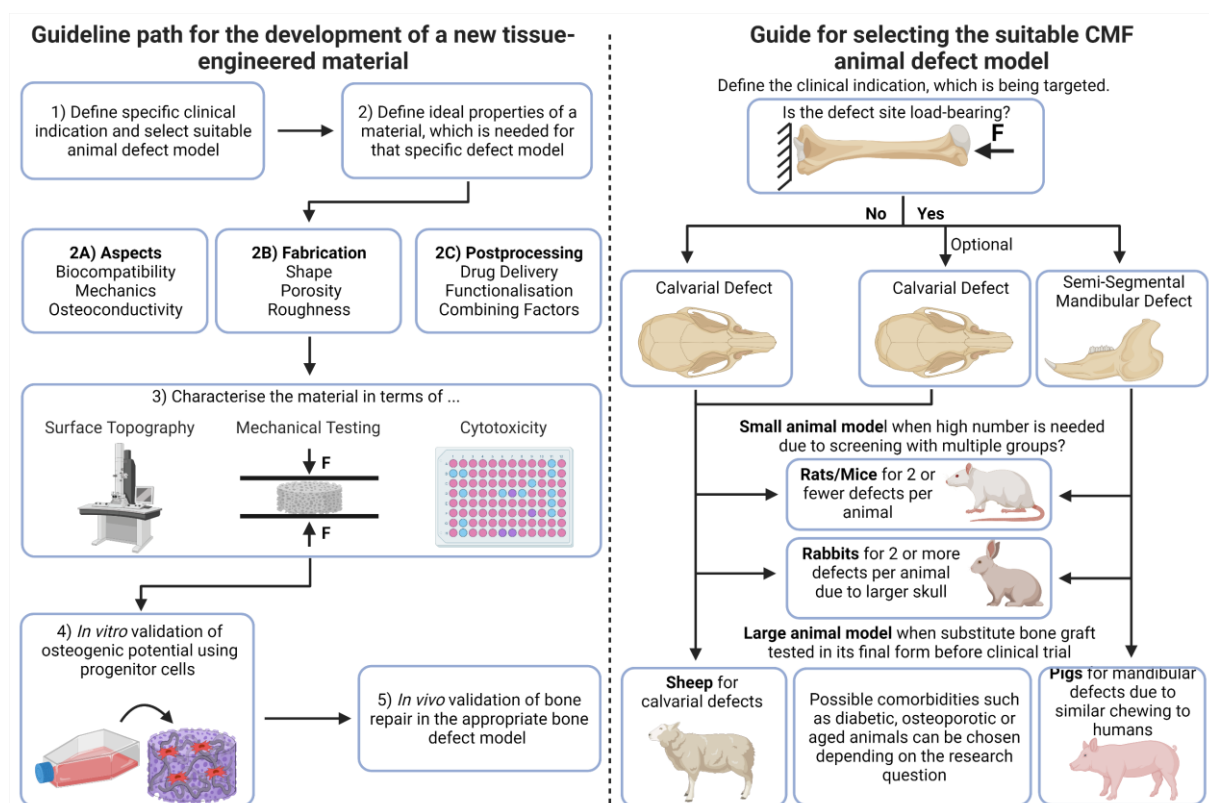


**Figure 5.5: Left schematic: Guideline path for the development of a new tissue-engineered material repair purposes, Right schematic: Guide for selecting the suitable CMF animal defect model.** Created with BioRender.com.

The clinical translation of a TE material requires a step-by-step approach that starts from a medical need and ultimately ends with a product on the market. Its success depends on clear communication, constant collaboration, and teamwork across multidisciplinary expertise (**Figure 5.6**). Without such an approach, we fear that the field of BTE may continue to frustrate, with a continued lack of viable BGS for replacement of autografts. Indeed, a search via "ClinicalTrials.gov" using the search terms "3D printing, 3D-printed - bone graft, substitute, or scaffold" for the efficacy

testing of 3D-printed BGS in patients demonstrates that only a limited number of 3D printed constructs have entered early clinical trials, with no published findings to date.

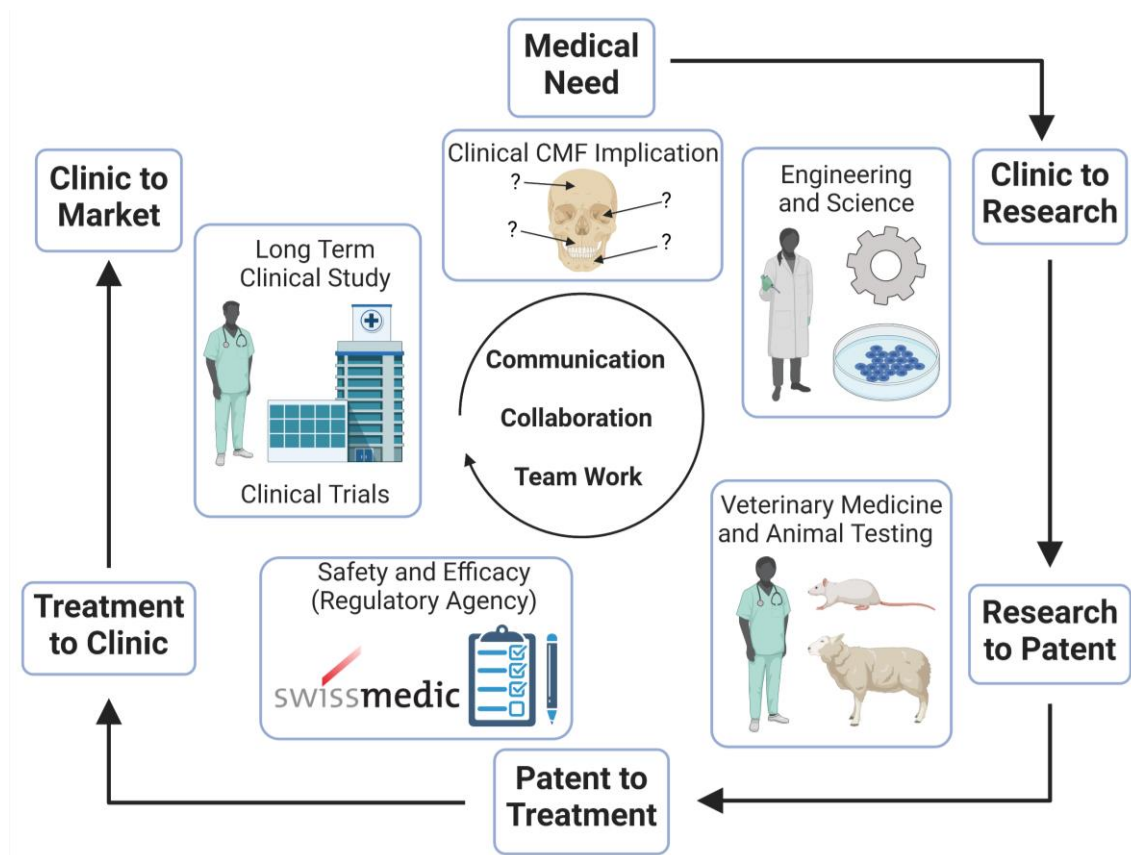


Figure 5.6: Ideal translational based on a multidisciplinary approach. Created with BioRender.com.

## 5.8 Conclusions

Tissue engineering has the potential to revolutionise the field of CMF bone regeneration but, so far, the implementation of promising materials/constructs into the clinic has been very limited. The provision of scientific evidence justifying the clinical translation of a tissue engineering product is a major undertaking and, in this respect, preclinical animal models are a critical resource necessary to test safety and efficacy. Although an experimental preclinical model cannot fully replicate the human disease, we should aim to maximise the quality of the experimental data generated to increase the translation potential of the material in question. With this aim in mind, the clinical

scenario should be used as main driver of the choice of the model and a rigorous scientific rationale should be applied, to justify the decision. The challenging nature of bone reparative approaches, requiring a thorough appreciation of both biological and mechanical processes involved, requires a multidisciplinary approach. Improvements to standardised assessment protocols across studies is encouraged, as well as sharing the knowledge and experiences of engineers, scientists, veterinarians, and CMF surgeons, to ultimately establish a series of robust guidelines supporting the development of a new tissue engineered material and to facilitate comparisons between results from different research groups.

**Conflict of interests:** The authors declare no conflict of interest.

**Table 5.1. Calvarial defect in preclinical animal models using the 3D printing approach.**

3D printed material	Animal Model (Strain, age, weight, # groups (# defects per group))	Defect (Shape, size, number, # defects per animal, fixation)	Clinical aim	Animal model justification	In vivo methods (Cutting tool, time points, analysis)	Results
PCL <sup>(9)</sup> /DCP <sup>(9)</sup> scaffolds seeded with hASC <sup>(9)</sup> <sup>341</sup>	Male FOXN1-knockout mice, 8 weeks, 3 groups (N=4)	Cylindrical 4 mm diameter, n=1	<b>CMF<sup>(9)</sup> bone regeneration</b>	No	4-mm circular knife, 6, 12 weeks, CT <sup>(9)</sup> , Histology (H&E <sup>(9)</sup> , Von Kossa/VGP <sup>(9)</sup> )	Greater bone regeneration with PCL/DCP scaffolds compared PCL only
CPC <sup>(1)</sup> scaffold coated with BSP <sup>(3)</sup> <sup>343</sup>	Female C57BL/6NRj mice, 6 weeks, 3 groups (N=14)	Cylindrical 2.7 mm diameter, n=1	CSD <sup>(1)</sup> bone defect repair	No	Drill, 8 weeks μCT <sup>(9)</sup> , Histology (H&E, MGT <sup>(9)</sup> ), Immunohistochemistry (OPN <sup>(9)</sup> , PECAM-1 <sup>(9)</sup> , VWF <sup>(9)</sup> )	Enhanced bone repair with CPC/BSP compared to empty defect and tendency compared to CPC only (no significance)
β-TCP <sup>(9)</sup> /FA <sup>(9)</sup> scaffold <sup>(9)</sup> <sup>342</sup>	Female immunodeficient NOD.CB17-Prkdc <sup>(scid)/J</sup> ("NOD-scid") mice, 8-10 weeks old, 24g, 5 groups, (N=1 or 5) and C57BL/6J BomTac mice, 4 groups, (N=2 or 6)	Cylindrical 4 mm diameter, n=1	<b>CMF bone regeneration</b>	No	Biopsy punch, 8 weeks, μCT, Histology (H&E), Immunohistochemistry (Vimentin)	Sintered β-TCP scaffolds visually promoted bone defect healing, but not β-TCP/FA, but the groups did not show significant differences in quantification
C3S <sup>(7)</sup> /MBG <sup>(9)</sup> scaffold <sup>(9)</sup> <sup>311</sup>	SD <sup>(1)</sup> male rats, 12 weeks old, 250-300g, 3 Groups (N=40)	Cylindrical 5 mm diameter, n=2	Large bone defect repair	No	Dental trephine, 8 weeks, μCT, PSFL <sup>(9)</sup> (2, 4 and 6 weeks), Histology (VGP)	Improved osteogenic capacity of C3S/MBG compared to C3S only and empty defect
PLA <sup>(7)</sup> /HAp <sup>(9)</sup> scaffold <sup>(9)</sup> <sup>356</sup>	SD male rats, 8 weeks old, 300-350g, 4 Groups (N=8)	Cylindrical 5 mm diameter, n=1	Large bone defect repair	No	Micro drills, 4 and 8 weeks, μCT, Histology (H&E), Immunohistochemistry (OCN <sup>(x)</sup> , Col-1 <sup>(y)</sup> )	Enhanced osteogenic capability with PLA/Hap compared to DBM <sup>(z)</sup> and empty defect, but not to non-printed β-TCP
PCL/PLGA <sup>(8a)</sup> /β-TCP scaffold doped with collagen <sup>(83)</sup>	SD male rats, 250-300g, 2 Groups (N=16)	Cylindrical 8 mm diameter, n=1	<b>Graft substitute for alveolar ridge repair</b>	No	Trephine burr, 2 and 8 weeks, Histology (H&E, MT <sup>(8b)</sup> )	No enhanced bone regeneration with PCL/PLGA/β-TCP compared to BCP <sup>(8c)</sup>

## Clinically Relevant Preclinical Animal Models for Testing novel Cranio-maxillofacial Bone 3D-printed Biomaterials

PCL scaffold coated with freeze dried PRP <sup>340</sup> /3 <sup>12</sup>	SD male rats, 200 g, 3 Groups (N=8)	Cylindrical 5 mm diameter, n=1	Bone defect repair	No	Trephine burr, 2, 4, 8 and 12 weeks, $\mu$ CT, Histology (H&E)	Greater bone formation with freeze dried PRP/PCL compared to traditional PRP-PCL and PCL only
CSH <sup>80</sup> /MBG scaffold <sup>313</sup>	SD mature male rats, 250 - 300 g, 4 Groups (N=24)	Cylindrical 5 mm diameter, n=2	Promote bone regeneration	No	Dental trephine, 8 weeks, $\mu$ CT, Histology (VGP)	Enhanced new bone formation with CSH/MBG compared to CSH only
PCL/ $\beta$ -TCP/bdECM <sup>81</sup> /BMP-2 <sup>89</sup> scaffold <sup>314</sup>	SD male rats, 12 weeks old, 250 - 300 g, 4 Groups (N=7)	Cylindrical 8 mm diameter, n=1	Enhance bone repair	No	Trephine burr, 4 weeks $\mu$ CT, Histology (H&E)	Higher new bone volume and area with PCL/ $\beta$ -TCP/bdECM/BMP-2 compared to PCL/ $\beta$ -TCP/bdECM, PCL/ $\beta$ -TCP and empty defect
$\beta$ -TCP scaffold with different pore sizes fabricated via 3D plotting <sup>345</sup>	SD rats, 12 weeks old, 180 - 200 g, 4 Groups (N=4-8)	Cylindrical 5 mm diameter, n=2	Enhance bone repair	No	Drill, 4, 8 and 12 weeks $\mu$ CT, mechanical testing, Histology (H&E)	Highest stiffness and enhanced new bone ingrowth with $\beta$ -TCP (100 $\mu$ m pore size) compared to 250 $\mu$ m, 400 $\mu$ m pore size and empty defect
PLA/PEG <sup>81</sup> /nHAp <sup>81</sup> /Dexa <sup>81</sup> scaffold <sup>315</sup>	Female rats, 200 - 300 g, 3 groups (N=N/A)	Cylindrical 8 mm diameter, n=1	CSD bone defect repair	No	Trephine burr, 4 and 12 weeks, $\mu$ CT, Histology (H&E)	Visually enhanced osteogenic response with PLA/PEG/nHAp with and without Dexa compared to empty defect
PIC <sup>316</sup> /MWCNT <sup>81</sup> scaffold <sup>316</sup>	SD male rats, 8 weeks old, 3 Groups (N=6)	Cylindrical 5 mm diameter, n=1	Large bone defect repair	No	Trephine burr, 2, 4 and 8 weeks, $\mu$ CT, Histology (H&E, MT), Immunofluorescence (Col-1, Runx2 <sup>81</sup> ), OCN Immunohistochemistry (CD31)	Promoted bone regeneration with PIC/MWCNT compared to PIC only and empty defect
HAp/F-PLGA <sup>81</sup> scaffold <sup>80</sup>	SD male rats, 500 g, 4 Groups (N=6-10)	Cylindrical 8 mm diameter, n=1	<b>CMF bone regeneration</b>	No	Trephine burr, 8 and 12 weeks, CBCT <sup>80</sup> , $\mu$ CT, Histology (H&E)	Enhanced bone repair with HAp/F-PLGA compared to empty defect, but not to F-PLGA only and autologous bone
AW/PLA (apatite-wollastonite) scaffold <sup>317</sup>	SD male rats, 12 weeks old, 350 g, 3 Groups (N=3-6)	Cylindrical 8 mm diameter, n=1	Mimic cortical and trabecular bone for better bone repair	No	Trephine burr, 12 weeks, Histology (H&E, Wright-Giemsa)	Enhanced newly formed bone with AW/PLA compared to AW only
HAp scaffold doped with BMP-2 <sup>318</sup>	SD male rats, 200-250 g, 3 Groups (N=8)	Cylindrical 5 mm diameter, n=1	Bone defect repair	No	Trephine burr, 8 weeks, $\mu$ CT, Histology (H&E, MT)	Enhanced bone healing with HAp/BMP-2 compared to HAp only and empty defect

## Clinically Relevant Preclinical Animal Models for Testing novel Cranio-maxillofacial Bone 3D-printed Biomaterials

PCL/PLGA/HAP scaffold combined with miR-148b-transfected rat BM-MSCs <sup>(a)(b)(c)(19)</sup>	Male Fischer 344 rats, 12 weeks old, 190-200 g, 3 groups (N=5)	Cylindrical 5 mm diameter, n=2	<b>CMF bone regeneration</b>	Yes	Trephine drill, 8 weeks, $\mu$ CT, Histology (H&E, MT), Immunohistochemistry (DAPI, F-ACTIN, Runx2, BSP)	More bone new formation with transfected-cell-laden scaffolds compared to cell-laden scaffold without transfection and empty defect
BCP/CHAp <sup>(a)(b)</sup> granules or disks combined with TBM <sup>(a)(b)(c)(20)</sup>	Lewis 1A-haplotype RT1a rats, 7 groups (N=6)	Cylindrical 5.5 mm diameter, n=2	<b>CMF bone regeneration</b>	Yes	Trephine burr, 7 weeks, $\mu$ CT, Histology (H&E, MGT), Immunohistochemistry (anti-CD31)	Greater new formation using BCP/CHAp/TBM disks compared to BCP/CHAp/TBM granules and empty defect
PEGDA <sup>(a)(b)</sup> /IECM <sup>(a)(b)</sup> scaffold fabricated via SLA <sup>(a)(b)(c)(26)</sup>	SD rats, 4 weeks old, 3 Groups (N=8)	Cylindrical 4 mm diameter, n=2	Bone defect repair	No	N/A, 4 and 8 weeks, $\mu$ CT, Histology (H&E, MT, MGT)	Better bone defect repair with PEGDA/IECM compared to PEGDA only and empty defect
$\beta$ -TCP scaffold seeded with osteogenic - and angiogenic-differentiated hUCMSCs <sup>(a)(b)(c)(24)</sup>	SD rats, 12 weeks old, 250 – 300g, 4 Groups (N=6)	Cylindrical 5 mm diameter, n=2	Large bone defect repair	No	Trephine burr, 4 weeks, $\mu$ CT, Histology (H&E, MT), Immunohistochemistry (CD31, CD34)	Enhanced bone repair with osteo- and angio-treated cell-laden $\beta$ -TCP compared to osteo-treated cell-laden $\beta$ -TCP, $\beta$ -TCP only and empty defect
PLA/HAP scaffold seeded with BM-MSCs with or without applying EMF <sup>(a)(b)(c)(25)</sup>	SD male rats, 12-13 weeks old, 280 – 320g, 5 Groups (N=24)	Cylindrical 6 mm diameter, n=1	<b>CMF bone regeneration</b>	No	Trephine burr, 4 and 12 weeks, $\mu$ CT, $\mu$ CT-based micro angiography (6 weeks), Histology (H&E, MT), mechanical testing	Higher new bone formation and improved neovascularisation with PLA/Hap/BM-MSC/EMF compared to PLA/Hap/BM-MSC, PLA/Hap/EMF, PLA/Hap and empty defect
Magnesium phosphate scaffold with and without micropores fabricated via salt leaching <sup>(321)</sup>	Aseptic male white rabbits, 12-15 weeks old, 4 groups (N=10)	Cylindrical 4- and 6 mm diameter, n=1	Study the effect of micropores for bone defect repair	No	Trephine burr, 4 and 8 weeks, $\mu$ CT, Histology (H&E, MT, TRAP)	Scaffolds with bigger micropores (25 and 53 $\mu$ m) show better lamellar structure and enhanced calcification compared to no micropores and empty defect
Sr <sup>(a)(b)(c)</sup> /MBG scaffold <sup>(335)</sup>	SD male rats, 12 weeks old, 3 groups (N=6)	Cylindrical, 5 mm, n=2	Bone defect repair	No	Trephine burr, 8 weeks, $\mu$ CT, Histology (tetracycline, alizarin red, calcein)	Enhanced new bone and vessel formation with Sr/MBG scaffold compared to MBG scaffold alone and empty defect
PCL coated with CaP <sup>(a)(b)(c)</sup> or additional antimicrobial Se <sup>(a)(b)(c)(22)</sup> nanoparticles <sup>(367)</sup>	SD male rats, 12 weeks old, 2 groups (N=6)	Cylindrical, 5 mm, n=2	Preventing bacterial colonization	No	N/A, 8 weeks, $\mu$ CT, Histology (H&E, MT)	Higher bone formation with PCL/CaP/Se scaffold compared to PCL/CaP



## Clinically Relevant Preclinical Animal Models for Testing novel Cranio-maxillofacial Bone 3D-printed Biomaterials

CDHAP <sup>ba)</sup> /col/BMP-2 scaffold <sup>336</sup>	SD male rats, 8 weeks old, 240 – 260g, 3 groups (N=8-10)	Cylindrical, 8 mm, n=1	<b>CMF bone regeneration</b>	No	Trepine Burr, 8 weeks, $\mu$ CT, Histology (H&E)	Similar bone formation with CDHAP/Col scaffold and CDHAP/Col/BMP-2 scaffold, but increased compared to empty defect
PCL scaffold functionalised with <sup>bb)</sup> PRF <sup>337</sup>	SD male rats, 8 weeks old, 4 groups (N=16)	Cylindrical, 6 mm, n=2	<b>CMF bone regeneration</b>	No	Trepine burr, 4 and 8 weeks, radiography, $\mu$ CT, Histology (H&E)	Enhanced bone formation of scaffolds (PCL and PCL/PRF) compared to empty defect and PRF alone, but similar results between PCL compared to PCL/PRF scaffold
Methacrylate/Silica scaffold <sup>d338</sup>	SD male rats, 8 weeks old, 250 $\pm$ 15 g, 2 groups (N=6)	Cylindrical, 8 mm, n=1	Bone defect repair	No	Trepine burr, 8 and 16 weeks, $\mu$ CT, Histology (H&E, MT), Immunohistochemistry (CD68, CD206, Col-1, OCN, DAPI, vWF, $\alpha$ -SMA <sup>bb)</sup> )	Enhanced Bone formation with Methacrylate/Silica scaffold compared to empty defect
PGSLP <sup>bb)</sup> scaffold loaded with DFO <sup>bb)</sup> -laden gelatin nanofibers <sup>368</sup>	SD male rats, 4 weeks old, 6 groups (N=N/A)	Cylindrical, 5 mm, n=N/A	Bone defect repair	No	N/A, 6 and 12 weeks, $\mu$ CT, Histology (H&E, MT), Immunohistochemistry (HIF-1 <sup>bb)</sup> , OPN, OCN)	Enhanced osteogenic and angiogenic activities with micro – and nanoporous structured PGSPLP/DFO scaffold compared to empty control, PGSPLP alone and porous structured PGSPLP without DFO
$\beta$ -TCP scaffold coated with microRNA-200c-laden col <sup>355</sup>	SD male rats, 12 weeks old, 6 groups (N=5)	Cylindrical, 9 mm, n=1	Bone defect repair	No	N/A, 4 weeks, $\mu$ CT, Histology (H&E, MT)	Enhanced bone regeneration with $\beta$ -TCP/Col/microRNA-200c compared to empty defect $\beta$ -TCP alone, $\beta$ -TCP/Col and $\beta$ -TCP/microRNA-200c
PCL scaffold combined with $\beta$ -TCP powder and/or dECM <sup>360</sup>	SD rats, N/A old, 4 groups (N=3-8)	Cylindrical, 8 mm, n=1	Treating bone fractures	No	Burr drill, 4 weeks, $\mu$ CT, Histology (MT), Immunohistochemistry (myeloid-related protein-14 MRP-14 <sup>bb)</sup> , OPN)	Faster bone formation and lower inflammatory response, with PCL/ $\beta$ -TCP/dECM scaffold compared to PCL alone, PCL/ $\beta$ -TCP and PCL/dECM
CSi/Mg <sup>bb)</sup> scaffold <sup>322</sup>	NZ <sup>ab)</sup> white rabbits, 2.8 kg, 4 groups (N=16)	Cylindrical 8 mm diameter, n=4	<b>Thin wall CMF bone defect repair</b>	No	Dental trephine burr, 6 and 12 weeks, mechanical testing, $\mu$ CT, Histology (VGP)	Enhanced new bone regeneration with CSi/Mg compared to CSi scaffolds only
CSi/Mg scaffold printed via SLP <sup>bb)</sup> or DLP <sup>bb)</sup> <sup>323</sup>	NZ male rabbits, 2.8 kg, 5 groups (N= $\sim$ 12)	Cylindrical 8 mm diameter, n=4	<b>Thin wall CMF bone defect repair</b>	No	Dental trephine burr, 4, 8 and 12 weeks, $\mu$ CT, Histology (VGP)	Higher osteogenic capacity with DLP compared to SLP and enhanced bone repair with CSi compared to CSi/Mg and empty defect

## Clinically Relevant Preclinical Animal Models for Testing novel Cranio-maxillofacial Bone 3D-printed Biomaterials

PCL scaffold with different porosity <sup>324</sup>	NZ male rabbits, 12-13 weeks old, 3.4 kg, 4 Groups (N=8)	Cylindrical 6 mm diameter, n=4	<b>Graft substitute for dentistry</b>	No	Trephine burr, 4 weeks, $\mu$ CT, Histology (H&E)	Enhanced new bone formation in PCL with 30% porosity compared to 50%, 70% and empty defect
HAp scaffold coated with nanoparticles composed of BMP-2 embedded in PCL <sup>325</sup>	NZ male white rabbits, 12 weeks old, 2-3 kg, 3 Groups (N=4)	Cylindrical 6 mm diameter, n=3	Bone defect repair	No	Trephine bar, 8 weeks $\mu$ CT, Histology (WGT)	Higher new bone formation with coated HAp compared to uncoated HAp and empty defect
PCL/ $\beta$ -TCP/ECM scaffold <sup>326</sup>	NZ male white rabbits, 12 weeks old, 3-3.5 kg, 5 Groups (N=3)	Cylindrical 8 mm diameter, n=4	Large bone defect repair	No	Dental drill, 6 and 12 weeks $\mu$ CT, Histology (H&E, MT, Von Kossa)	Enhanced bone regeneration with PCL/ $\beta$ -TCP/ECM compared to PCL/ECM, PCL/ $\beta$ -TCP, PCL and empty defect
PCL scaffold <sup>326</sup>	NZ white rabbits, 12 weeks old, 2.5 kg, 2 groups (N=N/A)	8-shaped, 5.6- and 7 mm diameter each defect (1 mm overlap, n=2)	Finding an optimal CSD model	No	Trephine burr, 1, 2, 4, 8, 12 and 16 weeks, CT, $\mu$ CT, Histology (H&E)	7 mm empty defect shows decreased bone healing abilities compared to 5 mm. Trend of enhanced bone repair with PCL compared to 7 mm empty defect (no significance)
Sr <sup>129</sup> /HAp scaffold <sup>346</sup>	NZ male white rabbits, 3 Groups (N=N/A)	Cylindrical 15 mm diameter, n=1	Enhanced bone augmentation and regeneration	No	Cranial drill, 4, 8 and 12 weeks, $\mu$ CT, Histology (H&E, MT)	Trend of more new bone formation with Sr/HAp compared to HAp only (no significance)
PCL/ $\beta$ -TCP/Col scaffold <sup>327</sup>	NZ white rabbits, 2.8 – 3.2 kg, 4 groups (N=10)	Cylindrical 8 mm diameter, n=4	<b>Alveolar bone defect repair</b>	No	Trephine burr, 2 and 8 weeks, $\mu$ CT, Histology (MT)	Trend of more new bone volume with PCL/ $\beta$ -TCP/Col compared to PCL/ $\beta$ -TCP, PCL only and empty defect (no significance)
PGA <sup>(b)</sup> scaffold combined with electrospun SF <sup>(m)</sup> membrane <sup>370</sup>	Rabbits, 8 weeks old, 230 – 280 g, 3 groups (N=3)	Cylindrical 8 mm diameter, n=4	Bone defect repair	No	N/A, 4 and 8 weeks, $\mu$ CT, Histology (H&E, MT)	Trend of greater bone regeneration with PGA/SF compared to PGA only and empty defect (no significance)

Data not available (N/A), <sup>(a)</sup>PCL: polycaprolactone, <sup>(b)</sup>DCB: decellularised bone), <sup>(c)</sup>hASC: human adipose-derived stem cell, <sup>(d)</sup>CMF: cranio-maxillofacial, <sup>(e)</sup>CT: computed tomography, <sup>(f)</sup>H&E: haematoxylin and eosin, <sup>(g)</sup>VGP: Van Gieson's picrofuchsin, <sup>(h)</sup>CPC: calcium phosphate cement, <sup>(i)</sup>BSP: bone sialoprotein, <sup>(j)</sup>CSD: critical-sized defect, <sup>(k)</sup> $\mu$ CT: microCT, <sup>(l)</sup>MGT: Masson Goldner Trichrome, <sup>(m)</sup>OPN: osteopontin, <sup>(n)</sup>PECAM-1: platelet endothelial cell adhesion molecule-1, <sup>(o)</sup>VWF: von Willebrand factor, <sup>(p)</sup> $\beta$ -TCP:  $\beta$ -tricalcium phosphate <sup>(q)</sup>FA: fatty acid, <sup>(r)</sup>C3S: tricalcium silicate, <sup>(s)</sup>MBG: mesoporous bioactive glass, <sup>(SD)</sup>: Sprague Dawley, <sup>(t)</sup>PSFL: polychrome sequential fluorescent labelling, <sup>(v)</sup>PLA: polylactic acid, <sup>(w)</sup>HAp: hydroxyapatite, <sup>(x)</sup>OCN: osteocalcin, <sup>(y)</sup>Col-1: collagen-1, <sup>(z)</sup>DBM: demineralised bone matrix, <sup>(aa)</sup>PLGA: poly(lactic-co-glycolic acid), <sup>(ab)</sup>MT: Masson's Trichrome, <sup>(ac)</sup>BGP: biphasic calcium phosphate, <sup>(ad)</sup>PRP: platelet-rich plasma, <sup>(ae)</sup>GSH: calcium sulfate hydrate, <sup>(af)</sup>dECM: bone demineralised and decellularised extracellular matrix, <sup>(ag)</sup>BMP-2: bone morphogenic protein-2, <sup>(ah)</sup>PEG: polyethylene glycol, <sup>(ai)</sup>nHAp: nano HAp, <sup>(aj)</sup>Dexa: dexamethasone, <sup>(ak)</sup>PLC: polyion complex, <sup>(al)</sup>WMCNT: multiwalled carbon nanotubes, <sup>(am)</sup>Runx2: runt-related transcription factor 2, <sup>(an)</sup>F-PLGA: fluffy PLGA, <sup>(ao)</sup>CBCT: cone beam CT, <sup>(ap)</sup>BM-MSC: bone marrow-derived mesenchymal stem cells,

<sup>a1)</sup>CHAp: carbonated HAp, <sup>a1)</sup>TBM: total bone marrow, <sup>a3)</sup>PEGDA: polyethylene glycol diacrylate, <sup>a1)</sup>ECM: tendon ECM, scaffold, <sup>a1)</sup>SLA: stereolithography, <sup>a1)</sup>hUCMSCs: human umbilical cord MSC, <sup>a1)</sup>EMF: electromagnentic field, <sup>a1)</sup>Sr: strontium, <sup>a1)</sup>CaP: calcium phosphate, <sup>a2)</sup>SE: selenium, <sup>a3)</sup>CDHAp: calcium-deficient hydroxyapatite, <sup>b1)</sup>PRF: plasma-rich-fibrin, <sup>b2)</sup> $\alpha$ -SMA: alpha-smooth muscle actin antibody, <sup>b1)</sup>PGSLP: poly (glycerol-co-sebacic acid-co-L-lactic acid-co-polyethylene glycol), <sup>b2)</sup>DFO: deferroxamine, <sup>b1)</sup>HIF-1- $\alpha$ : hypoxia inducible factor 1-alpha, <sup>b3)</sup>MRP-14: myeloid-related protein-14, <sup>b1)</sup>CSi/Mg: wollastonite doped with dilute magnesium, <sup>b1)</sup>NZ: New Zealand, <sup>b1)</sup>SLP: single-layer printing, <sup>b1)</sup>DLP: double-layer printing, <sup>b1)</sup>PGA: poly(glycolic acid), <sup>b1)</sup>SF: silk fibroin, <sup>b1)</sup>BFP1: bone forming peptide 1, <sup>b1)</sup>DIPY: dipyrindamole, <sup>b1)</sup>SB:stevener blue, <sup>b1)</sup>VEGF: vascular endothelial growth factor, <sup>b1)</sup>DCPD: dicalcium phosphate dihydrate, <sup>b1)</sup>nanoZIF-8: nanoscale zeolitic imidazolate framework-8

## Clinically Relevant Preclinical Animal Models for Testing novel Cranio-maxillofacial Bone 3D-printed Biomaterials

**Table 5.2. Mandibular defect in preclinical animal models using the 3D printing approach.**

3D printed material	Animal Model (Strain, age, weight, # groups (# defects per group))	Defect (Shape, size, number, # defects per animal, fixation)	Clinical aim	Animal model justification	In vivo methods (Cutting tool, time points, analysis)	Results
HAp <sup>(a)</sup> /PLGA <sup>(b)</sup> scaffold <sup>332</sup>	SD <sup>(c)</sup> male rats, 250 – 300 g, 2 groups (N=6-8)	Cylindrical 4 mm (0.5 mm depth), n=2	<b>Alveolar ridge augmentation</b>	No	Trephine burr, 4 weeks, early gene expression (day 7, Col-A1 <sup>(d)</sup> , VEGF <sup>(e)</sup> , Cbfa1 <sup>(f)</sup> ) μCT <sup>(g)</sup> , Histology (H&E <sup>(h)</sup> , MT <sup>(i)</sup> )	Enhanced newly formed bone with HAp/PLGA compared to empty defect
PVA <sup>(j)</sup> /PU <sup>(k)</sup> "LayFormm" scaffold <sup>346</sup>	SD male rats, 6 – 8 months old, 2 groups (N=6)	Semi segmental 5 x 2 x 3 mm <sup>3</sup> , n=2	<b>Craniofacial bone repair</b>	No	Spherical burr, 6 weeks, μCT, Histology (ALP <sup>(l)</sup> , TRAP <sup>(m)</sup> )	Increased mineralised tissue production with LayFormm compared to Norian putty
PCL <sup>(n)</sup> /TCP <sup>(o)</sup> /ME-HA <sup>(p)</sup> /ME-Ge <sup>(q)</sup> scaffold fabricated via dual printing doped with RVS <sup>(r)</sup> and SrRn <sup>(s)</sup> <sup>333</sup>	SD male rats, 280 – 330 g, 3 groups (N=5-6)	Cylindrical 4 mm, n=2	<b>CMF<sup>(t)</sup> bone reconstruction</b>	No	Trephine bur, 8 weeks, μCT, Histology (H&E, MT)	Promoted bone formation with drug loaded scaffolds compared to scaffold only and empty defect
Ti6Al4V <sup>(v)</sup> scaffold combined with ADSC <sup>(w)</sup> -laden Cellmatrix hydrogel <sup>354</sup>	SD rats, 8 weeks old, 3 groups (N=3)	Cylindrical 5 mm (1 mm depth), n=1	<b>Mandibular bone defect repair</b>	No	N/A, 12 weeks, μCT, Histology (VGP <sup>(w)</sup> )	Highest amount of new bone with Ti6Al4V/ADSC/Cellmatrix compared to Ti6Al4V/ADSC and Ti6Al4V only
PEKK <sup>(y)</sup> scaffold fabricated via SLS <sup>(z)</sup> seeded with ADSC <sup>350</sup>	NZ <sup>(z)</sup> rabbits, 2 groups (N=12)	Semi-segmental trapezoidal, 15 x 10 x 5 mm <sup>3</sup> , n=2	<b>Craniofacial bone reconstruction</b>	No	Diamond burr, 10 and 20 weeks, μCT, mechanical testing, Histology (MG-T <sup>(ab)</sup> )	Enhanced bone repair with PEEK/ADSC compared to empty defect. Higher compressive resistance in PEKK/ADSC compared to PEKK only and bone
CSI/Mg <sup>(ab)</sup> scaffold <sup>371</sup>	NZ male rabbits, 4 groups (N=16)	Square 10 x 6 x 4 mm <sup>3</sup> , n=N/A	<b>Alveolar bone repair</b>	No	N/A, 8 and 16 weeks, Radiography, CT, Histology(N/A)	Higher osteogenic capability with CSI/Mg compared to β-TCP, CSI only and bridgite after 16 weeks
β-TCP scaffold <sup>372</sup>	NZ adult rabbits, 35 kg, 1 group (N=5) (Pilot Study)	Complete segmental, 11 x 9 x 4.5 mm <sup>3</sup> , n=1, plate	<b>Mandibular bone reconstruction</b>	No	N/A, 8 weeks, μCT, Histology (Stevens's blue and VGP), backscatter electron microscopy	No enhanced bone repair with β-TCP compared to native bone

## Clinically Relevant Preclinical Animal Models for Testing novel Cranio-maxillofacial Bone 3D-printed Biomaterials

PLGA/nHAp <sup>(6c)</sup> scaffold containing BMP-2 <sup>(6d)</sup> and chitosan <sup>(6f)</sup>	NZ white rabbits, 13 weeks old, 2.5-3.5 kg, 2 groups (N=18)	Semi-segmental 13 x 6 x 4 mm <sup>3</sup> , n=2	<b>Large maxillary bone defect repair</b>	No	N/A, 4, 8 and 12 weeks, $\mu$ CT, Histology (H&E, MT), Immunohistochemistry (OCN <sup>(6e)</sup> )	Greater bone repair with PLGA/nHAp/BMP-2/chitosan compared to PLGA/nHAp
PCL/ $\beta$ -TCP scaffold seeded with osteogenic pre-differentiated TMSCs <sup>(6f)</sup> / <sup>(65)</sup>	NZ male white rabbits, 12 weeks old, 2.5-3 kg, 5 groups (N=2-4) ( <b>Pilot Study</b> )	Semi-segmental, 10 x 8 x 5 mm <sup>3</sup> , n=1, fixing plate	Large bone defect repair	No	Surgical drill and osteotomy, 12 weeks, CT, $\mu$ CT, mechanical testing, Histology (H&E, MT, Alizarin Red S), Immunohistochemistry (CD31)	Trend of enhanced repair with PCL/ $\beta$ -TCP/TMSCs (differentiated) compared to PCL/ $\beta$ -TCP/TMSCs (undifferentiated) PCL/ $\beta$ -TCP/PB, PCL/ $\beta$ -TCP and empty defect (no significance)
Bioglass scaffold functionalised with boron <sup>(34)</sup>	NZ male rabbits, 3.5 – 4 kg, 3 groups (N=4)	Cylindrical 8 mm (2 mm depth), n=1	<b>Mandibular bone defect repair</b>	No	Trepine bur, CT (4 and 8 weeks), Histology (2 and 4 weeks, H&E)	Enhanced bone repair with Bioglass/moron compared to HAp and empty defect
HAp/TCP scaffold fabricated via digital light processing-type 3D printing <sup>(36)</sup>	Adult beagle dogs, 3 groups (N=16)	Semi segmental 7 x 3 x 5 mm <sup>3</sup> , n=2, fixation pins	<b>Alveolar ridge augmentation</b>	No	Dental bur, 4 and 8 weeks, $\mu$ CT, Histology (H&E, MGT)	No difference in new bone formation with HAp/TCP compared to OSTEON
PCL/ $\beta$ -TCP doped with either BMP-2 or ABP <sup>(6g)</sup> / <sup>(48)</sup>	Male beagle dogs, 12-14 months old, 12.5 kg, 4 groups (N=4)	Semi segmental 20 x 10 x 10 mm <sup>3</sup> , n=2, fixation via wing structures on the scaffold	<b>Oromandibular bone reconstruction</b>	No	Reciprocating bone saw, 12 weeks, $\mu$ CT, Histology (H&E, MT)	More bone formation in drug-doped scaffolds compared to non-doped scaffold and empty defect
PCL/ $\beta$ -TCP doped with rhBMP-2 <sup>(6h)</sup> / <sup>(35)</sup>	Male beagle dogs, 12 - 14 kg, 4 groups (N=4)	Semi segmental 10 x 5 x 5 mm <sup>3</sup> , n=4,	<b>Mandibular bone defect repair</b>	No	Surgical bur, 12 weeks, $\mu$ CT, Histology (MT)	Increased newly formed bone with PCL/ $\beta$ -TCP compared to PCL only with or without rhBMP2
OCP <sup>(6i)</sup> scaffold functionalised with pDNA <sup>(6j)</sup> encoding VEGFA <sup>(37)</sup>	Adult male pigs, 50 Kg, 2 groups (N=4), titanium miniplate	Semi segmental 25 x 15 x 10 mm <sup>3</sup> , n=2, surgical guide plate	Large bone defect repair	No	N/A, 3 and 6 months, CT, Histology (H&E)	No enhanced bone repair with OCP/pDNA-VEGFA compared to OCP only
$\beta$ -TCP/PCL scaffold seeded with osteo-treated pBM <sup>(6k)</sup> progenitor cells <sup>(285)</sup>	Yucatan minipigs, N/A, 3 groups (N=3-6), ( <b>Pilot study</b> )	Semi segmental 20 x 20 x 7 mm <sup>3</sup> , n=6	<b>Improving deep bone penetration for craniofacial reconstruction</b>	Yes	Reciprocating bone saw, 8 weeks, Histology (H&E, DAPI), Immunohistochemistry (CD31)	More bone formation with cell-laden $\beta$ -TCP/PCL compared to cell-free $\beta$ -TCP/PCL, but less in the empty defect.

Data not available (N/A), <sup>(6)</sup>HAp: hydroxyapatite, <sup>(b)</sup>PLGA: poly(lactic-co-glycolic acid), <sup>(c)</sup>SD: Sprague Dawley, <sup>(d)</sup>Col-A1: collagen-A1, <sup>(e)</sup>VEGF: vascular endothelial growth factor, <sup>(f)</sup>Cbfa1: core-binding factor alpha-1, <sup>(g)</sup> $\mu$ CT: micro computed tomography, <sup>(h)</sup>H&E: haematoxylin and eosin, <sup>(i)</sup>MT: Masson's Trichrome, <sup>(j)</sup>pVA: polyvinyl alcohol, <sup>(k)</sup>PU: polyurethane, <sup>(l)</sup>ALP: alkaline phosphatase, <sup>(m)</sup>TRAP: tartrate

## **Clinically Relevant Preclinical Animal Models for Testing novel Cranio-maxillofacial Bone 3D-printed Biomaterials**

resistant acid phosphatase, <sup>10</sup>PCL: polycaprolactone, <sup>11</sup>TCP: tricalcium phosphate, <sup>12</sup>ME-HA: methacrylated hyaluronic acid, <sup>13</sup>ME-Gel: methacrylated gelatin, <sup>14</sup>RVS: resveratrol, <sup>15</sup>SrRn: strontium ranelate, <sup>16</sup>CMF: cranio-maxillofacial, <sup>17</sup>T6AIV: alpha beta titanium alloy, <sup>18</sup>ADSC: adipose-derived stem cell, <sup>19</sup>VGP: Van Gieson's picrofuchsin, <sup>20</sup>PEKK: polyetherketoneketone, <sup>21</sup>SLS: selective laser sintering, <sup>22</sup>NZ: New Zealand, <sup>23</sup>MGT: Masson Goldner Trichrome, <sup>24</sup>CSi/Mg: wollastonite substituted with magnesium, <sup>25</sup>nHAp: nano hydroxyapatite, <sup>26</sup>BMP-2: bone morphogenic protein-2, <sup>27</sup>OCN: osteocalcin, <sup>28</sup>TMSC: tonsil-derived mesenchymal stem cell, <sup>29</sup>ABP: autogenous bone particles, <sup>30</sup>hBMP-2: recombinant human BMP-2, <sup>31</sup>OCP: octacalcium phosphate, <sup>32</sup>pDNA: plasmid deoxyribonucleic acid, <sup>33</sup>PBM: porcine bone marrow, <sup>34</sup>SLA: stereolithography

Table 5.3. Orbital floor defect in preclinical animal models using the 3D printing approach.

Tissue engineering approach	Animal Model (Strain, age, weight, # groups (# defects per group))	Defect (Shape, size, number, # defects per animal, fixation)	Clinical aim	Animal model justification	In vivo methods (Cutting tool, time points, analysis)	Results
SLA <sup>a)</sup> 3D printed resorbable PTMC <sup>b)</sup> /HAp <sup>c)</sup> scaffold <sup>d20</sup>	Female skeletally mature, Swiss White Alpine sheep, 2 - 4 years old, ~69 kg, 2 groups (N=6)	Irregular shape, 6 x 9 mm <sup>2</sup> , n=1, fixation via titanium microscrews	<b>Repairing orbital floor defects</b>	Yes	Retractor + Pean forceps, 4, 8, 12 weeks, CT <sup>e)</sup> , Histology (Giemsa-Eosin)	Higher bone formation of resorbable scaffold compared to standardly used titanium mesh

Data not available (N/A), <sup>a)</sup>SLA: stereolithography, <sup>b)</sup>PTMC: poly(trimethylene carbonate), <sup>c)</sup>HAp: hydroxyapatite, <sup>d)</sup>CT: computed tomography

## **6 Standard *in vitro* Evaluations of Engineered Bone Substitutes are not Sufficient to Predict *in vivo* Preclinical Model Outcomes**

### **Statement of Significance:**

Preclinical testing of emerging biomaterials is a crucial step in their development cycle. Despite this, there is still significant discrepancy between *in vitro* and *in vivo* test results. Within this study we investigated multiple combinations of materials and osteogenic stimuli and demonstrated a poor correlation between the *in vitro* and *in vivo* data. We propose a rationale for why this may be the case and suggest a modified testing algorithm.

Note: This chapter was published in *Biomaterials* as **Standard *in vitro* Evaluations of Engineered Bone Substitutes are not Sufficient to Predict *in vivo* Preclinical Model Outcomes**, Luan P. Hatt†, Angela R. Armiento†, Karen Mys, Keith Thompson, Maria Hildebrand, Dirk Nehrbass, Werner E.G. Müller, David Eglin, Martin J. Stoddart

Reprinted with permission<sup>44</sup>. Copyright 2023, Elsevier

### Author Contributions:

†LPH and ARA contributed equally to this paper. LPH prepared the hydrogels and assisted in cell culturing, printed PCL constructs for the *in vivo* study, performed histological staining and microscopy of the *in vivo* study, analysis of the data, writing of the original draft, visualisation of the data and constructed the figures. ARA contributed to the paper in terms of conceptualisation of the experiments, methodology in the preparation of the hydrogels, cell culturing, *in vitro* release experiment, RT-qPCR analysis, *in vitro* von Kossa staining, data curation and preparation of graphs, as well as assistance in writing the original draft and reviewing and editing of the writing. KM contributed to the paper in terms



of methodology, analysis  $\mu$ Ct scanning and editing of the writing. KT contributed to the paper in terms of assistance in the conceptualisation of the study, validation of the experiments and reviewing and editing of the writing. MH contributed to the paper in terms of *in vivo* experiment coordination and reviewing and editing of the writing. DN contributed to the paper in terms H/E image analysis and reviewing and editing of the writing. WEGM contributed to the paper in terms assistance in the conceptualisation and provision polyP nanoparticles. DE contributed to the paper in terms assistance in the conceptualisation and reviewing and editing of the writing. MJS contributed to the paper in terms of conceptualisation of the study, provision of resources, acquisition of funding, supervision, leading the project administration and reviewing and editing of the writing. All authors read and approved the final manuscript.

## **Abstract**

Understanding the optimal conditions required for bone healing can have a substantial impact to target the problem of non-unions and large bone defects. The combination of bioactive factors, regenerative progenitor cells and biomaterials to form a tissue engineered (TE) complex is a promising solution but translation to the clinic has been slow. We hypothesised the typical material testing algorithm used is insufficient and leads to materials being mischaracterised as promising. In the first part of this study, human bone marrow – derived mesenchymal stromal cells (hBM-MSCs) were embedded in three commonly used biomaterials (hyaluronic acid methacrylate, gelatin methacrylate and fibrin) and combined with relevant bioactive osteogenesis factors (dexamethasone microparticles and polyphosphate nanoparticles) to form a TE construct that underwent *in vitro* osteogenic differentiation for 28 days. Gene expression of relevant transcription factors and osteogenic markers, and von Kossa staining were performed. In the second and third part of this study, the same combination of TE constructs were implanted subcutaneously (cell containing) in T cell-deficient athymic Crl:NIH-Foxn1<sup>mu</sup> rats for 8 weeks or cell free in an immunocompetent New Zealand white rabbit calvarial model for 6 weeks, respectively. Osteogenic performance was investigated via microCT imaging and histology staining. The *in vitro* study showed enhanced upregulation of relevant genes and significant mineral deposition within the three biomaterials, generally considered as a positive result. Subcutaneous implantation indicates none to minor ectopic bone formation. No enhanced calvarial bone healing was detected in implanted biomaterials compared to the empty defect. The reasons for the poor correlation of *in vitro* and *in vivo* outcomes are unclear and needs further investigation. This study highlights the discrepancy between *in vitro* and *in vivo* outcomes, demonstrating that *in vitro* data should be interpreted with extreme caution. *In vitro* models with higher complexity are necessary to increase value for translational studies.

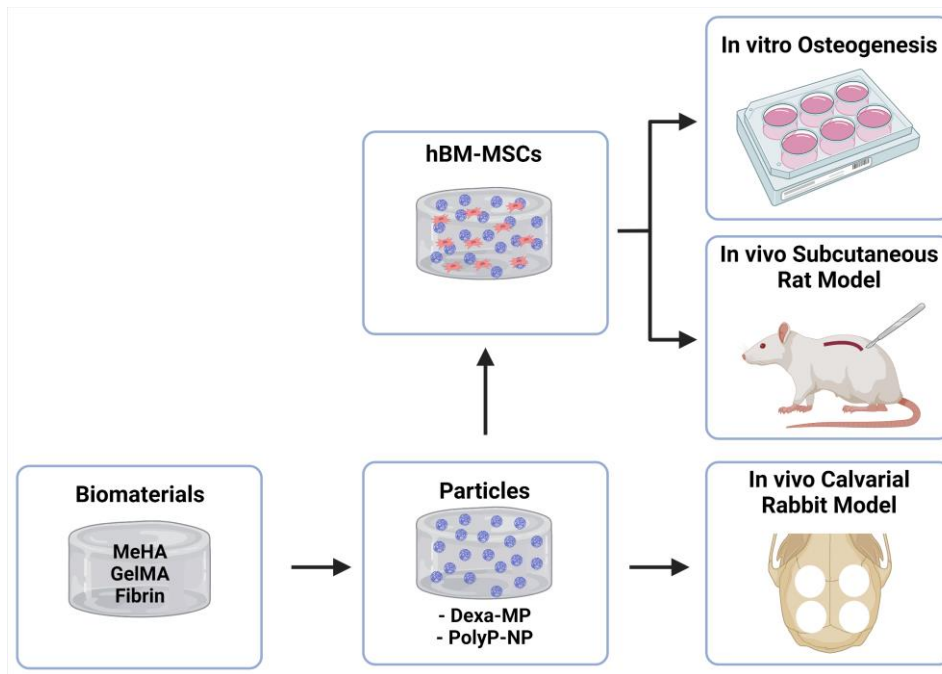
### ***Declaration of competing interest***

**Standard in vitro Evaluations of Engineered Bone Substitutes are not Sufficient to Predict in vivo Preclinical Model Outcomes**

---

The authors declare no conflict of interest.

**Keywords:** biomaterials, bone, preclinical models, translational science, osteogenesis



**Graphical Abstract:** *In vitro* and *in vivo* testing of tissue engineered constructs. Created with BioRender.com.

## **6.1 Introduction**

Considering its complex structure, bone is a tissue with a surprising regenerative capacity. Growth factors, multiple cell types and mechanical forces synergistically contribute to the healing process. While it is evident that bone can heal, it is still not clear why this is not always the case. Non-healing fractured bones (non-unions) and large bone defects of various pathological nature have serious healthcare implications across the population and represent challenging medical conditions for orthopaedic surgeons.

This clinical scenario has triggered a quest to identify the optimal conditions required for bone healing. The result is a multitude of tissue engineering (TE) approaches, combining various cell types and functional biomaterials in the presence of bioactive molecules, to create *in vitro* models of bone healing and to develop new therapies to restore lost bone<sup>199</sup>. Among the numerous natural biomaterials investigated, fibrin is easily obtained by the reaction of fibrinogen and thrombin, while hyaluronic acid (HA) and gelatin are widely used in their methacrylated form (MeHA and GelMA, respectively), which allows light-mediated tuneable crosslinking. Cells are also frequently encapsulated in these materials, particularly bone marrow-derived mesenchymal stromal cells (BM-MSCs). BM-MSCs have emerged as the archetypal cell in bone TE due to their relative ease of isolation and capacity *in vitro* to differentiate into relevant cell types for bone repair, such as chondrocytes and osteoblasts.

*In vitro* protocols for osteogenic differentiation of human BM-MSCs were originally established in the late 1990s<sup>374</sup> and continue to represent one of the fundamental assays to demonstrate MSC multilineage potential. The osteogenic cocktail contains  $\beta$ -glycerophosphate (BGP), dexamethasone (dexa) and ascorbic acid, supplemented to serum-containing culture medium. Within the osteogenic cocktail, ascorbic acid is essential for collagen fibrillation, while BGP provides an organic source of phosphate for hydroxyapatite (Hap) deposition during mineralisation. Inorganic alternatives to BGP are continuously investigated to obtain an optimum calcium:phosphate ratio more akin to that of carbonated Hap

present in human bone<sup>375</sup> and to have stable levels of free  $P_i$  levels during the *in vitro* culture<sup>146</sup>. Among the inorganic  $P_i$  sources, polyphosphates (polyP) are an effective substitute to BGP for osteogenic differentiation of human BM-MSCs in monolayer<sup>77</sup> and has been shown to be effective during bone formation *in vivo*<sup>42</sup>. During *in vitro* osteogenic differentiation, Dexa is essential for mineralisation, although, the specific contribution of Dexa to stimulate human BM-MSCs osteogenesis *in vitro* at the molecular level remains to be adequately described. Both 10 and 100 nM doses of Dexa are currently used<sup>376</sup> with the lower dose considered more physiologically relevant, while the magnitude of cellular response varies across donors<sup>377</sup>.

Despite numerous attempts at developing new biomaterials for bone regeneration, there have been few successes achieving clinical translation. A European multicentre analysis has reported a lack of correlation between *in vitro* and *in vivo* outcome with a surprisingly high failure of translation for biomaterials in the orthopaedic field<sup>45</sup>. Part of the reason for this may be the approaches commonly used to investigate the potential of new materials to repair bone. Strict guidelines are lacking and the International Organisation of Standardisation (ISO) protocols for Biological Evaluation of Medical Devices only requires *in vitro* cytotoxicity tests according to ISO 10993-1:2018 (Biological evaluation of medical devices — Part 1: Evaluation and testing within a risk management process).

In this study we follow a widely used approach to test biomaterials for TE purposes and demonstrate specific examples of promising *in vitro* TE constructs that fail to translate to the *in vivo* setting. We have employed one cell type (human BM-MSCs), three different biomaterials based on natural components of bone fracture callus (HA and fibrin) and extracellular matrix (collagen), and two bioactive molecules (Dexa and polyP). We start with an *in vitro* osteogenic differentiation assay and then proceeded to test these biomaterials in typically used *in vivo* model systems: a cell containing ectopic subcutaneous implantation in nude rats, and a cell free orthotopic calvarial defect model in rabbits.

**Standard *in vitro* Evaluations of Engineered Bone Substitutes are not Sufficient to Predict *in vivo* Preclinical Model Outcomes**

---

The results clearly show that standard *in vitro* evaluations are not sufficient to predict or justify follow up animal models and more representative *in vitro* tests are warranted to reduce the number of unproductive and expensive preclinical studies.

## 6.2 Material and Methods

Unless otherwise stated all reagents are from Sigma-Aldrich.

### ***Ethical approval***

Human MSCs used for both the *in vitro* experiment and the subcutaneous model are isolated from the bone marrow aspirate of a female patient (age 28) upon written consent and approval of Freiburg ethical committee (418/19).

All animal procedures are approved by the ethical committee of Grisons (Switzerland) and performed according to the Swiss Animal Protection Law in an AAALAC International-accredited facility (Authorisation Number: GR2018\_11 and 17\_2019).

### ***Fabrication of PCL Microspheres Loaded with Dexa***

Poly( $\epsilon$ -caprolactone) (PCL) microspheres loaded with Dexa are fabricated following a previously described method with minor modifications<sup>378</sup>. A total of 400 mg PCL (MW: 80'000 g/mol) is dissolved in 15 mL dichloromethane (DCM; Carl Roth) and 100 mg dexamethasone (Dexa, TCI Chemicals) is dissolved in 8 mL acetone. After 1 hour under moderate stirring, the two solutions are mixed. To create an emulsion, 1% poly(vinyl alcohol) (PVA; MW: 30000 g/mol) is used as aqueous phase. The PCL/Dexa solution is added dropwise to 100 mL of PVA solution, and the emulsion is obtained by probe sonication (Bandelin Sonopuls GM70) on ice with three bursts of 10 seconds at 700 W. The organic phase is allowed to evaporate overnight at room temperature under moderate stirring. To remove any agglomerate, the resulting microspheres are filtered using a 70  $\mu$ m cell strainer and the dispersion is centrifuged for 15 minutes at 37700 x g using an ultracentrifuge (Optima XE-90, Beckman Coulter). The collected microspheres are washed in Milli-Q® water to remove the excess of the PVA surfactant and thoroughly dispersed by sonication and re-collected by ultracentrifugation. After two washes, the microspheres are dispersed in Milli-Q® water, lyophilised, sterilised using ethylene oxide gas and stored at -20°C until use. SEM image of

Dexa-laden PCL microparticles is presented in **Supplementary Figure 6.1** The yield is quantified as dry weight of the microspheres.

To quantify the amount of encapsulated Dexa, high performance liquid chromatography (HPLC) is performed. The lyophilised microspheres are dissolved in a cosolvent system of 80/20 methanol/DCM to a concentration of 1 mg/mL. The DCM solvent is allowed to evaporate overnight at room temperature and the next day the volume is adjusted with methanol to reach the previous concentration of 1 mg/mL. The PCL is precipitated and removed via filtration and the Dexa remained solubilised in methanol. A standard curve is prepared using a solution of Dexa in methanol: 100, 30, 20, 15, 10, 5 and 2 µg/mL. All solutions are filtered with 0.22 µm Phenex syringe filters (Phenomenex) before loading in the HPLC (Agilent Technologies 1260 Infinity). UV absorption is measured at 239 nm. The efficiency of encapsulation is calculated according to the following equation:  $EE\% = (\text{Dexa}_{\text{encapsulated}}/\text{Dexa}_{\text{initial}}) \times 100\%$ .  $\text{Dexa}_{\text{encapsulated}}$  is the amount of Dexa quantified via HPLC and  $\text{Dexa}_{\text{initial}}$  is the amount of Dexa added to the emulsion. Three independent batches are fabricated following the described procedure.

### ***In Vitro Release of Dexa from PCL Microspheres***

A total of 10 mg of Dexa-loaded microspheres is incubated in 1 mL of phosphate buffered saline (PBS) at 37°C under mild shaking. At each time point (0.5, 1, 2, 4, 6, 8, 24, 48, 96 h and 5, 6, 7, 8, 11, 12, 13, 15 and 20 days), the samples are centrifuged at 12000 x g for 10 min and the supernatant is removed and replaced with 1 mL fresh PBS. The Dexa released is quantified via HPLC using a standard curve as described in the previous section ("***Fabrication of PCL microspheres loaded with Dexa***").

### ***Synthesis of Methacrylate Hyaluronic Acid and Gelatin***

Methacrylated hyaluronic acid (MeHA) is synthesised according to previously reported protocol<sup>379</sup>. Briefly, hyaluronic acid sodium salt from *Streptococcus equi* (280 kDa, Contipro Biotech S.R.O.) is fully dissolved at 5% (w/v) in distilled water



at room temperature. Methacrylic anhydride (MA) is added dropwise to the hyaluronic acid solution under vigorous stirring. The solution is allowed to react for 4 h under stirring and the pH is maintained between 7.5 and 8.5. After overnight stirring the solution is dialysed against distilled water for 1 week. The solution is lyophilised and stored at -20°C until use.

Gelatin methacryloyl (GelMA) is synthesised through the reaction of gelatin and MA, as described previously<sup>380</sup>. Briefly, type A porcine skin gelatin (Bloom 180) is mixed at 10% (w/v) into PBS at 60°C and stirred until fully dissolved. MA is added dropwise to the gelatin solution (0.14 mL/g of gelatin) under stirring conditions at 50°C. The solution is allowed to react for 3 h at 50°C and then is diluted 5 times with PBS. The mixture is dialysed against distilled water using 12-14 kDa cut-off dialysis tubing for 1 week at 40°C to remove unreacted MA. The solution is lyophilised and stored at -20°C until use.

The degree of methacrylation of MeHA and of GelMA is quantified by <sup>1</sup>H nuclear magnetic resonance (NMR) as 47% and 55%, respectively. NMR spectra are presented in **Supplementary Figure 6.2** Before cell encapsulation and animal surgeries, the lyophilised materials are sterilised using ethylene oxide gas.

### ***In Vitro* Osteogenic Differentiation within 3D Hydrogels**

#### *Cell encapsulation and osteogenic differentiation*

Human bone marrow derived MSCs are isolated and cryopreserved according to established protocol<sup>76</sup>. Upon thawing, the cells are expanded until passage 3 as previously described<sup>77</sup>. MeHA (2% w/v) and GelMA (8% w/v) are dissolved in Irgacure (0.3% w/v) solution. Fibrinogen (28 mg/mL) is prepared in 0.9% NaCl containing 1000 U aprotinin (Carl Roth). All the solutions are kept at 37°C until cell encapsulation. For each biomaterial four groups are created (**Table 6.1**): 1. Biomaterial + cells (MSCs); 2. Biomaterial + cells + 10 mg/mL DEXA-loaded microspheres (MSCs + DEXA); 3. Biomaterial + cells + 30 µg/mL polyP nanoparticles (MSCs + polyP); and 4. Biomaterial + cells + 10 mg/mL DEXA-loaded microspheres + 30 µg/mL polyP (MSCs + DEXA + polyP). MSCs are

## Standard in vitro Evaluations of Engineered Bone Substitutes are not Sufficient to Predict in vivo Preclinical Model Outcomes

suspended in MeHA, GelMA or fibrinogen ( $\pm$  Dexa and/or polyP) at a final density of  $20 \times 10^6$  cells/mL. Cylindrical cell-laden hydrogels (100  $\mu$ L volume; containing  $2 \times 10^6$  cells) are produced in 4% (w/v) agarose moulds, created using a 6 mm diameter biopsy punch (Braun). MeHA and GelMA are subsequently crosslinked within a BioLink® BLX 365 irradiation system (Witec AG) at 1 J, for 1.5 minutes and 10 minutes, respectively. The cell-laden fibrinogen is then supplemented with thrombin (1:1 volume) just before casting into the moulds and clotting is obtained at 37°C within 30 minutes. The final concentration of fibrinogen, aprotinin and thrombin is 14 mg/mL, 500 U/mL and 2 U/mL, respectively.

**Table 6.4. MSCs-laden biomaterials with and without particles**

Group	Dexa-loaded microspheres (mg/mL)	PolyP nanoparticles ( $\mu$ g/mL)
1	-	-
2	10	-
3	-	30
4	10	30

dexa: dexamethasone, polyP: polyphosphate.

Cell-laden hydrogels are pre-incubated in osteocontrol (OC) medium (Dulbecco's Modified Eagle Medium (DMEM 1 g/L glucose, Gibco), 10% FBS (Gibco), and 100 U/mL plus 100  $\mu$ g/mL penicillin and streptomycin, respectively) for the first 24 h. After this period (day 0), the samples are cultured in OC medium supplemented with the osteogenic cocktail (10 nM dexamethasone (dexa), 50  $\mu$ g/mL ascorbic acid 2-phosphate and 10 mM  $\beta$ -glycerophosphate). 6-Aminocaproic acid (5  $\mu$ M) is added to the culture medium of fibrin gels to reduce the cell-induced shrinkage. Medium change is performed three times per week and cultures are repeated with 3 technical replicates for each group and analysis.

### *RNA isolation and RT-qPCR*

Cell-laden hydrogels are harvested at day 0 and 28 and RNA is extracted according to previously described protocol<sup>381</sup> with modifications for fibrin gels. Briefly, MeHA and GelMA samples are pulverised, lysed in TRI-Reagent® (1 mL/sample, supplemented with 5 µL/mL of Polyacryl Carrier; both Molecular Research Center Inc.) and homogenised using QIAshredder columns (Qiagen). Fibrin samples are directly lysed in TRI-Reagent® and homogenised using QIAshredder columns. Phase separation and precipitation is obtained using 1-bromo-3-chloropropane (BCP) and isopropanol, respectively. Gene expression analysis is carried out using two-step reverse transcription quantitative polymerase chain reaction (RT-qPCR). Total RNA (250 ng) is reverse transcribed using random hexamers and SuperScript™ VILO™ (Invitrogen), according to manufacturer's instructions and real time qPCR is carried out using TaqMan® Universal Master Mix with 5 ng of cDNA in a 10 µL reaction volume. Each PCR reaction is performed in technical triplicates for 40 cycles using a QuantStudio® 6 Flex Real-Time PCR System (Applied Biosystems®). Primers used are listed in **Supplementary Table 6.1**. Data are analysed according the  $\Delta\Delta C_t$  method using *RPLP0* as normaliser and day 0 samples as calibrator.

#### *Cytological preparation and von Kossa staining*

At day 0 and day 28 cell-laden hydrogels are rinsed in PBS and fixed in 10% neutral buffered formalin for 24 h. Samples are rinsed in tap water and transferred to 5% sucrose solution in PBS at 4°C. After overnight incubation, the samples are embedded in cryocompound and sectioned (12 µm) using a Microm HM560 cryostat (Thermo Fisher Scientific® Inc.). Von Kossa staining is carried out according to the routine protocol. Briefly, the sections are brought to deionised water and then flooded with 5% silver nitrate aqueous solution for 30 minutes while exposed to strong natural light. After a wash in deionised water, the sections are treated with 5% sodium thiosulfate for 10 minutes and then washed again with running tap water first and deionised water after. Nuclear fast red is used as a counterstain. The sections are then dehydrated in an ethanol gradient, cleared in xylene and mounted using Eukitt® Quick-hardening mounting medium. Images

are acquired using BX63F light microscope equipped with a DP74 digital camera (Olympus).

### ***In Vivo Subcutaneous Model***

#### ***3D printing of PCL holders and biomaterial preparation***

Polycaprolactone (PCL) holders are printed using RegenHU 3D Discovery® Bioprinter (RegenHU). PCL pellets (MW: 68'413) are melted at 75°C in the heated tank. The printhead is set at 70°C and a stainless steel needle (0.33 mm in diameter) is used with a rate of movement of 4 mm/second and step height between each layer set to 0.26 mm in the Z direction. The following dimensions are used: 0.8 cm inner diameter, 1.2 cm outer diameter and 0.5 cm height (Fehler! Verweisquelle konnte nicht gefunden werden. **Figure 6.1A**). PCL sample holders are sterilised using ethylene oxide gas.

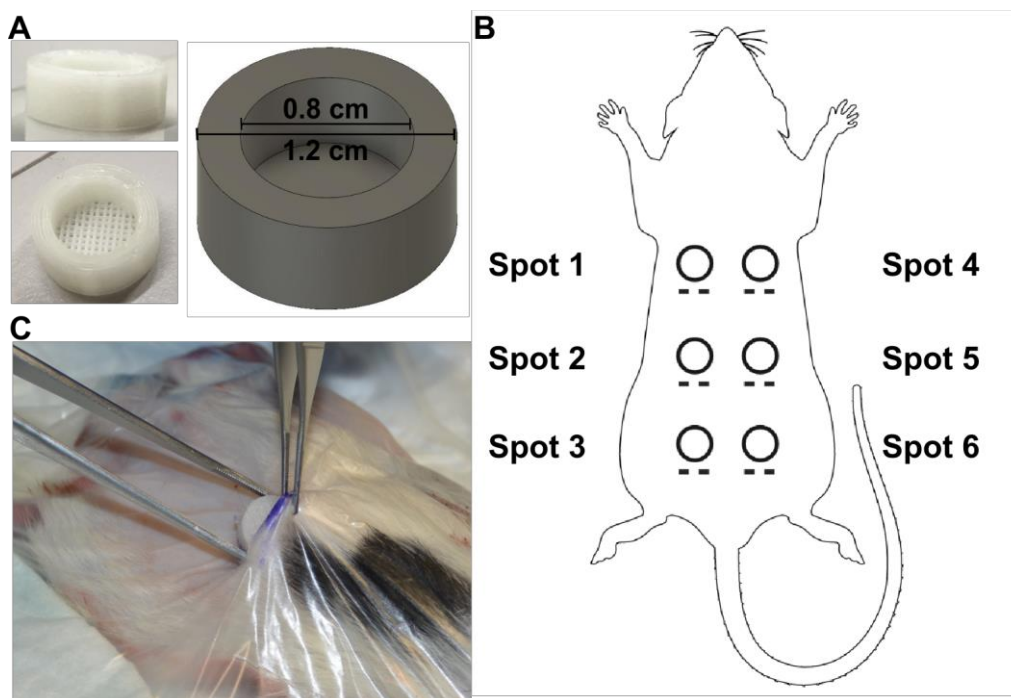


**Figure 6.1: Subcutaneous model in T cell-deficient athymic rats.** A. photograph and 3D render of 3D printed PCL holder used to contain the biomaterials; B. Sample distribution for the subcutaneous model; C. Photograph demonstrating implantation of the PCL holder containing the biomaterial with its open side facing the body.

For each biomaterial (MeHA, GelMA, fibrin) five groups are created with 6 replicates per group: 1. Biomaterial (Biomaterial only); 2. Biomaterial + cells (MSCs); 3. Biomaterial + cells + 10 mg/mL Dexamethasone-loaded microspheres (MSCs + Dexamethasone); 4. Biomaterial + cells + 30 µg/mL polyphosphazene nanoparticles (MSCs + polyP); and 5. Biomaterial + cells + 10 mg/mL Dexamethasone-loaded microspheres + 30 µg/mL polyP (MSCs + Dexamethasone + polyP). The cell encapsulation is carried out just before the implantation according to procedure described in section 0 and the biomaterials (200 µl) are transferred into the 3D printed PCL holders to constitute the implants for the subcutaneous model.

#### *Animal housing and randomisation*

A total of 20 skeletally mature (9 – 11-week-old) female T cell-deficient athymic Crl:NIH-Foxn1<sup>tmu</sup> rats (Charles River) with average preoperative weight of 173.4 ± 12.3 g are included in the subcutaneous model study. The rats are randomly allocated to experimental groups and are group-housed in IVC cages (up to 4 rats/cage) with 12 hours light/dark cycle. They receive mouse and rat maintenance food and water *ad libitum* and are acclimatised to the housing conditions for at least 2 weeks before surgery. The surgeon and post-op care givers are blinded to group allocation.

#### *Surgical procedure*

Rats receive 2 mL pre-warmed Ringer's solution administered subcutaneously before surgery. General anaesthesia is induced and maintained with 6 – 8% and 2 – 3% sevoflurane (Sevoflurane Baxter®, Baxter AG) in 0.6 – 1 L/min oxygen, respectively. Carprofen (5 mg/Kg, Norocarp®, Ufamed AG) and buprenorphine (0.1 mg/Kg, Bupaq®, Streuli Pharma AG) are administered subcutaneously as pre-emptive analgesics.

The animal is placed in ventral recumbency and the back from neck to tail based is aseptically prepared. Incision foil is placed over the back of the animal. Using a dummy PCL sample holder, the positions of the implants are marked onto the skin with a sterile skin marker according to distribution in scheme in **Figure 6.1B**

and **Supplementary Table 6.2**. The most caudal pockets (Spot 3 and 6) are prepared first, to avoid an implantation above the hips. Next, implants are inserted in spot 2 and 5 and finally in spot 1 and 4. Each incision is done using a scalpel blade no. 15 and it is approximately 2 cm in length. At each incision, a subcutaneous pocket is created bluntly using scissors in cranial direction. The implant is inserted into the subcutaneous pocket with the open side of the PCL holder facing the body (**Figure 6.1C**). The skin is closed by intra cutaneous suturing of the skin (5-0 VICRYL RAPIDE® C-3 reverse cutting, Ethicon).

Paracetamol (Dafalgan Sirup 3%, Bristol Myers Squibb SA) is added to the drinking water (7 mL/100 mL) as analgesic for 4 days post-surgery.

#### *Micro computed tomography*

At the end point (8 weeks) general anaesthesia is induced and maintained with 6 – 8% and 2 – 3% Sevoflurane in 0.6 – 1 L/min oxygen, respectively. Animals are euthanised via intracardiac injection of 1 mL Pentobarbital (200 mg/mL). All the implants with the surrounding soft tissue and skin are collected and stored in 4% buffered formalin for imaging. Fixed implants are scanned via micro computed tomography (CT) using VivaCT40 (Scanco Medical AG), as previously described<sup>382</sup>. Briefly, a 10 mm long ROI, with a  $\varnothing$ 25.6 mm field of view are scanned. The X-ray tube is operated at 70 kV voltage, 114  $\mu$ A current, with a 0.5 mm aluminium filter. 1000 projections are acquired over 180° rotation, with 200 ms integration time, resulting in a scan time of 21 min.

#### *von Kossa staining*

After imaging via microCT, undecalcified sections are obtained after embedding in LR White resin and are stained using von Kossa according to a routine protocol.

#### **Calvarial Defect Model**

For each biomaterial (MeHA, GelMA and fibrin) four groups are created (all cell-free) with 6 replicates per group: 1. Biomaterial (Biomaterial only); 2. Biomaterial + 10 mg/mL Dexamethasone-loaded microspheres (Dexa); 3. Biomaterial + 30 µg/mL polyP nanoparticles (polyP); and 4. Biomaterial + 10 mg/mL Dexamethasone-loaded microspheres + 30 µg/mL polyP (Dexa+ polyP). The biomaterials are prepared just before the implantation according to procedure described in section "Cell encapsulation and osteogenic differentiation". Materials were implanted directly into the defect without a PCL sample holder.

### *Animal housing*

A total of 18 skeletally mature (older than 24-week-old) female, immunocompetent New Zealand white rabbits with average preoperative weight of  $3.4 \pm 0.2$  Kg are included in the calvarial defect model study. During the acclimatisation period (8 weeks) the rabbits are group housed with a 12 h dark/12 h light cycle, fed with hay, carrots, fennel, parsley, and supplemental feed for rabbits (Biomill) *ad libitum*.

### *Surgical procedure*

Rabbits are sedated with an intramuscular injection of 0.2 mg/Kg medetomidine (Medetor®, Virbac AG), 0.5 mg/Kg midazolam (Dormicum®, Roche) and 0.005 mg/Kg fentanyl (Sintenyf®, Roche) and general anaesthesia is induced with intravenous injection of 0.2 mg/Kg propofol (Propofol 1% MCT®, Fresenius). Animals are placed in sternal recumbency, intubated, and maintained under general anaesthesia with 1.8 – 2.5% sevoflurane in 0.6 – 1 L/min oxygen. As pre-operative analgesic, transdermal fentanyl patches (12 µg/hour, Fentanyl-Mepha®, Mepha Pharma AG) are applied at right ear base and carprofen (4 mg/Kg, Rimadyl®, Pfizer) is administered intravenously. During surgery, fentanyl is administered via constant rate infusion in an ear vein catheter at 30 mcg/kg/h (Fentanyl Sintetica 0.5 mL/10 mL Sintetica SA). The dorsal aspect of the head is clipped and aseptically prepared. A skin incision is made on midline from the nasal bone to the occipital crest using a scalpel blade no. 10 and the

occipitalis and temporalis muscles are reflected. A bone cutting jig is placed on the midline, spanning the left and right parietal bones just caudal to the horizontal suture line, and the locations of the four evenly distributed defects are marked through blunt dissections of the periosteum. Following removal of the jig the periosteum of these four locations is further roughened using a scalpel blade no. 15 to help the following engagement of the perforator with the bone. Four craniotomy defects (6 mm diameter) are then created using an Anspach drill (Depuy Synthes) and a 9 mm Codman perforator (Integra Life Science)<sup>383</sup>. Any remaining bone piece is gently removed from the defect site. The biomaterials are press-fit into the defects (**Figure 6.2A**) according to distribution scheme reported in **Figure 6.2B** and **Supplementary Table 6.3**. The subcutaneous tissues are closed with a simple interrupted suture pattern (4-0 MONOCRYL, Ethicon), and the skin is closed using 5-0 VICRYL RAPIDE® with an intradermal pattern. **Figure 6.2: Calvarial defect model in New Zealand white rabbits.** A. Photograph showing the defects soon after creation (upper row) and after material implantation (lower row); B. Sample distribution for the calvarial defect model. Post-operative analgesia is administered to the animals through subcutaneous injections of 50 µg/Kg buprenorphine (Bupaq®, Streuli Pharma AG) directly after surgery, 6 – 8 hours later and the morning of the following day and of 4 mg/Kg Rimadyl® the morning after and then every 24 hours for 72 hours. Transdermal fentanyl patches are removed at 96 h. Empty controls (16 samples) are historical data from a previous project<sup>384</sup>.

#### *Micro computed tomography*

MicroCT scanning is carried out under general anaesthesia postoperatively (Day 0) and after euthanasia (6 weeks) using a high resolution peripheral quantitative computed tomography (XtremeCT, Scanco Medical AG) at 82 µm voxel size and using 200 ms integration time. After euthanasia, also a microCT scan (VivaCT40, Scanco Medical AG) is performed at 19 µm voxel size using the following scan parameters: 70 kV, 114 µm and 400 ms integration time.



The standard Scanco segmentation for both scanners is used to segment the samples using Scanco's IPL analysis software (XtremeCT: a Laplace-Hamming filter combined with a global threshold; VivaCT40: a Gaussian filter combined with a global threshold). Postoperative and subsequent scans are overlaid using in Amira 2019.4 (Thermo Fisher Scientific, USA) and a cylinder of 6 mm diameter are placed in the defect site. The bone volume (BV) in the cylinder is calculated in both scans. New bone volume fraction is calculated as  $BV/TV = (BV_{\text{euthanasia}} - BV_{\text{postoperatively}})/TV$ , where the total volume (TV) of the defect was calculated as a cylinder of 6mm diameter (defect size) with an estimated thickness of 1.5 mm.

#### *Semi-quantitative histopathological evaluation*

Following euthanasia with an overdose of pentobarbital, the calvaria containing the 4 defects is resected from the skull using an oscillating saw and it is stored in 4% buffered formalin for histological processing. Undecalcified sections are obtained after embedding in methylmethacrylate and are stained using Giemsa-Eosin according to a routine protocol. Histopathological severity is assessed using a 6-point grading scheme (0 – 5). Among others, semi-quantitative analysis is focused on new bone formation, namely the defect closure, which can be characterised by two parameters: 1) the size ( $\mu\text{m}^2$ ) of the defect area filled with new bone tissue; and 2) the distance ( $\mu\text{m}$ ) of the defect diameter spanned by bone tissue. Additionally, parameters characterizing the biomaterial itself (amount, surface irregularity, fragmentation, pores), its relationship towards the host tissue (cell infiltration, osseous integration, mineralisation) and its capacity to induce inflammatory cell reactions (granulocytic, lymphocytic, granulomatous, fibrotic capsule formation) are analysed. Finally, unintended changes of the adjacent brain tissue (hemosiderin deposition, astrocytosis, prolapse of brain tissue and nests of meningeal tissue in the defect, biomaterial in the brain) are also recorded.

#### **Statistical Analyses**

**Standard in vitro Evaluations of Engineered Bone Substitutes are not Sufficient to Predict in vivo Preclinical Model Outcomes**

---

Normally distributed data is assessed using one way ANOVA, with Tukey's multiple comparison test. Semiquantitative data is assessed using Kruskal-Wallis. Data is analysed in GraphPad Prism 8 software (GraphPad Software, San Diego, CA, USA)  $p < 0.05$  being considered significant.

## 6.3 Results

### *In vitro* release of dexamethasone from PCL microspheres

The PCL microspheres are produced with an efficiency of Dexamethasone (Dexa) encapsulation of  $51.37\% \pm 14.71$ , which corresponds to  $99.5 \mu\text{mol}$  and  $0.678 \mu\text{mol}$  per mg of PCL. The quantification via HPLC shows a 35% of Dexa release over a period of 500 hours with over 15% Dexa being released in the first 48 h (**Figure 6.3A**). Cumulative drug release of Dexa is fitted using the conventional model Korsmeyer-Peppas, which is defined as  $K_{kp} \cdot t^n$ ,  $K_{kp}$  being the release constant,  $t$  the time and  $n$  the slope as described previously<sup>378</sup>. Dexa drug release can be plotted as logarithmic scale: linear trendlines with  $R^2 = 0.979$ ,  $n = 0.313$  and  $R^2 = 0.955$ ,  $n = 0.2972$  for the release of the total amount of Dexa and the percentage, respectively, indicating a purely diffusion-based drug release with negligible effects of polymer erosion (**Figure 6.3B**).

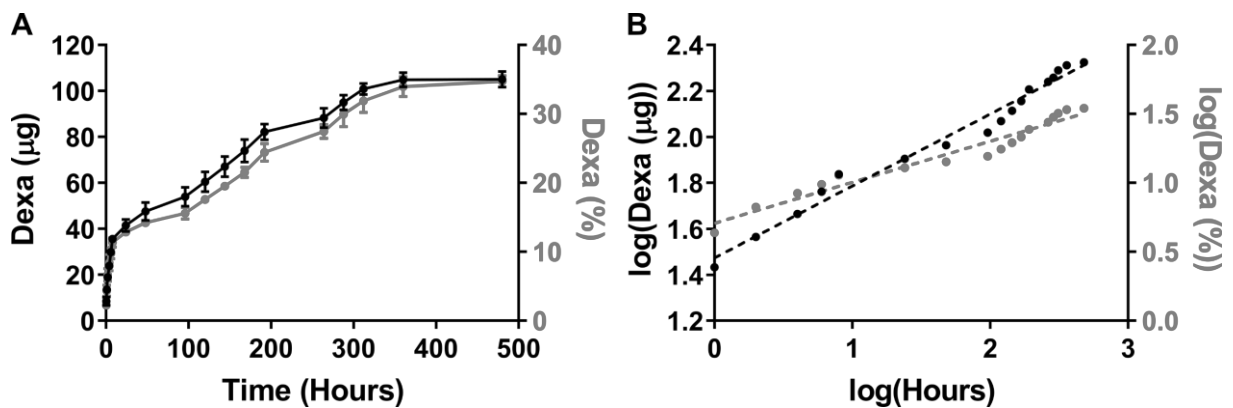


**Figure 6.3:** *In vitro* release of dexamethasone from PCL microspheres. A) The release of dexamethasone (dexa) from PCL microspheres is measured *in vitro* up to 500 hours and expressed as total amount ( $\mu\text{g}$ ) and percentage of encapsulated dexa. Data are shown as mean  $\pm$  S.D. of three independent batches; B) Dexa release remodelled to fit the Korsmeyer-Peppas model for sustained drug release.

### **Gene Expression Profile of BM-MSCs under Osteogenic Culture Conditions**

The differentiation of BM-MSCs into osteoblasts is characterised by the gene expression of specific transcription factors and mineralisation associated

markers. For this reason, we studied the expression of the transcription factors Runx2, Sox9, Runx2/Sox9 ratio<sup>163</sup>, PPAR $\gamma$  and Sp7, and alkaline phosphatase (ALP) and integrin binding sialoprotein (IBSP) as proteins involved in the mineralisation process (**Figure 6.4**). The addition of Dexa downregulates the expression of Runx2, Sox9 and PPAR $\gamma$  in MeMA, but upregulates the Runx2/Sox9 ratio and ALPL. Gene expression values in GelMA is unchanged when Dexa is added, except for ALPL. Dexa causes a high upregulation of ALPL in Fibrin, an upregulation in Runx2 and the Runx2/Sox9 ratio and a downregulation in PPAR $\gamma$ . The addition of Dexa to all three biomaterials upregulates the expression of ALPL, which is not the case when Dexa is combined with polyP, or polyP alone. The addition of polyP causes downregulation in ALPL in all biomaterials and in PPAR $\gamma$  in MeHA and Fibrin, an upregulation of Sox9 in all biomaterials or stays unchanged in the other groups. The combination of both bioactive factors does not follow the trend of each factor individually, but increases the Runx2/Sox9 ratio in GelMA and polyP. Each of the bioactive factors and in combination leads to a downregulation of the PPAR $\gamma$  gene in MeHA and fibrin, but not in GelMA.

## Standard in vitro Evaluations of Engineered Bone Substitutes are not Sufficient to Predict in vivo Preclinical Model Outcomes

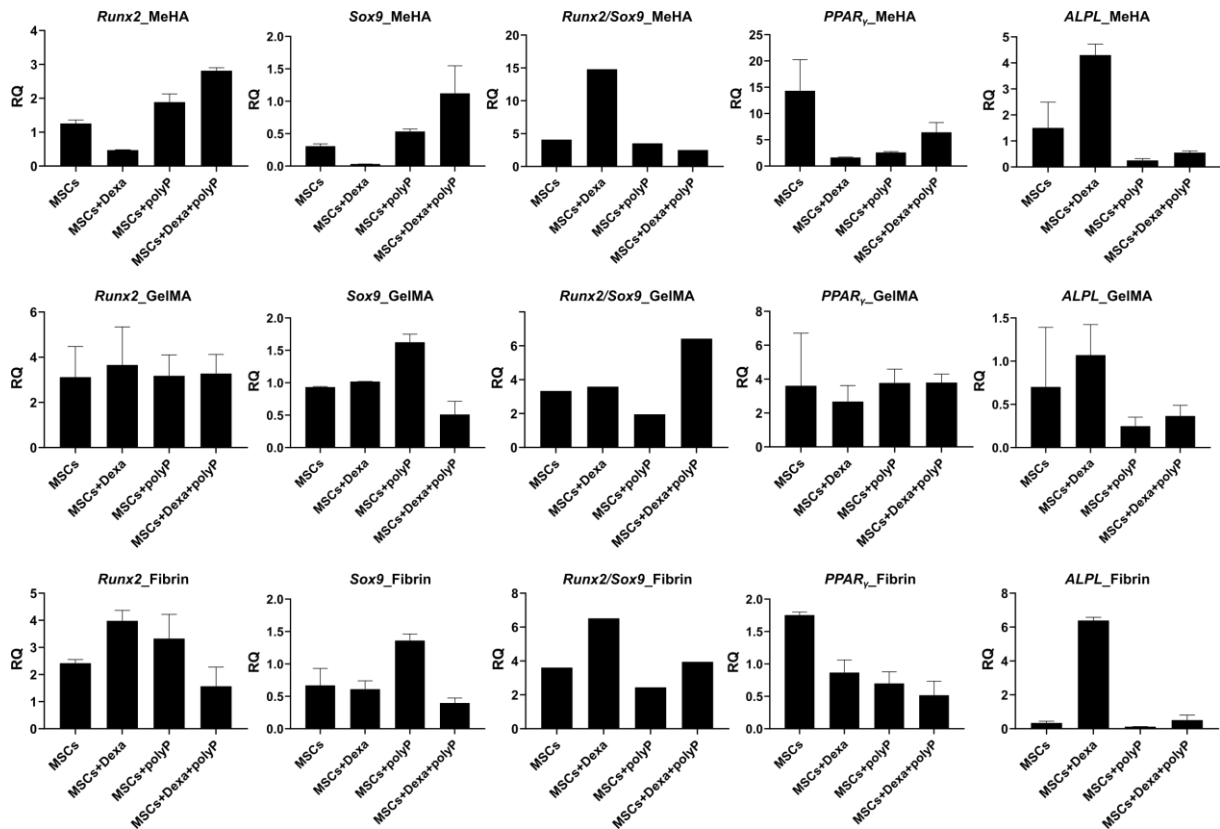


**Figure 6.4:** *In vitro* gene expression profile of BM-MSCs under osteogenic culture conditions within different biomaterials. Relative quantification (RQ) at day 28 calculated using the  $2^{-\Delta\Delta C_t}$  formula with *RPLP0* as reference gene and sample at day 0 as calibrator. All the data are shown as mean  $\pm$  SEM of three replicates. *RUNX2*: Runt related transcription factor 2; *SOX9*: SRY-Box transcription factor; *ALPL*: Alkaline phosphatase, biomineralisation associated; *PPAR $\gamma$* : peroxisome proliferator activated receptor gamma; *RPLP0*: ribosomal protein lateral stalk subunit P0.

### ***In Vitro* Osteogenic Differentiation is Confirmed by von Kossa Staining and Gene Expression of Markers Associated to Mineralisation**

All three tested cell-laden biomaterials with or without the addition of Dexa and/or polyP show promising osteogenic potential, indicated by positive von Kossa staining (**Figure 6.5A**) and upregulation of osteogenically-relevant gene expression markers *IBSP* and *SP7* (**Figure 6.5B**). No osteogenic response was detected in biomaterial only (**Supplementary Figure 6.3**). The osteogenic response is enhanced when Dexa is added to GelMA and Fibrin, or when polyP is added to MeHA, demonstrated by increased mineral deposition seen in the von

## Standard *in vitro* Evaluations of Engineered Bone Substitutes are not Sufficient to Predict *in vivo* Preclinical Model Outcomes

Kossa images and upregulation of the IBSP and SP7 genes. The addition of polyP in fibrin with and without Dexa shows increased mineralisation, but does not correlate to the gene expression profile, likely due to artifacts, which could be caused by the shrinkage behaviour of fibrin, making fibrin the least stable biomaterial used.

All materials were then tested *in vivo* in a subcutaneous implantation model in nude rats.

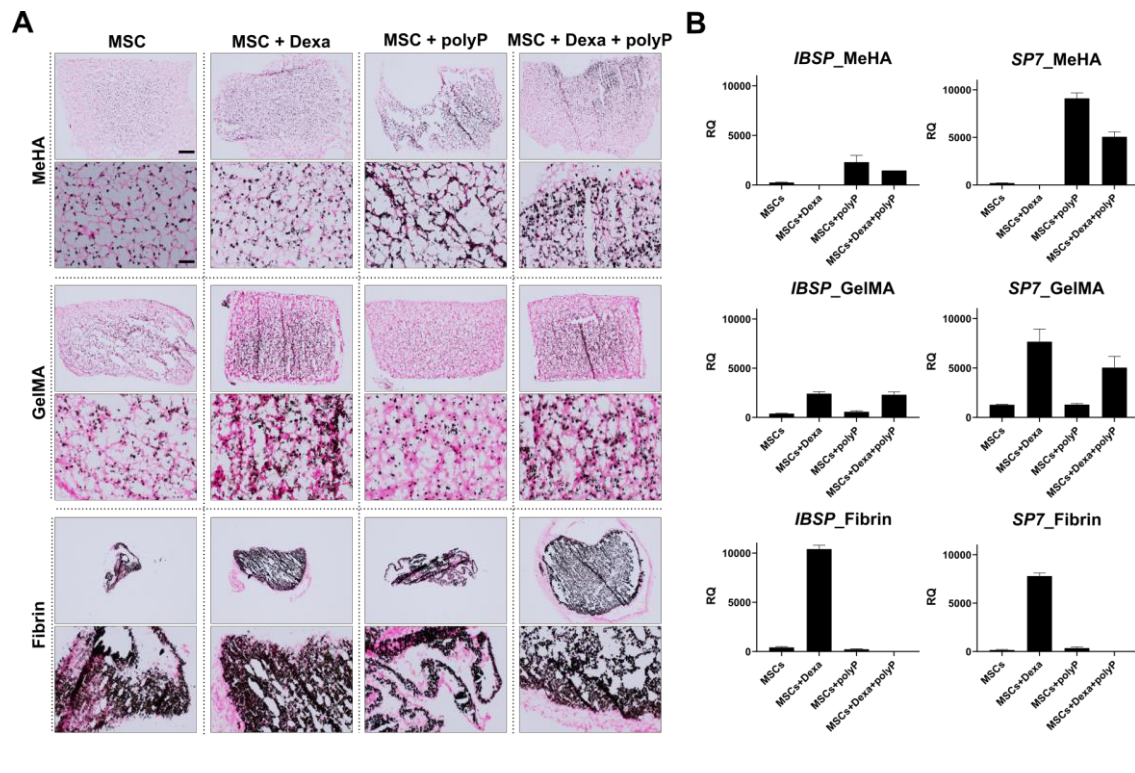


**Figure 6.5: von Kossa staining and gene expression of markers associated to late *in vitro* mineralisation.** A. Representative images of von Kossa staining at day 28. Scale bars are 500 and 100  $\mu\text{m}$  for the low and high magnification, respectively; B. Relative quantification (RQ) at day 28 calculated using the  $2^{-\Delta\Delta C_t}$  formula with *RPLP0* as reference gene and sample at day 0 as calibrator. All the data are showed as mean  $\pm$  SEM of three replicates. *IBSP*: integrin binding sialoprotein; *SP7*: Sp7 transcription factor; *RPLP0*: ribosomal protein lateral stalk subunit P0.

All materials were then tested *in vivo* in a subcutaneous implantation model in nude rats.

### Subcutaneous Model in Nude Rats

The subcutaneous surgery was performed in two sessions: surgery 1 included nine animals (6 samples per animal), of which one animal (Animal #218011) was lost before the surgery (**Table 6.2**) and surgery 2 included ten animals (6 samples per animal) (**Table 6.3**). Both tables include notes about deviations. An overview of the initial body weight loss of surgery 1 and 2 is shown in **Supplementary Figure 6.4** and **Supplementary Figure 6.5**, respectively. Based on the body weight loss observed in surgery 1, surgery 2 focused on the comparison between the effects of the cells and the effect of Dexa inclusion. The overall substantial body weight loss is caused by a systemic response triggered by the implantation of the biomaterials. Three and two animals from surgery 1 and 2, respectively, were excluded due to severe weight lost (highlighted as bold in **Table 6.2** and **Table 6.3**). Implanted biomaterials with and without bioactive factors did not produce consistent mineralisation, as no ectopic mineralisation was detected based on von Kossa staining of histology slides (**Supplementary Figure 6.6A**). MeHA combined with Dexa and polyP showed moderate mineralisation as determined by MicroCT images and von Kossa staining (**Supplementary Figure 6.6B**). Subsequently, all the samples were then assessed in the orthotopic calvarial defect model in rabbits.

**Table 6.5. Overview of sample allocation for surgery 1 of subcutaneous implantation in nude rats**

<b>Rat #</b>	<b>Spot 1</b>	<b>Spot 2</b>	<b>Spot 3</b>	<b>Spot 4</b>	<b>Spot 5</b>	<b>Spot 6</b>
218001	MeHA	GelMA	N/A	Fibrin	PCL only	N/A
218002	MeHA*	GelMA	N/A	Fibrin	PCL only	N/A
218003	MeHA*	GelMA	N/A	Fibrin	PCL only	N/A
<b>218004</b>	MeHA+MSC	GelMA+MSC	Fibrin+MSC	MeHA+MSC+Dexa*	GelMA+MSC+Dexa	Fibrin+MSC+Dexa
<b>218005</b>	MeHA+MSC	GelMA+MSC	Fibrin+MSC	MeHA+MSC+Dexa*	GelMA+MSC+Dexa	Fibrin+MSC+Dexa
<b>218006</b>	MeHA+MSC	GelMA+MSC	Fibrin+MSC	MeHA+MSC+Dexa	GelMA+MSC+Dexa	Fibrin+MSC+Dexa
218007	MeHA+MSC+polyP	GelMA+MSC+polyP	Fibrin+MSC+polyP	MeHA+MSCs+Dexa+polyP*	GelMA+MSC+Dexa+polyP	Fibrin+MSC+Dexa+polyP
218008	MeHA+MSC+polyP	GelMA+MSC+polyP	Fibrin+MSC+polyP	MeHA+MSCs+Dexa+polyP	GelMA+MSC+Dexa+polyP	Fibrin+MSC+Dexa+polyP
<b>218009</b>	MeHA+MSC+polyP*	GelMA+MSC+polyP	Fibrin+MSC+polyP	MeHA+MSCs+Dexa+polyP*	GelMA+MSC+Dexa+polyP	Fibrin+MSC+Dexa+polyP

\*Gel broke while implanting (n=7/15 MeHA samples); **in bold** animals euthanised at day 4, before endpoint, due to severe weight loss (n=3/9 animals); *in italics* animals with severe weight loss but not sufficient for exclusion (n=3/9 animals).



**Table 6.6. Overview of sample allocation for surgery 2 of subcutaneous implantation in nude rats**

Rat #	Spot 1	Spot 2	Spot 3	Spot 4	Spot 5	Spot 6
218010	MeHA+MSC	GeIMA+MSC	Fibrin+MSC	MeHA+MSC*	GeIMA+MSC	Fibrin+MSC
218016**	MeHA+MSC	GeIMA+MSC	Fibrin+MSC	MeHA+MSC	GeIMA+MSC	Fibrin+MSC
218012	MeHA+MSC	GeIMA+MSC	Fibrin+MSC	MeHA+MSC*	GeIMA+MSC	Fibrin+MSC
218013	MeHA	GeIMA	Fibrin	MeHA+Dexa*	GeIMA+Dexa	Fibrin+Dexa
218014	MeHA	GeIMA	Fibrin	MeHA+Dexa	GeIMA+Dexa	Fibrin+Dexa
218015	MeHA	GeIMA	Fibrin	MeHA+Dexa	GeIMA+Dexa	Fibrin+Dexa
<u>218017</u>	MeHA+polyP	GeIMA+polyP	Fibrin+polyP	MeHA+Dexa+polyP*	GeIMA+Dexa+ polyP	Fibrin+Dexa+polyP
<b>218018</b>	MeHA+polyP*	GeIMA+polyP	Fibrin+polyP	MeHA+Dexa+polyP*	GeIMA+Dexa+ polyP	Fibrin+Dexa+polyP
218019	MeHA+MSC	GeIMA+MSC	Fibrin+MSC	MeHA+MSC+Dexa*	GeIMAMSC+ Dexa	Fibrin+MSC+Dexa
<b>218020</b>	MeHA+MSC*	GeIMA+MSC	Fibrin+MSC	MeHA+MSC+Dexa*	GeIMA+MSC+ Dexa	Fibrin+MSC+Dexa

## **Standard in vitro Evaluations of Engineered Bone Substitutes are not Sufficient to Predict in vivo Preclinical Model Outcomes**

\*Gel broke while implanting (n=8/20 MeHA samples); \*\*Animal replaced 218011 excluded due to a rash; **In bold** animals euthanised at day 5, before endpoint, due to severe weight loss (n=2/10 animals); *In italic* animals with severe weight loss but not enough for exclusion (n=4/10 animals); Underlined are animals that did not recover from anaesthesia (n=1/10 animals). **In bold** animals euthanised at day 4, before endpoint, due to severe weight loss (n=3/9 animals); *In italics* animals with severe weight loss but not sufficient for exclusion (n=3/9 animals)

### ***Calvarial Defect Model in Rabbit***

The calvaria surgery was performed in three repetitions, with 6 animals per biomaterial in each repetition (4 samples per animal), with notes about deviations (**Table 6.4**). Data was compared to historical empty controls of previously published work using the same model system<sup>384</sup> in line with 3R principles. BV/TV values based on CT scanning and semiquantitative histopathological analysis correlate in terms of bone repair of the empty defect and the biomaterials with and without bioactive factors after 6 weeks of implantation (**Figure 6.6**). Representative microCT images are presented in **Supplementary Figure 6.7**. The empty defect shows slightly improved bone regeneration compared to the other groups. The implantation of biomaterials with and without the addition of bioactive factors did not improve the bone regeneration outcome and the defect remained without mineralisation. Histology images independent of the treatment show that gap closure for all tested biomaterials is by areas of newly formed trabecular bone (stained rose) is generally quite low and is only visible at the periphery of the osteotomy edges (**Figure 6.7**). Masson's trichrome images are presented in **Supplementary Figure 6.8**. In some spots a thin layer of bone at the meningeal/inner side of the defect leads to partial defect bridging (least pronounced in GelMA, highest in Empty; in biomaterial-treated spots a complete bridging was never observed). Direct contact of bone to biomaterial (osseous integration) was nearly absent and only recorded in very few spots for very short distances. MeHA (stained light blue to blue) displays pronounced fragmentation, indicating a certain fragility of this biomaterial and cell infiltration is dramatically limited to only superficial areas (**Table 6.5**) investigated via a blinded semiquantitative scoring system. MeHA also displays low amounts of inflammatory cell infiltrates (lymphocytic and granulomatous in nature), with a low tendency for a fibrous encapsulation.

**Standard in vitro Evaluations of Engineered Bone Substitutes are not Sufficient to Predict in vivo Preclinical Model Outcomes**

**Table 6.7. Overview of surgery results (calvarial defect model in rabbit)**

Rabbit #	Spot A	Spot B	Spot C	Spot D
319068	<u>Fibrin</u>	MeHA+Dexa	GelMA+polyP	<u>Fibrin+Dexa+polyP</u>
319069	<b>Fibrin</b>	MeHA+Dexa	GelMA+polyP	<b><u>Fibrin+Dexa+polyP</u></b>
319073	Fibrin	<b>MeHA+Dexa</b>	GelMA+polyP	<b>Fibrin+Dexa+polyP</b>
319079	Fibrin	MeHA+Dexa	<b><u>GelMA+polyP</u></b>	<b>Fibrin+Dexa+polyP</b>
319080	Fibrin	<b><u>MeHA+Dexa</u></b>	<i>GelMA+polyP</i>	<b>Fibrin+Dexa+polyP</b>
319086	Fibrin	MeHA+Dexa	<u><i>GelMA+polyP</i></u>	<b><i>Fibrin+Dexa+polyP</i></b>
319070	<u>MeHA</u>	<b><u>GelMA+Dexa</u></b>	Fibrin+polyP	<b>MeHA+Dexa+polyP</b>
319074	MeHA	GelMA+Dexa	<b><u>Fibrin+polyP</u></b>	MeHA+Dexa+polyP
319075	MeHA	<u>GelMA+Dexa</u>	Fibrin+polyP	MeHA+Dexa+polyP
319076	MeHA	GelMA+Dexa	<u>Fibrin+polyP</u>	<i>MeHA+Dexa+polyP</i>
319081	<b>MeHA</b>	<b><u>GelMA+Dexa</u></b>	<b>Fibrin+polyP</b>	<b>MeHA+Dexa+polyP</b>
319082	MeHA	<b>GelMA+Dexa</b>	<b>Fibrin+polyP</b>	MeHA+Dexa+polyP
319071	<b>GelMA</b>	<b>Fibrin+Dexa</b>	MeHA+polyP	<b>GelMA+Dexa+polyP</b>
319077	GelMA	<b><u>Fibrin+Dexa</u></b>	<u><i>MeHA+polyP</i></u>	GelMA+Dexa+polyP
319078	GelMA	<b>Fibrin+Dexa</b>	MeHA+polyP	GelMA+Dexa+polyP
319083	GelMA	<b>Fibrin+Dexa</b>	<i>MeHA+polyP</i>	<b><i>GelMA+Dexa+polyP</i></b>
319084	GelMA	<b><u>Fibrin+Dexa</u></b>	<b><u>MeHA+polyP</u></b>	GelMA+Dexa+polyP
319085	<b>GelMA</b>	<b><u>Fibrin+Dexa</u></b>	<b>MeHA+polyP</b>	GelMA+Dexa+polyP

Grey: animals with macroscopic *dura mater* injury defined by surgery observation in at least one spot (n 13/34); underlined: spots with macroscopically altered/intact/not attached *dura mater* defined by surgery observation (n=18/88); **bold**: spots with microscopic *dura mater* injury (n= 43/88 spots; defined by presence of meningeal tissue nests in defect); italic: spots with hydrogel not fitting well into the defect (n 8/72 treated spots)

**Standard in vitro Evaluations of Engineered Bone Substitutes are not Sufficient to Predict in vivo Preclinical Model Outcomes**

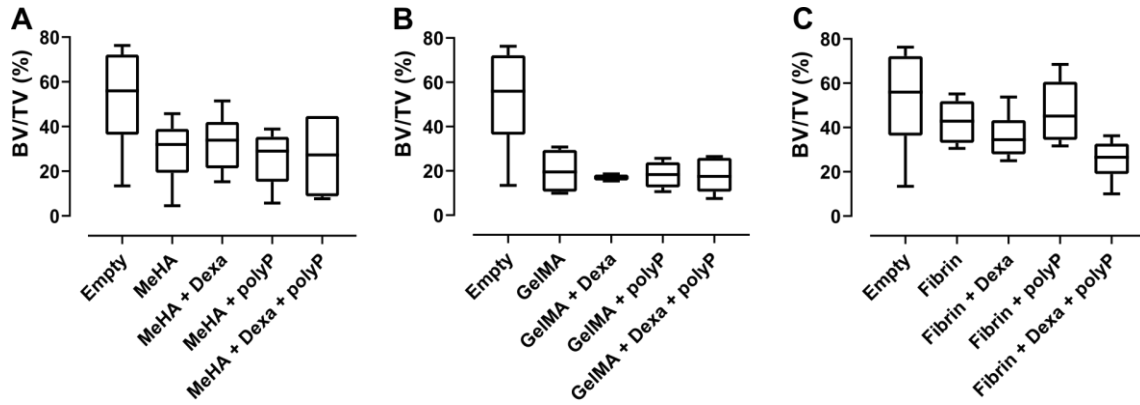


**Figure 6.2: Bone volume fraction for calvarial defect model in rabbit.** Ratios of bone volume (BV) and total volume (TV) post euthanasia (6 weeks post-surgery) are calculated based on XtremeCT post-euthanasia (6 weeks post injury).

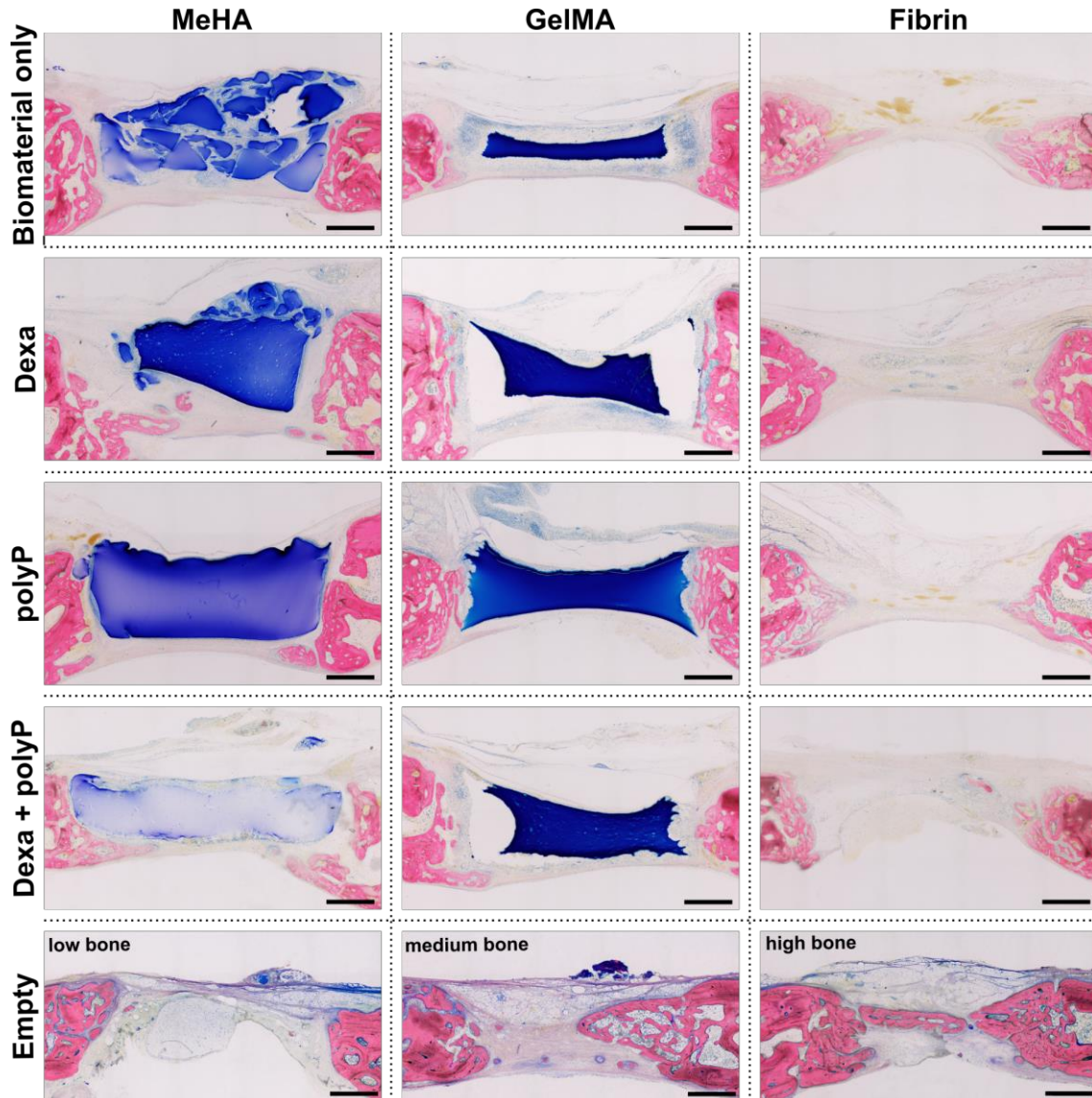


**Figure 6.7: (calvarial defect model in rabbit).** Histopathological changes in representative calvarial defects in rabbit for each treatment group (6 weeks post surgery; Giemsa Eosin stained, MMA-embedded thick-sections, scale bar 1 mm). The representative images show the inter-animal variability of empty spots. Overall, the median amount of bone is higher than that of the 3 biomaterials. Scale bars are 1 cm.

**Table 6.8. Results of semiquantitative histopathological analysis of the calvarial defects**

Parameter	MeHA	GelMA	Fibrin	Empty
Number of samples (n)	23*	23**	24	16

**Standard in vitro Evaluations of Engineered Bone Substitutes are not Sufficient to Predict in vivo Preclinical Model Outcomes**

---

<b>Bone tissue</b>				
Defect closure, bone, area	1.7	1.3	2.2	2.3
Defect bridging, bone, span/length	2.0	1.7	2.6	3.0
<b>Biomaterial properties</b>				
Amount, blue material	3.6****	3.6	1.4***	1.0***
Surface irregularity, hydrogel	1.4	2.4	1.5***	0.0
Fragmentation, hydrogel	2.2*****	0.7	2.8***	1.0***
Pores, hydrogel	1.7	1.9	1.2***	0.0
<b>Host tissue reaction</b>				
Cell infiltration, into biomaterial	0.9	0.5	0.4***	0.0
Osseous integration of biomaterial	0.7	0.3	0.0	0.0
Mineralisation of biomaterial	0.0	0.3	0.0	0.0
<b>Inflammatory reaction</b>				
Inflammation, granulocytic/purulent	0.2	0.0	0.0	0.0
Inflammation, lymphocytic	1.6	3.0	2.0	0.3
Inflammation, granulomatous	1.0	2.2	1.1	0.1
Fibrosis (e.g. capsule formation)	2.2	1.3	1.0***	1.3

\*: 1 sample of MeHA was excluded due loss of gel during post-mortem handling;  
 \*\*: 1 sample of GelMA was excluded due to loss of gel during post-mortem handling.  
 \*\*\*: values compromised/too high (spill-over of MeHA into neighbouring fibrin-treated or empty spot, n= 21/39 defects)

\*\*\*\*: value compromised/too low (spill-over of MeHA- into neighbouring spots, n=9/39 defects)

\*\*\*\*\*: value compromised/too high (due to damage/fragmentation during surgery, n=9/39 defects)

In contrast to MeHA, GelMA (stained dark blue) displays nearly no fragmentation but a pronounced tendency to shrink. Similarly, cell infiltration was nearly absent in GelMA constructs. Compared to MeHA, the inflammatory cell infiltrates (both lymphocytic and granulomatous) are more pronounced in GelMA, reaching moderate amounts. In contrast, the tendency to form a fibrotic capsule is lower.

Fibrin constructs are observed to be completely resorbed by 6 weeks post-surgery, with increased evidence of partial bridging when compared to MeHA and GelMA biomaterials. Inflammatory cell infiltration (lymphocytic and granulomatous) is low to low and comparable with MeHA.

## **6.4 Discussion**

Bone is a complex tissue and is characterised by constant remodelling that occurs throughout life. Healthy bone is extremely tough and resilient and has incredible self-healing potential leaving a regenerated defect without scars. With the current lifestyle changes and increasing aging population, combined with the diminished bone healing capacity in elderly patients, suggests that healing complications associated with bone fractures (e.g., delayed bone healing and potential progression to non-union) are estimated to rise<sup>385,386</sup>. The current standard of care (SOC), which involves bone grafting from autologous tissue or allografts, as well as implantation of BMP-2-laden collagen sponges, are associated with significant drawbacks<sup>32</sup>, thus necessitating a search for alternative bone regenerative biomaterials. A tissue engineered scaffold can provide a new alternative solution but, despite extensive research, recent advances in this field show a low clinical translation rate, potentially due the complexity of the tissue engineering approach but also due to the methods typically used to screen potential therapies. The reproducibility and reliability of any research study is based on the robustness of the methods and is negatively affected when insufficient information and details are provided. In the case of animal studies, the consequence is not only a lack of reproducibility and reliability but most importantly the resulting experimental animals being wasted. Therefore,



for science and ethics it is crucial to fully report on animal data using reporting structures such as the ARRIVE guidelines 2.0<sup>387</sup>.

The combination of cells, biomaterials and factors are difficult to assess using only simple *in vitro* tests, and preclinical models need to be more robustly chosen to answer the question at hand. In this study we sought to assess the performance of a variety of tissue engineering relevant biomaterials both *in vitro* and in two preclinical models commonly used to assess efficacy: an ectopic rodent subcutaneous implant model and a rabbit calvarial defect model. We adopted the typical workflow of a biomaterial-based research study including the design, conduct and analysis and will discuss common pitfalls.

Within this study we chose materials that have generated positive *in vitro* results and used bioactive factors with known *in vitro* and *in vivo* osteogenic potential. Dexamethasone (Dexa) is a routinely used osteogenic and chondrogenic *in vitro* supplement<sup>388</sup>, which has also shown benefits in clinical bone regeneration<sup>389</sup>. Polyphosphazene (PolyP) is an inorganic energy source with strong wound healing<sup>390</sup> and osteoinductive potential both *in vitro* and *in vivo*, including in calvarial models<sup>391,392</sup>. The presented results showed promising osteogenic potential of MSCs-laden biomaterials (MeHA, GelMA, fibrin) in combination with bioactive factors (Dexamethasone, polyP NP) *in vitro*, based on gene expression of relevant markers and von Kossa staining. The cell concentration within the biomaterials is based on a previous work<sup>393</sup>.

When studying new bone biomaterials, promising *in vitro* results often do not correlate with the outcome obtained from the *in vivo* experiments. While this is anecdotally discussed, there are very few papers that directly address this issue<sup>45</sup>. Thus, there is a need to investigate this discrepancy further and use the data obtained to improve the process used to test next generation bone biomaterials. Why *in vitro* data leads to false positive results are still largely unknown and yet it is a major weakness in the material development pathway.

Therefore, a particular focus must be placed on the limitations of each assay utilised. *In vitro* assays typically use only one cell type and use a classical dexamethasone containing osteogenic medium<sup>377,394</sup>. However, bone can heal via two different routes, either intramembranous bone formation, where the infiltrating cells differentiate directly into an osteoblast phenotype, or endochondral ossification, which utilises an initial cartilage template formed as a result of chondrogenic differentiation of callus-infiltrating MSCs, which subsequently mineralises into bone tissue. These two pathways require different conditions, both in the scaffold design and the *in vitro* culture media used<sup>199</sup>. Therefore, it should also be considered whether osteogenic medium should be the standard when testing materials where the endochondral route is expected to be the primary mechanism of action. While these are the classically accepted pathways, evidence is emerging that the actual process of fracture repair and bone formation may be more complex<sup>395,396</sup>. This should also be considered when designing the testing protocol for new materials. A further consideration is whether the planned clinical use would include cell encapsulation and delivery, or whether a cell-free material will be implanted with subsequent cell infiltration. Effective testing of these conditions *in vitro* will require a source of cells capable of undergoing differentiation. While the initial *in vitro* tests will require cells being encapsulated and differentiation assessed, an additional cell migration assay would be warranted when the final implanted material is planned to be used in a cell free approach and therefore requires cell infiltration.

Within this study, each material demonstrated *in vitro* osteogenic differentiation of encapsulated hMSCs with various degrees of success. Yet cell free orthotopic implantation suggested there was limited cell infiltration, leading to no intramembranous bone formation. The materials used in this study have been utilised in various bone healing studies and each has a range of potential permutations in formulation (e.g. crosslinking and resulting mechanical properties). The need for cell migration and the effect of each modification on the ability of cells to enter the gel should also be considered and reported during the initial material assessments.

As the *in vitro* work showed promise, all materials were tested using encapsulated hMSCs in a nude rat subcutaneous model. In our data, subcutaneous implantation of MSC-laden biomaterials did not lead to ectopic mineralisation, despite the presence of osteogenic cells and osteogenic induction signals, a situation similar to the *in vitro* study where mineralisation occurred. Given the inherent inter-donor variability in osteogenic and chondrogenic potential of human MSCs, we used the same donor for both the *in vitro* and *in vivo* experiments to avoid donor-specific differences. The reasons for the poor correlation of *in vitro* and *in vivo* outcomes are unclear, with potential off target effects or doses of bioactive factors. Previous studies have demonstrated ectopic bone formation using subcutaneous implantation, where a common theme is the incorporation of an osteoinductive component such as BMP-2 or demineralised bone that drives the osteogenic response<sup>397-399</sup>. This suggests that the subcutaneous model requires the implantation of all the required differentiation drivers. The implantation of cell-laden biomaterials in nude mice is an established procedure, however, when using human cells in a nude rat model, it should not be overlooked that although they lack T cells, the Crl:NIH-Foxn1*rmu* rats have a normal complement of B and NK cells, which may still respond to the xenogeneic cells. MSCs have immunosuppressive potential<sup>400,401</sup>, but their implantation within immunocompromised animal models may diminish the translational aspect, due to the importance of the immune system for optimal bone healing. Initial inflammation is beneficial for bone healing<sup>402</sup>, but maintained inflammation impairs healing<sup>403</sup>. A way to potentially improve efficacy testing of hMSC – laden biomaterials and its clinical translation is the use of humanised mice engrafted with functional human cells. Bone healing has been shown to be dependent on the immune status of the animal by implanting MSC-laden alginate hydrogels into T cell-deficient nude rats and comparing the response to immunocompetent rats<sup>404</sup>. Nude rats display improved healing response in muscle tissue compared to competent rats, indicating an incomplete understanding how animal models respond when biomaterials are applied<sup>405</sup>.

To establish the role on the *in vivo* model in data interpretation, all materials were then tested cell-free within an intramembranous orthotopic calvarial defect model in immunocompetent animals. The implanted material led to a reduced bone formation when compared to the empty defect, with the difference being more extreme in the MeHA and GelMA groups, while the bone formation using fibrin was similar in volume. The histological evaluation supported this conclusion and indicated this was due to a lack of cell migration into the defect, further highlighting the critical role on a migration assay in the materials development algorithm. Furthermore, dexamethasone-laden biomaterials did not enhance calvarial bone repair compared to the empty defect. Other publications using these biomaterials implanted in calvarial defect reported positive data<sup>406-412</sup>, which indicates the exact formulation is key to the response obtained<sup>413</sup>.

This raises questions regarding the workflow that should be adopted when testing new materials for osteogenic differentiation. Taken together it suggests improvements can be made to the bone testing algorithm. We would suggest routine use of a migration assay, humanised rodent models to allow the use of human cells, and *in vitro* challenge of the materials with immune cells to assess unwanted inflammatory responses. One key change could be the implantation of proposed materials into an orthotopic model, such as a drill hole model, early in the development cycle. This would identify failures at an early time point, allowing optimisation to be focused on materials that have already shown potential in an orthotopic environment. Due to the increasing evidence of immunological regulation of healing, this should ideally be done in an immune competent animal to identify early any unexpected reactions. Substantial effort is often placed into optimizing *in vitro* osteogenesis when there is no guarantee this will reflect the final orthotopic function. An early orthotopic screen *in vivo* would highlight which materials offer true potential thus reducing the effort placed to test materials *in vitro* that are destined to fail *in vivo*. Furthermore, the adequacy of the *in vivo* model in assessing complex TE approaches, and how to ask the right question with the right model (e.g. direct *versus* indirect bone formation) when using

combinations of cells, bioactive factors and biomaterials while also applying the 3Rs, must not be overlooked.

In conclusion, despite promising *in vitro* data, 12 material combinations utilizing 3 different base materials all failed to lead to bone formation in an orthotopic model. Optimisation of *in vitro* material testing protocols may identify some of these failures at an earlier time point and more studies are needed to understand how host responses to biomaterials differ based on the animal model used.

## 6.5 Funding

This study is funded by the AO CMF.

## 6.6 Acknowledgements

Acknowledgements The authors would like to thank Mr. Flavio Linardi for the MeHA and GelMA synthesis and the staff of the preclinical and histology facility of the AO Research Institute Davos for the animal surgeries and the histological preparation.

## 6.7 Supplementary Materials

**Supplementary Table 6.1. Primers/probes used for qPCR**

Gene	Assay ID <sup>1</sup>	Forward/Reverse/Probe
<i>ALPL</i>	Hs00758162_m1	
<i>IBSP</i>	Hs00173720_m1	
<i>PPAR<math>\gamma</math></i>	Hs00234592_m1	
<i>SOX9</i>	Hs00165814_m1	
<i>SP7</i>	Hs00541729_m1	
<i>RPLP0</i>		5'-TGG GCA AGA ACA CCA TGA TG-3' 5'-CGG ATA TGA GGC AGC AGT TTC-3'

**Standard in vitro Evaluations of Engineered Bone Substitutes are not Sufficient to Predict in vivo Preclinical Model Outcomes**

5'-AGG GCA CCT GGA AAA CAA CCC AGC-3'

*RUNX2* 5'-AGC AAG GTT CAA CGA TCT GAG AT-3'

5'-TTT GTG AAG ACG GTT ATG GTC AA-3'

5'-TGA AAC TCT TGC CTC GTC CAC TCC G-3'

*ALPL*: Alkaline phosphatase, biomineralisation associated; *IBSP*: integrin binding sialoprotein; *PPAR $\gamma$* : peroxisome proliferator activated receptor gamma; *SOX9*: SRY-Box transcription factor 9; *SP7*: Sp7 transcription factor; *RPLP0*: ribosomal protein lateral stalk subunit P0; *RUNX2*: Runt related transcription factor 2. <sup>1</sup>TaqMan® Gene Expression Assay (Applied Biosystems®).

**Supplementary Table 6.2. Sample distribution for subcutaneous model in rat**

Rat #	Spot 1	Spot 2	Spot 3	Spot 4	Spot 5	Spot 6
218001	MeHA	GelMA	N/A	Fibrin	PCL only	N/A
218002	MeHA*	GelMA	N/A	Fibrin	PCL only	N/A
218003	MeHA*	GelMA	N/A	Fibrin	PCL only	N/A
218004	MeHA+MSC	GelMA+MSC	Fibrin+MSC	MeHA+MSC+ Dexa*	GelMA+MSC+ Dexa	Fibrin+MSC+Dexa
218005	MeHA+MSC	GelMA+MSC	Fibrin+MSC	MeHA+MSC+ Dexa*	GelMA+MSC+ Dexa	Fibrin+MSC+Dexa
218006	MeHA+MSC	GelMA+MSC	Fibrin+MSC	MeHA+MSC+ Dexa	GelMA+MSC+ Dexa	Fibrin+MSC+Dexa
218007	MeHA+MSC+ polyP	GelMA+MSC+ polyP	Fibrin+MSC +polyP	MeHA+MSCs+ Dexa+polyP*	GelMA+MSC+ Dexa+polyP	Fibrin+MSC+Dexa +polyP
218008	MeHA+MSC+ polyP	GelMA+MSC+ polyP	Fibrin+MSC +polyP	MeHA+MSCs+ Dexa+polyP	GelMA+MSC+ Dexa+polyP	Fibrin+MSC+Dexa +polyP
218009	MeHA+MSC+ polyP*	GelMA+MSC+ polyP	Fibrin+MSC +polyP	MeHA+MSCs+ Dexa+polyP*	GelMA+MSC+ Dexa+polyP	Fibrin+MSC+Dexa +polyP
218010	MeHA+MSC	GelMA+MSC	Fibrin+MSC	MeHA+MSC*	GelMA+MSC	Fibrin+MSC

**Standard in vitro Evaluations of Engineered Bone Substitutes are not Sufficient to Predict in vivo Preclinical Model Outcomes**

218016	MeHA+MSC	GelMA+MSC	Fibrin+MSC	MeHA+MSC	GelMA+MSC	Fibrin+MSC
218012	MeHA+MSC	GelMA+MSC	Fibrin+MSC	MeHA+MSC*	GelMA+MSC	Fibrin+MSC
218013	MeHA	GelMA	Fibrin	MeHA+Dexa*	GelMA+Dexa	Fibrin+Dexa
218014	MeHA	GelMA	Fibrin	MeHA+Dexa	GelMA+Dexa	Fibrin+Dexa
218015	MeHA	GelMA	Fibrin	MeHA+Dexa	GelMA+Dexa	Fibrin+Dexa
218017	MeHA+polyP	GelMA+polyP	Fibrin+polyP	MeHA+Dexa+polyP*	GelMA+Dexa+polyP	Fibrin+Dexa+polyP
218018	MeHA+polyP*	GelMA+polyP	Fibrin+polyP	MeHA+Dexa+polyP*	GelMA+Dexa+polyP	Fibrin+Dexa+polyP
218019	MeHA+MSC	GelMA+MSC	Fibrin+MSC	MeHA+MSC+Dexa*	GelMA+MSC+Dexa	Fibrin+MSC+Dexa
218020	MeHA+MSC*	GelMA+MSC	Fibrin+MSC	MeHA+MSC+Dexa*	GelMA+MSC+Dexa	Fibrin+MSC+Dexa

MeHA: methacrylated hyaluronic acid; GelMA: gelatin methacryloyl; PCL: polycaprolactone; MSC: mesenchymal stromal cell; polyP: polyphosphate;

**Supplementary Table 6.3. Sample distribution for calvarial defect model in rabbit**

Rabbit #	Spot A	Spot B	Spot C	Spot D
319068	Fibrin	MeHA+Dexa	GelMA+polyP	Fibrin+Dexa+polyP
319069	Fibrin	MeHA+Dexa	GelMA+polyP	Fibrin+Dexa+polyP
319073	Fibrin	MeHA+Dexa	GelMA+polyP	Fibrin+Dexa+polyP
319079	Fibrin	MeHA+Dexa	GelMA+polyP	Fibrin+Dexa+polyP
319080	Fibrin	MeHA+Dexa	GelMA+polyP	Fibrin+Dexa+polyP
319086	Fibrin	MeHA+Dexa	GelMA+polyP	Fibrin+Dexa+polyP
319070	MeHA	GelMA+Dexa	Fibrin+polyP	MeHA+Dexa+polyP

**Standard in vitro Evaluations of Engineered Bone Substitutes are not Sufficient to Predict in vivo Preclinical Model Outcomes**

---

319074	MeHA	GelMA+Dexa	Fibrin+polyP	MeHA+Dexa+polyP
319075	MeHA	GelMA+Dexa	Fibrin+polyP	MeHA+Dexa+polyP
319076	MeHA	GelMA+Dexa	Fibrin+polyP	MeHA+Dexa+polyP
319081	MeHA	GelMA+Dexa	Fibrin+polyP	MeHA+Dexa+polyP
319082	MeHA	GelMA+Dexa	Fibrin+polyP	MeHA+Dexa+polyP
<hr/>				
319071	GelMA	Fibrin+Dexa	MeHA+polyP	GelMA+Dexa+polyP
319077	GelMA	Fibrin+Dexa	MeHA+polyP	GelMA+Dexa+polyP
319078	GelMA	Fibrin+Dexa	MeHA+polyP	GelMA+Dexa+polyP
319083	GelMA	Fibrin+Dexa	MeHA+polyP	GelMA+Dexa+polyP
319084	GelMA	Fibrin+Dexa	MeHA+polyP	GelMA+Dexa+polyP
319085	GelMA	Fibrin+Dexa	MeHA+polyP	GelMA+Dexa+polyP

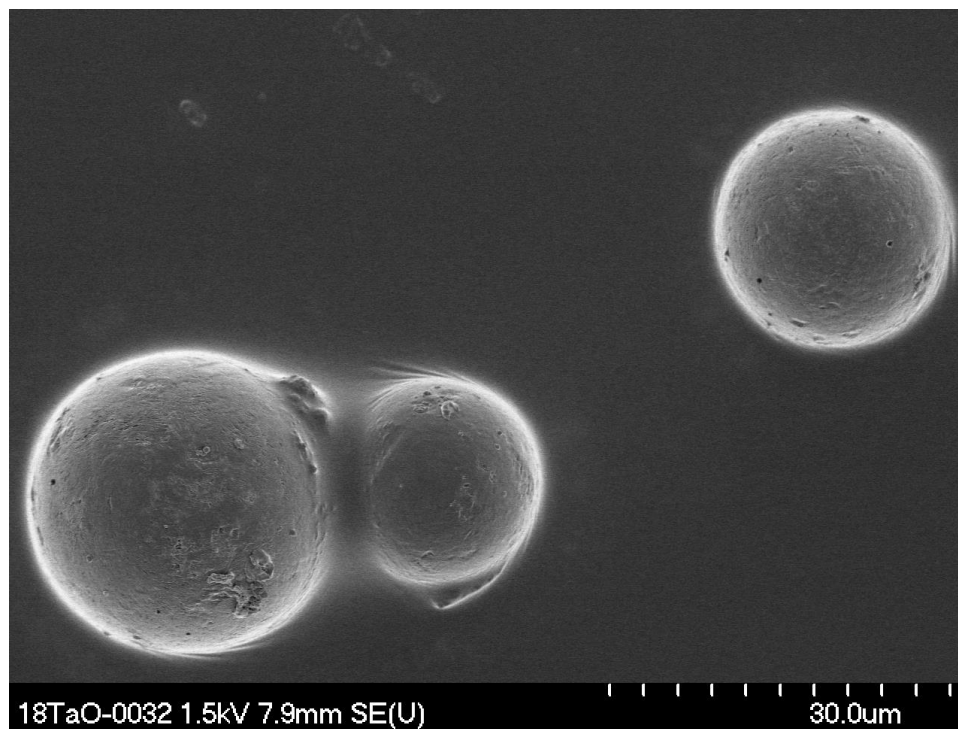
---

MeHA: methacrylated hyaluronic acid; Dexa: dexamethasone; GelMA: gelatin methacryloyl; polyP: polyphosphate.

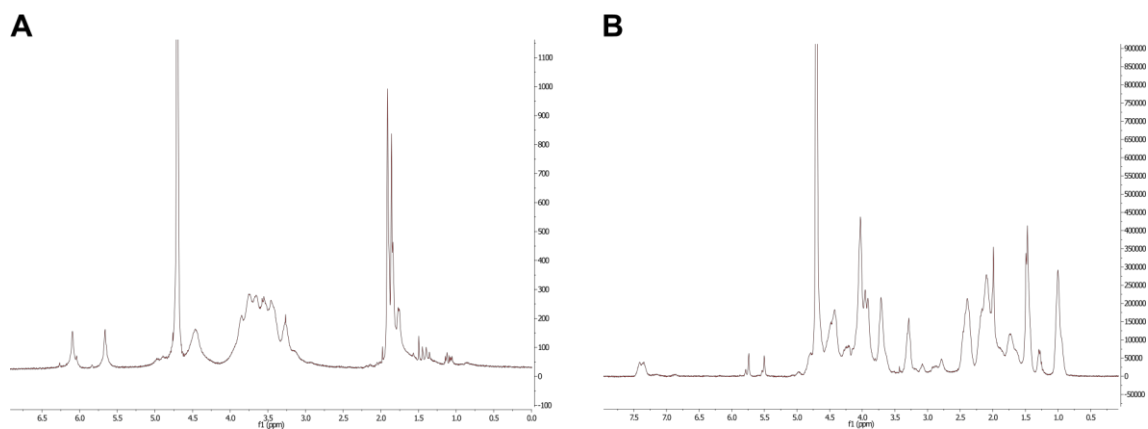


**Standard in vitro Evaluations of Engineered Bone Substitutes are not Sufficient to Predict in vivo Preclinical Model Outcomes**

---

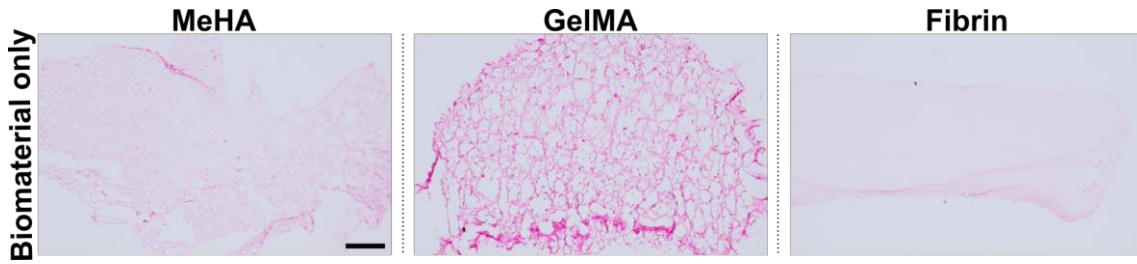


**Supplementary Figure 6.1: SEM image of DEXA-laden PCL microparticles**

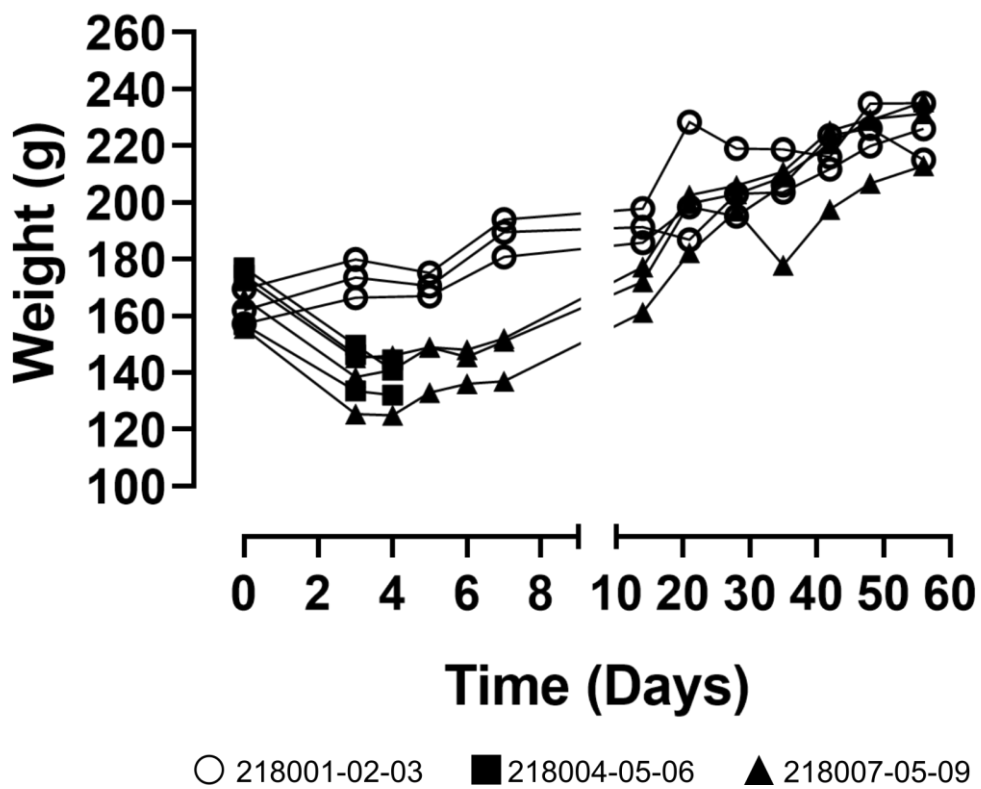


**Supplementary Figure 6.2: NMR spectra of A) MeHA and B) GelMA**

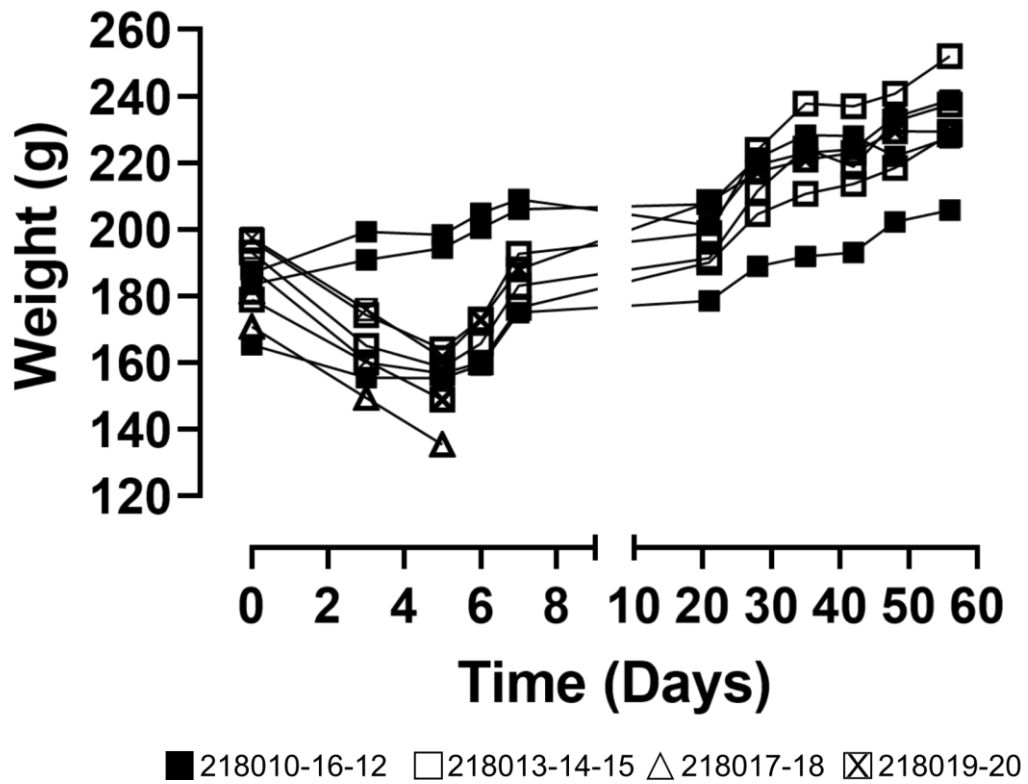
Standard in vitro Evaluations of Engineered Bone Substitutes are not Sufficient to Predict in vivo Preclinical Model Outcomes



Supplementary Figure 6.3. Representative images of biomaterials only stained with von Kossa at day 0, scale bar 500  $\mu$ m.

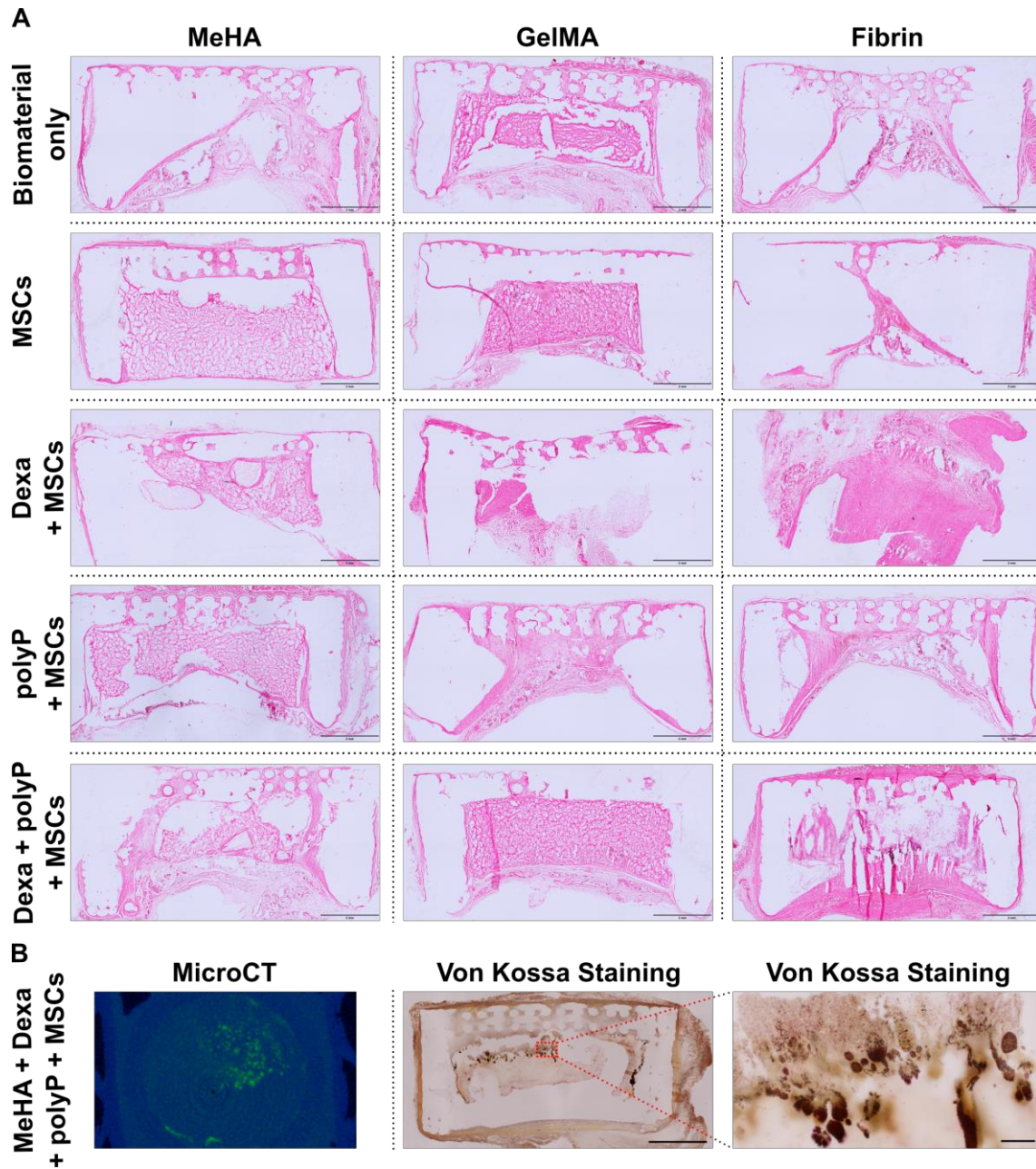


Supplementary Figure 6.4. Body weight loss after first surgery of subcutaneous implantation in nude rats.



Supplementary Figure 6.5. Initial body weight loss after second surgery (Subcutaneous implantation in nude rats).

**Standard in vitro Evaluations of Engineered Bone Substitutes are not Sufficient to Predict in vivo Preclinical Model Outcomes**

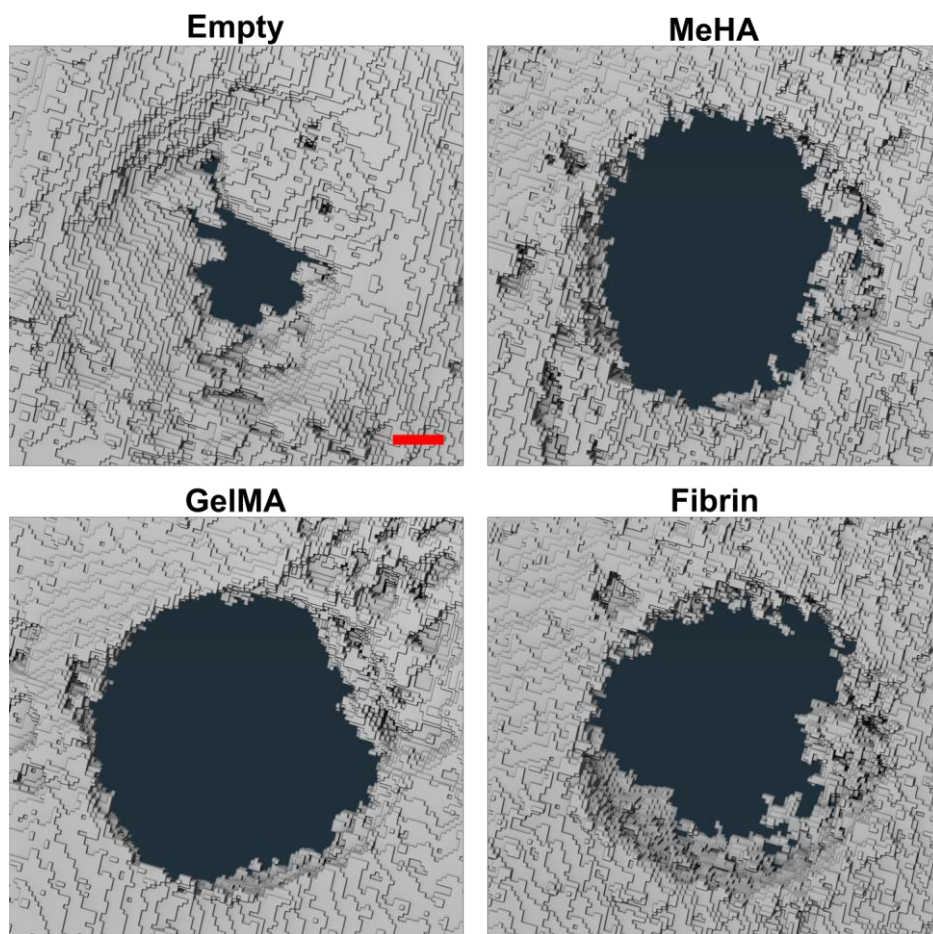


**Supplementary Figure 6.6. Subcutaneous implantation of cell-laden biomaterials with and without bioactive factors** A) von Kossa histology staining, scale bar: 2mm, B) MicroCT and von Kossa staining of cell-laden MeHA loaded with Dexa and polyP, scale bar 2 mm and 100  $\mu$ m.

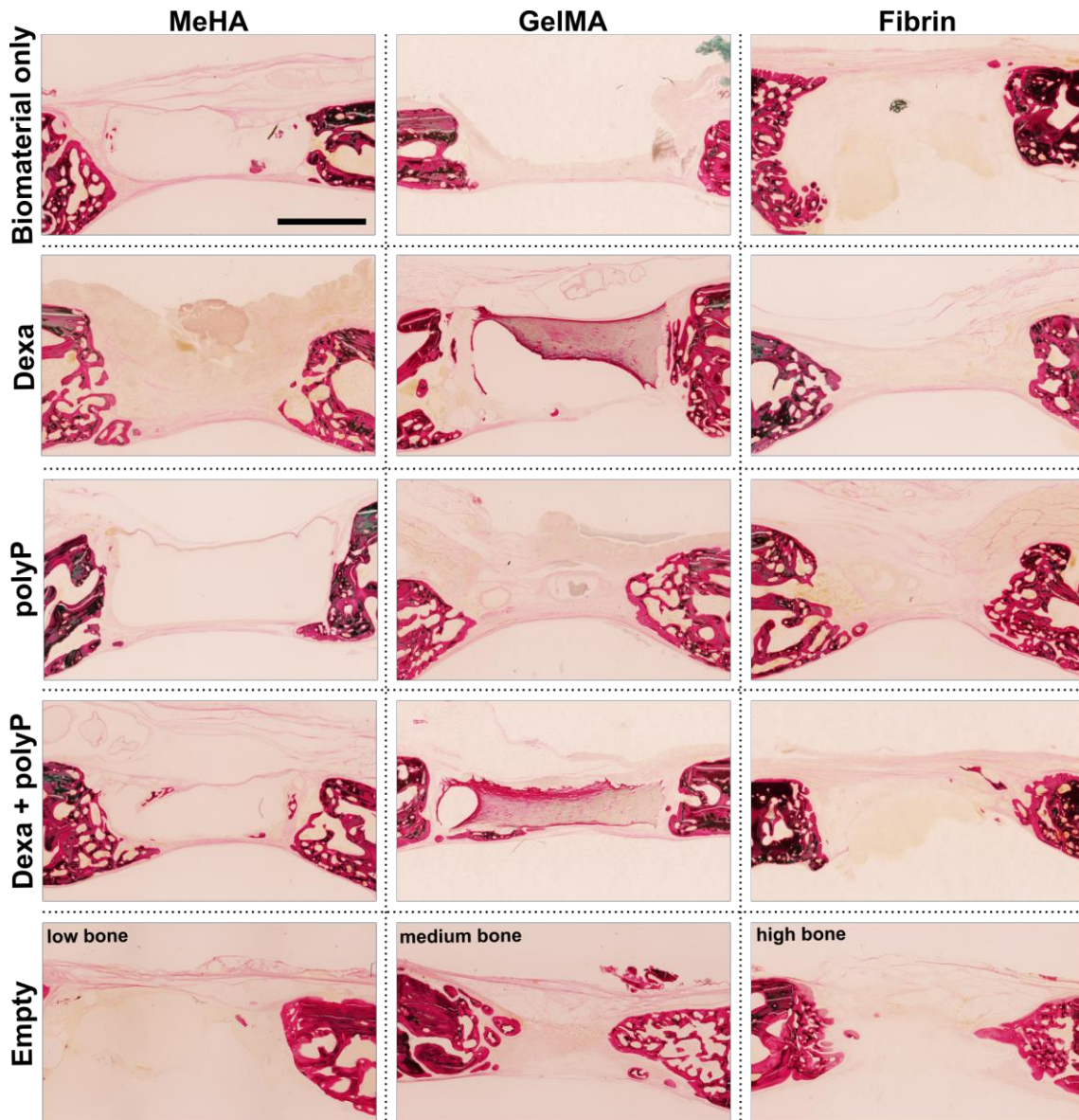


**Standard in vitro Evaluations of Engineered Bone Substitutes are not Sufficient to Predict in vivo Preclinical Model Outcomes**

---



**Supplementary Figure 6.7. Representative microCT images** of rabbit calvarial defect model after 6 weeks of implantation. Scale bar: 1 mm.



**Supplementary Figure 6.8. (calvarial defect model in rabbit). Histopathological changes in representative calvarial defects in rabbit for each treatment group (6 weeks post surgery; Masson's trichrome stained). Scale bar: 2 mm.**

## 7 Concluding Remarks

The pursuit of creating and validating BGSs to repair large CMF bone defects presents a notably complex challenge due to the field's inherently interdisciplinary nature. This endeavour necessitates a comprehensive grasp of various scientific domains including material science, chemistry, engineering, biology, ethics, and medicine. Bone is a very symbiotic tissue, engaging in strong interactions with cells and processes involved in angiogenesis, innervation, and immunity. Each of these aspects have a distinct yet interconnected role in maintaining bone homeostasis. To effectively navigate through this complex research field, a wide range of skills in laboratory techniques and methodological approaches is essential. The conversion of theoretical knowledge into research practises employs proficiencies in fabrication, synthesis, mechanical assessment, *in vitro* culture, assorted assays and histology techniques such as staining and microscopy. By merging interdisciplinary knowledge and methodical practices, researchers explore the possibilities to find an effective solution and advance the field of BTE.

The overall objective of this thesis was to apply the acquired knowledge and skill set towards developing and validating various BGSs. These substitutes are intended to achieve functional and aesthetic repair of large bone defects in the CMF region with the goal to dethrone ABG as the SOC. These attempts include the following developments:

- 1) A fabrication process to create porous PLGA/ $\beta$ -TCP/(TPU) scaffolds through a solvent-based 3D printing approach.
- 2) A workflow to construct layered 3D-printed PCL frameworks featuring an interlocking mechanism inspired by LEGO® block system, which facilitates the spatial distribution of cell-laden collagen membranes.
- 3) A drug delivery system that enables the transportation and release of bioactive factors such as DEXA-MP and polyP-NP incorporated within various hydrogels including fibrin, GelMA and MeHA.

## Concluding Remarks

---

Following thorough evaluation of the osteogenic capacity of these BGSs using established validation protocols including *in vitro* MSC osteogenesis, subcutaneous or calvarial implantation *in vivo*, it has become evident that these traditionally applied validation processes present limitations. The *in vitro* experiments highlight osteoconductive properties under the influence of a potent osteogenic cocktail that does not accurately resemble the physiological conditions of bone formation. The study in chapter 6 revealed that the promising outcome observed *in vitro* did not align with the negative results obtained from the *in vivo* study. Consequently, the conclusions drawn from these *in vitro* assessment raise concerns regarding their predictive capacity for *in vivo* scenarios. Evaluating a BGSs osteoinductivity is therefore more important as indicator of *in vivo* success. However, due to the substantial discrepancy between *in vitro* and *in vivo*, employing the standard *in vitro* models is not suitable to evaluate osteoinductivity. Therefore, I conclude that *in vitro* assessment, as currently employed, lacks the capacity to effectively validate the osteogenic capacity of a BGS and needs to be improved to provide representative data during the validation process. However, it is worth acknowledging the role of *in vitro* studies to discover and deepen our understanding of fundamental mechanisms underlying bone repair.

Following a toxicity assessment, I suggest to directly employ preliminary animal studies using small animals such as rodents or mice. This way, a more accurate assessment of the BGS's osteoinductive properties can be made early on. This preliminary study serves as the initial checkpoint before continuing with further validation through animal studies employing large animals such as sheep or minipigs.

Our comprehensive literature review regarding the utilisation of animal model for validating 3D-printed scaffolds to be employed in the CMF region, has identified limitations. In summary, the studies lack standardisation, making a comparison challenging, the majority only included an empty defect as the control and used a different bone type as they intended to heal and investigate. These limitations



## Concluding Remarks

---

could attribute to the poor clinical translation. Therefore, animal studies should be standardised, employ a positive control such as ABG as reference and should be implanted in the intended defect size, using a large animal model in the late stage.

The field of BTE has used significant research efforts a substantial funding towards advancing patient care. However, concrete improvements in outcomes are still lacking. Despite numerous published studies on the discovery of the ideal properties of biomaterials such as mechanics, porosity, roughness, or degradation<sup>414-417</sup>, a consensus has not been achieved. For instance, while researchers suggest that matching the mechanical properties of the BGS to natural bone<sup>183,418,419</sup>, I propose that the primary focus should be on the BGS's bioactivity and ideal mechanical strength is of secondary importance, particularly in the clinic, where load would be distributed using metal implants. Bone healing can be promoted by biomaterials with different mechanical properties ranging from rigid metals<sup>420-422</sup> to soft hydrogels<sup>10,423</sup>, as long as the material possess osteogenic cues that can initiate the healing process. Therefore, mechanical strength is primarily relevant in load bearing defects sites where resistance to screw-plate fixation is essential.

Additionally, researchers advocate for aligning the rate of degradation with the natural pace of bone remodelling<sup>92,424,425</sup>. However, I propose that the rate of biodegradation is of secondary importance. Functional outcome can still be attained even if the BGS remains in place for months following the healing process. In my opinion, the ongoing intensive search for the biomaterial's ideal properties should undergo a shift in focus. Instead, the priority should be directed towards discovering novel potent osteogenic inducers. However, a BGS that is composed of a scaffold combined with an novel osteogenic inducer is considered a high risk invasive medical device, categorised as class III<sup>426</sup> and requires a rigorous clinical conformity assessment to proof safety and efficacy before it can be used for clinical use. Furthermore, the focus should also be directed towards developing an innovative delivery system for rhBMP-2 into the defect side,

## Concluding Remarks

---

allowing for its bone healing capacity without causing associated side effects. The already existing clinical approval for the delivery of rhBMP-2 using collagen sponges could be advantageous to obtain clinical approval of a novel delivery system without the need to repeat the rigorous and expensive clinical investigation from the start. It is essential to refocus our priorities and concentrate on infusing the BGS with bioactive elements that trigger the initial cascade of healing for successful bone repair.

Looking into future perspectives, the presented work holds potential to be improved, particularly in the domains of vascularisation and innervation, both of which are tightly connected to bone healing. Optimal bone regeneration is closely coupled with angiogenesis, which is mediated by vascular endothelial growth factor (VEGF) in synergy with BMP-2, the main osteogenic inducer.<sup>427,428</sup> Upon BGS implantation, vessel infiltration becomes essential to provide nutrients and oxygen, as well as to remove waste products. The use of endothelial cells has been extensively investigated as a cell type to be combined with the BGS to allow anastomosis and enhance vascularisation. While vascularisation has received considerable attention in the research field, innervation has been largely neglected, despite the importance of both aspects. Innervation plays a crucial role in successful bone tissue regeneration and is primarily regulated by nerve growth factor.<sup>429</sup> In addition to the requirement of a BGS to provide osteogenic and angiogenic cues, including factors that support nerve growth and innervation can contribute to improved bone tissue regeneration outcomes. Addressing both vascularisation and innervation in a coupled fashion is necessary to overcome the limitations within the framework of this thesis.

Despite substantial efforts and many published research papers, the shift from ABG to BGS remains to take place. Two main avenues with distinct fundamentals could be pursued in the future to enhance this transition.

- 1) High-risk, high-reward projects with translation potential: An approach with potential for fast and direct translation into clinical practise could enhance the paradigm shift. By overturning conventional approaches by innovative

## Concluding Remarks

---

methodologies, we could unlock breakthroughs that can transform the field of BTE. However, I posit that there is still a lack of understanding of fundamental biology, particularly in cell biology.

- 2) Increased investment in fundamental biology: Basic research is aiming at comprehending and manipulating cell behaviour, partially interesting in stem cell research. Foundational insights of bone regeneration are yet to be discovered and could be the key for revolutionary therapeutic approaches.

Both these approaches could potentially be a plausible strategy for advancing the field of BTE. A combination of high-risk, high-reward projects and fundamental research could offer a balanced approach to forward us into a successful era of BGS developments.

## References

- 1 Ji, W. *et al.* Local delivery of small and large biomolecules in craniomaxillofacial bone. *Adv Drug Deliv Rev* **64**, 1152-1164 (2012). <https://doi.org/10.1016/j.addr.2012.03.003>
- 2 Breeland, G., Sinkler, M. A. & Menezes, R. G. in *StatPearls [Internet]* (StatPearls Publishing, 2022).
- 3 Migliorini, F., La Padula, G., Torsiello, E., Spiezia, F., Oliva, F. & Maffulli, N. Strategies for large bone defect reconstruction after trauma, infections or tumour excision: a comprehensive review of the literature. *Eur. J. Med. Res.* **26**, 118 (2021). <https://doi.org/10.1186/s40001-021-00593-9>
- 4 Hatt, L. P., Thompson, K., Helms, J. A., Stoddart, M. J. & Armiento, A. R. Clinically relevant preclinical animal models for testing novel cranio-maxillofacial bone 3D-printed biomaterials. *Clin Transl Med* **12**, e690 (2022). <https://doi.org/10.1002/ctm2.690>
- 5 Xue, N. *et al.* Bone Tissue Engineering in the Treatment of Bone Defects. *Pharmaceuticals (Basel)* **15** (2022). <https://doi.org/10.3390/ph15070879>
- 6 Amini, A. R., Laurencin, C. T. & Nukavarapu, S. P. Bone tissue engineering: recent advances and challenges. *Crit Rev Biomed Eng* **40**, 363-408 (2012). <https://doi.org/10.1615/critrevbiomedeng.v40.i5.10>
- 7 Dec, P., Modrzejewski, A. & Pawlik, A. Existing and Novel Biomaterials for Bone Tissue Engineering. *Int J Mol Sci* **24** (2022). <https://doi.org/10.3390/ijms24010529>
- 8 Qu, H., Fu, H., Han, Z. & Sun, Y. Biomaterials for bone tissue engineering scaffolds: a review. *RSC Adv* **9**, 26252-26262 (2019). <https://doi.org/10.1039/c9ra05214c>
- 9 Yu, X., Tang, X., Gohil, S. V. & Laurencin, C. T. Biomaterials for Bone Regenerative Engineering. *Adv Healthc Mater* **4**, 1268-1285 (2015). <https://doi.org/10.1002/adhm.201400760>
- 10 Yue, S., He, H., Li, B. & Hou, T. Hydrogel as a Biomaterial for Bone Tissue Engineering: A Review. *Nanomaterials (Basel)* **10** (2020). <https://doi.org/10.3390/nano10081511>
- 11 Bahram, M., Mohseni, N. & Moghtader, M. in *Emerging concepts in analysis and applications of hydrogels* (IntechOpen, 2016).
- 12 van der Heide, D., Cidonio, G., Stoddart, M. J. & D'Este, M. 3D printing of inorganic-biopolymer composites for bone regeneration. *Biofabrication* **14** (2022). <https://doi.org/10.1088/1758-5090/ac8cb2>

## References

---

- 13 Madden, L. R. *et al.* Proangiogenic scaffolds as functional templates for cardiac tissue engineering. *Proc. Natl. Acad. Sci. U. S. A.* **107**, 15211-15216 (2010). <https://doi.org:10.1073/pnas.1006442107>
- 14 Bai, F. *et al.* The correlation between the internal structure and vascularization of controllable porous bioceramic materials in vivo: a quantitative study. *Tissue Eng Part A* **16**, 3791-3803 (2010). <https://doi.org:10.1089/ten.TEA.2010.0148>
- 15 Zhu, X. D. *et al.* Effect of surface structure on protein adsorption to biphasic calcium-phosphate ceramics in vitro and in vivo. *Acta Biomater* **5**, 1311-1318 (2009). <https://doi.org:10.1016/j.actbio.2008.11.024>
- 16 O'Brien, F. J. Biomaterials & scaffolds for tissue engineering. *Materials Today* **14**, 88-95 (2011). [https://doi.org:https://doi.org/10.1016/S1369-7021\(11\)70058-X](https://doi.org:https://doi.org/10.1016/S1369-7021(11)70058-X)
- 17 Jang, J.-W., Min, K.-E., Kim, C., Shin, J., Lee, J. & Yi, S. Review: Scaffold Characteristics, Fabrication Methods, and Biomaterials for the Bone Tissue Engineering. *International Journal of Precision Engineering and Manufacturing* **24**, 511-529 (2023). <https://doi.org:10.1007/s12541-022-00755-7>
- 18 Sampath, U., Ching, Y. C., Chuah, C. H., Sabariah, J. J. & Lin, P. C. Fabrication of Porous Materials from Natural/Synthetic Biopolymers and Their Composites. *Materials (Basel)* **9** (2016). <https://doi.org:10.3390/ma9120991>
- 19 Zhou, Y., Chyu, J. & Zumwalt, M. Recent Progress of Fabrication of Cell Scaffold by Electrospinning Technique for Articular Cartilage Tissue Engineering. *Int J Biomater* **2018**, 1953636 (2018). <https://doi.org:10.1155/2018/1953636>
- 20 Wu, J. & Hong, Y. Enhancing cell infiltration of electrospun fibrous scaffolds in tissue regeneration. *Bioact Mater* **1**, 56-64 (2016). <https://doi.org:10.1016/j.bioactmat.2016.07.001>
- 21 Winarso, R., Anggoro, P. W., Ismail, R., Jamari, J. & Bayuseno, A. P. Application of fused deposition modeling (FDM) on bone scaffold manufacturing process: A review. *Heliyon* **8**, e11701 (2022). <https://doi.org:10.1016/j.heliyon.2022.e11701>
- 22 Sta Agueda, J. R. H. *et al.* 3D printing of biomedically relevant polymer materials and biocompatibility. *MRS Commun* **11**, 197-212 (2021). <https://doi.org:10.1557/s43579-021-00038-8>
- 23 Godoy-Gallardo, M., Portolés-Gil, N., López-Periago, A. M., Domingo, C. & Hosta-Rigau, L. Multi-layered polydopamine coatings for the

## References

---

- immobilization of growth factors onto highly-interconnected and bimodal PCL/HA-based scaffolds. *Mater. Sci. Eng. C Mater. Biol. Appl.* **117**, 111245 (2020). <https://doi.org/10.1016/j.msec.2020.111245>
- 24 Perez, J. R., Kouroupis, D., Li, D. J., Best, T. M., Kaplan, L. & Correa, D. Tissue Engineering and Cell-Based Therapies for Fractures and Bone Defects. *Front Bioeng Biotechnol* **6**, 105 (2018). <https://doi.org/10.3389/fbioe.2018.00105>
- 25 Schu, S. *et al.* Immunogenicity of allogeneic mesenchymal stem cells. *J Cell Mol Med* **16**, 2094-2103 (2012). <https://doi.org/10.1111/j.1582-4934.2011.01509.x>
- 26 Kangari, P., Talaei-Khozani, T., Razeghian-Jahromi, I. & Razmkhah, M. Mesenchymal stem cells: amazing remedies for bone and cartilage defects. *Stem Cell. Res. Ther.* **11**, 492 (2020). <https://doi.org/10.1186/s13287-020-02001-1>
- 27 Weatherall, E. L. *et al.* Differentiation Potential of Mesenchymal Stem/Stromal Cells Is Altered by Intrauterine Growth Restriction. *Front Vet Sci* **7**, 558905 (2020). <https://doi.org/10.3389/fvets.2020.558905>
- 28 Qin, Y., Guan, J. & Zhang, C. Mesenchymal stem cells: mechanisms and role in bone regeneration. *Postgrad. Med. J.* **90**, 643-647 (2014). <https://doi.org/10.1136/postgradmedj-2013-132387>
- 29 Paulini, M. *et al.* Recombinant Proteins-Based Strategies in Bone Tissue Engineering. *Biomolecules* **12** (2021). <https://doi.org/10.3390/biom12010003>
- 30 Haidar, Z. S., Hamdy, R. C. & Tabrizian, M. Delivery of recombinant bone morphogenetic proteins for bone regeneration and repair. Part A: Current challenges in BMP delivery. *Biotechnol. Lett.* **31**, 1817-1824 (2009). <https://doi.org/10.1007/s10529-009-0099-x>
- 31 Laurencin, C. T., Ashe, K. M., Henry, N., Kan, H. M. & Lo, K. W. Delivery of small molecules for bone regenerative engineering: preclinical studies and potential clinical applications. *Drug Discov. Today* **19**, 794-800 (2014). <https://doi.org/10.1016/j.drudis.2014.01.012>
- 32 James, A. W. *et al.* A Review of the Clinical Side Effects of Bone Morphogenetic Protein-2. *Tissue Eng Part B Rev* **22**, 284-297 (2016). <https://doi.org/10.1089/ten.TEB.2015.0357>
- 33 Hickey, T., Kreutzer, D., Burgess, D. J. & Moussy, F. Dexamethasone/PLGA microspheres for continuous delivery of an anti-inflammatory drug for implantable medical devices. *Biomaterials* **23**, 1649-1656 (2002). [https://doi.org/10.1016/s0142-9612\(01\)00291-5](https://doi.org/10.1016/s0142-9612(01)00291-5)

## References

---

- 34 Stefani, R. M. *et al.* Sustained low-dose dexamethasone delivery via a PLGA microsphere-embedded agarose implant for enhanced osteochondral repair. *Acta Biomater* **102**, 326-340 (2020). <https://doi.org/10.1016/j.actbio.2019.11.052>
- 35 Wang, Y. *et al.* Progress and Applications of Polyphosphate in Bone and Cartilage Regeneration. *Biomed Res Int* **2019**, 5141204 (2019). <https://doi.org/10.1155/2019/5141204>
- 36 Wang, L. *et al.* Polyphosphate enhanced biomimetic mineralization of 3D printing scaffolds for bone regeneration. *Composites Part B: Engineering* **239**, 109989 (2022). <https://doi.org/https://doi.org/10.1016/j.compositesb.2022.109989>
- 37 Müller, W. E. G. *et al.* Biologization of Allogeneic Bone Grafts with Polyphosphate: A Route to a Biomimetic Periosteum. *Adv Funct Mater* **29**, 1905220 (2019). <https://doi.org/https://doi.org/10.1002/adfm.201905220>
- 38 Langenbach, F. & Handschel, J. Effects of dexamethasone, ascorbic acid and  $\beta$ -glycerophosphate on the osteogenic differentiation of stem cells in vitro. *Stem Cell Res Ther* **4**, 117 (2013). <https://doi.org/10.1186/scrt328>
- 39 Yuasa, M. *et al.* Dexamethasone enhances osteogenic differentiation of bone marrow- and muscle-derived stromal cells and augments ectopic bone formation induced by bone morphogenetic protein-2. *PLoS One* **10**, e0116462 (2015). <https://doi.org/10.1371/journal.pone.0116462>
- 40 Tavakoli-darestani, R., Manafi-rasi, A. & Kamrani-rad, A. Dexamethasone-loaded hydroxyapatite enhances bone regeneration in rat calvarial defects. *Mol Biol Rep* **41**, 423-428 (2014). <https://doi.org/10.1007/s11033-013-2876-9>
- 41 Wang, X., Schröder, H. C. & Müller, W. E. G. Amorphous polyphosphate, a smart bioinspired nano-/bio-material for bone and cartilage regeneration: towards a new paradigm in tissue engineering. *J Mater Chem B* **6**, 2385-2412 (2018). <https://doi.org/10.1039/c8tb00241j>
- 42 Müller, W. E. G. *et al.* Amorphous, Smart, and Bioinspired Polyphosphate Nano/Microparticles: A Biomaterial for Regeneration and Repair of Osteo-Articular Impairments In-Situ. *Int J Mol Sci* **19** (2018). <https://doi.org/10.3390/ijms19020427>
- 43 Müller, W. E. G. *et al.* Fabrication of amorphous strontium polyphosphate microparticles that induce mineralization of bone cells in vitro and in vivo. *Acta Biomater* **50**, 89-101 (2017). <https://doi.org/10.1016/j.actbio.2016.12.045>

## References

---

- 44 Hatt, L. P. *et al.* Standard in vitro evaluations of engineered bone substitutes are not sufficient to predict in vivo preclinical model outcomes. *Acta Biomater* (2022). <https://doi.org:10.1016/j.actbio.2022.08.021>
- 45 Hulsart-Billström, G. *et al.* A surprisingly poor correlation between in vitro and in vivo testing of biomaterials for bone regeneration: results of a multicentre analysis. *Eur Cell Mater* **31**, 312-322 (2016). <https://doi.org:10.22203/ecm.v031a20>
- 46 Cramer, E. E. A., Ito, K. & Hofmann, S. Ex vivo Bone Models and Their Potential in Preclinical Evaluation. *Curr Osteoporos Rep* **19**, 75-87 (2021). <https://doi.org:10.1007/s11914-020-00649-5>
- 47 Fini, M. & Giardino, R. In vitro and in vivo tests for the biological evaluation of candidate orthopedic materials: Benefits and limits. *J Appl Biomater Biomech* **1**, 155-163 (2003).
- 48 Gomes, P. S. & Fernandes, M. H. Rodent models in bone-related research: the relevance of calvarial defects in the assessment of bone regeneration strategies. *Lab. Anim.* **45**, 14-24 (2011). <https://doi.org:10.1258/la.2010.010085>
- 49 Sparks, D. S. *et al.* A preclinical large-animal model for the assessment of critical-size load-bearing bone defect reconstruction. *Nat. Protoc.* **15**, 877-924 (2020). <https://doi.org:10.1038/s41596-019-0271-2>
- 50 Hatt, L. P. *et al.* Micro-porous PLGA/ $\beta$ -TCP/TPU scaffolds prepared by solvent-based 3D printing for bone tissue engineering purposes. *Regenerative Biomaterials* (2023). <https://doi.org:10.1093/rb/rbad084>
- 51 Rana, M. *et al.* Reconstruction of mandibular defects - clinical retrospective research over a 10-year period. *Head Neck Oncol.* **3**, 23 (2011). <https://doi.org:10.1186/1758-3284-3-23>
- 52 Li, Z., Wang, Q. & Liu, G. A Review of 3D Printed Bone Implants. *Micromachines (Basel)* **13** (2022). <https://doi.org:10.3390/mi13040528>
- 53 Niaounakis, M. *Biopolymers: reuse, recycling, and disposal.* (William Andrew, 2013).
- 54 Grémare, A. *et al.* Characterization of printed PLA scaffolds for bone tissue engineering. *J Biomed Mater Res A* **106**, 887-894 (2018). <https://doi.org:10.1002/jbm.a.36289>
- 55 Bachtiar, E. W., Amir, L. R., Suhardi, P. & Abas, B. Scaffold degradation during bone tissue reconstruction in *Macaca nemestrina* mandible. *Interv Med Appl Sci* **8**, 77-81 (2016). <https://doi.org:10.1556/1646.8.2016.2.5>



## References

---

- 56 Li, X., Zou, Q., Wei, J. & Li, W. The degradation regulation of 3D printed scaffolds for promotion of osteogenesis and in vivo tracking. *Composites Part B: Engineering* **222**, 109084 (2021). <https://doi.org/10.1016/j.compositesb.2021.109084>
- 57 Bernardo, M. P. *et al.* PLA/Hydroxyapatite scaffolds exhibit in vitro immunological inertness and promote robust osteogenic differentiation of human mesenchymal stem cells without osteogenic stimuli. *Sci. Rep.* **12**, 2333 (2022). <https://doi.org/10.1038/s41598-022-05207-w>
- 58 Wang, W. *et al.* Fabrication and properties of PLA/nano-HA composite scaffolds with balanced mechanical properties and biological functions for bone tissue engineering application. *Nanotechnol Rev* **10**, 1359-1373 (2021). <https://doi.org/10.1515/ntrev-2021-0083>
- 59 Wang, W. *et al.* 3D printing of PLA/n-HA composite scaffolds with customized mechanical properties and biological functions for bone tissue engineering. *Compos B Eng* **224**, 109192 (2021). <https://doi.org/10.1016/j.compositesb.2021.109192>
- 60 Zhang, B. *et al.* 3D printed bone tissue regenerative PLA/HA scaffolds with comprehensive performance optimizations. *Mater Des* **201**, 109490 (2021). <https://doi.org/10.1016/j.matdes.2021.109490>
- 61 Melčová, V. *et al.* FDM 3D Printed Composites for Bone Tissue Engineering Based on Plasticized Poly(3-hydroxybutyrate)/poly(D,L-lactide) Blends. *Polymers (Basel)* **12** (2020). <https://doi.org/10.3390/polym12122806>
- 62 Schneider, M. *et al.* Surface Etching of 3D Printed Poly(lactic acid) with NaOH: A Systematic Approach. *Polymers (Basel)* **12** (2020). <https://doi.org/10.3390/polym12081711>
- 63 Gregor, A. *et al.* Designing of PLA scaffolds for bone tissue replacement fabricated by ordinary commercial 3D printer. *J. Biol. Eng.* **11**, 31 (2017). <https://doi.org/10.1186/s13036-017-0074-3>
- 64 Bobbert, F. S. L. & Zadpoor, A. A. Effects of bone substitute architecture and surface properties on cell response, angiogenesis, and structure of new bone. *J Mater Chem B* **5**, 6175-6192 (2017). <https://doi.org/10.1039/c7tb00741h>
- 65 Zhang, K., Fan, Y., Dunne, N. & Li, X. Effect of microporosity on scaffolds for bone tissue engineering. *Regen Biomater* **5**, 115-124 (2018). <https://doi.org/10.1093/rb/rby001>

## References

---

- 66 Puleo, D. A. & Bizios, R. *Biological interactions on materials surfaces: understanding and controlling protein, cell, and tissue responses*. (Springer, 2009).
- 67 Qiu, Z. Y., Chen, C., Wang, X. M. & Lee, I. S. Advances in the surface modification techniques of bone-related implants for last 10 years. *Regen Biomater* **1**, 67-79 (2014). <https://doi.org/10.1093/rb/rbu007>
- 68 Ma, Z., Mao, Z. & Gao, C. Surface modification and property analysis of biomedical polymers used for tissue engineering. *Colloids Surf. B. Biointerfaces* **60**, 137-157 (2007). <https://doi.org/10.1016/j.colsurfb.2007.06.019>
- 69 Kazimierczak, P. & Przekora, A. Osteoconductive and osteoinductive surface modifications of biomaterials for bone regeneration: A concise review. *Coatings (Basel)* **10**, 971 (2020).
- 70 Serra, T., Planell, J. A. & Navarro, M. High-resolution PLA-based composite scaffolds via 3-D printing technology. *Acta Biomater* **9**, 5521-5530 (2013). <https://doi.org/10.1016/j.actbio.2012.10.041>
- 71 Geven, M. A., Sprecher, C., Guillaume, O., Eglin, D. & Grijpma, D. W. Micro-porous composite scaffolds of photo-crosslinked poly(trimethylene carbonate) and nano-hydroxyapatite prepared by low-temperature extrusion-based additive manufacturing. *Polym Adv Technol* **28**, 1226-1232 (2017). [https://doi.org:https://doi.org/10.1002/pat.3890](https://doi.org/https://doi.org/10.1002/pat.3890)
- 72 Mi, H. Y., Jing, X., Napiwocki, B. N., Hagerty, B. S., Chen, G. & Turng, L. S. Biocompatible, degradable thermoplastic polyurethane based on polycaprolactone-block-polytetrahydrofuran-block-polycaprolactone copolymers for soft tissue engineering. *J Mater Chem B* **5**, 4137-4151 (2017). <https://doi.org/10.1039/c7tb00419b>
- 73 Gogolewski, S. Selected topics in biomedical polyurethanes. A review. *Colloid Polym Sci* **267**, 757-785 (1989).
- 74 Rodríguez-Parada, L., de la Rosa, S. & Mayuet, P. F. Influence of 3D-Printed TPU Properties for the Design of Elastic Products. *Polymers (Basel)* **13** (2021). <https://doi.org/10.3390/polym13152519>
- 75 Bagnol, R. *et al.* Coaxial micro-extrusion of a calcium phosphate ink with aqueous solvents improves printing stability, structure fidelity and mechanical properties. *Acta Biomater* **125**, 322-332 (2021). <https://doi.org/10.1016/j.actbio.2021.02.022>
- 76 Gardner, O. F., Alini, M. & Stoddart, M. J. Mesenchymal Stem Cells Derived from Human Bone Marrow. *Methods Mol Biol* **1340**, 41-52 (2015). [https://doi.org/10.1007/978-1-4939-2938-2\\_3](https://doi.org/10.1007/978-1-4939-2938-2_3)

## References

---

- 77 Phelipe Hatt, L., Thompson, K., Müller, W. E. G., Stoddart, M. J. & Armiento, A. R. Calcium Polyphosphate Nanoparticles Act as an Effective Inorganic Phosphate Source during Osteogenic Differentiation of Human Mesenchymal Stem Cells. *Int J Mol Sci* **20** (2019). <https://doi.org:10.3390/ijms20225801>
- 78 Thommes, M. *et al.* Physisorption of gases, with special reference to the evaluation of surface area and pore size distribution (IUPAC Technical Report). *Pure Appl. Chem.* **87**, 1051-1069 (2015).
- 79 Shim, J. H. *et al.* Efficacy of rhBMP-2 loaded PCL/PLGA/ $\beta$ -TCP guided bone regeneration membrane fabricated by 3D printing technology for reconstruction of calvaria defects in rabbit. *Biomed Mater* **9**, 065006 (2014). <https://doi.org:10.1088/1748-6041/9/6/065006>
- 80 Shim, J.-H. *et al.* Comparative Efficacies of a 3D-Printed PCL/PLGA/ $\beta$ -TCP Membrane and a Titanium Membrane for Guided Bone Regeneration in Beagle Dogs. *Polymers (Basel)* **7**, 2061-2077 (2015).
- 81 Won, J. Y. *et al.* Evaluation of 3D printed PCL/PLGA/ $\beta$ -TCP versus collagen membranes for guided bone regeneration in a beagle implant model. *Biomed Mater* **11**, 055013 (2016). <https://doi.org:10.1088/1748-6041/11/5/055013>
- 82 Guo, T. *et al.* 3D printing PLGA: a quantitative examination of the effects of polymer composition and printing parameters on print resolution. *Biofabrication* **9**, 024101 (2017). <https://doi.org:10.1088/1758-5090/aa6370>
- 83 Hwang, K. S. *et al.* Comparative Efficacies of Collagen-Based 3D Printed PCL/PLGA/ $\beta$ -TCP Composite Block Bone Grafts and Biphasic Calcium Phosphate Bone Substitute for Bone Regeneration. *Materials (Basel)* **10** (2017). <https://doi.org:10.3390/ma10040421>
- 84 Kankala, R. K., Xu, X. M., Liu, C. G., Chen, A. Z. & Wang, S. B. 3D-Printing of Microfibrous Porous Scaffolds Based on Hybrid Approaches for Bone Tissue Engineering. *Polymers (Basel)* **10** (2018). <https://doi.org:10.3390/polym10070807>
- 85 La, W.-G., Jang, J., Kim, B. S., Lee, M. S., Cho, D.-W. & Yang, H. S. Systemically replicated organic and inorganic bony microenvironment for new bone formation generated by a 3D printing technology. *RSC Advances* **6**, 11546-11553 (2016). <https://doi.org:10.1039/C5RA20218C>
- 86 Moncal, K. K. *et al.* 3D printing of poly( $\epsilon$ -caprolactone)/poly(D,L-lactide-co-glycolide)/hydroxyapatite composite constructs for bone tissue engineering. *J Mater Res* **33**, 1972-1986 (2018). <https://doi.org:10.1557/jmr.2018.111>

## References

---

- 87 Rasoulianboroujeni, M. *et al.* Development of 3D-printed PLGA/TiO(2) nanocomposite scaffolds for bone tissue engineering applications. *Mater. Sci. Eng. C Mater. Biol. Appl.* **96**, 105-113 (2019). <https://doi.org/10.1016/j.msec.2018.10.077>
- 88 Jakus, A. E. *et al.* Hyperelastic "bone": A highly versatile, growth factor-free, osteoregenerative, scalable, and surgically friendly biomaterial. *Sci. Transl. Med.* **8**, 358ra127 (2016). <https://doi.org/10.1126/scitranslmed.aaf7704>
- 89 Huang, Y. H. *et al.* Three-Dimensionally Printed Hyperelastic Bone Scaffolds Accelerate Bone Regeneration in Critical-Size Calvarial Bone Defects. *Plast. Reconstr. Surg.* **143**, 1397-1407 (2019). <https://doi.org/10.1097/prs.0000000000005530>
- 90 Chang, P. C. *et al.* Regeneration of critical-sized mandibular defect using a 3D-printed hydroxyapatite-based scaffold: An exploratory study. *J. Periodontol.* **92**, 428-435 (2021). <https://doi.org/10.1002/jper.20-0110>
- 91 Deng, N. *et al.* Experimental study of rhBMP-2 chitosan nano-sustained release carrier-loaded PLGA/nHA scaffolds to construct mandibular tissue-engineered bone. *Arch. Oral Biol.* **102**, 16-25 (2019). <https://doi.org/10.1016/j.archoralbio.2019.03.023>
- 92 Lai, Y. *et al.* Osteogenic magnesium incorporated into PLGA/TCP porous scaffold by 3D printing for repairing challenging bone defect. *Biomaterials* **197**, 207-219 (2019). <https://doi.org/10.1016/j.biomaterials.2019.01.013>
- 93 Kolan, K. *et al.* Solvent based 3D printing of biopolymer/bioactive glass composite and hydrogel for tissue engineering applications. *Procedia CIRP* **65**, 38-43 (2017).
- 94 Gonçalves, E. M. *et al.* Three-dimensional printed PCL-hydroxyapatite scaffolds filled with CNTs for bone cell growth stimulation. *J Biomed Mater Res B Appl Biomater* **104**, 1210-1219 (2016). <https://doi.org/10.1002/jbm.b.33432>
- 95 Guo, T., Lim, C., Noshin, M., Ringel, J. P. & Fisher, J. P. 3D Printing Bioactive PLGA Scaffolds Using DMSO as a Removable Solvent. *Bioprinting* **10** (2018). <https://doi.org/10.1016/j.bprint.2018.e00038>
- 96 Schemitsch, E. H. Size Matters: Defining Critical in Bone Defect Size! *J Orthop Trauma* **31 Suppl 5**, S20-S22 (2017). <https://doi.org/10.1097/BOT.0000000000000978>

## References

---

- 97 Makadia, H. K. & Siegel, S. J. Poly Lactic-co-Glycolic Acid (PLGA) as Biodegradable Controlled Drug Delivery Carrier. *Polymers (Basel)* **3**, 1377-1397 (2011). <https://doi.org:10.3390/polym3031377>
- 98 Ke, D., Dernell, W., Bandyopadhyay, A. & Bose, S. Doped tricalcium phosphate scaffolds by thermal decomposition of naphthalene: Mechanical properties and in vivo osteogenesis in a rabbit femur model. *J Biomed Mater Res B Appl Biomater* **103**, 1549-1559 (2015). <https://doi.org:10.1002/jbm.b.33321>
- 99 Liu, H., Slamovich, E. B. & Webster, T. J. Less harmful acidic degradation of poly(lactico-glycolic acid) bone tissue engineering scaffolds through titania nanoparticle addition. *Int J Nanomedicine* **1**, 541-545 (2006). <https://doi.org:10.2147/nano.2006.1.4.541>
- 100 Feng, B. *et al.* The effect of pore size on tissue ingrowth and neovascularization in porous bioceramics of controlled architecture in vivo. *Biomed Mater* **6**, 015007 (2011). <https://doi.org:10.1088/1748-6041/6/1/015007>
- 101 Reinwald, Y., Johal, R., Ghaemmaghami, A., Rose, F., Howdle, S. & Shakesheff, K. Interconnectivity and permeability of supercritical fluid-foamed scaffolds and the effect of their structural properties on cell distribution. *Polymer* **55**, 435-444 (2014).
- 102 Dong, J. *et al.* Solvent-cast 3D printing of magnesium scaffolds. *Acta Biomater* **114**, 497-514 (2020). <https://doi.org:10.1016/j.actbio.2020.08.002>
- 103 Al-Maharma, A. Y., Patil, S. P. & Markert, B. Effects of porosity on the mechanical properties of additively manufactured components: A critical review. *Mater Res Express* **7**, 122001 (2020).
- 104 Aqida, S., Ghazali, M. I. & Hashim, J. Effect of porosity on mechanical properties of metal matrix composite: an overview. *J Teknol*, 17-32 (2004).
- 105 Wang, S., Kowal, T. J., Marei, M. K., Falk, M. M. & Jain, H. Nanoporosity significantly enhances the biological performance of engineered glass tissue scaffolds. *Tissue Eng Part A* **19**, 1632-1640 (2013). <https://doi.org:10.1089/ten.TEA.2012.0585>
- 106 Rho, J. Y., Ashman, R. B. & Turner, C. H. Young's modulus of trabecular and cortical bone material: ultrasonic and microtensile measurements. *J Biomech.* **26**, 111-119 (1993). [https://doi.org:10.1016/0021-9290\(93\)90042-d](https://doi.org:10.1016/0021-9290(93)90042-d)

## References

---

- 107 Xu, T., Shen, W., Lin, X. & Xie, Y. M. Mechanical Properties of Additively Manufactured Thermoplastic Polyurethane (TPU) Material Affected by Various Processing Parameters. *Polymers (Basel)* **12** (2020). <https://doi.org/10.3390/polym12123010>
- 108 Wang, H. *et al.* Thermoplastic polyurethane with controllable degradation and critical anti-fouling properties. *Biomater Sci* **9**, 1381-1396 (2021). <https://doi.org/10.1039/d0bm01967d>
- 109 Anderson, M. *et al.* Three-dimensional printing of clinical scale and personalized calcium phosphate scaffolds for alveolar bone reconstruction. *Dent. Mater.* **38**, 529-539 (2022). <https://doi.org/10.1016/j.dental.2021.12.141>
- 110 Twohig, C. *et al.* A dual-ink 3D printing strategy to engineer pre-vascularized bone scaffolds in-vitro. *Mater. Sci. Eng. C Mater. Biol. Appl.* **123**, 111976 (2021). <https://doi.org/10.1016/j.msec.2021.111976>
- 111 Ahlfeld, T. *et al.* 3D Plotted Biphasic Bone Scaffolds for Growth Factor Delivery: Biological Characterization In Vitro and In Vivo. *Adv Healthc Mater* **8**, e1801512 (2019). <https://doi.org/10.1002/adhm.201801512>
- 112 Korn, P. *et al.* 3D Printing of Bone Grafts for Cleft Alveolar Osteoplasty - In vivo Evaluation in a Preclinical Model. *Front Bioeng Biotechnol* **8**, 217 (2020). <https://doi.org/10.3389/fbioe.2020.00217>
- 113 Yenyol, S. & Ricci, J. L. Alkaline phosphatase levels of murine pre-osteoblastic cells on anodized and annealed titanium surfaces. *Eur Oral Res* **52**, 12-19 (2018). <https://doi.org/10.26650/eor.2018.78387>
- 114 Sharma, U., Pal, D. & Prasad, R. Alkaline phosphatase: an overview. *Indian J. Clin. Biochem.* **29**, 269-278 (2014). <https://doi.org/10.1007/s12291-013-0408-y>
- 115 Sinclair, S. S. & Burg, K. J. Effect of osteoclast co-culture on the differentiation of human mesenchymal stem cells grown on bone graft granules. *J Biomater Sci Polym Ed* **22**, 789-808 (2011). <https://doi.org/10.1163/092050610x496260>
- 116 Sinha, K. M. & Zhou, X. Genetic and molecular control of osterix in skeletal formation. *J Cell Biochem* **114**, 975-984 (2013). <https://doi.org/10.1002/jcb.24439>
- 117 Si, J., Wang, C., Zhang, D., Wang, B. & Zhou, Y. Osteopontin in Bone Metabolism and Bone Diseases. *Med. Sci. Monit.* **26**, e919159 (2020). <https://doi.org/10.12659/msm.919159>

## References

---

- 118 Siddappa, R., Licht, R., van Blitterswijk, C. & de Boer, J. Donor variation and loss of multipotency during in vitro expansion of human mesenchymal stem cells for bone tissue engineering. *J. Orthop. Res.* **25**, 1029-1041 (2007). <https://doi.org:10.1002/jor.20402>
- 119 Stroncek, D. F. *et al.* Human Mesenchymal Stromal Cell (MSC) Characteristics Vary Among Laboratories When Manufactured From the Same Source Material: A Report by the Cellular Therapy Team of the Biomedical Excellence for Safer Transfusion (BEST) Collaborative. *Front Cell Dev Biol* **8**, 458 (2020). <https://doi.org:10.3389/fcell.2020.00458>
- 120 Marrella, A. *et al.* Engineering vascularized and innervated bone biomaterials for improved skeletal tissue regeneration. *Mater Today (Kidlington)* **21**, 362-376 (2018). <https://doi.org:10.1016/j.mattod.2017.10.005>
- 121 Hatt, L., Van Der Heide, D., Armiento, A. & Stoddart, M.  $\beta$ -TCP from 3D-printed composite scaffolds acts as an effective phosphate source during osteogenic differentiation of human mesenchymal stromal cells. *Frontiers in Cell and Developmental Biology* **11** (2023). <https://doi.org:10.3389/fcell.2023.1258161>
- 122 Paré, A., Bossard, A., Laure, B., Weiss, P., Gauthier, O. & Corre, P. Reconstruction of segmental mandibular defects: Current procedures and perspectives. *Laryngoscope Investig Otolaryngol* **4**, 587-596 (2019). <https://doi.org:10.1002/lio2.325>
- 123 Kemp, K. C., Hows, J. & Donaldson, C. Bone marrow-derived mesenchymal stem cells. *Leuk Lymphoma* **46**, 1531-1544 (2005). <https://doi.org:10.1080/10428190500215076>
- 124 Rong, Q. *et al.* A novel method to improve the osteogenesis capacity of hUCMSCs with dual-directional pre-induction under screened co-culture conditions. *Cell Prolif.* **53**, e12740 (2020). <https://doi.org:10.1111/cpr.12740>
- 125 Tu, C. *et al.* Effects of electromagnetic fields treatment on rat critical-sized calvarial defects with a 3D-printed composite scaffold. *Stem Cell. Res. Ther.* **11**, 433 (2020). <https://doi.org:10.1186/s13287-020-01954-7>
- 126 Khojasteh, A., Behnia, H., Hosseini, F. S., Dehghan, M. M., Abbasnia, P. & Abbas, F. M. The effect of PCL-TCP scaffold loaded with mesenchymal stem cells on vertical bone augmentation in dog mandible: a preliminary report. *J Biomed Mater Res B Appl Biomater* **101**, 848-854 (2013). <https://doi.org:10.1002/jbm.b.32889>
- 127 Probst, F. A. *et al.* Bone regeneration of minipig mandibular defect by adipose derived mesenchymal stem cells seeded tri-calcium phosphate-

## References

---

- poly(D,L-lactide-co-glycolide) scaffolds. *Sci. Rep.* **10**, 2062 (2020). <https://doi.org/10.1038/s41598-020-59038-8>
- 128 Yamada, M., Shiota, M., Yamashita, Y. & Kasugai, S. Histological and histomorphometrical comparative study of the degradation and osteoconductive characteristics of alpha- and beta-tricalcium phosphate in block grafts. *J Biomed Mater Res B Appl Biomater* **82**, 139-148 (2007). <https://doi.org/10.1002/jbm.b.30715>
- 129 Liu, B. & Lun, D. X. Current application of  $\beta$ -tricalcium phosphate composites in orthopaedics. *Orthop. Surg.* **4**, 139-144 (2012). <https://doi.org/10.1111/j.1757-7861.2012.00189.x>
- 130 Salamanca, E. *et al.* Fabrication of Polylactic Acid/ $\beta$ -Tricalcium Phosphate FDM 3D Printing Fiber to Enhance Osteoblastic-Like Cell Performance. *Front Mater* **8**, 683706 (2021).
- 131 Zhao, D. *et al.* Poly(lactic-co-glycolic acid)-based composite bone-substitute materials. *Bioact Mater* **6**, 346-360 (2021). <https://doi.org/10.1016/j.bioactmat.2020.08.016>
- 132 Kang, Y. *et al.* Enhanced mechanical performance and biological evaluation of a PLGA coated  $\beta$ -TCP composite scaffold for load-bearing applications. *Eur Polym J* **47**, 1569-1577 (2011). <https://doi.org/10.1016/j.eurpolymj.2011.05.004>
- 133 Bongio, M., van den Beucken, J. J., Leeuwenburgh, S. C. & Jansen, J. A. Preclinical evaluation of injectable bone substitute materials. *J. Tissue Eng. Regen. Med.* **9**, 191-209 (2015). <https://doi.org/10.1002/term.1637>
- 134 Zha, K., Tian, Y., Panayi, A. C., Mi, B. & Liu, G. Recent Advances in Enhancement Strategies for Osteogenic Differentiation of Mesenchymal Stem Cells in Bone Tissue Engineering. *Front Cell Dev Biol* **10**, 824812 (2022). <https://doi.org/10.3389/fcell.2022.824812>
- 135 Maniatopoulos, C., Sodek, J. & Melcher, A. H. Bone formation in vitro by stromal cells obtained from bone marrow of young adult rats. *Cell Tissue Res* **254**, 317-330 (1988). <https://doi.org/10.1007/bf00225804>
- 136 Tenenbaum, H. C. Role of organic phosphate in mineralization of bone in vitro. *J Dent Res* **60 Spec No C**, 1586-1589 (1981). <https://doi.org/10.1177/0022034581060003s0801>
- 137 Nantavisai, S., Egusa, H., Osathanon, T. & Sawangmake, C. Mesenchymal stem cell-based bone tissue engineering for veterinary practice. *Heliyon* **5**, e02808 (2019). <https://doi.org/10.1016/j.heliyon.2019.e02808>



## References

---

- 138 He, P., Mann-Collura, O., Fling, J., Edara, N., Hetz, R. & Razzaque, M. S. High phosphate actively induces cytotoxicity by rewiring pro-survival and pro-apoptotic signaling networks in HEK293 and HeLa cells. *FASEB J.* **35**, e20997 (2021). <https://doi.org/10.1096/fj.202000799RR>
- 139 Di Marco, G. S. *et al.* High phosphate directly affects endothelial function by downregulating annexin II. *Kidney Int.* **83**, 213-222 (2013). <https://doi.org/10.1038/ki.2012.300>
- 140 Giachelli, C. M. The emerging role of phosphate in vascular calcification. *Kidney Int.* **75**, 890-897 (2009). <https://doi.org/10.1038/ki.2008.644>
- 141 Zhou, C., Shi, Z., Ouyang, N. & Ruan, X. Hyperphosphatemia and Cardiovascular Disease. *Front Cell Dev Biol* **9**, 644363 (2021). <https://doi.org/10.3389/fcell.2021.644363>
- 142 Anand, A. & Aoyagi, H. Understudied Hyperphosphatemia (Chronic Kidney Disease) Treatment Targets and New Biological Approaches. *Medicina (Kaunas)* **59** (2023). <https://doi.org/10.3390/medicina59050959>
- 143 Beck, G. R., Jr. Inorganic phosphate as a signaling molecule in osteoblast differentiation. *J Cell Biochem* **90**, 234-243 (2003). <https://doi.org/10.1002/jcb.10622>
- 144 Liu, Y. K. *et al.* The effect of extracellular calcium and inorganic phosphate on the growth and osteogenic differentiation of mesenchymal stem cells in vitro: implication for bone tissue engineering. *Biomed Mater* **4**, 025004 (2009). <https://doi.org/10.1088/1748-6041/4/2/025004>
- 145 Camalier, C. E. *et al.* An integrated understanding of the physiological response to elevated extracellular phosphate. *J Cell Physiol* **228**, 1536-1550 (2013). <https://doi.org/10.1002/jcp.24312>
- 146 Schäck, L. M. *et al.* The Phosphate Source Influences Gene Expression and Quality of Mineralization during In Vitro Osteogenic Differentiation of Human Mesenchymal Stem Cells. *PLoS One* **8**, e65943-e65943 (2013). <https://doi.org/10.1371/journal.pone.0065943>
- 147 Kuss, M. A. *et al.* Prevascularization of 3D printed bone scaffolds by bioactive hydrogels and cell co-culture. *J Biomed Mater Res B Appl Biomater* **106**, 1788-1798 (2018). <https://doi.org/10.1002/jbm.b.33994>
- 148 Ebrahimi, Z., Irani, S., Ardeshiryajimi, A. & Seyedjafari, E. Enhanced osteogenic differentiation of stem cells by 3D printed PCL scaffolds coated with collagen and hydroxyapatite. *Sci. Rep.* **12**, 12359 (2022). <https://doi.org/10.1038/s41598-022-15602-y>

## References

---

- 149 Nyberg, E., Rindone, A., Dorafshar, A. & Grayson, W. L. Comparison of 3D-Printed Poly- $\epsilon$ -Caprolactone Scaffolds Functionalized with Tricalcium Phosphate, Hydroxyapatite, Bio-Oss, or Decellularized Bone Matrix. *Tissue Eng Part A* **23**, 503-514 (2017). <https://doi.org/10.1089/ten.TEA.2016.0418>
- 150 Qian, G., Fan, P., He, F. & Ye, J. Novel Strategy to Accelerate Bone Regeneration of Calcium Phosphate Cement by Incorporating 3D Plotted Poly(lactic-co-glycolic acid) Network and Bioactive Wollastonite. *Adv Healthc Mater* **8**, e1801325 (2019). <https://doi.org/10.1002/adhm.201801325>
- 151 Jiao, X. *et al.* 3D-Printed  $\beta$ -Tricalcium Phosphate Scaffolds Promote Osteogenic Differentiation of Bone Marrow-Deprived Mesenchymal Stem Cells in an N6-methyladenosine-Dependent Manner. *Int J Bioprint* **8**, 544 (2022). <https://doi.org/10.18063/ijb.v8i2.544>
- 152 Meesuk, L. *et al.* Osteogenic differentiation and proliferation potentials of human bone marrow and umbilical cord-derived mesenchymal stem cells on the 3D-printed hydroxyapatite scaffolds. *Sci. Rep.* **12**, 19509 (2022). <https://doi.org/10.1038/s41598-022-24160-2>
- 153 Armiento, A. R., Ladner, Y. D., Della Bella, E. & Stoddart, M. J. Isolation and In Vitro Chondrogenic Differentiation of Human Bone Marrow-Derived Mesenchymal Stromal Cells. *Methods Mol Biol* **2598**, 65-73 (2023). [https://doi.org/10.1007/978-1-0716-2839-3\\_6](https://doi.org/10.1007/978-1-0716-2839-3_6)
- 154 Della Bella, E. *et al.* Dexamethasone Induces Changes in Osteogenic Differentiation of Human Mesenchymal Stromal Cells via SOX9 and PPAR $\gamma$ , but Not RUNX2. *Int. J. Mol. Sci.* **22**, 4785 (2021). <https://doi.org/10.3390/ijms22094785>
- 155 Wallin, R. F. & Arscott, E. A practical guide to ISO 10993-5: Cytotoxicity. *Medical Device and Diagnostic Industry* **20**, 96-98 (1998).
- 156 Zhu, M., Kohan, E., Bradley, J., Hedrick, M., Benhaim, P. & Zuk, P. The effect of age on osteogenic, adipogenic and proliferative potential of female adipose-derived stem cells. *J. Tissue Eng. Regen. Med.* **3**, 290-301 (2009). <https://doi.org/10.1002/term.165>
- 157 Horinouchi, C. D., Barisón, M. J., Robert, A. W., Kuligovski, C., Aguiar, A. M. & Dallagiovanna, B. Influence of donor age on the differentiation and division capacity of human adipose-derived stem cells. *World J. Stem Cells* **12**, 1640-1651 (2020). <https://doi.org/10.4252/wjsc.v12.i12.1640>
- 158 Chen, Y. *et al.* Type-I collagen produced by distinct fibroblast lineages reveals specific function during embryogenesis and Osteogenesis

## References

---

- Imperfecta. *Nat Commun* **12**, 7199 (2021).  
<https://doi.org/10.1038/s41467-021-27563-3>
- 159 Mollentze, J., Durandt, C. & Pepper, M. S. An In Vitro and In Vivo Comparison of Osteogenic Differentiation of Human Mesenchymal Stromal/Stem Cells. *Stem Cells Int.* **2021**, 9919361 (2021).  
<https://doi.org/10.1155/2021/9919361>
- 160 Komori, T. Regulation of osteoblast differentiation by transcription factors. *J Cell Biochem* **99**, 1233-1239 (2006). <https://doi.org/10.1002/jcb.20958>
- 161 Pokrovskaya, L. A., Nadezhdin, S. V., Zubareva, E. V., Burda, Y. E. & Gnezdyukova, E. S. Expression of RUNX2 and Osterix in Rat Mesenchymal Stem Cells during Culturing in Osteogenic-Conditioned Medium. *Bull. Exp. Biol. Med.* **169**, 571-575 (2020).  
<https://doi.org/10.1007/s10517-020-04931-5>
- 162 Komori, T. Runx2, an inducer of osteoblast and chondrocyte differentiation. *Histochem. Cell Biol.* **149**, 313-323 (2018).  
<https://doi.org/10.1007/s00418-018-1640-6>
- 163 Loebel, C., Czekanska, E. M., Bruderer, M., Salzmann, G., Alini, M. & Stoddart, M. J. In vitro osteogenic potential of human mesenchymal stem cells is predicted by Runx2/Sox9 ratio. *Tissue Eng Part A* **21**, 115-123 (2015). <https://doi.org/10.1089/ten.TEA.2014.0096>
- 164 Trivedi, S. *et al.* A quantitative method to determine osteogenic differentiation aptness of scaffold. *J Oral Biol Craniofac Res* **10**, 158-160 (2020). <https://doi.org/10.1016/j.jobcr.2020.04.006>
- 165 Levitt, M. D., Hapak, S. M. & Levitt, D. G. Alkaline Phosphatase Pathophysiology with Emphasis on the Seldom-Discussed Role of Defective Elimination in Unexplained Elevations of Serum ALP - A Case Report and Literature Review. *Clin. Exp. Gastroenterol.* **15**, 41-49 (2022).  
<https://doi.org/10.2147/ceg.S345531>
- 166 Gao, M. M. *et al.* Transcriptional activation of ENPP1 by osterix in osteoblasts and osteocytes. *Eur Cell Mater* **36**, 1-14 (2018).  
<https://doi.org/10.22203/eCM.v036a01>
- 167 Nam, H. K., Liu, J., Li, Y., Kragor, A. & Hatch, N. E. Ectonucleotide pyrophosphatase/phosphodiesterase-1 (ENPP1) protein regulates osteoblast differentiation. *J. Biol. Chem.* **286**, 39059-39071 (2011).  
<https://doi.org/10.1074/jbc.M111.221689>
- 168 Roberts, F., Zhu, D., Farquharson, C. & Macrae, V. E. ENPP1 in the Regulation of Mineralization and Beyond. *Trends Biochem. Sci.* **44**, 616-628 (2019). <https://doi.org/10.1016/j.tibs.2019.01.010>

## References

---

- 169 Pujari-Palmer, M. *et al.* Pyrophosphate Stimulates Differentiation, Matrix Gene Expression and Alkaline Phosphatase Activity in Osteoblasts. *PLoS One* **11**, e0163530 (2016). <https://doi.org/10.1371/journal.pone.0163530>
- 170 Othman, Z. *et al.* The role of ENPP1/PC-1 in osteoinduction by calcium phosphate ceramics. *Biomaterials* **210**, 12-24 (2019). <https://doi.org/10.1016/j.biomaterials.2019.04.021>
- 171 Szeri, F. *et al.* The membrane protein ANKH is crucial for bone mechanical performance by mediating cellular export of citrate and ATP. *PLoS Genet.* **16**, e1008884 (2020). <https://doi.org/10.1371/journal.pgen.1008884>
- 172 Minashima, T., Quirno, M., Lee, Y. J. & Kirsch, T. The role of the progressive ankylosis protein (ANK) in adipogenic/osteogenic fate decision of precursor cells. *Bone* **98**, 38-46 (2017). <https://doi.org/10.1016/j.bone.2017.03.003>
- 173 Granchi, D. *et al.* Gene expression patterns related to osteogenic differentiation of bone marrow-derived mesenchymal stem cells during ex vivo expansion. *Tissue Eng Part C Methods* **16**, 511-524 (2010). <https://doi.org/10.1089/ten.TEC.2009.0405>
- 174 Roberts, S., Narisawa, S., Harmey, D., Millán, J. L. & Farquharson, C. Functional involvement of PHOSPHO1 in matrix vesicle-mediated skeletal mineralization. *J Bone Miner Res* **22**, 617-627 (2007). <https://doi.org/10.1359/jbmr.070108>
- 175 Dillon, S., Staines, K. A., Millán, J. L. & Farquharson, C. How To Build a Bone: PHOSPHO1, Biomineralization, and Beyond. *JBMR Plus* **3**, e10202 (2019). <https://doi.org/10.1002/jbm4.10202>
- 176 Hsu, S. N. *et al.* Increased PHOSPHO1 expression mediates cortical bone mineral density in renal osteodystrophy. *J. Endocrinol.* **254**, 153-167 (2022). <https://doi.org/10.1530/joe-22-0097>
- 177 Meleti, Z., Shapiro, I. M. & Adams, C. S. Inorganic phosphate induces apoptosis of osteoblast-like cells in culture. *Bone* **27**, 359-366 (2000). [https://doi.org/10.1016/s8756-3282\(00\)00346-x](https://doi.org/10.1016/s8756-3282(00)00346-x)
- 178 Ismail, M. B. & Darwich, K. Reconstruction of large mandibular bone defects extended to the condyle using patient-specific implants based on CAD-CAM technology and 3D printing. *Advances in Oral and Maxillofacial Surgery* **5**, 100229 (2022). <https://doi.org/10.1016/j.adoms.2021.100229>
- 179 Panicker, P. P., Mohan, S. P., Nallusamy, J., Lakshmi, S. J., Johny, J. & Bhaskaran, M. K. Reconstruction of Craniofacial Bone Defects with Autologous Human Bone Marrow Stem Cells and Autogenous Bone

## References

---

- Grafts: A Case Report with Review of Literature. *J. Pharm. Bioallied Sci.* **12**, S394-s398 (2020). [https://doi.org:10.4103/jpbs.JPBS\\_116\\_20](https://doi.org:10.4103/jpbs.JPBS_116_20)
- 180 Titsinides, S., Agrogiannis, G. & Karatzas, T. Bone grafting materials in dentoalveolar reconstruction: A comprehensive review. *Jpn. Dent. Sci. Rev.* **55**, 26-32 (2019). <https://doi.org:10.1016/j.jdsr.2018.09.003>
- 181 de Silva, L., Bernal, P. N., Rosenberg, A., Malda, J., Levato, R. & Gawlitta, D. Biofabricating the vascular tree in engineered bone tissue. *Acta Biomater* **156**, 250-268 (2023). <https://doi.org:10.1016/j.actbio.2022.08.051>
- 182 Rezania, N., Asadi-Eydivand, M., Abolfathi, N., Bonakdar, S., Mehrjoo, M. & Solati-Hashjin, M. Three-dimensional printing of polycaprolactone/hydroxyapatite bone tissue engineering scaffolds mechanical properties and biological behavior. *J. Mater. Sci. Mater. Med.* **33**, 31 (2022). <https://doi.org:10.1007/s10856-022-06653-8>
- 183 Zhao, S. *et al.* Fabrication and Biological Activity of 3D-Printed Polycaprolactone/Magnesium Porous Scaffolds for Critical Size Bone Defect Repair. *ACS Biomater Sci Eng* **6**, 5120-5131 (2020). <https://doi.org:10.1021/acsbiomaterials.9b01911>
- 184 Omar, O., Elgali, I., Dahlin, C. & Thomsen, P. Barrier membranes: More than the barrier effect? *J. Clin. Periodontol.* **46 Suppl 21**, 103-123 (2019). <https://doi.org:10.1111/jcpe.13068>
- 185 An, Y. Z., Strauss, F. J., Park, J. Y., Shen, Y. Q., Thoma, D. S. & Lee, J. S. Membrane fixation enhances guided bone regeneration in standardized calvarial defects: A pre-clinical study. *J. Clin. Periodontol.* **49**, 177-187 (2022). <https://doi.org:10.1111/jcpe.13583>
- 186 Blatt, S. *et al.* Biofunctionalization of porcine-derived collagen matrices with platelet rich fibrin: influence on angiogenesis in vitro and in vivo. *Clin. Oral Investig.* **24**, 3425-3436 (2020). <https://doi.org:10.1007/s00784-020-03213-8>
- 187 Kozlovsky, A. *et al.* Bio-degradation of a resorbable collagen membrane (Bio-Gide) applied in a double-layer technique in rats. *Clin. Oral Implants Res.* **20**, 1116-1123 (2009). <https://doi.org:10.1111/j.1600-0501.2009.01740.x>
- 188 Schlegel, A. K., Möhler, H., Busch, F. & Mehl, A. Preclinical and clinical studies of a collagen membrane (Bio-Gide). *Biomaterials* **18**, 535-538 (1997). [https://doi.org:10.1016/s0142-9612\(96\)00175-5](https://doi.org:10.1016/s0142-9612(96)00175-5)
- 189 Liu, Q., Li, M., Wang, S., Xiao, Z., Xiong, Y. & Wang, G. Recent Advances of Osterix Transcription Factor in Osteoblast Differentiation and Bone

## References

---

- Formation. *Front Cell Dev Biol* **8**, 601224 (2020). <https://doi.org/10.3389/fcell.2020.601224>
- 190 Rosen, E. D. *et al.* PPAR gamma is required for the differentiation of adipose tissue in vivo and in vitro. *Mol Cell* **4**, 611-617 (1999). [https://doi.org/10.1016/s1097-2765\(00\)80211-7](https://doi.org/10.1016/s1097-2765(00)80211-7)
- 191 Kannan, S., Ghosh, J. & Dhara, S. K. Osteogenic differentiation potential of porcine bone marrow mesenchymal stem cell subpopulations selected in different basal media. *Biol Open* **9** (2020). <https://doi.org/10.1242/bio.053280>
- 192 Ren, Z. *et al.* Repairing a bone defect with a three-dimensional cellular construct composed of a multi-layered cell sheet on electrospun mesh. *Biofabrication* **9**, 025036 (2017). <https://doi.org/10.1088/1758-5090/aa747f>
- 193 Subbiah, R. *et al.* 3D Printing of Microgel-Loaded Modular Microcages as Instructive Scaffolds for Tissue Engineering. *Adv Mater* **32**, e2001736 (2020). <https://doi.org/10.1002/adma.202001736>
- 194 Seunghun, S. L. *et al.* 3D-Printed LEGO<sup>®</sup>-inspired Titanium Scaffolds for Patient-Specific Regenerative Medicine. *bioRxiv*, 2023.2003.2030.534953 (2023). <https://doi.org/10.1101/2023.03.30.534953>
- 195 Marionneaux, A., Walters, J., Guo, H. & Mercuri, J. Tailoring the subchondral bone phase of a multi-layered osteochondral construct to support bone healing and a cartilage analog. *Acta Biomater* **78**, 351-364 (2018). <https://doi.org/10.1016/j.actbio.2018.08.009>
- 196 Li, Y. *et al.* Collagen-based biomaterials for bone tissue engineering. *Materials & Design* **210**, 110049 (2021). <https://doi.org/10.1016/j.matdes.2021.110049>
- 197 Geiger, M., Li, R. H. & Friess, W. Collagen sponges for bone regeneration with rhBMP-2. *Adv Drug Deliv Rev* **55**, 1613-1629 (2003). <https://doi.org/10.1016/j.addr.2003.08.010>
- 198 Sbricoli, L., Guazzo, R., Annunziata, M., Gobbato, L., Bressan, E. & Nastri, L. Selection of Collagen Membranes for Bone Regeneration: A Literature Review. *Materials (Basel)* **13** (2020). <https://doi.org/10.3390/ma13030786>
- 199 Armiento, A. R., Hatt, L. P., Sanchez Rosenberg, G., Thompson, K. & Stoddart, M. J. Functional Biomaterials for Bone Regeneration: A Lesson in Complex Biology. *Adv Funct Mater* **30**, 1909874 (2020). <https://doi.org/10.1002/adfm.201909874>

## References

---

- 200 Li, Y., Chen, S. K., Li, L., Qin, L., Wang, X. L. & Lai, Y. X. Bone defect animal models for testing efficacy of bone substitute biomaterials. *J Orthop Translat* **3**, 95-104 (2015). <https://doi.org:10.1016/j.jot.2015.05.002>
- 201 Singh, H., Greenfield, J. P. & Anand, V. K. *Pediatric Endoscopic Endonasal Skull Base Surgery*. (Thieme, 2020).
- 202 Cardaropoli, G., Araujo, M. & Lindhe, J. Dynamics of bone tissue formation in tooth extraction sites. An experimental study in dogs. *J Clin Periodontol* **30**, 809-818 (2003).
- 203 Quarto, N., Wan, D. C., Kwan, M. D., Panetta, N. J., Li, S. & Longaker, M. T. Origin matters: differences in embryonic tissue origin and Wnt signaling determine the osteogenic potential and healing capacity of frontal and parietal calvarial bones. *Journal of bone and mineral research : the official journal of the American Society for Bone and Mineral Research* **25**, 1680-1694 (2010). <https://doi.org:10.1359/jbmr.091116>
- 204 Anderson, B. W., Kortz, M. W. & Al Kharazi, K. A. in *StatPearls [Internet]* (StatPearls Publishing, 2020).
- 205 Senarath-Yapa, K., Li, S., Meyer, N. P., Longaker, M. T. & Quarto, N. Integration of multiple signaling pathways determines differences in the osteogenic potential and tissue regeneration of neural crest-derived and mesoderm-derived calvarial bones. *International journal of molecular sciences* **14**, 5978-5997 (2013). <https://doi.org:10.3390/ijms14035978>
- 206 Einhorn, T. A. The cell and molecular biology of fracture healing. *Clin Orthop Relat Res*, S7-21 (1998). <https://doi.org:10.1097/00003086-199810001-00003>
- 207 Bahney, C. S. *et al.* Cellular biology of fracture healing. *Journal of orthopaedic research : official publication of the Orthopaedic Research Society* **37**, 35-50 (2019). <https://doi.org:10.1002/jor.24170>
- 208 Bolander, M. E. Regulation of fracture repair by growth factors. *Proc Soc Exp Biol Med* **200**, 165-170 (1992). <https://doi.org:10.3181/00379727-200-43410a>
- 209 Barnes, G. L., Kostenuik, P. J., Gerstenfeld, L. C. & Einhorn, T. A. Growth factor regulation of fracture repair. *J Bone Miner Res* **14**, 1805-1815 (1999). <https://doi.org:10.1359/jbmr.1999.14.11.1805>
- 210 Knight, M. N. & Hankenson, K. D. Mesenchymal Stem Cells in Bone Regeneration. *Advances in wound care* **2**, 306-316 (2013). <https://doi.org:10.1089/wound.2012.0420>

## References

---

- 211 Glatt, V., Evans, C. H. & Tetsworth, K. Reverse dynamisation: a modern perspective on Stephan Perren's strain theory. *Eur Cell Mater* **41**, 668-679 (2021). <https://doi.org/10.22203/eCM.v041a43>
- 212 Perren, S. M. Evolution of the internal fixation of long bone fractures. The scientific basis of biological internal fixation: choosing a new balance between stability and biology. *J Bone Joint Surg Br* **84**, 1093-1110 (2002). <https://doi.org/10.1302/0301-620x.84b8.13752>
- 213 Yang, Y. Q., Tan, Y. Y., Wong, R., Wenden, A., Zhang, L. K. & Rabie, A. B. The role of vascular endothelial growth factor in ossification. *Int J Oral Sci* **4**, 64-68 (2012). <https://doi.org/10.1038/ijos.2012.33>
- 214 Doll, B. A., Sfeir, C., Azari, K., Holland, S. & Hollinger, J. O. in *Bone Regeneration and Repair* (eds Jay R. Lieberman & Gary E. Friedlaender) Ch. Chapter 17, 337-358 (Humana Press, 2005).
- 215 Craft, P. D., Mani, M. M., Pazel, J. & Masters, F. W. Experimental study of healing in fractures of membranous bone. *Plast Reconstr Surg* **53**, 321-325 (1974). <https://doi.org/10.1097/00006534-197403000-00013>
- 216 Paccione, M. F., Warren, S. M., Spector, J. A., Greenwald, J. A., Bouletreau, P. J. & Longaker, M. T. A mouse model of mandibular osteotomy healing. *J Craniofac Surg* **12**, 444-450 (2001). <https://doi.org/10.1097/00001665-200109000-00008>
- 217 Marsell, R. & Einhorn, T. A. The biology of fracture healing. *Injury* **42**, 551-555 (2011). <https://doi.org/10.1016/j.injury.2011.03.031>
- 218 Stegen, S., van Gastel, N. & Carmeliet, G. Bringing new life to damaged bone: the importance of angiogenesis in bone repair and regeneration. *Bone* **70**, 19-27 (2015). <https://doi.org/10.1016/j.bone.2014.09.017>
- 219 Giannoudis, P. V., Dinopoulos, H. & Tsiridis, E. Bone substitutes: an update. *Injury* **36** Suppl **3**, S20-27 (2005). <https://doi.org/10.1016/j.injury.2005.07.029>
- 220 An, H. S., Simpson, J. M., Glover, J. M. & Stephany, J. Comparison between allograft plus demineralized bone matrix versus autograft in anterior cervical fusion. A prospective multicenter study. *Spine (Phila Pa 1976)* **20**, 2211-2216 (1995).
- 221 Gazdag, A. R., Lane, J. M., Glaser, D. & Forster, R. A. Alternatives to Autogenous Bone Graft: Efficacy and Indications. *J Am Acad Orthop Surg* **3**, 1-8 (1995). <https://doi.org/10.5435/00124635-199501000-00001>



## References

---

- 222 Dimitriou, R., Jones, E., McGonagle, D. & Giannoudis, P. V. Bone regeneration: current concepts and future directions. *BMC Med* **9**, 66 (2011). <https://doi.org:10.1186/1741-7015-9-66>
- 223 Chen, C. H. *et al.* An osteopenic/osteoporotic phenotype delays alveolar bone repair. *Bone* **112**, 212-219 (2018). <https://doi.org:10.1016/j.bone.2018.04.019>
- 224 Kingsmill, V. J., Boyde, A. & Jones, S. J. The resorption of vital and devitalized bone in vitro: significance for bone grafts. *Calcif Tissue Int* **64**, 252-256 (1999). <https://doi.org:10.1007/s002239900612>
- 225 Zerbo, I. R., de Lange, G. L., Joldersma, M., Bronckers, A. L. & Burger, E. H. Fate of monocortical bone blocks grafted in the human maxilla: a histological and histomorphometric study. *Clin Oral Implants Res* **14**, 759-766 (2003). <https://doi.org:10.1046/j.0905-7161.2003.00967.x>
- 226 Solakoglu, O., Steinbach, B., Gotz, W., Heydecke, G., Pantel, K. & Schwarzenbach, H. Characterization of circulating DNA in plasma of patients after allogeneic bone grafting. *Clin Oral Investig* **23**, 4243-4253 (2019). <https://doi.org:10.1007/s00784-019-02867-3>
- 227 Rodella, L. F., Favero, G., Boninsegna, R., Borgonovo, A., Rezzani, R. & Santoro, F. TGF-beta1 and VEGF after fresh frozen bone allograft insertion in oral-maxillo-facial surgery. *Histol Histopathol* **25**, 463-471 (2010). <https://doi.org:10.14670/HH-25.463>
- 228 Shimoazono, Y., Hurley, E. T., Nguyen, J. T., Deyer, T. W. & Kennedy, J. G. Allograft Compared with Autograft in Osteochondral Transplantation for the Treatment of Osteochondral Lesions of the Talus. *J Bone Joint Surg Am* **100**, 1838-1844 (2018). <https://doi.org:10.2106/JBJS.17.01508>
- 229 Schmitt, C. M., Doering, H., Schmidt, T., Lutz, R., Neukam, F. W. & Schlegel, K. A. Histological results after maxillary sinus augmentation with Straumann(R) BoneCeramic, Bio-Oss(R), Puros(R), and autologous bone. A randomized controlled clinical trial. *Clin Oral Implants Res* **24**, 576-585 (2013). <https://doi.org:10.1111/j.1600-0501.2012.02431.x>
- 230 Aro, H. T. & Aho, A. J. Clinical use of bone allografts. *Ann Med* **25**, 403-412 (1993). <https://doi.org:10.3109/07853899309147303>
- 231 Tilkeridis, K., Touzopoulos, P., Ververidis, A., Christodoulou, S., Kazakos, K. & Drosos, G. I. Use of demineralized bone matrix in spinal fusion. *World J Orthop* **5**, 30-37 (2014). <https://doi.org:10.5312/wjo.v5.i1.30>
- 232 Ratko, T. A., Belinson, S. E., Samson, D. J., Bonnell, C., Ziegler, K. M. & Aronson, N. in *Bone Morphogenetic Protein: The State of the Evidence of*

## References

---

- On-Label and Off-Label Use AHRQ Technology Assessments* (Agency for Healthcare Research and Quality (US), 2010).
- 233 Kaigler, D. *et al.* Platelet-derived growth factor applications in periodontal and peri-implant bone regeneration. *Expert Opin Biol Ther* **11**, 375-385 (2011). <https://doi.org/10.1517/14712598.2011.554814>
- 234 Shah, P., Keppler, L. & Rutkowski, J. A review of platelet derived growth factor playing pivotal role in bone regeneration. *J Oral Implantol* **40**, 330-340 (2014). <https://doi.org/10.1563/AAID-JOI-D-11-00173>
- 235 Kuroda, Y., Kawai, T., Goto, K. & Matsuda, S. Clinical application of injectable growth factor for bone regeneration: a systematic review. *Inflamm Regen* **39**, 20 (2019). <https://doi.org/10.1186/s41232-019-0109-x>
- 236 Pearson, H. B. *et al.* Effects of Bone Morphogenetic Protein-2 on Neovascularization During Large Bone Defect Regeneration. *Tissue Eng Part A* **25**, 1623-1634 (2019). <https://doi.org/10.1089/ten.TEA.2018.0326>
- 237 Wong, D. A., Kumar, A., Jatana, S., Ghiselli, G. & Wong, K. Neurologic impairment from ectopic bone in the lumbar canal: a potential complication of off-label PLIF/TLIF use of bone morphogenetic protein-2 (BMP-2). *Spine J* **8**, 1011-1018 (2008). <https://doi.org/10.1016/j.spinee.2007.06.014>
- 238 Kaneko, H. *et al.* Direct stimulation of osteoclastic bone resorption by bone morphogenetic protein (BMP)-2 and expression of BMP receptors in mature osteoclasts. *Bone* **27**, 479-486 (2000). [https://doi.org/10.1016/s8756-3282\(00\)00358-6](https://doi.org/10.1016/s8756-3282(00)00358-6)
- 239 Zara, J. N. *et al.* High doses of bone morphogenetic protein 2 induce structurally abnormal bone and inflammation in vivo. *Tissue Eng Part A* **17**, 1389-1399 (2011). <https://doi.org/10.1089/ten.TEA.2010.0555>
- 240 Devine, J. G., Dettori, J. R., France, J. C., Brodt, E. & McGuire, R. A. The use of rhBMP in spine surgery: is there a cancer risk? *Evidence-based spine-care journal* **3**, 35-41 (2012). <https://doi.org/10.1055/s-0031-1298616>
- 241 Carragee, E. J. *et al.* Cancer risk after use of recombinant bone morphogenetic protein-2 for spinal arthrodesis. *J Bone Joint Surg Am* **95**, 1537-1545 (2013). <https://doi.org/10.2106/JBJS.L.01483>
- 242 Pountos, I., Panteli, M., Georgouli, T. & Giannoudis, P. V. Neoplasia following use of BMPs: is there an increased risk? *Expert Opin Drug Saf* **13**, 1525-1534 (2014). <https://doi.org/10.1517/14740338.2014.968124>
- 243 Maroulakos, M., Kamperos, G., Tayebi, L., Halazonetis, D. & Ren, Y. Applications of 3D printing on craniofacial bone repair: A systematic

## References

---

- review. *Journal of Dentistry* **80**, 1-14 (2019).  
[https://doi.org:https://doi.org/10.1016/j.jdent.2018.11.004](https://doi.org/https://doi.org/10.1016/j.jdent.2018.11.004)
- 244 Wan, Z., Zhang, P., Liu, Y., Lv, L. & Zhou, Y. Four-dimensional bioprinting: Current developments and applications in bone tissue engineering. *Acta Biomaterialia* **101**, 26-42 (2020).  
<https://doi.org:https://doi.org/10.1016/j.actbio.2019.10.038>
- 245 Samavedi, S., Whittington, A. R. & Goldstein, A. S. Calcium phosphate ceramics in bone tissue engineering: a review of properties and their influence on cell behavior. *Acta Biomater* **9**, 8037-8045 (2013).  
<https://doi.org:10.1016/j.actbio.2013.06.014>
- 246 Kroeze, R., Helder, M., Govaert, L. & Smit, T. Biodegradable Polymers in Bone Tissue Engineering. *Materials* **2**, 833-856 (2009).  
<https://doi.org:10.3390/ma2030833>
- 247 Yu, P. *et al.* Bone-Inspired Spatially Specific Piezoelectricity Induces Bone Regeneration. *Theranostics* **7**, 3387-3397 (2017).  
<https://doi.org:10.7150/thno.19748>
- 248 Zhao, Y. *et al.* Magnetic bioinspired micro/nanostructured composite scaffold for bone regeneration. *Colloids and Surfaces B: Biointerfaces* **174**, 70-79 (2019).  
<https://doi.org:https://doi.org/10.1016/j.colsurfb.2018.11.003>
- 249 Sydney Gladman, A., Matsumoto, E. A., Nuzzo, R. G., Mahadevan, L. & Lewis, J. A. Biomimetic 4D printing. *Nature Materials* **15**, 413-418 (2016).  
<https://doi.org:10.1038/nmat4544>
- 250 Baker, R. M., Tseng, L. F., Iannolo, M. T., Oest, M. E. & Henderson, J. H. Self-deploying shape memory polymer scaffolds for grafting and stabilizing complex bone defects: A mouse femoral segmental defect study. *Biomaterials* **76**, 388-398 (2016).  
<https://doi.org:10.1016/j.biomaterials.2015.10.064>
- 251 Montoya, C., Du, Y., Gianforcaro, A. L., Orrego, S., Yang, M. & Lelkes, P. I. On the road to smart biomaterials for bone research: definitions, concepts, advances, and outlook. *Bone Research* **9**, 12 (2021).  
<https://doi.org:10.1038/s41413-020-00131-z>
- 252 Jin, Y. Z. & Lee, J. H. Mesenchymal Stem Cell Therapy for Bone Regeneration. *Clin Orthop Surg* **10**, 271-278 (2018).  
<https://doi.org:10.4055/cios.2018.10.3.271>
- 253 Annamalai, R. T., Hong, X., Schott, N. G., Tiruchinapally, G., Levi, B. & Stegemann, J. P. Injectable osteogenic microtissues containing mesenchymal stromal cells conformally fill and repair critical-size defects.

## References

---

- Biomaterials* **208**, 32-44 (2019).  
[https://doi.org:https://doi.org/10.1016/j.biomaterials.2019.04.001](https://doi.org/10.1016/j.biomaterials.2019.04.001)
- 254 Chamieh, F. *et al.* Accelerated craniofacial bone regeneration through dense collagen gel scaffolds seeded with dental pulp stem cells. *Scientific Reports* **6**, 38814 (2016). [https://doi.org:10.1038/srep38814](https://doi.org/10.1038/srep38814)
- 255 Liu, J. *et al.* Pre-vascularization in fibrin Gel/PLGA microsphere scaffolds designed for bone regeneration. *NPG Asia Materials* **10**, 827-839 (2018). [https://doi.org:10.1038/s41427-018-0076-8](https://doi.org/10.1038/s41427-018-0076-8)
- 256 Miller, J. S. *et al.* Rapid casting of patterned vascular networks for perfusable engineered three-dimensional tissues. *Nature Materials* **11**, 768-774 (2012). [https://doi.org:10.1038/nmat3357](https://doi.org/10.1038/nmat3357)
- 257 Cui, H., Zhu, W., Nowicki, M., Zhou, X., Khademhosseini, A. & Zhang, L. G. Hierarchical Fabrication of Engineered Vascularized Bone Biphasic Constructs via Dual 3D Bioprinting: Integrating Regional Bioactive Factors into Architectural Design. *Adv Healthc Mater* **5**, 2174-2181 (2016). [https://doi.org:10.1002/adhm.201600505](https://doi.org/10.1002/adhm.201600505)
- 258 Li, J., Wei, J., Li, A., Liu, H., Sun, J. & Qiao, H. A Dual Peptide Sustained-Release System Based on Nanohydroxyapatite/Polyamide 66 Scaffold for Synergistic-Enhancing Diabetic Rats' Fracture Healing in Osteogenesis and Angiogenesis. *Frontiers in Bioengineering and Biotechnology* **9** (2021). [https://doi.org:10.3389/fbioe.2021.657699](https://doi.org/10.3389/fbioe.2021.657699)
- 259 Lin, H., Tang, Y., Lozito, T. P., Oyster, N., Wang, B. & Tuan, R. S. Efficient in vivo bone formation by BMP-2 engineered human mesenchymal stem cells encapsulated in a projection stereolithographically fabricated hydrogel scaffold. *Stem Cell Research & Therapy* **10**, 254 (2019). [https://doi.org:10.1186/s13287-019-1350-6](https://doi.org/10.1186/s13287-019-1350-6)
- 260 Khorsand, B. *et al.* Regeneration of bone using nanoplex delivery of FGF-2 and BMP-2 genes in diaphyseal long bone radial defects in a diabetic rabbit model. *J Control Release* **248**, 53-59 (2017). [https://doi.org:10.1016/j.jconrel.2017.01.008](https://doi.org/10.1016/j.jconrel.2017.01.008)
- 261 Schlundt, C. *et al.* Macrophages in bone fracture healing: Their essential role in endochondral ossification. *Bone* **106**, 78-89 (2018). [https://doi.org:10.1016/j.bone.2015.10.019](https://doi.org/10.1016/j.bone.2015.10.019)
- 262 Batoon, L., Millard, S. M., Raggatt, L. J. & Pettit, A. R. Osteomacs and Bone Regeneration. *Curr Osteoporos Rep* **15**, 385-395 (2017). [https://doi.org:10.1007/s11914-017-0384-x](https://doi.org/10.1007/s11914-017-0384-x)
- 263 Li, L., Crosby, K. & Sawicki, M. Effects of Surface Roughness of Hydroxyapatite on Cell Attachment and Proliferation. *Journal of*

## References

---

- Biotechnology & Biomaterials* **02** (2012). <https://doi.org/10.4172/2155-952x.1000150>
- 264 Silva, T. S., Machado, D. C., Viezzer, C., Silva Junior, A. N. & Oliveira, M. G. Effect of titanium surface roughness on human bone marrow cell proliferation and differentiation: an experimental study. *Acta Cir Bras* **24**, 200-205 (2009). <https://doi.org/10.1590/s0102-86502009000300007>
- 265 Yeung, T. *et al.* Effects of substrate stiffness on cell morphology, cytoskeletal structure, and adhesion. *Cell Motil Cytoskeleton* **60**, 24-34 (2005). <https://doi.org/10.1002/cm.20041>
- 266 Park, J. S. *et al.* The effect of matrix stiffness on the differentiation of mesenchymal stem cells in response to TGF-beta. *Biomaterials* **32**, 3921-3930 (2011). <https://doi.org/10.1016/j.biomaterials.2011.02.019>
- 267 Engler, A. J., Sen, S., Sweeney, H. L. & Discher, D. E. Matrix elasticity directs stem cell lineage specification. *Cell* **126**, 677-689 (2006). <https://doi.org/10.1016/j.cell.2006.06.044>
- 268 Dewey, M. J. & Harley, B. A. C. Biomaterial design strategies to address obstacles in craniomaxillofacial bone repair. *RSC Advances* **11**, 17809-17827 (2021). <https://doi.org/10.1039/D1RA02557K>
- 269 Crist, T. E., Mathew, P. J., Plotsker, E. L., Sevilla, A. C. & Thaller, S. R. Biomaterials in Craniomaxillofacial Reconstruction: Past, Present, and Future. *Journal of Craniofacial Surgery* **32**, 535-540 (2021). <https://doi.org/10.1097/scs.00000000000007079>
- 270 Tomar, G. B. *et al.* in *Tissue Engineering and the 5 R's-Reconstruction, Restoration, Replacement, Repair and Regeneration* (IntechOpen, 2020).
- 271 McGovern, J. A., Griffin, M. & Hutmacher, D. W. Animal models for bone tissue engineering and modelling disease. *Dis Model Mech* **11**, dmm033084 (2018). <https://doi.org/10.1242/dmm.033084>
- 272 Samsonraj, R. M., Dudakovic, A., Zan, P., Pichurin, O., Cool, S. M. & van Wijnen, A. J. A Versatile Protocol for Studying Calvarial Bone Defect Healing in a Mouse Model. *Tissue Eng Part C Methods* **23**, 686-693 (2017). <https://doi.org/10.1089/ten.TEC.2017.0205>
- 273 Cooper, G. M., Mooney, M. P., Gosain, A. K., Campbell, P. G., Losee, J. E. & Huard, J. Testing the critical size in calvarial bone defects: revisiting the concept of a critical-size defect. *Plast Reconstr Surg* **125**, 1685-1692 (2010). <https://doi.org/10.1097/PRS.0b013e3181cb63a3>

## References

---

- 274 Neagu, T. P., Țigliș, M., Cocoloș, I. & Jecan, C. R. The relationship between periosteum and fracture healing. *Rom J Morphol Embryol* **57**, 1215-1220 (2016).
- 275 Niedermair, T., Straub, R. H., Brochhausen, C. & Grässel, S. Impact of the Sensory and Sympathetic Nervous System on Fracture Healing in Ovariectomized Mice. *International journal of molecular sciences* **21**, 405 (2020). <https://doi.org:10.3390/ijms21020405>
- 276 Li, Z. *et al.* Fracture repair requires TrkA signaling by skeletal sensory nerves. *The Journal of Clinical Investigation* **129**, 5137-5150 (2019). <https://doi.org:10.1172/JCI128428>
- 277 Brierly, G. I., Tredinnick, S., Lynham, A. & Woodruff, M. A. Critical Sized Mandibular Defect Regeneration in Preclinical In Vivo Models. *Curr Mol Biol Rep* **2**, 83-89 (2016). <https://doi.org:10.1007/s40610-016-0036-4>
- 278 Sidell, D. R. *et al.* Composite mandibulectomy: a novel animal model. *Otolaryngol Head Neck Surg* **146**, 932-937 (2012). <https://doi.org:10.1177/0194599811435633>
- 279 Chaudhary, N., Lovald, S. T., Wagner, J., Khraishi, T. & Baack, B. Experimental and Numerical Modeling of Screws Used for Rigid Internal Fixation of Mandibular Fractures. *Modelling and Simulation in Engineering* **2008**, 1-11 (2008). <https://doi.org:10.1155/2008/628120>
- 280 Guillaume, O. *et al.* Orbital floor repair using patient specific osteoinductive implant made by stereolithography. *Biomaterials* **233**, 119721 (2020). <https://doi.org:10.1016/j.biomaterials.2019.119721>
- 281 Starch-Jensen, T. & Jensen, J. D. Maxillary Sinus Floor Augmentation: a Review of Selected Treatment Modalities. *Journal of oral & maxillofacial research* **8**, e3-e3 (2017). <https://doi.org:10.5037/jomr.2017.8303>
- 282 Esposito, M., Grusovin, M. G., Felice, P., Karatzopoulos, G., Worthington, H. V. & Coulthard, P. The efficacy of horizontal and vertical bone augmentation procedures for dental implants - a Cochrane systematic review. *Eur J Oral Implantol* **2**, 167-184 (2009).
- 283 Bathla, S. C., Fry, R. R. & Majumdar, K. Maxillary sinus augmentation. *Journal of Indian Society of Periodontology* **22**, 468-473 (2018). [https://doi.org:10.4103/jisp.jisp\\_236\\_18](https://doi.org:10.4103/jisp.jisp_236_18)
- 284 Santagata, M. *et al.* Maxillary Sinus Augmentation with Autologous and Heterologous Bone Graft: A Clinical and Radiographic Report of Immediate and Delayed Implant Placement. *Journal of maxillofacial and oral surgery* **13**, 401-408 (2014). <https://doi.org:10.1007/s12663-013-0569-5>

## References

---

- 285 Konopnicki, S. *et al.* Tissue-engineered bone with 3-dimensionally printed beta-tricalcium phosphate and polycaprolactone scaffolds and early implantation: an in vivo pilot study in a porcine mandible model. *J Oral Maxillofac Surg* **73**, 1016 e1011-1016 e1011 (2015). <https://doi.org/10.1016/j.joms.2015.01.021>
- 286 Imola, M. J. & Liddell, A. Temporomandibular joint reconstruction. *Curr Opin Otolaryngol Head Neck Surg* **24**, 336-342 (2016). <https://doi.org/10.1097/MOO.0000000000000282>
- 287 Almarza, A. J. *et al.* Preclinical Animal Models for Temporomandibular Joint Tissue Engineering. *Tissue engineering. Part B, Reviews* **24**, 171-178 (2018). <https://doi.org/10.1089/ten.TEB.2017.0341>
- 288 Pilawski, I. *et al.* Interspecies Comparison of Alveolar Bone Biology, Part I: Morphology and Physiology of Pristine Bone. *JDR Clin Trans Res*, 2380084420936979 (2020). <https://doi.org/10.1177/2380084420936979>
- 289 Bilezikian, J. P., Raisz, L. G. & Rodan, G. A. *Principles of bone biology*. 2nd edn, (Academic Press, 2002).
- 290 Stadlinger, B., Pourmand, P., Locher, M. C. & Schulz, M. C. Systematic review of animal models for the study of implant integration, assessing the influence of material, surface and design. *J Clin Periodontol* **39 Suppl 12**, 28-36 (2012). <https://doi.org/10.1111/j.1600-051X.2011.01835.x>
- 291 Spicer, P. P., Kretlow, J. D., Young, S., Jansen, J. A., Kasper, F. K. & Mikos, A. G. Evaluation of bone regeneration using the rat critical size calvarial defect. *Nat Protoc* **7**, 1918-1929 (2012). <https://doi.org/10.1038/nprot.2012.113>
- 292 Lemperle, S. M., Calhoun, C. J., Curran, R. W. & Holmes, R. E. Bony healing of large cranial and mandibular defects protected from soft-tissue interposition: A comparative study of spontaneous bone regeneration, osteoconduction, and cancellous autografting in dogs. *Plast Reconstr Surg* **101**, 660-672 (1998). <https://doi.org/10.1097/00006534-199803000-00013>
- 293 Schmitz, J. P. & Hollinger, J. O. The critical size defect as an experimental model for craniomandibulofacial nonunions. *Clin Orthop Relat Res*, 299-308 (1986).
- 294 da Silva Morais, A., Oliveira, J. M. & Reis, R. L. Small Animal Models. *Adv Exp Med Biol* **1059**, 423-439 (2018). [https://doi.org/10.1007/978-3-319-76735-2\\_19](https://doi.org/10.1007/978-3-319-76735-2_19)

## References

---

- 295 Pearce, A. I., Richards, R. G., Milz, S., Schneider, E. & Pearce, S. G. Animal models for implant biomaterial research in bone: a review. *Eur Cell Mater* **13**, 1-10 (2007). <https://doi.org/10.22203/ecm.v013a01>
- 296 Aerssens, J., Boonen, S., Lowet, G. & Dequeker, J. Interspecies differences in bone composition, density, and quality: potential implications for in vivo bone research. *Endocrinology* **139**, 663-670 (1998). <https://doi.org/10.1210/endo.139.2.5751>
- 297 Bagi, C. M., Berryman, E. & Moalli, M. R. Comparative bone anatomy of commonly used laboratory animals: implications for drug discovery. *Comp Med* **61**, 76-85 (2011).
- 298 Baron, R., Tross, R. & Vignery, A. Evidence of sequential remodeling in rat trabecular bone: morphology, dynamic histomorphometry, and changes during skeletal maturation. *Anat Rec* **208**, 137-145 (1984). <https://doi.org/10.1002/ar.1092080114>
- 299 Vieira, A. E. *et al.* Intramembranous bone healing process subsequent to tooth extraction in mice: micro-computed tomography, histomorphometric and molecular characterization. *PLoS One* **10**, e0128021 (2015). <https://doi.org/10.1371/journal.pone.0128021>
- 300 Li, F. *et al.* Efficacy of Recombinant Human BMP2 and PDGF-BB in Orofacial Bone Regeneration: A Systematic Review and Meta-analysis. *Sci Rep* **9**, 8073 (2019). <https://doi.org/10.1038/s41598-019-44368-z>
- 301 Wancket, L. M. Animal Models for Evaluation of Bone Implants and Devices: Comparative Bone Structure and Common Model Uses. *Vet Pathol* **52**, 842-850 (2015). <https://doi.org/10.1177/0300985815593124>
- 302 Clark, D., Nakamura, M., Miclau, T. & Marcucio, R. Effects of Aging on Fracture Healing. *Curr Osteoporos Rep* **15**, 601-608 (2017). <https://doi.org/10.1007/s11914-017-0413-9>
- 303 Zhang, Y. *et al.* Comparing immunocompetent and immunodeficient mice as animal models for bone tissue engineering. *Oral Dis* **21**, 583-592 (2015). <https://doi.org/10.1111/odi.12319>
- 304 Akhter, M. P., Fan, Z. & Rho, J. Y. Bone intrinsic material properties in three inbred mouse strains. *Calcif Tissue Int* **75**, 416-420 (2004). <https://doi.org/10.1007/s00223-004-0241-7>
- 305 Sellers, R. S., Clifford, C. B., Treuting, P. M. & Brayton, C. Immunological variation between inbred laboratory mouse strains: points to consider in phenotyping genetically immunomodified mice. *Vet Pathol* **49**, 32-43 (2012). <https://doi.org/10.1177/0300985811429314>



## References

---

- 306 Manigrasso, M. B. & O'Connor, J. P. Comparison of fracture healing among different inbred mouse strains. *Calcif Tissue Int* **82**, 465-474 (2008). <https://doi.org/10.1007/s00223-008-9144-3>
- 307 Haffner-Luntzer, M., Kovtun, A., Rapp, A. E. & Ignatius, A. Mouse Models in Bone Fracture Healing Research. *Current Molecular Biology Reports* **2**, 101-111 (2016). <https://doi.org/10.1007/s40610-016-0037-3>
- 308 Begg, D. J., Purdie, A. C., de Silva, K., Dhand, N. K., Plain, K. M. & Whittington, R. J. Variation in susceptibility of different breeds of sheep to *Mycobacterium avium* subspecies *paratuberculosis* following experimental inoculation. *Vet Res* **48**, 36 (2017). <https://doi.org/10.1186/s13567-017-0440-7>
- 309 Skogh, A. C., Kihlstrom, L., Neovius, E., Persson, C., Beckman, M. O. & Engstrand, T. Variation in calvarial bone healing capacity: a clinical study on the effects of BMP-2-hydrogel or bone autograft treatments at different cranial locations. *J Craniofac Surg* **24**, 339-343 (2013). <https://doi.org/10.1097/SCS.0b013e31827ff2b6>
- 310 Ghiasi, M. S., Chen, J., Vaziri, A., Rodriguez, E. K. & Nazarian, A. Bone fracture healing in mechanobiological modeling: A review of principles and methods. *Bone Rep* **6**, 87-100 (2017). <https://doi.org/10.1016/j.bonr.2017.03.002>
- 311 Pei, P., Qi, X., Du, X., Zhu, M., Zhao, S. & Zhu, Y. Three-dimensional printing of tricalcium silicate/mesoporous bioactive glass cement scaffolds for bone regeneration. *J Mater Chem B* **4**, 7452-7463 (2016). <https://doi.org/10.1039/c6tb02055k>
- 312 Li, J., Chen, M., Wei, X., Hao, Y. & Wang, J. Evaluation of 3D-Printed Polycaprolactone Scaffolds Coated with Freeze-Dried Platelet-Rich Plasma for Bone Regeneration. *Materials (Basel)* **10** (2017). <https://doi.org/10.3390/ma10070831>
- 313 Qi, X. *et al.* Three dimensional printing of calcium sulfate and mesoporous bioactive glass scaffolds for improving bone regeneration in vitro and in vivo. *Sci Rep* **7**, 42556 (2017). <https://doi.org/10.1038/srep42556>
- 314 Bae, E. B. *et al.* Efficacy of rhBMP-2 Loaded PCL/beta-TCP/bdECM Scaffold Fabricated by 3D Printing Technology on Bone Regeneration. *Biomed Res Int* **2018**, 2876135 (2018). <https://doi.org/10.1155/2018/2876135>
- 315 Li, X. *et al.* Composite PLA/PEG/nHA/Dexamethasone Scaffold Prepared by 3D Printing for Bone Regeneration. *Macromol Biosci* **18**, e1800068 (2018). <https://doi.org/10.1002/mabi.201800068>

## References

---

- 316 Cui, H. *et al.* Direct 3D printing of a tough hydrogel incorporated with carbon nanotubes for bone regeneration. *J Mater Chem B* **7**, 7207-7217 (2019). <https://doi.org:10.1039/c9tb01494b>
- 317 Tcacencu, I. *et al.* Osseointegration of porous apatite-wollastonite and poly(lactic acid) composite structures created using 3D printing techniques. *Mater Sci Eng C Mater Biol Appl* **90**, 1-7 (2018). <https://doi.org:10.1016/j.msec.2018.04.022>
- 318 Chen, G. *et al.* A three-dimensional (3D) printed biomimetic hierarchical scaffold with a covalent modular release system for osteogenesis. *Mater Sci Eng C Mater Biol Appl* **104**, 109842 (2019). <https://doi.org:10.1016/j.msec.2019.109842>
- 319 Moncal, K. K. *et al.* Collagen-infilled 3D printed scaffolds loaded with miR-148b-transfected bone marrow stem cells improve calvarial bone regeneration in rats. *Mater Sci Eng C Mater Biol Appl* **105**, 110128 (2019). <https://doi.org:10.1016/j.msec.2019.110128>
- 320 Paré, A. *et al.* Tailored Three-Dimensionally Printed Triply Periodic Calcium Phosphate Implants: A Preclinical Study for Craniofacial Bone Repair. *ACS Biomater Sci Eng* **6**, 553-563 (2020). <https://doi.org:10.1021/acsbiomaterials.9b01241>
- 321 Kim, J. A., Lim, J., Naren, R., Yun, H. S. & Park, E. K. Effect of the biodegradation rate controlled by pore structures in magnesium phosphate ceramic scaffolds on bone tissue regeneration in vivo. *Acta Biomater* **44**, 155-167 (2016). <https://doi.org:10.1016/j.actbio.2016.08.039>
- 322 Sun, M. *et al.* Systematical Evaluation of Mechanically Strong 3D Printed Diluted magnesium Doping Wollastonite Scaffolds on Osteogenic Capacity in Rabbit Calvarial Defects. *Sci Rep* **6**, 34029 (2016). <https://doi.org:10.1038/srep34029>
- 323 Shao, H. *et al.* Bone regeneration in 3D printing bioactive ceramic scaffolds with improved tissue/material interface pore architecture in thin-wall bone defect. *Biofabrication* **9**, 025003 (2017). <https://doi.org:10.1088/1758-5090/aa663c>
- 324 Shim, J. H. *et al.* Porosity effect of 3D-printed polycaprolactone membranes on calvarial defect model for guided bone regeneration. *Biomed Mater* **13**, 015014 (2017). <https://doi.org:10.1088/1748-605X/aa9bbc>
- 325 Kim, B. S., Yang, S. S. & Kim, C. S. Incorporation of BMP-2 nanoparticles on the surface of a 3D-printed hydroxyapatite scaffold using an  $\epsilon$ -polycaprolactone polymer emulsion coating method for bone tissue

## References

---

- engineering. *Colloids Surf B Biointerfaces* **170**, 421-429 (2018).  
<https://doi.org/10.1016/j.colsurfb.2018.06.043>
- 326 Lee, K. G. *et al.* Rabbit Calvarial Defect Model for Customized 3D-Printed Bone Grafts. *Tissue Eng Part C Methods* **24**, 255-262 (2018).  
<https://doi.org/10.1089/ten.TEC.2017.0474>
- 327 Pae, H. C. *et al.* 3D-printed polycaprolactone scaffold mixed with  $\beta$ -tricalcium phosphate as a bone regenerative material in rabbit calvarial defects. *J Biomed Mater Res B Appl Biomater* **107**, 1254-1263 (2019).  
<https://doi.org/10.1002/jbm.b.34218>
- 328 Lee, S. J. *et al.* Development of a three-dimensionally printed scaffold grafted with bone forming peptide-1 for enhanced bone regeneration with in vitro and in vivo evaluations. *J Colloid Interface Sci* **539**, 468-480 (2019).  
<https://doi.org/10.1016/j.jcis.2018.12.097>
- 329 Lee, S. H. *et al.* Evaluation of mechanical strength and bone regeneration ability of 3D printed kagome-structure scaffold using rabbit calvarial defect model. *Mater Sci Eng C Mater Biol Appl* **98**, 949-959 (2019).  
<https://doi.org/10.1016/j.msec.2019.01.050>
- 330 Wang, M. M. *et al.* Dipyridamole-loaded 3D-printed bioceramic scaffolds stimulate pediatric bone regeneration in vivo without disruption of craniofacial growth through facial maturity. *Sci Rep* **9**, 18439 (2019).  
<https://doi.org/10.1038/s41598-019-54726-6>
- 331 Zhong, L. *et al.* 3D printing of metal-organic framework incorporated porous scaffolds to promote osteogenic differentiation and bone regeneration. *Nanoscale* **12**, 24437-24449 (2020).  
<https://doi.org/10.1039/d0nr06297a>
- 332 Chang, P. C. *et al.* Regeneration of critical-sized mandibular defect using a 3D-printed hydroxyapatite-based scaffold: An exploratory study. *J Periodontol* (2020). <https://doi.org/10.1002/jper.20-0110>
- 333 Zhang, W. *et al.* 3D printed composite scaffolds with dual small molecule delivery for mandibular bone regeneration. *Biofabrication* **12**, 035020 (2020). <https://doi.org/10.1088/1758-5090/ab906e>
- 334 Zhang, P. *et al.* Customized Borosilicate Bioglass Scaffolds With Excellent Biodegradation and Osteogenesis for Mandible Reconstruction. *Front Bioeng Biotechnol* **8**, 610284 (2020).  
<https://doi.org/10.3389/fbioe.2020.610284>
- 335 Zhao, S. *et al.* Three-dimensional printed strontium-containing mesoporous bioactive glass scaffolds for repairing rat critical-sized

## References

---

- calvarial defects. *Acta Biomaterialia* **12**, 270-280 (2015).  
<https://doi.org/10.1016/j.actbio.2014.10.015>
- 336 Han, S. H. *et al.* Enhanced healing of rat calvarial defects with 3D printed calcium-deficient hydroxyapatite/collagen/bone morphogenetic protein 2 scaffolds. *Journal of the Mechanical Behavior of Biomedical Materials* **108**, 103782 (2020).  
<https://doi.org/10.1016/j.jmbbm.2020.103782>
- 337 Chen, M.-C., Chiu, H.-C., Kuo, P.-J., Chiang, C.-Y., Fu, M. M. & Fu, E. Bone formation with functionalized 3D printed poly- $\epsilon$ -caprolactone scaffold with plasma-rich-fibrin implanted in critical-sized calvaria defect of rat. *Journal of Dental Sciences* **16**, 1214-1221 (2021).  
<https://doi.org/10.1016/j.jds.2021.01.015>
- 338 Chung, J. J. *et al.* 3D Printed Porous Methacrylate/Silica Hybrid Scaffold for Bone Substitution. *Advanced Healthcare Materials* **10**, 2100117 (2021). <https://doi.org/10.1002/adhm.202100117>
- 339 Lee, J. Y. *et al.* 3D-Printed Barrier Membrane Using Mixture of Polycaprolactone and Beta-Tricalcium Phosphate for Regeneration of Rabbit Calvarial Defects. *Materials (Basel)* **14** (2021).  
<https://doi.org/10.3390/ma14123280>
- 340 Shen, C. *et al.* Transforming the Degradation Rate of  $\beta$ -tricalcium Phosphate Bone Replacement Using 3-Dimensional Printing. *Ann Plast Surg* (2021). <https://doi.org/10.1097/sap.0000000000002965>
- 341 Hung, B. P. *et al.* Three-Dimensional Printing of Bone Extracellular Matrix for Craniofacial Regeneration. *ACS Biomater Sci Eng* **2**, 1806-1816 (2016). <https://doi.org/10.1021/acsbiomaterials.6b00101>
- 342 Jensen, M. B. *et al.* Treating mouse skull defects with 3D-printed fatty acid and tricalcium phosphate implants. *J Tissue Eng Regen Med* **14**, 1858-1868 (2020). <https://doi.org/10.1002/term.3146>
- 343 Baranowski, A. *et al.* Evaluation of Bone Sialoprotein Coating of Three-Dimensional Printed Calcium Phosphate Scaffolds in a Calvarial Defect Model in Mice. *Materials (Basel)* **11** (2018).  
<https://doi.org/10.3390/ma11112336>
- 344 Zhang, H. *et al.* Three dimensional printed polylactic acid-hydroxyapatite composite scaffolds for prefabricating vascularized tissue engineered bone: An in vivo bioreactor model. *Sci Rep* **7**, 15255 (2017).  
<https://doi.org/10.1038/s41598-017-14923-7>
- 345 Diao, J. *et al.* 3D-Plotted Beta-Tricalcium Phosphate Scaffolds with Smaller Pore Sizes Improve In Vivo Bone Regeneration and

## References

---

- Biomechanical Properties in a Critical-Sized Calvarial Defect Rat Model. *Adv Healthc Mater* **7**, e1800441 (2018). <https://doi.org/10.1002/adhm.201800441>
- 346 Luo, Y., Chen, S., Shi, Y. & Ma, J. 3D printing of strontium-doped hydroxyapatite based composite scaffolds for repairing critical-sized rabbit calvarial defects. *Biomed Mater* **13**, 065004 (2018). <https://doi.org/10.1088/1748-605X/aad923>
- 347 Liu, F. *et al.* Osteogenesis of 3D printed macro-pore size biphasic calcium phosphate scaffold in rabbit calvaria. *J Biomater Appl* **33**, 1168-1177 (2019). <https://doi.org/10.1177/0885328218825177>
- 348 Lee, S., Choi, D., Shim, J. H. & Nam, W. Efficacy of three-dimensionally printed polycaprolactone/beta tricalcium phosphate scaffold on mandibular reconstruction. *Sci Rep* **10**, 4979 (2020). <https://doi.org/10.1038/s41598-020-61944-w>
- 349 Cooke, M. E. *et al.* 3D Printed Polyurethane Scaffolds for the Repair of Bone Defects. *Front Bioeng Biotechnol* **8**, 557215 (2020). <https://doi.org/10.3389/fbioe.2020.557215>
- 350 Roskies, M. G. *et al.* Three-dimensionally printed polyetherketoneketone scaffolds with mesenchymal stem cells for the reconstruction of critical-sized mandibular defects. *Laryngoscope* **127**, E392-e398 (2017). <https://doi.org/10.1002/lary.26781>
- 351 Park, S. A., Lee, H. J., Kim, S. Y., Kim, K. S., Jo, D. W. & Park, S. Y. Three-dimensionally printed polycaprolactone/beta-tricalcium phosphate scaffold was more effective as an rhBMP-2 carrier for new bone formation than polycaprolactone alone. *J Biomed Mater Res A* (2020). <https://doi.org/10.1002/jbm.a.37075>
- 352 Percie du Sert, N. *et al.* The ARRIVE guidelines 2.0: Updated guidelines for reporting animal research. *Journal of Cerebral Blood Flow & Metabolism* **40**, 1769-1777 (2020).
- 353 Bouyer, M. *et al.* 3D-printed scaffold combined to 2D osteoinductive coatings to repair a critical-size mandibular bone defect. *Materials Today Bio* **11**, 100113 (2021). [https://doi.org:https://doi.org/10.1016/j.mtbio.2021.100113](https://doi.org/https://doi.org/10.1016/j.mtbio.2021.100113)
- 354 Zhou, X., Zhang, D., Wang, M., Zhang, D. & Xu, Y. Three-Dimensional Printed Titanium Scaffolds Enhance Osteogenic Differentiation and New Bone Formation by Cultured Adipose Tissue-Derived Stem Cells Through the IGF-1R/AKT/Mammalian Target of Rapamycin Complex 1 (mTORC1) Pathway. *Med Sci Monit* **25**, 8043-8054 (2019). <https://doi.org/10.12659/msm.918517>

## References

---

- 355 Remy, M. T. *et al.* Rat Calvarial Bone Regeneration by 3D-Printed  $\beta$ -Tricalcium Phosphate Incorporating MicroRNA-200c. *ACS Biomaterials Science & Engineering* **7**, 4521-4534 (2021). <https://doi.org/10.1021/acsbiomaterials.0c01756>
- 356 Zhang, H. *et al.* Three dimensional printed macroporous polylactic acid/hydroxyapatite composite scaffolds for promoting bone formation in a critical-size rat calvarial defect model. *Sci Technol Adv Mater* **17**, 136-148 (2016). <https://doi.org/10.1080/14686996.2016.1145532>
- 357 Sun, W. *et al.* The mechanosensitive Piezo1 channel is required for bone formation. *Elife* **8** (2019). <https://doi.org/10.7554/eLife.47454>
- 358 Kim, J. W. *et al.* Bone Regeneration Capability of 3D Printed Ceramic Scaffolds. *Int J Mol Sci* **21** (2020). <https://doi.org/10.3390/ijms21144837>
- 359 Megías Barrera, J., García-Consuegra, L., Novoa, A., Costilla, S., Junquera, S. & Ascani, G. Histological and radiological evaluation of subcutaneous implants in mouse of a 3D-printable material (Fulcure 720) and experimental application in mandibular reconstruction. *J Stomatol Oral Maxillofac Surg* **119**, 88-92 (2018). <https://doi.org/10.1016/j.jormas.2017.11.004>
- 360 Yun, S. *et al.* Bone Fracture-Treatment Method: Fixing 3D-Printed Polycaprolactone Scaffolds with Hydrogel Type Bone-Derived Extracellular Matrix and  $\beta$ -Tricalcium Phosphate as an Osteogenic Promoter. *International Journal of Molecular Sciences* **22**, 9084 (2021).
- 361 Koons, G. L., Diba, M. & Mikos, A. G. Materials design for bone-tissue engineering. *Nature Reviews Materials* **5**, 584-603 (2020). <https://doi.org/10.1038/s41578-020-0204-2>
- 362 Yan, Y. *et al.* Vascularized 3D printed scaffolds for promoting bone regeneration. *Biomaterials* **190-191**, 97-110 (2019). <https://doi.org/10.1016/j.biomaterials.2018.10.033>
- 363 Lin, D., Chai, Y., Ma, Y., Duan, B., Yuan, Y. & Liu, C. Rapid initiation of guided bone regeneration driven by spatiotemporal delivery of IL-8 and BMP-2 from hierarchical MBG-based scaffold. *Biomaterials* **196**, 122-137 (2019). <https://doi.org/10.1016/j.biomaterials.2017.11.011>
- 364 Arnold, A. M., Holt, B. D., Daneshmandi, L., Laurencin, C. T. & Sydlik, S. A. Phosphate graphene as an intrinsically osteoinductive scaffold for stem cell-driven bone regeneration. *Proceedings of the National Academy of Sciences* **116**, 4855 (2019). <https://doi.org/10.1073/pnas.1815434116>

## References

---

- 365 Tang, G. *et al.* Recent Trends in the Development of Bone Regenerative Biomaterials. *Frontiers in Cell and Developmental Biology* **9** (2021). <https://doi.org/10.3389/fcell.2021.665813>
- 366 Luo, Y. *et al.* Desktop-Stereolithography 3D Printing of a Polyporous Extracellular Matrix Bioink for Bone Defect Regeneration. *Front Bioeng Biotechnol* **8**, 589094 (2020). <https://doi.org/10.3389/fbioe.2020.589094>
- 367 Vaquette, C., Bock, N. & Tran, P. A. Layered Antimicrobial Selenium Nanoparticle–Calcium Phosphate Coating on 3D Printed Scaffolds Enhanced Bone Formation in Critical Size Defects. *ACS Applied Materials & Interfaces* **12**, 55638-55648 (2020). <https://doi.org/10.1021/acsami.0c17017>
- 368 Geng, M. *et al.* Construction of a nanofiber network within 3D printed scaffolds for vascularized bone regeneration. *Biomaterials Science* **9**, 2631-2646 (2021). <https://doi.org/10.1039/D0BM02058C>
- 369 Kim, J. Y. *et al.* Synergistic Effects of Beta Tri-Calcium Phosphate and Porcine-Derived Decellularized Bone Extracellular Matrix in 3D-Printed Polycaprolactone Scaffold on Bone Regeneration. *Macromol Biosci* **18**, e1800025 (2018). <https://doi.org/10.1002/mabi.201800025>
- 370 Kim, B. N., Ko, Y. G., Yeo, T., Kim, E. J., Kwon, O. K. & Kwon, O. H. Guided Regeneration of Rabbit Calvarial Defects Using Silk Fibroin Nanofiber-Poly(glycolic acid) Hybrid Scaffolds. *ACS Biomater Sci Eng* **5**, 5266-5272 (2019). <https://doi.org/10.1021/acsbiomaterials.9b00678>
- 371 Shao, H. *et al.* Custom Repair of Mandibular Bone Defects with 3D Printed Bioceramic Scaffolds. *J Dent Res* **97**, 68-76 (2018). <https://doi.org/10.1177/0022034517734846>
- 372 Lopez, C. D. *et al.* Three dimensionally printed bioactive ceramic scaffold osseointegration across critical-sized mandibular defects. *J Surg Res* **223**, 115-122 (2018). <https://doi.org/10.1016/j.jss.2017.10.027>
- 373 Bozo, I. Y. *et al.* 3D Printed Gene-activated Octacalcium Phosphate Implants for Large Bone Defects Engineering. *Int J Bioprint* **6**, 275 (2020). <https://doi.org/10.18063/ijb.v6i3.275>
- 374 Jaiswal, N., Haynesworth, S. E., Caplan, A. I. & Bruder, S. P. Osteogenic differentiation of purified, culture-expanded human mesenchymal stem cells in vitro. *J Cell Biochem* **64**, 295-312 (1997).
- 375 Cassella, J. P., Garrington, N., Stamp, T. C. & Ali, S. Y. An electron probe X-ray microanalytical study of bone mineral in osteogenesis imperfecta. *Calcif Tissue Int* **56**, 118-122 (1995). <https://doi.org/10.1007/bf00296342>

## References

---

- 376 Seong, J. M., Kim, B. C., Park, J. H., Kwon, I. K., Mantalaris, A. & Hwang, Y. S. Stem cells in bone tissue engineering. *Biomed Mater* **5**, 062001 (2010). <https://doi.org/10.1088/1748-6041/5/6/062001>
- 377 Walsh, S., Jordan, G. R., Jefferiss, C., Stewart, K. & Beresford, J. N. High concentrations of dexamethasone suppress the proliferation but not the differentiation or further maturation of human osteoblast precursors in vitro: relevance to glucocorticoid-induced osteoporosis. *Rheumatology (Oxford)* **40**, 74-83 (2001). <https://doi.org/10.1093/rheumatology/40.1.74>
- 378 Rotman, S. G. *et al.* Development of bone seeker–functionalised microspheres as a targeted local antibiotic delivery system for bone infections. *J Orthop Translat* **21**, 136-145 (2020). [https://doi.org:https://doi.org/10.1016/j.jot.2019.07.006](https://doi.org/https://doi.org/10.1016/j.jot.2019.07.006)
- 379 Burdick, J. A., Chung, C., Jia, X., Randolph, M. A. & Langer, R. Controlled degradation and mechanical behavior of photopolymerized hyaluronic acid networks. *Biomacromolecules* **6**, 386-391 (2005). <https://doi.org/10.1021/bm049508a>
- 380 Van Den Bulcke, A. I., Bogdanov, B., De Rooze, N., Schacht, E. H., Cornelissen, M. & Berghmans, H. Structural and rheological properties of methacrylamide modified gelatin hydrogels. *Biomacromolecules* **1**, 31-38 (2000). <https://doi.org/10.1021/bm990017d>
- 381 Hasler, J., Hatt, L. P., Stoddart, M. J. & Armiento, A. R. Stable Reference Genes for qPCR Analysis in BM-MSCs Undergoing Osteogenic Differentiation within 3D Hyaluronan-Based Hydrogels. *Int J Mol Sci* **21** (2020). <https://doi.org/10.3390/ijms21239195>
- 382 Stadelmann, V. A. *et al.* Longitudinal time-lapse in vivo micro-CT reveals differential patterns of peri-implant bone changes after subclinical bacterial infection in a rat model. *Sci. Rep.* **10**, 20901 (2020). <https://doi.org/10.1038/s41598-020-77770-z>
- 383 Guillaume, O. *et al.* Introduction of the Anspach drill as a novel surgical driller for creating calvarial defects in animal models. *J. Orthop. Res.* **37**, 1183-1191 (2019). <https://doi.org/10.1002/jor.24265>
- 384 Guillaume, O. *et al.* Surface-enrichment with hydroxyapatite nanoparticles in stereolithography-fabricated composite polymer scaffolds promotes bone repair. *Acta Biomater* **54**, 386-398 (2017). <https://doi.org/10.1016/j.actbio.2017.03.006>
- 385 Zhang, C. *et al.* Incidence of and trends in hip fracture among adults in urban China: A nationwide retrospective cohort study. *PLoS Med.* **17**, e1003180 (2020). <https://doi.org/10.1371/journal.pmed.1003180>



## References

---

- 386 Adami, G. *et al.* Osteoporosis in 10 years time: a glimpse into the future of osteoporosis. *Ther Adv Musculoskelet Dis* **14**, 1759720x221083541 (2022). <https://doi.org/10.1177/1759720x221083541>
- 387 Percie du Sert, N. *et al.* Reporting animal research: Explanation and elaboration for the ARRIVE guidelines 2.0. *PLoS Biol.* **18**, e3000411 (2020). <https://doi.org/10.1371/journal.pbio.3000411>
- 388 Pittenger, M. F. *et al.* Multilineage potential of adult human mesenchymal stem cells. *Science* **284**, 143-147 (1999). <https://doi.org/10.1126/science.284.5411.143>
- 389 Miller, M. A. *et al.* Autologous bone grafting on steroids: preliminary clinical results. A novel treatment for nonunions and segmental bone defects. *Int Orthop* **35**, 599-605 (2011). <https://doi.org/10.1007/s00264-010-1013-9>
- 390 Schepler, H. *et al.* Acceleration of chronic wound healing by bio-inorganic polyphosphate: In vitro studies and first clinical applications. *Theranostics* **12**, 18-34 (2022). <https://doi.org/10.7150/thno.67148>
- 391 Müller, W. E. G. *et al.* Amplified morphogenetic and bone forming activity of amorphous versus crystalline calcium phosphate/polyphosphate. *Acta Biomater* **118**, 233-247 (2020). <https://doi.org/10.1016/j.actbio.2020.10.023>
- 392 Müller, W. E. G., Tolba, E., Schröder, H. C., Muñoz-Espí, R., Diehl-Seifert, B. & Wang, X. Amorphous polyphosphate-hydroxyapatite: A morphogenetically active substrate for bone-related SaOS-2 cells in vitro. *Acta Biomater* **31**, 358-367 (2016). <https://doi.org/10.1016/j.actbio.2015.11.060>
- 393 Visser, J. *et al.* Endochondral bone formation in gelatin methacrylamide hydrogel with embedded cartilage-derived matrix particles. *Biomaterials* **37**, 174-182 (2015). <https://doi.org/10.1016/j.biomaterials.2014.10.020>
- 394 Cheng, S. L., Yang, J. W., Rifas, L., Zhang, S. F. & Avioli, L. V. Differentiation of human bone marrow osteogenic stromal cells in vitro: induction of the osteoblast phenotype by dexamethasone. *Endocrinology* **134**, 277-286 (1994). <https://doi.org/10.1210/endo.134.1.8275945>
- 395 Hu, D. P. *et al.* Cartilage to bone transformation during fracture healing is coordinated by the invading vasculature and induction of the core pluripotency genes. *Development* **144**, 221-234 (2017). <https://doi.org/10.1242/dev.130807>
- 396 Wong, S. A., Rivera, K. O., Miclau, T., Alsberg, E., Marcucio, R. S. & Bahney, C. S. Microenvironmental Regulation of Chondrocyte Plasticity in Endochondral Repair—A New Frontier for Developmental Engineering.

## References

---

- Frontiers in Bioengineering and Biotechnology* **6** (2018).  
<https://doi.org/10.3389/fbioe.2018.00058>
- 397 Yan, H. J. *et al.* Synthetic design of growth factor sequestering extracellular matrix mimetic hydrogel for promoting in vivo bone formation. *Biomaterials* **161**, 190-202 (2018).  
<https://doi.org/10.1016/j.biomaterials.2018.01.041>
- 398 Yamamoto, M., Tabata, Y. & Ikada, Y. Ectopic bone formation induced by biodegradable hydrogels incorporating bone morphogenetic protein. *J Biomater Sci Polym Ed* **9**, 439-458 (1998).  
<https://doi.org/10.1163/156856298x00550>
- 399 Lantigua, D., Wu, X., Suvarnapathaki, S., Nguyen, M. A. & Camci-Unal, G. Composite Scaffolds from Gelatin and Bone Meal Powder for Tissue Engineering. *Bioengineering (Basel)* **8** (2021).  
<https://doi.org/10.3390/bioengineering8110169>
- 400 Podestà, M. A., Remuzzi, G. & Casiraghi, F. Mesenchymal Stromal Cells for Transplant Tolerance. *Front. Immunol.* **10**, 1287 (2019).  
<https://doi.org/10.3389/fimmu.2019.01287>
- 401 Thitiset, T., Damrongsakkul, S., Yodmuang, S., Leraanansaksiri, W., Apinun, J. & Honsawek, S. A novel gelatin/chitooligosaccharide/demineralized bone matrix composite scaffold and periosteum-derived mesenchymal stem cells for bone tissue engineering. *Biomater Res* **25**, 19 (2021). <https://doi.org/10.1186/s40824-021-00220-y>
- 402 Schmidt-Bleek, K., Kwee, B. J., Mooney, D. J. & Duda, G. N. Boon and Bane of Inflammation in Bone Tissue Regeneration and Its Link with Angiogenesis. *Tissue Eng Part B Rev* **21**, 354-364 (2015).  
<https://doi.org/10.1089/ten.TEB.2014.0677>
- 403 Schlundt, C. *et al.* Individual Effector/Regulator T Cell Ratios Impact Bone Regeneration. *Front. Immunol.* **10**, 1954 (2019).  
<https://doi.org/10.3389/fimmu.2019.01954>
- 404 Garske, D. S. *et al.* Alginate Hydrogels for In Vivo Bone Regeneration: The Immune Competence of the Animal Model Matters. *Tissue Eng Part A* **26**, 852-862 (2020). <https://doi.org/10.1089/ten.TEA.2019.0310>
- 405 McClure, M. J. *et al.* RNU (Foxn1 (RNU)-Nude) Rats Demonstrate an Improved Ability to Regenerate Muscle in a Volumetric Muscle Injury Compared to Sprague Dawley Rats. *Bioengineering (Basel)* **8** (2021).  
<https://doi.org/10.3390/bioengineering8010012>

## References

---

- 406 Kim, B. S., Shkempi, F. & Lee, J. In Vitro and In Vivo Evaluation of Commercially Available Fibrin Gel as a Carrier of Alendronate for Bone Tissue Engineering. *Biomed Res Int* **2017**, 6434169 (2017). <https://doi.org/10.1155/2017/6434169>
- 407 Komatsu, K. *et al.* Cationized gelatin hydrogels mixed with plasmid DNA induce stronger and more sustained gene expression than atelocollagen at calvarial bone defects in vivo. *J Biomater Sci Polym Ed* **27**, 419-430 (2016). <https://doi.org/10.1080/09205063.2016.1139486>
- 408 Lin, S. *et al.* Tailored biomimetic hydrogel based on a photopolymerised DMP1/MCF/gelatin hybrid system for calvarial bone regeneration. *J Mater Chem B* **6**, 414-427 (2018). <https://doi.org/10.1039/c7tb02130e>
- 409 Chen, M. C., Chiu, H. C., Kuo, P. J., Chiang, C. Y., Fu, M. M. & Fu, E. Bone formation with functionalized 3D printed poly- $\epsilon$ -caprolactone scaffold with plasma-rich-fibrin implanted in critical-sized calvaria defect of rat. *J Dent Sci* **16**, 1214-1221 (2021). <https://doi.org/10.1016/j.jds.2021.01.015>
- 410 Zhang, Y. *et al.* Efficient regeneration of rat calvarial defect with gelatin-hydroxyapatite composite cryogel. *Biomed Mater* **15**, 065005 (2020). <https://doi.org/10.1088/1748-605X/ab9422>
- 411 Yeom, J., Hwang, B. W., Yang, D. J., Shin, H. I. & Hahn, S. K. Effect of osteoconductive hyaluronate hydrogels on calvarial bone regeneration. *Biomater Res* **18**, 8 (2014). <https://doi.org/10.1186/2055-7124-18-8>
- 412 Agrali, O. B. *et al.* Evaluation of the Effectiveness of Esterified Hyaluronic Acid Fibers on Bone Regeneration in Rat Calvarial Defects. *Biomed Res Int* **2018**, 3874131 (2018). <https://doi.org/10.1155/2018/3874131>
- 413 Li, Z. & Helms, J. A. Drill Hole Models to Investigate Bone Repair. *Methods Mol Biol* **2221**, 193-204 (2021). [https://doi.org/10.1007/978-1-0716-0989-7\\_12](https://doi.org/10.1007/978-1-0716-0989-7_12)
- 414 Sohn, H. S. & Oh, J. K. Review of bone graft and bone substitutes with an emphasis on fracture surgeries. *Biomater Res* **23**, 9 (2019). <https://doi.org/10.1186/s40824-019-0157-y>
- 415 Haugen, H. J., Lyngstadaas, S. P., Rossi, F. & Perale, G. Bone grafts: which is the ideal biomaterial? *J. Clin. Periodontol.* **46 Suppl 21**, 92-102 (2019). <https://doi.org/10.1111/jcpe.13058>
- 416 Wang, W. & Yeung, K. W. K. Bone grafts and biomaterials substitutes for bone defect repair: A review. *Bioact Mater* **2**, 224-247 (2017). <https://doi.org/10.1016/j.bioactmat.2017.05.007>

## References

---

- 417 Fernandez de Grado, G. *et al.* Bone substitutes: a review of their characteristics, clinical use, and perspectives for large bone defects management. *J Tissue Eng* **9**, 2041731418776819 (2018). <https://doi.org/10.1177/2041731418776819>
- 418 Cheng, G., Guo, S., Wang, N., Xiao, S., Jiang, B. & Ding, Y. A novel lamellar structural biomaterial and its effect on bone regeneration. *RSC Adv* **10**, 39072-39079 (2020). <https://doi.org/10.1039/d0ra05760f>
- 419 Javaid, S., Gorji, H. T., Soulami, K. B. & Kaabouch, N. Identification and ranking biomaterials for bone scaffolds using machine learning and PROMETHEE. *Research on Biomedical Engineering* **39**, 129-138 (2023). <https://doi.org/10.1007/s42600-022-00257-5>
- 420 Shayesteh Moghaddam, N. *et al.* Metals for bone implants: safety, design, and efficacy. *Biomanufacturing Reviews* **1**, 1 (2016). <https://doi.org/10.1007/s40898-016-0001-2>
- 421 Zhou, J. *et al.* Evolution from Bioinert to Bioresorbable: In Vivo Comparative Study of Additively Manufactured Metal Bone Scaffolds. *Adv Sci (Weinh)*, e2302702 (2023). <https://doi.org/10.1002/advs.202302702>
- 422 Zhang, J. *et al.* Biodegradable metals for bone fracture repair in animal models: a systematic review. *Regen Biomater* **8**, rbaa047 (2021). <https://doi.org/10.1093/rb/rbaa047>
- 423 Liu, X., Sun, S., Wang, N., Kang, R., Xie, L. & Liu, X. Therapeutic application of hydrogels for bone-related diseases. *Front Bioeng Biotechnol* **10**, 998988 (2022). <https://doi.org/10.3389/fbioe.2022.998988>
- 424 Dumas, J. E. *et al.* Balancing the rates of new bone formation and polymer degradation enhances healing of weight-bearing allograft/polyurethane composites in rabbit femoral defects. *Tissue Eng Part A* **20**, 115-129 (2014). <https://doi.org/10.1089/ten.TEA.2012.0762>
- 425 Gerhardt, L. C. & Boccaccini, A. R. Bioactive Glass and Glass-Ceramic Scaffolds for Bone Tissue Engineering. *Materials (Basel)* **3**, 3867-3910 (2010). <https://doi.org/10.3390/ma3073867>
- 426 Hollister, S. J. *et al.* Design control for clinical translation of 3D printed modular scaffolds. *Ann Biomed Eng* **43**, 774-786 (2015). <https://doi.org/10.1007/s10439-015-1270-2>
- 427 Rady, A. A. M., Hamdy, S. M., Abdel-Hamid, M. A., Hegazy, M. G. A., Fathy, S. A. & Mostafa, A. A. The role of VEGF and BMP-2 in stimulation of bone healing with using hybrid bio-composite scaffolds coated implants in animal model. *Bulletin of the National Research Centre* **44**, 131 (2020). <https://doi.org/10.1186/s42269-020-00369-x>

## References

---

- 428 Geng, Y. *et al.* BMP-2 and VEGF-A modRNAs in collagen scaffold synergistically drive bone repair through osteogenic and angiogenic pathways. *Commun Biol* **4**, 82 (2021). <https://doi.org:10.1038/s42003-020-01606-9>
- 429 Liu, S. *et al.* Nerves within bone and their application in tissue engineering of bone regeneration. *Front. Neurol.* **13**, 1085560 (2022). <https://doi.org:10.3389/fneur.2022.1085560>

## **Acknowledgements**

During the past 4 years of my PhD studies, I had the privilege to learn from my mentors, who guided me through this challenging and fulfilling time of research. I had the opportunity to work alongside amazing colleagues and friends, who helped me grow not only as a scientist, but also as a person. I had a highly valuable supporting system from family, friends, and my partner, who were always there for me when I needed them. These important people I would like to thank.

To Martin, for giving me the opportunity to be one of your PhD students and letting me work and grow as part of your team. For giving me the freedom to experiment and to fail. For giving me amazing people to work for and with. For giving me your trust, guidance, mentorship, advice, inputs, support, and time during my journey to obtain this title. I am grateful for the opportunities you gave me. Thank you.

To Marcy, for accepting to be my university supervisor and taking the time for meetings, giving me support and advice and going through my thesis. Your scientific inputs have always been highly valuable to me. I am grateful for encouragement. Thank you.

To Angela, for taking me under your wing and teaching me everything you know about science. Not only for your close and direct supervision, but also your friendship. For your constant support, help and patience through the whole PhD. For pushing me and bringing the best out of me. For showing me how to be pure and honest in the lab. I am grateful for everything you taught me. Thank you.

To Keith, for seeing potential in me and recruiting me to be part of your team before I started the PhD. For your constant support and guidance. For all the time and effort, you put towards helping me, especially for teaching me scientific writing and revising my papers. Your intellect and patience are an inspiration to me. Thank you.

## Acknowledgements

---

To Fergal, for being part of the examination committee and taking time to go through my thesis. Your research has been an inspiration to me, and I highly value your scientific expertise.

To Daphne, for being my closest collaborator, colleague, officemate, ally, companion, and friend in the lab. For your honesty, support, and pastries/cakes. For all the awesome dinner parties and vacations, we had. Thank you for being my partner in crime.

To Sylvie and Maria for closely working with me in the lab. For providing valuable scientific input, effort and output that brought the project steps closer to reaching our goals. Thank you for all your support and fun we had in the lab.

To all the current and former members of the progenitor cell biology group Yann, Elena, Géraldine, Laura, Liru, Carolina, Ursula, Simona and Priscilla for your support, knowledge, and countless valuable meetings and discussions not only about science itself, but also about how to be a scientist. Thank you for making me feel part of a team.

To my family, my parents Hans and Emmanuela, my brothers Hans and Raphael (+ Seraina and Luana) and my sister Jackeline for your immense mental support and having my back. I am grateful to be part of this beautiful family. Home is where you are. Thank you.

To all my friends from Davos, Zürich, Liechtenstein, and Germany for always being there for me. For the countless laughs, movie nights, sport sessions, parties, holidays, and adventures. For an unforgettable and precious time. I am grateful to have such a great support system and close friendships. Thank you.

To my amazing partner Franziska, for sharing this journey with me. For your support, warmth, kind hearth, and love. I am grateful for the passions we share. Thank you for everything and more.

# LUAN PHELIPE HATT

## Curriculum Vitae

✉ Im Quäderle 2, 9490 Vaduz, Liechtenstein  
📅 20.03.1994 🇩🇪 German/Brazilian  
📧 hatt.phelipe@gmail.com ☎ +423 78 666 33  
🌐 linkedin.com/in/phelipehatt



## PROFILE

I am a doctoral candidate in the field of progenitor cell biology for bone tissue engineering purposes. With over five years of project management expertise within a research institute, I have demonstrated my ability to manage my own projects and gain necessary laboratory and scientific skills in material sciences, biology and biomedical engineering. My academic and research experience has gained me outstanding communication and organizational skills, enabling me to work effectively and responsibly in a collaborative and interdisciplinary team. My Ph.D. project involved the development and validation of biomaterials for bone tissue engineering purposes

## EXPERIENCE

### AO Research Institute (ARI) Davos

#### Doctoral Candidate at the Progenitor Cell Biology Group

📅 01.2020 – 12.2023 📍 Davos, CH

- Research regarding bone regeneration using personalised cutting-edge medical technologies

#### Research Intern at the Biomedical Materials - and Bone Biology Group

📅 09.2018 – 12.2019 📍 Davos, CH

#### Research Fellow: Master Thesis at the Biomedical Materials Group

📅 04.2018 – 09.2018 📍 Davos, CH

### ETH Zurich

#### Research Intern at the Institute for Biomechanics

📅 02.2017 – 06.2017 📍 Zurich, CH

- Research regarding skin repair applications.

#### Teaching Assistant at the Institute for Biomechanics

📅 09.2015 – 02.2017 📍 Zurich, CH

Lead over exercise classes and assisting students in small groups

- Product Design in Medical Engineering
- Biomechanics

## EDUCATION

### ETH Zurich

#### Master's degree in Medical Technologies

📅 02.2017 – 02.2019 📍 Zurich, CH

- Focus on biomaterials for translational medicine

#### Bachelor's degree in Health Science and Technology

📅 09.2013 – 02.2017 📍 Zurich, CH

### KTH Stockholm

#### Exchange semester in Medical Engineering

📅 08.2017 – 01.2018 📍 Stockholm, S

## PERSONAL COMPETENCES

- Analytical and problem-solving skills
- Project management and organizational skills
- Communication and presentation skills
- Team-player and leadership skills
- Proficient in English and German (written and verbal)

## PROFESSIONAL COMPETENCES

- Cell culturing and molecular biology techniques
- Biomaterials and chemical/mechanical analysis
- Microscope: SEM, Confocal, Optical, Fluorescence
- Computer: MS Office, Matlab, R, CAD, ImageJ

## ACHIEVEMENTS

- Led interdisciplinary projects to conduct cutting-edge research in tissue engineering and regenerative medicine
- Published multiple research papers in reputable scientific journals
- Collaborated with industry partners to translate research findings into practical applications
- Presented research findings at international conferences

## EXTRACURRICULAR ENGAGEMENT

### Teaching Certificate

#### In Health Sciences and Technology

📅 08.2021 – 10.2023 📍 Zurich, CH

#### Board member in the student association

##### President

📅 12.2015 – 02.2017 📍 Zurich, CH

#### Culture and Events

📅 11.2014 - 12.2015 📍 Zurich, CH

## REFERENCES

### Prof. Dr. Martin Stoddart

📧 martin.stoddart@aofoundation.org

✉ Progenitor Cell Biology Group at ARI Davos

☎ +41 81 414 24 48

### Dr. Angela Armiento

📧 angela.armiento@ucb.com

✉ Senior Research Scientist at UCB

☎ +44 7536397676



## List of Publications

Van der Heide D., **Hatt L. P.**, Della Bella E., Hangartner A., Yuan H., De Groot-Barrère F., Stoddart M. J., D'Este M. 3D Printing and osteogenic properties of a Composite Ink Consisting of Collagen, Hyaluronic Acid and Calcium Phosphate. *Acta Biomater*, 2023 (under revision)

**Hatt, L. P.**, Van der Heide D., Armiento A. R., Stoddart M. J.  $\beta$ -TCP from 3D-printed composite scaffolds acts as an effective phosphate source during osteogenic differentiation of human mesenchymal stromal cells. *Front Cell Dev Biol*, 2023, 11, 1258161.

**Hatt, L. P.**, Wirth, S., Ristaniemi, A., Ciric, D. J., Thompson, K., Eglin, D., Stoddart M. J., Armiento, A. R. Micro-porous PLGA/ $\beta$ -TCP/TPU scaffolds prepared by solvent-based 3D printing for bone tissue engineering purposes. *Regen Biomater*, 2023, rbad084.

**Hatt, L. P.**, Armiento, A. R., Mys, K., Thompson, K., Hildebrand, M., Nehrbass, D., Müller W. E. G., Zeiter S., Eglin D., Stoddart, M. J. Standard *in vitro* evaluations of engineered bone substitutes are not sufficient to predict *in vivo* preclinical model outcomes. *Acta Biomater*, 2023, 156, 177-189.

**Hatt, L. P.**, Thompson, K., Helms, J. A., Stoddart, M. J., Armiento, A. R. Clinically relevant preclinical animal models for testing novel craniomaxillofacial bone 3D-printed biomaterials. *Clin Transl Med*, 2022, 12(2), e690.

Armiento, A.R., **Hatt, L. P.**, Sanchez, G., Thompson, K., Stoddart, M. J. Functional Biomaterials for Bone Regeneration: A Lesson in Complex Biology. *Adv Funct Mater*, 2020, 1909874

## List of Publications

---

Hasler, J., **Hatt, L. P.**, Stoddart, M. J., Armiento, A. R. Stable reference genes for qPCR analysis in BM-MSCs undergoing osteogenic differentiation within 3D hyaluronan-based hydrogels. *Int J Mol Sci*, 2020 21(23), 9195.

**Hatt, P. L.**, Thompson, K., Mueller, W.E.G., Stoddart, M. J., Armiento, A.R. Calcium Polyphosphate Nanoparticles Act as an Effective Inorganic Phosphate Source During Osteogenic Differentiation of Human Mesenchymal Stem Cells. *Int J Mol Sci*, 2019, 20, 5801

## List of Conference Attendances

### Oral Presentations:

$\beta$ -TCP from 3D-printed scaffold can act as an effective phosphate source during osteogenic differentiation of human mesenchymal stromal cells, European Cells and Materials Conference, 2023 (**Best Oral Presentation Award**)

Delivery of mesenchymal stromal cells using collagen membranes embedded in LEGO®-inspired multicomponent scaffolds for personalised mandibular defect repair, Swiss Society for Biomaterials and Regenerative Medicine, 2022

Delivery of mesenchymal stromal cells using collagen membranes embedded in LEGO®-inspired multicomponent scaffolds for personalised mandibular defect repair, Tissue Engineering and Regenerative Medicine International Society, 2022

LEGO®-inspired multicomponent 3D-printed bone substitute for personalised facial bone repair, Graubünden forscht, 2022

LEGO®-inspired microporous scaffolds for personalised mandibular bone repair, Tissue Engineering and Regenerative Medicine International Society, 2021

LEGO®-inspired microporous scaffolds for personalised mandibular bone repair, Swiss Society for Biomaterials and Regenerative Medicine, 2021

Calcium polyphosphate nanoparticles act as effective inorganic phosphate source during the in vitro osteogenic differentiation of human mesenchymal stem cells, Swiss Society for Biomaterials and Regenerative Medicine, Young Scientist Symposium, 2020

Ca-Polyphosphate-NP as inorganic phosphate source during the in vitro osteogenic differentiation of human bone marrow-derived MSCs, Swiss Bone and Mineral Society, 2019

### **Rapid Fire + Poster Presentations:**

$\beta$ -TCP from 3D-printed scaffold can act as an effective phosphate source during osteogenic differentiation of human mesenchymal stromal cells, European Society for Biomaterials, 2023

$\beta$ -TCP from 3D-printed scaffold can act as an effective phosphate source during osteogenic differentiation of human mesenchymal stromal cells, Swiss Society for Biomaterials and Regenerative Medicine, Young Scientist Symposium, 2023

### **Poster Presentations:**

$\beta$ -TCP from 3D-printed scaffold can act as an effective phosphate source during osteogenic differentiation of human mesenchymal stromal cells, Orthopaedic

Research Society, 2023 Microporous PLGA/ $\beta$ -TCP/TPU scaffolds prepared by solvent based 3D printing for bone tissue engineering purposes, European Cells and Materials Conference, 2023